HAL
open science

Energy Conversion Processes related to Dipolarization Fronts in the Earth's magnetotail

Soboh Alqeeq

To cite this version:

Soboh Alqeeq. Energy Conversion Processes related to Dipolarization Fronts in the Earth's magnetotail. Astrophysics [astro-ph]. Sorbonne Université, 2022. English. NNT : 2022SORUS504 . tel-04050012

HAL Id: tel-04050012

https://theses.hal.science/tel-04050012v1

Submitted on 29 Mar 2023

HAL is a multi-disciplinary open access archive for the deposit and dissemination of scientific research documents, whether they are published or not. The documents may come from teaching and research institutions in France or abroad, or from public or private research centers.

L'archive ouverte pluridisciplinaire **HAL**, est destinée au dépôt et à la diffusion de documents scientifiques de niveau recherche, publiés ou non, émanant des établissements d'enseignement et de recherche français ou étrangers, des laboratoires publics ou privés.

Energy Conversion Processes related to Dipolarization Fronts in the Earth's magnetotail

Thèse de doctorat de la Sorbonne Université de Paris

Ecole Doctorale Astronomie et Astrophysique d'Ile de France

Spécialité de doctorat : Astronomie et Astrophysique

Thèse présentée et soutenue à Jussieu, le 21/12/2022, par

SOBOH W. S. ALQEEQ

Composition du Jury :

Karine Issautier Directrice de recherche, CNRS et Observatoire de Paris	Présidente
Claire Foullon Researcher, University of Exeter	Rapportrice
Thierry Passot Directeur de recherche, CNRS et Observatoire de la Côte d'Azur	Rapporteur
Cecilia Norgren Researcher, University of Bergen	Examinatrice
Christian Jacquey Astronome, Observatoire Midi-Pyrénées et Université Toulouse III	Examinateur
Suleiman Baraka Researcher, University of Alberta	Examinateur
Patrick Canu Directeur de recherche, CNRS	Directeur de thèse
Olivier Le Contel Chargé de recherche, HDR, CNRS	Co-directeur de thèse

SORBONNE UNIVERSITÉ

Thèse de doctorat

Acknowledgment

I would like to convey my heartfelt gratitude to everyone who supported me during my PhD project.

First and foremost, I must respect and appreciate my family. My parents (Wajih and Hannan) devotedly spent their entire life motivating their kids to go for higher education to create change in the world with unwavering support and commitment. I would like to thank my wife, Sara for her patience in my absence, her endless support and the beauty she added to my life. You have made my colourless life into colourful life. Thanks to my brothers and sisters Nemer, Abed, Haneen and Tasneem for making me happy in this life. Without their love and faith amidst all the difficulties, I would not have made it this far. In particular, I would like to thank my grandmother Sakiba and my all my uncles and my aunts. I am greatly indebted to the memory of my aunt Najah, who is the epitome of strength, beauty and purity. I wouldn't be who I am today if it wasn't for you. I am extremely grateful to you.

I would like to thank my advisors Olivier Le Contel and Patrick Canu. I'm deeply grateful for your patience and your guidance. Olivier, thank you for believing in this ambitious, challenging, and fascinating project. Exciting for me. Throughout this project, I faced a lot of troubles but it was also a great opportunity to meet and work with people of extraordinary value and experience. Olivier, I thank you in every sense of the word for what I have become today. Over the past three years, I have learned a lot from you and developed my abilities and capabilities. I still thank you for supporting my idea of working on Python. Thank you Olivier for your support and your time.

I would like to express my gratitude to Cecilia Norgren, Christian Jacquey, Suleiman Baraka and Karine Issautier, who agreed to be members of my PhD committee. It has been a real honour for me. In particular, I would like to thank the two referees, Claire Foullon and Thierry Passot, for the interest they showed in my investigation and for having read my manuscript so thoroughly. I'm grateful to Fabrice Mottez and Lotfi Ben Jaffel who have been the members of my comité de suivi de thèse.

I would like to thank all the members of the Plasmas Spatiaux group of the Laboratoire de Physique des Plasmas (LPP). In particular, I would like to thank Thomas Chust and Alessandro Retinò, who has always been always ready to discuss and support, and also Gaëtan Gauthier, Lina Hadid, Dominique Fontaine, Laurent Mirioni, Alexis Jeandet and many others. Gaëtan, Theo Pellegrin and Mohammed Baraka, it has been a pleasure to share the office with you. Thank you for all the kind moments.

Thank you to Fatima Mehrez and Mohammed Mazen for all the great discussions about science, art, life, and history and all the optimistic energy.

I would like to thank the entire MMS team for providing data publicly available from the MMS Science Data Center (http://lasp.colorado.edu/mms/sdc/public/) and the SPEDAS software team in particular E. Grimes for pyspedas effort developments. I would like to thank the scientists that I had the opportunity to meet during workshops and international conferences, especially Daniel J. Gershman, Rumi Nakamura, Daniel Schmid and Giulia Cozzani. I would like to thank them for the fruitful discussions we had. A particular thanks to Rumi Nakamura, for her encouraging, kind words and thanks for the kind invitation to visit the Austrian Academy of Sciences (OeAW). They mean a lot to me.

Thank you to Young Dae Yoon, Jérémy Dargent, Emanuele Cazzola and Smilei team. Your contribution has been vital and an enormous part of what I have known about simulations reached from you. Thank you for your patience and your fervour, working on the Smilei PIC code has been really enriching for me.

I'm deeply grateful to Suleiman who has always supported me and believed in me. You have given me a great opportunity by introducing me to Olivier as a very enthusiastic student and a hard worker in research. Thanks for the influence you have made in my life by supervising my books e.g., Introduction to Astronomy and Light is the Messenger of Heaven to Earth.

I'm enormously thankful to Zeyad Al Sahhar, who is an example of strength and honesty to me. Thanks for all the grateful discussions about science and all the positive energy. Thanks for your time and various tips in life.

I would to thank, Michel Meyer, Claude Thomas and Yolande Klein, who are given me great help in learning French.

Finally, I would like to point out that my PhD project has been realised thanks to the co-funding from the Centre National d'Etudes Spatiales (CNES) and the PAUSE program (http://www.college-de-france.fr/le-college/programme-pause).

Résumé
Des écoulements rapides de plasma ont été détectés depuis longtemps dans le côté nuit de la magnétosphère terrestre, la queue géomagnétique. Différents processus de formation tels que la reconnexion magnétique ou l'instabilité cinétique de ballonnement-interchange sont toujours étudiés. Lors de leur propagation vers la Terre, ces écoulements produisent une brusque augmentation de la composante nord du champ magnétique appelée front de dipolarisation (DF). Ces structures cinétiques contribuent de manière significative à la dissipation d'énergie dans la magnétosphère. Cette étude a pour but de mieux comprendre les processus de conversion d'énergie décrits par le terme $\mathbf{J} \cdot \mathbf{E}$ ($\mathbf{J}$ étant la densité de courant et $\mathbf{E}$ le champ électrique) qui se produisent au voisinage de ces fronts et à déterminer leur rôle dans le cycle global de l'énergie dans la magnétosphère. En utilisant les mesures *in situ* de la mission Magnétosphérique Multiscale, constituée de quatre satellites identiques évoluant dans une configuration tétraédrique et séparés à l'échelle des électrons, j'ai d'abord étudié les structures de densité de courant, les différents termes de la loi d'Ohm, et les processus de conversion d'énergie de 6 fronts. J'ai montré que les ions étaient découplés du champ magnétique principalement par l'effet du champ électrique de Hall mais que la contribution du terme lié au gradient de pression électronique pourrait être aussi significative. Cela implique aussi que les électrons pourraient être aussi découplés au niveau du front par le terme lié à leur gradient de pression dans la loi d'Ohm. En ce qui concerne les processus de conversion d'énergie dans le référentiel du satellite, l'énergie est transférée des champs électromagnétiques au plasma en amont du front (région de dissipation ou de charge) alors qu'elle est transférée du plasma aux champs (région de dynamo ou de générateur) en aval. Cette inversion de la conversion d'énergie est causée par l'inversion du courant diamagnétique dominé par le gradient de pression des ions au niveau du front. Dans le référentiel fluide (électrons ou ions), l'énergie est transférée aux champs en raison du champ électrique associé au gradient de pression électronique ce qui pourrait contribuer au ralentissement de l'écoulement. De plus, il est montré que les processus de conversion d'énergie ne sont pas homogènes à l'échelle électronique principalement en raison des variations du champ électrique. Ces résultats d'études de cas ont été étendus grâce à une étude statistique réalisée sur l'ensemble de la saison 2017 durant laquelle MMS était localisée dans la queue géomagnétique. A partir de cette étude, il s'avère que deux classes de DF peuvent être distinguées. La classe I (74,4%) correspond aux propriétés standards des DF et à une dissipation d'énergie. La classe II (25,6%), qui est nouvelle, inclut les 6 DF précédemment discutés et correspond à une bosse du champ magnétique associée à un minimum des pressions ionique et électronique et à une inversion du processus de conversion d'énergie (dissipation puis dynamo). L'origine possible de cette deuxième classe est discutée. Pour les deux classes de DF, il est montré que le processus de conversion d'énergie dans le réferentiel du satellite est gouverné par le courant diamagnétique dominé par le gradient de pression des ions. Dans le référentiel fluide, il est lié au gradient de pression des

électrons.

Résumé pour le domaine public
Des écoulements rapides de plasma sont détectés depuis longtemps dans le côté nuit de la magnétosphère terrestre, la queue géomagnétique. En se propageant vers la Terre, ces écoulements produisent une forte augmentation de la composante nord du champ magnétique appelée front de dipolarisation (DF) et contribuent de manière significative à la dissipation d'énergie dans la magnétosphère. En utilisant les mesures *in situ* recueillies en 2017 par la mission Magnétosphérique Multiscale, constituée de quatre satellites identiques évoluant dans une configuration tétraédrique et séparés à l'échelle des électrons, deux classes de DF peuvent être distinguées. La classe I (74,4%) présente des propriétés DF standards et à une dissipation d'énergie alors qu'une nouvelle classe II (25,6%) correspond à une bosse du champ magnétique et une inversion du transfert d'énergie (dissipation puis dynamo). Pour les deux classes, la conversion d'énergie est gouvernée par le gradient de pression des ions.

Summary

Fast plasma flows have been detected in the nightside of the Earth's magnetosphere, the magnetotail, for a long time. Different processes such as magnetic reconnection or kinetic ballooning-interchange instability are still investigated. While propagating Earthward, these flows generate a sharp increase of the northward component of the magnetic field named dipolarisation front (DF). These kinetic scale structures contribute significantly to the energy dissipation in the magnetosphere. This study aims at better understanding the energy conversion processes described by $\mathbf{J} \cdot \mathbf{E}$ ($\mathbf{J}$ being the current density and $\mathbf{E}$ the electric field) which occur in the vicinity of these fronts and at determining their role in the energy global cycle of the magnetosphere. Using in situ measurements from the Magnetospheric Multiscale mission, which consists of four identical satellites evolving in a tetrahedral configuration and separated at electron scales, I have first investigated the current density structures, the different terms of the Ohm's law, and the energy conversion processes for 6 DFs. I found that for all DFs, ions are mainly decoupled from the magnetic field by the Hall electric field but the term related to the electron pressure gradient could also contribute. It implies that electrons could be decoupled at DF by their own pressure gradient term in the Ohm's law. Regarding the energy conversion processes in the spacecraft frame, the energy is transferred from the electromagnetic fields to the plasma ahead of the DF (dissipation or loading region) whereas it is transferred from the plasma to the fields (dynamo or generator region) behind the front. This energy conversion reversal is caused by the reversal of the ion diamagnetic current at DF. In the fluid frame, the energy is always transferred to the fields, due to the electric field generated by the electron pressure gradient, which could contribute to the slow-

down of the flow. Furthermore, it is shown that the energy conversion processes are not homogeneous at the electron scale mostly due to the variations of the electric fields. These case study results have been extended thanks to a statistical study carried out over the full 2017 magnetotail season. From this study, it turns out that two DF classes can be distinguished : class I (74.4%) corresponds to the standard DF properties and energy dissipation whereas a new class II (25.6%), which includes the 6 DF previously discussed, corresponds to a bump of the magnetic field associated with a minimum of the ion and electron pressures and a reversal of the energy conversion process. The possible origin of this second class is discussed. For both DF classes, it is shown that the energy conversion process in the spacecraft frame is driven by the diamagnetic current dominated by the ion pressure gradient. In the fluid frame, it is driven by the electron pressure gradient.

Summary for public domain

Fast plasma flows have been detected in the nightside of the Earth's magnetosphere, the magnetotail, for a long time. While propagating toward the Earth, these flows generate a sharp increase of the northward component of the magnetic field named dipolarisation front (DF) which contribute significantly to the energy dissipation in the magnetosphere. Using in situ measurements gathered in 2017 by the Magnetospheric Multiscale mission, which consists of four identical satellites evolving in a tetrahedral configuration and separated at electron scales, two DF classes can be distinguished. Class I (74.4%) presents standard DF properties and energy transfer from the electromagnetic fields to the plasma whereas a new class II (25.6%) corresponds to a bump of the magnetic field and a reversal of the energy transfer (dissipation then dynamo). For both classes, this energy transfer is driven by the ion pressure gradient.

Table of Content

Table of Content ix

List of Figures xvi

List of Tables xvii

Acronyms xix

1 Introduction 1

1.1 Preface 1
1.2 The Earth's magnetosphere environment 5
1.3 Dipolarization front (DF) 6
1.4 Thesis organisation 8

2 An overview of DF in the Earth's magnetotail 11

2.1 Introduction 12
2.2 General properties of DFs : standard case 12
2.3 Formation mechanisms of DF 14
2.3.1 DFs generated by magnetic reconnection 15
2.3.2 DFs generated by kinetic ballooning interchange instability 16
2.3.3 DFs generated by low entropy magnetic flux tube instability 17
2.4 DF modellings using MHD 18
2.5 DF properties at ion and electron scales 19
2.6 Wave measurements in the vicinity of DFs 19
2.7 Energy conversion processes at DFs 21
2.8 Current density structures associated with DFs 22
2.9 Summary 25

3 MMS mission and methods of space data analysis 27
3.1 Introduction . . . 28
3.2 The MMS mission . . . 28
3.2.1 Orbit and mission phases . . . 29
3.2.2 The spacecraft . . . 33
3.2.3 Data Products . . . 39
3.3 Discontinuity analysis . . . 39
3.3.1 Minimum Variance Analysis (MVA) . . . 39
3.3.2 Timing analysis (a multi-satellite method) . . . 41
3.3.3 Gradient estimate (a single-satellite method) . . . 42
3.4 Current density computations . . . 42
3.4.1 Current density computation using particle (FPI) measurements . . . 44
3.4.2 Current density computation using the curlometer (multi-satellite) technique and the magnetic field (FGM) measurements . . . 44
3.4.3 Diamagnetic current density estimates . . . 46
3.5 Superposed epoch analysis (SEA) . . . 46

4 The homogeneity of energy conversion 49
4.1 Data and Methods . . . 50
4.2 Overview of classical DF properties . . . 50
4.3 Current density and Hall electric field comparisons . . . 54
4.4 Analysis of Ohm's Law . . . 56
4.5 Energy conversion processes at the DF . . . 60
4.6 Discussion and summary . . . 68

5 A statistical study of DFs observed by MMS 73
5.1 Introduction . . . 74
5.2 Data, Methods and Event Selection . . . 74
5.2.1 Data . . . 74
5.2.2 Selection criteria . . . 74
5.2.3 Methods . . . 75
5.3 Statistical overview of classical DF properties . . . 77
5.4 Current density structures associated with DF . . . 81
5.5 Statistical analysis of the Ohm's Law . . . 82
5.6 Energy conversion at DF . . . 84
5.7 Discussion and summary of the DF statistical study . . . 88
5.8 The nature of the class II DFs . . . 91

6 Conclusions and outlook 93
6.1 Summary of main results . . . 93
6.2 Further works . . . 96

A Programming Environments **97**
A.1 PYSPEDAS 97
A.2 AIDApy 97
A.3 SpacePy 98
A.4 Github 98

B Supplementary materials of Chapter 4 **99**

C Supplementary materials of Chapter 5 **131**

D Publications and Communications **141**
D.1 Publications 141
D.2 Communications 141
D.3 Collaboration 143

Bibliography **145**

List of Figures

1.1 Examples of astrophysical plasmas. [A] Activity in the plasma of the Sun corona. Image credit by NASA/SDO/AIA. [B] Artist's concept of a supermassive black hole. Image credit by NASA/JPL-Caltech. [C] The Eagle Nebula. Image credit by NASA, ESA and the Hubble Heritage Team (STScI/AURA). 2

1.2 Graphical image representing the effect of the solar wind in plasma domesticating of the Earth's magnetosphere, (Nagy et al., 2016). . 3

1.3 (A) Schematic image representing the structure of Earth's magnetosphere and the process of reconnection between the geomagnetic and interplanetary fields. Image credit by : National Academy Press, (Board et al., 2004). (B) Magnetic reconnection in the tail of Earth's magnetosphere, ESA/ATG medialab. (C) Schematic of the dipolarization front structure in the Earth's magnetotail (modified from (e. g., Fu et al., 2012a; Huang et al., 2015; Fu et al., 2020)) 7

2.1 DF signature (vertical red dashed line) denoted DF1 in GSE frame, all data are averaged over the four satellites. Panel (A) shows the magnetic field components and their magnitude, (B) the components of ion velocity and the X component of the V_{H+} proton velocity, (C) the electron and ion temperatures with the isotropic proton temperature, (D) the electron density, (E) the ion and electron pressures. Vertical black dashed line indicates a possible flux rope signature. 13

2.2 A schematic presenting the DF formation from the magnetic reconnection process (adapted from Xu et al. (2018); Fu et al. (2020)). . 15

2.3 A schematic presenting the ballooning instability (adapted from Ohtani and Tamao (1993)). 16

2.4 Schematic image representing the association between Energy Conversion Regions (ECRs) and BBFs in the equatorial plane (adapted from Hamrin et al. (2011)). 23
2.5 Schematic presenting the FAC structures associated with the DF with (b) a magnetic dip in the current sheet plane as region 1 and (c) without a magnetic dip as region 2 (adapted from Sun et al. (2013)). 24

3.1 MMS orbital geometry and science Region of Interest (ROI). Adapted from Tooley et al. (2016). 30
3.2 A day in the life of MMS orbit indicates the region of interest in light yellow (ROI). 32
3.3 FIELDS sensors on the MMS spacecraft. Adapted from Burch et al. (2015) 34
3.4 (a) The magnetic ring cores, with their drive windings, the sense windings, and their relative positions and orientations. (b) The elements are shown in part (a) situated within a set of feedback windings. Adapted from Russell et al. (2016) 35
3.5 Each FPI 180° polar angle top hat is mounted so that the 180° fan spans from the spacecraft spin axis to the anti-spin axis. Each sensor is oriented so that the 16 pixels (each nominally 11.25° wide) of its 180° Field Of View (FOV) are viewing radially in velocity space, spanning the 180° pole-to-pole range in the spinning spacecraft reference frame, Adapted from Pollock et al. (2016). 36
3.6 To meet temporal requirements, thirty-two azimuthal fields of view using eight spectrometers (four dual spectrometers) are deployed around each MMS observatory perimeter. Nominally identical fields of view are provided for electrons and for ions. Eight spectrometers for each species, each exercising four deflected fields of view, yields thirty-two azimuth samples for each species, Adapted from Pollock et al. (2016). 37
3.7 Schematic drawing of the HPCA sensor showing the main optical design elements together with characteristic ion and electron trajectories. The ion trajectories through the ESA are shown with the RF field operating to deflect protons (black trajectories) while transmitting O+ (red trajectories), Adapted from Young et al. (2016). 38
3.8 Detection of measurements by MMS, the magnetic field measurements are marked by a plane moving with time, that is, the different magnetic field populations are seen as a change in the time series, and all spacecraft are assumed to be planar on the scale of the tetrahedron. 43
3.9 Schematic representation of the current density estimation using the Curlometer technique. 45

3.10 Example of SEA using MMS dataset for DF events. The black line marks the superposed epoch median, the red dashed line marks the superposed epoch mean, and the blue fill marks the range. 48

4.1 DF1 signature in LMN frame, all data are averaged over the four satellites then time averaged at 0.3 s. Panel (A) shows the magnetic field components and its magnitude, (B) the components of ion velocity from FPI and the N component of the V_{H+} HPCA velocity, (C) the electron and ion temperatures from FPI with the isotropic proton temperature from HPCA, (D) the electron density, (E) the ion and electron pressures from FPI. Vertical black dashed lines indicate possible flux rope signatures (see text). 53

4.2 DF1 LMN frame, comparison between current densities calculated from $\mathbf{J}_{part} = en_e(\mathbf{v}_i - \mathbf{v}_e)$ and $\mathbf{J}_{curl} = \nabla \times \mathbf{B}/\mu_0$: (A) along L, (B) along M, (C) along N, and Hall electric field comparison between two computations $\mathbf{J}_{part}/(en_e)$ and $\mathbf{J}_{curl}/(en_e)$: (D) along L, (E) along M, (F) along N. 55

4.3 Panels A, B, and C show L, M, N components of Ion Ohm's Law terms respectively : $\mathbf{E}+\mathbf{v_i}\times\mathbf{B}$ (blue line), $(\mathbf{J}_{part}\times\mathbf{B})/(ne)$ (orange line). Panel C also includes electron pressure gradient term along N (green line). 58

4.4 Panels A, B, and C shows L, M, N components of electron Ohm's Law terms respectively : $\mathbf{E} + \mathbf{v_e} \times \mathbf{B}$ (blue line), and $\mathbf{E} + \mathbf{v_i} \times \mathbf{B} - (\mathbf{J}_{curl} \times \mathbf{B})/(ne)$(orange line). Panel C also includes electron pressure gradient term along N (green line). 59

4.5 For DF1 event and in LMN frame : (A) Magnitude and components of the magnetic field, (B) Electric field components, (C) Current density components using $\mathbf{J}_{part}$, (D) Energy conversion $\mathbf{j}_{part} \cdot \mathbf{E}$ (in the spacecraft frame). 62

4.6 For DF1 event and in LMN frame : (A) Components of the Electric field, (B) Current density components using $\mathbf{J}_{part}$, (C) Energy conversion $\mathbf{j}_{part} \cdot \mathbf{E}$ (in the spacecraft frame), (D) Separate contributions of energy conversion term $\mathbf{j}_{part} \cdot \mathbf{E}$ (GSE) and , (E) Separate contributions of energy conversion term $\mathbf{j}_{part} \cdot \mathbf{E}$ (LMN). 63

4.7 For DF1 event and in LMN frame : (A) Components of the electric field in the electron frame ($\mathbf{E}' = \mathbf{E} + \mathbf{V}_e \times \mathbf{B}$), (B) Current density components using $\mathbf{J}_{part}$, (C) Energy conversion $\mathbf{j}_{part} \cdot \mathbf{E}'$ (in the fluid frame), (D) Separate contributions of energy conversion term $\mathbf{j}_{part} \cdot \mathbf{E}'$ (GSE) and (E) Separate contributions of energy conversion term $\mathbf{j}_{part} \cdot \mathbf{E}'$ (LMN) including the contribution of the electron pressure gradient $(-J_N.\nabla P_e/(en))$. 64

4.8 Comparison of the energy conversion term in both electron and ion frames. (A) Four spacecraft average of the energy conversion using $\mathbf{J}_{curl}$, (B) Four spacecraft average of the energy conversion using $\mathbf{J}_{part}$, (C) Energy conversion using $\mathbf{J}_{part}$ for MMS1 (black), MMS2 (red), MMS3 (green), and MMS4 (blue). 65
4.9 Components of the current density obtained from FPI in GSE for each MMS satellite and the four spacecraft average (panels A, B and C). Panel D shows the standard deviation SD($\mathbf{j}$) of each component of the current density. Panel E shows the SD($\mathbf{j}$) normalized by the current density error bar, see text for details. 66
4.10 Same as Figure 4.9 for the electric field in the electron frame ($\mathbf{E}' = \mathbf{E} + \mathbf{V}_e \times \mathbf{B}$). Panel E shows the standard deviation normalized by the error bar of $\mathbf{E}'$, see text for details. 67

5.1 An overview of all DFs events that match the selection criteria. Panels (A) XY and (B) XZ position of MMS during the observations of the 132 DF events in GSE. 76
5.2 MMS orbit regarding the magnetotail season of 2017 (1st of May to end of July in GSE frame. Panel (A) show MMS orbit in XY plane and (B) in XZ plane. 76
5.3 Histograms of the normal components in GSE, from TA panels (A), (B) and (C) and from MVAB panels (D), (E), and (F). Panel (G) shows the magnitude of the normal velocity obtained by TA. . . . 78
5.4 Superposed epoch analysis plots of DF signatures using 132 DFs, in their respective LMN frame, all data being time averaged at 0.3 s. In each panel, the black line marks the superposed epoch median, the red dashed line marks the superposed epoch mean, and the blue fill marks the interquartile range. (A) Magnetic field B_L, (B) electron density N_e, (C) and (D) electron and ion pressures from FPI, (E) HPCA proton temperature T_{H^+}, (F) and (G) perpendicular electron T^e_{perp} and ion T^i_{perp} temperatures from FPI, (H) HPCA normal proton bulk velocity $V_{H^+_,N}$, (I) FPI normal ion bulk velocity vi_N. 80
5.5 An overview of the class I and class II events that match the selection criteria. The colors represent the change in the northward magnetic field component $< B_z >$ time averaged over the full DF time interval, and the arrows represent the DF velocity perpendicular to the boundary (obtained by TA), projected onto the XY plane in GSE. 81
5.6 For both categories, superposed epoch analysis of the current densities along M calculated by using : (A) $J_{dia-e} = B_L/B^2\nabla_n P_e$, (B) $J_{dia-i} = B_L/B^2\nabla_n P_i$, (C) $J_{dia-tot} = B_L/B^2\nabla_n(P_e + P_i)$, (D) $\mathbf{J}_{curl} = (\nabla \times \mathbf{B})/\mu_0$, (E) $\mathbf{J}_{part} = en_e(\mathbf{v}_i - \mathbf{v}_e)$. Same color code as Figure 5.4. 83

5.7 Superposed epoch analysis of the ion generalized Ohm's law comparison between different terms. Panel (A) includes the electron pressure gradient term along N. Panels (B), (C) and (D) shows L, M, N components of the electric field $\mathbf{E}^{'} = \mathbf{E} + \mathbf{v_i} \times \mathbf{B}$ and panels (E), (F) and (G) shows L, M, N components of the Hall electric field $\mathbf{J}_{part}/(en_e)$, all data being time averaged at 0.3 s. Same color code as Figure 5.4. 85
5.8 Superposed epoch analysis of the electron generalised Ohm's law comparison between different terms. Panel (A) includes the electron pressure gradient term along N. Panels (B), (C) and (D) shows L, M, N components of the electric field $\mathbf{E}^{'} = \mathbf{E} + \mathbf{v_e} \times \mathbf{B}$, all data being time averaged at 0.3 s. Same color code as Figure 5.4. 86
5.9 Superposed epoch plots of the energy conversion processes. (A) the magnetic field B_L, (B) the electric field E_M, (C) the energy conversion term in s/c frame $\mathbf{j} \cdot \mathbf{E}$, (D) the energy conversion term in electron frame $\mathbf{j} \cdot (\mathbf{E} + \mathbf{v}_e \times \mathbf{B})$, and (E) the current density $Jpart_M$. Same color code as Figure 5.4. 87
5.10 Superposed epoch analysis of the SD of class I and class II for each component of the current density and the electric field in the fluid frame ($\mathbf{E}' = \mathbf{E} + \mathbf{v}_e \times \mathbf{B}$) in GSE, all data being time averaged at 0.3 s. For context, panel (A) the SD($E_x^{'}$), and (B) the SD($E_y^{'}$), and (C) the SD($E_z^{'}$),(D) the SD($Jpart_x$), (E) the SD($Jpart_y$), (F) the SD($Jpart_z$). Same color code as Figure 5.4 89

B.1 Same as Fig. 4.1 for DF2a,b signatures. 100
B.2 Same as Fig. 4.1 for DF3a,b signatures. 101
B.3 Same as Fig. 4.1 for DF4 signature. 102
B.4 Same as Fig. 4.2 for DF2a,b signatures. 103
B.5 Same as Fig. 4.2 for DF3a,b signatures. 104
B.6 Same as Fig. 4.2 for DF4 signature. 105
B.7 Same as Fig. 4.3 for DF2a,b. 106
B.8 Same as Fig. 4.3 for DF3a,b. 107
B.9 Same as Fig. 4.3 for DF4. 108
B.10 Same as Fig. 4.4 for DF2a,b. 109
B.11 Same as Fig. 4.4 for DF3a,b. 110
B.12 Same as Fig. 4.4 for DF4. 111
B.13 Same as Fig. 4.5 for DF2a,b. 112
B.14 Same as Fig. 4.5 for DF3a,b. 113
B.15 Same as Fig. 4.5 for DF4. 114
B.16 Same as Fig. 4.6 for DF2a,b. 115
B.17 Same as Fig. 4.6 for DF3a,b. 116
B.18 Same as Fig. 4.6 for DF4. 117
B.19 Same as Fig. 4.6 for DF2a,b. 118

B.20 Same as Fig. 4.6 for DF3a,b. 119
B.21 Same as Fig. 4.6 for DF4. 120
B.22 Same as Fig. 4.8 for DF2a,b. 121
B.23 Same as Fig. 4.8 for DF3a,b. 122
B.24 Same as Fig. 4.8 for DF4. 123
B.25 Same as Fig. 4.9 for DF2a,b signatures. 124
B.26 Same as Fig. 4.9 for DF3a,b signatures. 125
B.27 Same as Fig. 4.9 for DF4 signature. 126
B.28 Same as Fig. 4.10 for DF2a,b. 127
B.29 Same as Fig. 4.10 for DF3a,b. 128
B.30 Same as Fig. 4.10 for DF4. 129

List of Tables

2.1 Comparison between Dipolarization and DFs 14

3.1 Characteristical values (in km) of electron and ion inertial lengths and Larmor radii at the magnetopause and in the magnetotail. . . 29
3.2 MMS mission phases 31
3.3 Top level burst-mode parameters. Adapted from Burch et al. (2016) 32

4.1 Minimum Variance Analysis (MVAB) Results : Eigenvalue ratios and vectors (in GSE). 52
4.2 Timing analysis Results : Normal vectors and velocity (in GSE) with estimated DF thickness δ. 54

6.1 Summary of class I and class II signatures 95

C.1 MMS located RE [GSE] 132
C.2 MMS located RE [GSE] 133
C.3 The Minimum Variance Analysis Results For Class I (1) 134
C.4 The Minimum Variance Analysis Results For Class I (2) 135
C.5 The Minimum Variance Analysis Results For Class II 136
C.6 The Timing analysis Results For Class I (1) 137
C.7 The Timing analysis Results For Class I (2) 138
C.8 The Timing analysis Results For Class II 139

Acronyms

DF	Dipolarization Front
SW	Solar Wind
IMF	Interplanetary Magnetic Field
ESA	European Space Agency
MMS	Magnetospheric Multiscale
NASA	National Aeronautics and Space Administration
EDR	Electron Diffusion Region
CNES	Centre National d'Etudes Spatiales
MHD	Magnetohydrodynamics
AU	Astronmical Unit
SD	Standard Deviation
GSE	Geocentric Solar Ecliptic coordinate system
GSM	Geocentric Solar Magnetospheric coordinate system
$\mathbf{R}_E$	Earth radius
WW	whistler waves
LHDI	Lower Hybrid Drift Instability
ESW	Electrostatic Solitary Waves
EMW	Electromagnetic Solitary Waves
EMIC	Electromagnetic Ion Cyclotron
FPR	Flux Pileup Region
LHW	Lower Hybrid Waves
FACs	Field-Aligned Currents
ECRs	Energy Conversion Regions
CLR	Concentrated Load Region

CGR Concentrated Generator Region
VDF Velocity Distribution Function
SDP Spin-Plane Double Probe
ADP Axial Double Probe
FGM FluxGate Magnetometer
FPI Fast Plasma Investigation
VDF Velocity Distribution Functions
HPCA Hot Plasma Composition Analyzer
MVAB Minimum Variance Analysis on Magnetic Field
TA Timing Analysis
SEA Superposed Epoch Analysis
ROI Regions Of Interest
FOM Figure Of Merit
SITL Scientist-in-the-Loop
EDP Electric field Double Probe
DFG Digital Fluxgate
AFG Analog Fluxgate
DIS Dual Ion Spectrometers
DES Dual Electron Spectrometers
ASPOC Active control of the spacecraft potential
ESA Electrostatic analyzer
MCP Multi-channel plate
SDC Science Data Center
SPEDAS Space Physics Environment Data Analysis Software
ML Machine learning
DL Deep learning
AI Artificial Intelligence
CDF Common Data Format
MVA Minimum Variance Analysis
MVAB Minimum Variance Analysis of the Magnetic field
MVAE Maximum Variance Analysis of the Electric field
AIDA Artificial Intelligence for heliophysics Data Analysis
SpacePy Tools for Space Science Applications
IDL Interactive Data Language

PIC Particle In Cell

SeaPy State Estimation and Analysis in Python

ROI Region of Interest

IRFU Swedish Institute of Space Physics

LASP Laboratory for Atmospheric and Space Physics

LPP Laboratory of Plasma Physics

KTH KTH Royal Institute of Technology

IRAP Institut de Recherche en Astrophysique et Planetologie

MCPs MicroChannel Plates

GSFC Goddard Space Flight Center

THEMIS Time History of Events and Macroscale Interactions during Substorms

1D One Dimension

2D Two Dimension

3D Three Dimension

AE Auroral Electrojet

s/c Spacecraft

BICI Ballooning-Interchange Instability

BBF Bursty Bulk Flows

LMN Local Boundary Normal Coordinate System

FOV Field Of View

Chapitre 1

Introduction

"Read : In the Name of your Lord, who created. Created man from a clinging clot. Read : And your Lord is the Most Generous. He Who taught by the pen. Taught man what he never knew."

The Quran, *Surat Al-Alaq (The Clot)*

Contents

1.1 Preface **1**
1.2 The Earth's magnetosphere environment **5**
1.3 Dipolarization front (DF) **6**
1.4 Thesis organisation **8**

1.1 Preface

In physics we have four different states of matter, solid, liquid, gas, and finally plasma. A plasma is described as a gas globally neutral and composed of charged particles. Plasma can be produced via different ways : heating an ordinary gas to a particular temperature which enables collisions to separate the charged particles, photoionization by an intense light source, large amplitude high-frequency electric fields, ... More than 99% of all known matter in the universe is in the plasma state see Figure 1.1 (e. g., Baumjohann et al., 1999). This means that plasma is a very important state of matter to study. This applies to all disciplines in which plasma can make a real change in the development of the cognitive structure through scientific applications such as medicine, energy, propulsion, and others. Thus the study of astrophysical and space plasmas of the solar system is not only very important for itself but also because it can contribute to make progress in other fields using plasma as a state of matter.

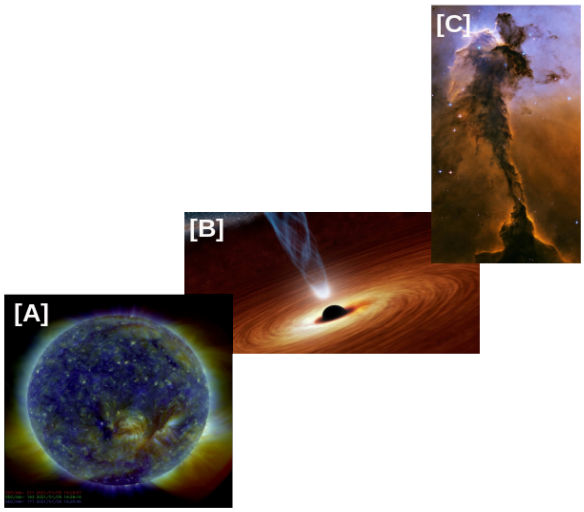

FIGURE 1.1 – Examples of astrophysical plasmas. [A] Activity in the plasma of the Sun corona. Image credit by NASA/SDO/AIA. [B] Artist's concept of a supermassive black hole. Image credit by NASA/JPL-Caltech. [C] The Eagle Nebula. Image credit by NASA, ESA and the Hubble Heritage Team (STScI/AURA).

.

Space plasma is a complex part of plasma physics. For instance, lots of complex physical processes result from the interaction between the Sun and the Earth. Relatively recently the concept of space weather has been associated with the Sun-Earth interactions that can affect the performance of technological systems and/or human life, Williamson et al. (2010). The Solar Wind (SW) is the most important actor of the space weather. This is an outflow of plasma radially ejected by the Sun through the solar system. Its interaction with the internal Earth's dipolar magnetic field generates the magnetosphere. This interaction also produces two fundamental boundaries upstream of the planet : the Bow shock and the magnetopause which separates the shocked SW from the magnetosphere. Thus the SW transporting the Interplanetary Magnetic Field (IMF) is first decelerated at the Bow shock and then deviated at the magnetopause. Due to that interaction the magnetic field around the Earth forms a magnetic bubble girdling the Earth, the magnetosphere detailed in the next section. The magnetosphere shape is compressed on the dayside by the SW while it is extended into a long tail region on the nightside known as the magnetotail, see Figure 1.2 (e.g., Nagy et al., 2016).

One part of the solar energy and plasma reach the Earth via the SW and enter the magnetosphere via different processes : from the dayside reconnection process when the IMF is directed southward in the opposite direction of Earth's dipole, by lobe reconnection or Kelvin-Helmholtz instability when the IMF is directed northward and by diffusion process via wave-particle interactions. Then

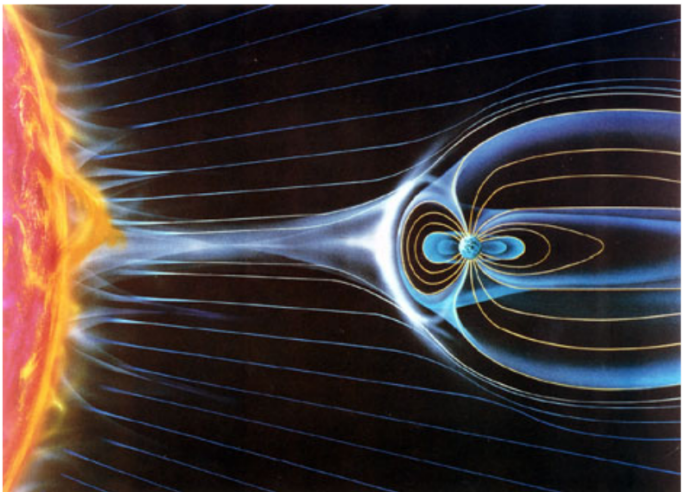

FIGURE 1.2 – Graphical image representing the effect of the solar wind in plasma domesticating of the Earth's magnetosphere, (Nagy et al., 2016).

the energy and plasma are accumulated in the magnetotail and can be suddenly released via instability like collisionless magnetic reconnection or ballooning mode generating fast plasma flows (Baumjohann et al., 1990; Angelopoulos et al., 1992) and auroras see Fig 1.3. This global cycle of energy is also named magnetospheric substorms and their onset mechanism is still a matter of debate (e. g., Lui, 2001; Angelopoulos et al., 2008; Liu et al., 2012; Sitnov et al., 2019).

Fast earthward plasma flows generate an increase of the northward component of the magnetic field called Dipolarization Front (DF). More generally, DFs are magnetic structures that occur due to the propagation of fast plasma flows in the planetary magnetospheres, and have been observed in the Mercury (e. g., Dewey et al., 2018), Earth (e. g., Runov et al., 2009; Sergeev et al., 2009), Saturn (e. g., Xu et al., 2021; Smith et al., 2018), and Jupiter (e. g., Artemyev et al., 2013, 2020) magnetospheres.

If fast flows (Baumjohann et al., 1990) or Bursty Bulk Flows (BBF), which are fast flows lasting about 10 min with a speed larger than 400 km/s (Angelopoulos et al., 1992), have been known for a long time, DFs and their relation with fast flows have been unveiled by the Time History of Events and Macroscale Interactions during Substorms (THEMIS) mission thanks to its five probes radially distributed in the magnetotail (e. g., Runov et al., 2009; Sergeev et al., 2009; Angelopoulos et al., 2013) and also studied by tetrahedral multisatellite missions like the Cluster mission from the European Space Agency (ESA) launched in 2000 (Escoubet and Goldstein, 2001) and more recently the Magnetospheric Multiscale (MMS) mission from the National Aeronautics and Space Administration (NASA) launched in 2015 (Burch et al., 2015).

While the Cluster orbit was polar and satellite separations were between 100

to 10000 km (fluid to ion scales), MMS evolves along an elliptical equatorial orbit with separations near the electron Larmor radius in the Earth magnetosphere (7 to 40 km, Burch et al., 2015). Based on what is stated in (Burch et al., 2015), the principal scientific objective of the MMS mission is to "understand the microphysics of magnetic reconnection by determining the kinetic processes occurring in the electron diffusion region that are responsible for collisionless magnetic reconnection, especially how reconnection is initiated." The Electron Diffusion Region (EDR) is the region where electrons decouple from the magnetic field and magnetic lines reconnect. MMS tetrahedral satellite configuration (like Cluster) allows an estimate of the local current density from the calculation of the curl of the magnetic field measured on four points. Furthermore, the high temporal resolution of the particle detectors which provide the distribution functions at 30 ms for electrons and 150 ms for ions also allows measuring the current density independently of the magnetic field measurements. From these diagnostics, one can also detect the sudden increases of the magnetic field such as DFs associated with thin current sheets and plasma jets propagating at high speed through the magnetotail (e. g., Nakamura et al., 2009; Sitnov and Swisdak, 2011; Liu et al., 2013; Hwang et al., 2014; Schmid et al., 2015). Strong energy dissipation and particle acceleration occur at the fronts while the detailed mechanisms are still ill-understood. Intense lower hybrid wave emissions associated with the front density gradients (e. g., Hosner et al., 2022) and whistler-mode waves downstream of the fronts (e. g., Breuillard et al., 2016) as well as electromagnetic solitary waves (e. g., Le Contel et al., 2017) have been already identified.

The general problem of understanding energy conversion processes in the Earth's magnetosphere in terms of structures and dynamics of systems at the ion and/or electron scales remains a key research topic for magnetospheric and space plasma physicists. This is a quite complex problem that no single study could handle in a satisfactory way.

In this PhD project, my research program focuses on the energy conversion processes associated with DFs observed in the Earth's magnetotail using in-situ measurements provided by the MMS mission. This program research aims at improving our understanding of the role of DFs in the energy global cycle of the magnetosphere. It includes a detailed observational study of six DF events detected during a substorm period. Then in order to extend the results found from these case studies, I have carried out a statistical study over the full magnetotail season in 2017 including more than one hundred cases of DFs, supported by multiple comparisons with previous statistical studies.

1.2 The Earth's magnetosphere environment

As a general characteristic of the plasma system, the plasma particles react collectively to electromagnetic forces ; the fields can be modified by the plasma charge and current densities and reciprocally. As a matter of fact, magnetospheric physics deals with collisionless plasmas as the mean free path of particles is much larger than the size of the system so the kinetic description is based on the Vlasov equation, i.e. the Boltzmann equation without the collisional term, coupled with the Maxwell equations (e. g., Kivelson et al., 1995). Moreover, different approaches and simplifications can be used to solve the system and to understand the mechanisms and dynamics of particles depending notably on the spatial and time scales of the particular process to be studied.

Basically three principal approaches can be used to resolving the plasma system and understanding its mechanisms of action : (1) the fluid approach (e.g., Magnetohydrodynamics (MHD) and multi-fluids) assuming that the spatial (time) scale of the system is larger than the particle Larmor radii (resp. longer than the particle gyroperiods), (2) the fully kinetic approach (with no limitations on spatial and time scales), and (3) hybrid approaches describing the full dynamics of ions but considering electron as a fluid.

The Earth's magnetosphere environment is a considerable research area regarding the study of plasma physics. One can consider it as the closest space plasma physics laboratory that enables us to build new scientific knowledge. It contains many fundamental processes that can influence the plasma dynamics such as collisionless magnetic reconnection, plasma turbulence, collisionless shocks, particle acceleration and fast plasma flows, plasma heating ...

As we previously mentioned, the Earth's magnetosphere is formed by the interaction of the SW with the Earth's magnetic field. The SW is a permanent high-speed plasma outflow that originates from the Sun's corona. Biermann (1951) suggested the existence of a continuous solar wind. Parker presented a model (hydrodynamic) of the SW based on a detailed mathematical theory (Parker, 1958). All properties of the solar wind flow can change through the heliosphere as a function of time. However, the average values for the main solar wind properties at the Earth distance (1 Astronmical Unit (AU)) can be listed : a flow speed $\sim$ 450 km/s, a plasma density $\sim$ 6.8 p.cm^{-3}, and ion and electron temperatures $\sim 1.2 \times 10^5$ K and $\sim 1.4 \times 10^5$ K respectively and magnetic field strength $\sim$ 7 nT. Furthermore, the SW properties depend on the region of its formation. Two fundamental types of it are known as "fast" SW ($V_{fast} \sim 650$ km/s) often coming from the coronal holes which are regions of intense magnetic field (e. g., Gabriel et al., 2003) and "slow" SW ($V_{slow} \sim 350$ km/s) issued from the equatorial region (e. g., Ohmi et al., 2004). On the other hand, the Earth's magnetic field is produced by internal convection inside the core of the planet made of molten iron that acts as a natural dynamo. The Earth's magnetic field axis is tilted by 11 degrees from

the rotational spin axis. Figure 1.3 presents the Earth's magnetosphere as one can describe as the region of space where the Earth's magnetic field affects any electrically charged particles.

As mentioned earlier, my investigations concentrate in the Earth's magnetotail observations. However below, I describe briefly the other regions.

The Bow Shock can be described as evidence of the deflection, the slowdown, and the heating of the SW by a planet, (e. g., Slavin et al., 1979). In the Earth's case, the terrestrial magnetic field provides an obstruction to the SW while for unmagnetized planet like Venus or Mars it is directly the planet surface ; a shock territory is formed upstream of the planet, as a standing shock wave, issued from the interaction of the supersonic, and super alfvénic SW and the planet.

Due to the non stationarity of the SW, the location, size, and shape of the shock wave can vary.

The magnetosheath is a region between the bow shock and the magnetosphere and is formed by the shocked SW downstream of the shock, (e. g., Kivelson et al., 1995). Due to the shock physics which converts the motion energy in thermal energy, the magnetosheath plasma is much hotter, slower, and denser than the SW.

The magnetopause is the current sheet which separates the shocked SW in the magnetosheath from the Earth's magnetospheric region (see Figure 1.3). The magnetopause can be also identified as a discontinuity where the pressure balance between the dynamic pressure of the SW and the magnetic pressure of Earth's dipole field is reached (e. g., Kivelson et al., 1995). Indeed, on the magnetosheath side it is usually assumed that the SW dynamic pressure has been mostly converted in thermal pressure and on the magnetospheric side, dynamic and thermal pressures are much smaller than the magnetic pressure term produced by the Earth's magnetic field.

The Polar Cusps are the regions which can be thought as the contact area between the magnetosheath and the magnetosphere plasmas. In these regions, the Earth's magnetic field has a polar shape and null magnetic field areas both in the northern and southern hemispheres.

1.3 Dipolarization front (DF)

Fast plasma flows in the magnetotail have been investigated for a long time thanks to in-situ space measurements. They contribute significantly to the energy, plasma, and magnetic flux transports in the Earth's magnetosphere (e. g., Baumjohann et al., 1990; Angelopoulos et al., 1992; Shiokawa et al., 1997, 1998). They are thought to be generated by magnetic reconnection (e. g., Sitnov et al., 2009; Drake et al., 2014; Fu et al., 2013), kinetic ballooning interchange instability (Pritchett and Coroniti, 2010) or low entropy magnetic flux tubes (Pontius and Wolf, 1990) ; they can be related to a global scale substorm activity or appear as isolated

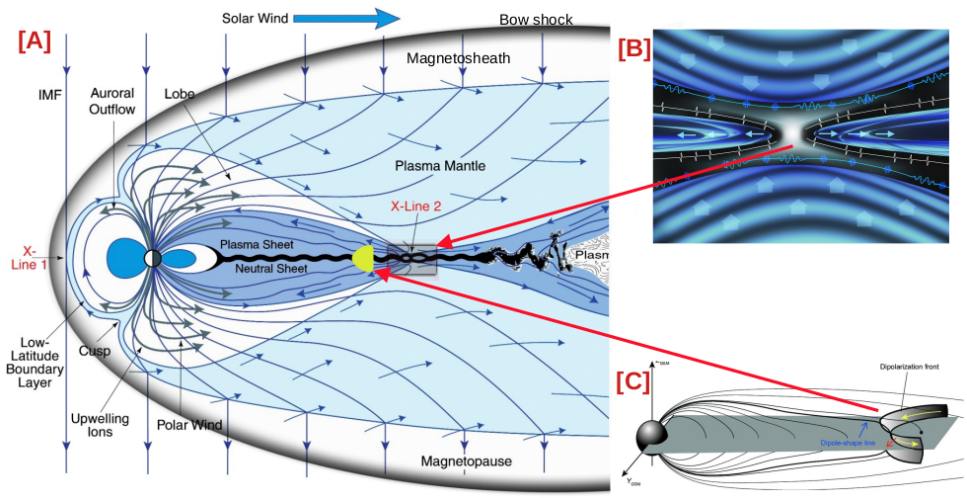

FIGURE 1.3 – (A) Schematic image representing the structure of Earth's magnetosphere and the process of reconnection between the geomagnetic and interplanetary fields. Image credit by : National Academy Press, (Board et al., 2004). (B) Magnetic reconnection in the tail of Earth's magnetosphere, ESA/ATG medialab. (C) Schematic of the dipolarization front structure in the Earth's magnetotail (modified from (e. g., Fu et al., 2012a; Huang et al., 2015; Fu et al., 2020))

.

structures.

DFs, which are mostly characterized by a sharp and transient increase of the normal component (northward) of the magnetic field in the magnetotail, are formed by the fast plasma flow or can be also embedded in the flow. Indeed, using the five THEMIS probes radially distributed in the central plasma sheet, Runov et al. (2009) demonstrated that DFs are coherent forms propagating earthward over a distance of more than 10 Earth radius (R_E) at a velocity of $\sim$ 300 km/s and having a front thickness of around the ion inertial length. They suggested that these DF signatures were consistent with the leading edge of a fast plasma flow generated by a burst of magnetic reconnection in the mid-tail obtained in kinetic simulations (e. g., Sitnov et al., 2009).

The sharp increase of the magnetic field is often interpreted as the development of a magnetic field pile up region behind the front. These fronts can be also preceded by a decrease in the normal component (e. g., Ohtani et al., 2004; Runov et al., 2009; Schmid et al., 2015). The whole spatial scale of DF along its direction of propagation is about few ion inertial lengths (c/ω_{pi}, where ω_{pi} is the ion plasma frequency, Liu et al., 2013; Fu et al., 2012a; Khotyaintsev et al., 2011). A recent review by Fu et al. (2020) has focused on their important role in particle acceleration mechanisms. Using THEMIS data, Angelopoulos et al. (2013) showed that DFs can play a crucial role in the energy dissipation processes occurring in the

magnetotail. This PhD thesis aims at investigating energy conversion processes associated with DFs at ion and electron scales using recent data provided by the MMS mission.

1.4 Thesis organisation

In the following, we shall give an outline of the main idea of each chapter :

Chapter 2 displays an overview of DF observations in the Earth's magnetotail and current knowledge about this topic. In addition, we discuss the possible mechanisms for generating DF, and DF properties at MHD, ion and electron scales. Furthermore, energy conversion processes, structures of the current wedge associated with DF and wave activity in particular about lower-hybrid waves related to DF are briefly also described.

Chapter 3 describes the MMS mission providing information about the spacecraft, the instrumentation suite, the orbit, and data products. Furthermore, different classical methods of spacecraft data analysis used to better understand the physics of DF are detailed.

Chapter 4 summarises my results on the energy conversion processes occurring in the vicinity of DFs. They have been obtained from the detailed analysis of 6 DFs detected by MMS on 23rd of July 2017. In particular, it shows the evaluation of the different terms of Ohm's law for electrons and ions confirming the ion decoupling at DFs by the Hall electric field and the electron pressure gradient ; electron being also decoupled at DF due to the effect of their pressure gradient. In the spacecraft frame, energy is transferred to the plasma ahead of the DF and to the electromagnetic fields behind. In the fluid frame, energy is found to be transferred to the fields only. In addition, the homogeneity of energy conversion processes is investigated using Standard Deviation (SD) estimates of the current density $\mathbf{J}$ and electric field $\mathbf{E}^{'}$ in the plasma frame. It is shown that energy conversion processes occurring in the vicinity of DFs are not homogeneous at the electron scales mostly due to the electric field variations.

Chapter 5 extends the case study results using a statistical study of DF events detected by MMS during the full magnetotail season of 2017 (april-september so including the 6 DF events described in chapter 4). Using a superposed epoch analysis of various DF physical quantities, I have shown that most of the case study results are general. However, I have proposed to distinguish two subcategories of DFs notably depending on the sign of the energy conversion term $\mathbf{J} \cdot \mathbf{E}$. In the spacecraft frame, energy is dissipated ahead of DF for 74.4% of events while 25.6% of event present a reversal of the energy conversion process. The first class corresponds

to the standard DF case whereas the second class is new and its origin is discussed.

Finally in chapter 6, I summarise my main results and discuss further works.

Chapitre 2

An overview of dipolarisation fronts (DFs) in the Earth's magnetotail

"Justice is the soul of the universe."

Omar Khayyam, *The Sufistic Quatrains, p.680, 2015.*

Contents

2.1 Introduction **12**
2.2 General properties of DFs : standard case **12**
2.3 Formation mechanisms of DF **14**
2.3.1 DFs generated by magnetic reconnection 15
2.3.2 DFs generated by kinetic ballooning interchange instability 16
2.3.3 DFs generated by low entropy magnetic flux tube instability 17
2.4 DF modellings using MHD **18**
2.5 DF properties at ion and electron scales **19**
2.6 Wave measurements in the vicinity of DFs **19**
2.7 Energy conversion processes at DFs **21**
2.8 Current density structures associated with DFs **22**
2.9 Summary **25**

2.1 Introduction

Based on the important role that DFs play in the Earth's magnetosphere environment, this chapter reviews some of the main concepts that are associated with DFs and that are extensively used throughout the thesis. Firstly, the general properties of DF are described in section 2.2. Then a brief idea of the formation mechanisms of DFs is given in section 2.3. Previous studies using different MHD modellings of DFs are reviewed in section 2.4 and DF properties at kinetic scale are pointed out in section 2.5. Section 2.6 describes lower hybrid waves are frequently observed growing in the vicinity of DFs. Energy conversion processes and current density structures associated with DFs are presented in section 2.7 and section 2.8 respectively. Finally, the main results are summarized in section 2.9.

2.2 General properties of DFs : standard case

In this section, we describe the standard properties of the most common DF category from one event embedded in a fast earthward flow detected by MMS during a substorm period around 16 : 45 UT on the 23rd of July 2017 (Alqeeq et al., 2022). Figure 2.1 displays general properties of DF from data in Geocentric Solar Ecliptic coordinate system (GSE) (where X is directed toward the Sun, Z is perpendicular to the ecliptic plane and Y is directed duskward). Magnetic field components and magnitude are plotted in Figure 2.1A, ion velocity components and the X component of the proton velocity (V_{H+}) in Figure 2.1B, ion and electron temperatures in Figure 2.1C, electron density in Figure 2.1D, and finally ion and electron pressure variations in Figure 2.1E. Details about the MMS instruments are provided in chapter 3. This DF event is identified by a vertical red dashed line (maximum of the B_z component). Vertical black dashed line indicates a possible signature of flux ropes (a large increase of the total magnetic field due to an increase of the cross-tail Y component, associated with a bipolar signature of another component) ahead of the DF signature (Alqeeq et al., 2022).

As illustrated by Figure 2.1, a standard DF can be identified as a transition between a relatively cold dense plasma at rest with respect to a hot tenuous fast earthward moving plasma with specific characteristics. Its general properties correspond to a sharp increase of the northward magnetic field, a decrease in density, an increase in temperature, a decrease in plasma pressure and an increase in V_{H+} (e. g., Schmid et al., 2015; Alqeeq et al., 2022).

Regarding the spatial scale of DFs, Nakamura et al. (2004) investigated spatial gradients of high-speed flows in the mid-tail plasma sheet using multi-satellite Cluster observations. They found that the typical scales of fast flows/BBFs are

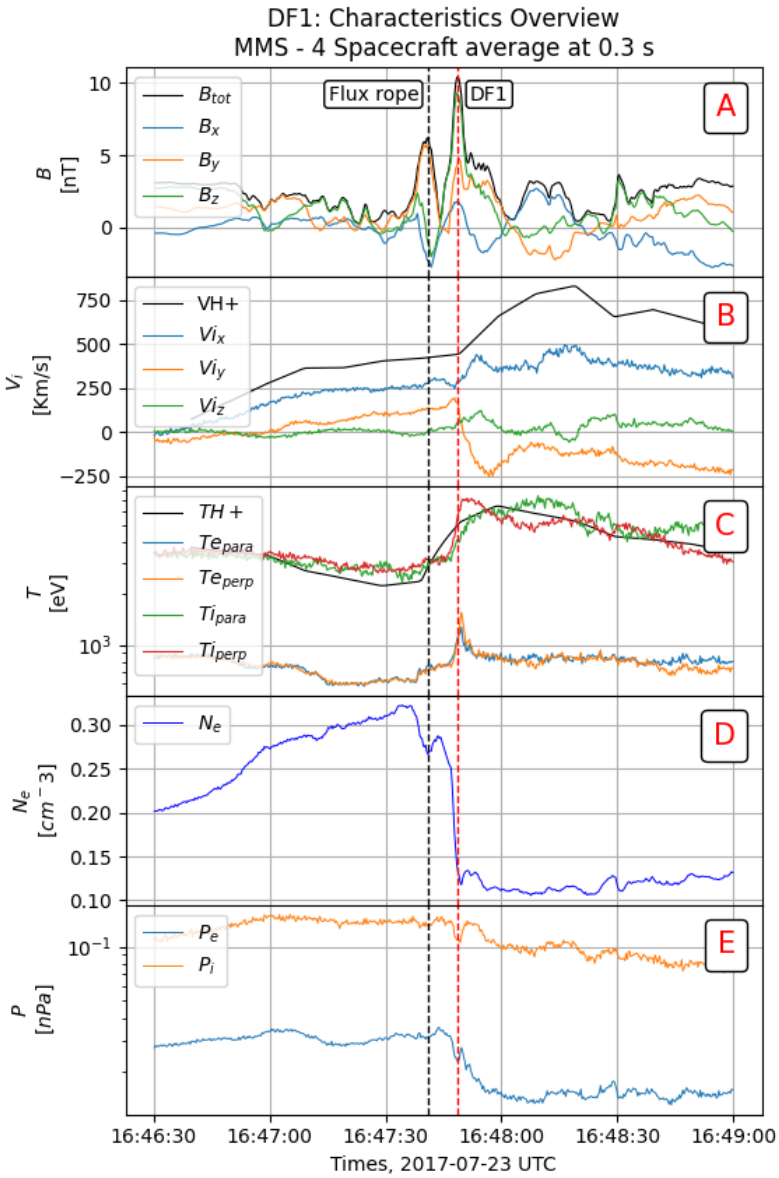

FIGURE 2.1 – DF signature (vertical red dashed line) denoted DF1 in GSE frame, all data are averaged over the four satellites. Panel (A) shows the magnetic field components and their magnitude, (B) the components of ion velocity and the X component of the V_{H+} proton velocity, (C) the electron and ion temperatures with the isotropic proton temperature, (D) the electron density, (E) the ion and electron pressures. Vertical black dashed line indicates a possible flux rope signature.

about 2–3 R_E in the dawn-dusk direction and 1.5–2 R_E in the north-south direction. These scales are considered as upper limits for DFs which can correspond to the flow front or can be embedded in these fast flows.

Based on these observations of standard DF signatures, it is important to point out the differences with the dipolarization process which is also invoked in relation with substorms. A dipolarization of the magnetotail is a large scale process which occurs after the substorm onset (e. g., Pu et al., 1999; Lui, 2011; Tang et al., 2013; Lui, 2013; Hwang et al., 2014). It is the consequence of the current disruption in the near-Earth magnetotail (whatever the instability considered as a substorm trigger) leading to an increase of the northward component of the magnetic field which remains large until the next substorm development. Conversely, a DF is a local transient structure ; the increase of the northward component is transient (typically few tens of seconds). The principle differences are summarized in Table 2.1.

TABLE 2.1 – Comparison between Dipolarization and DFs

#	Comparison	Dipolarization	DF
1	B_z increase	Rapid ∼a few min and large scale >∼ 10 R_E	Transient ∼1-2 min and localised $\sim 3-4$ R_E
2	Propagation	Tailward	Earthward
3	Magnetic fluctuations	Large > 20 nT	Medium/Small $2-20$ nT
4	Source	Current disruption	Fast flows (see section 2.3)
5	When	Always related to substorm onset	After substorm onset or isolated
6	What is ?	Global reconfiguration of the near-Earth magnetotail	Boundary between a relatively cold and dense plasma at rest and a hot tenuous fastly moving plasma

2.3 Formation mechanisms of DF

DFs are considered as a tangential discontinuity (velocity and magnetic field are tangential so with no normal component of the magnetic field and no plasma flux flowing through it) separating a relatively cold dense plasma at rest from a hot tenuous plasma in rapid motion. The origin of the fast flows and their related DFs is still a matter of debate. The main formation mechanisms currently studied are : magnetic reconnection (e. g., Sitnov et al., 2009; Drake et al., 2014), kinetic ballooning interchange instability (e. g., Pritchett and Coroniti, 2010; Panov et al., 2022) or low entropy magnetic flux tubes (e. g., Pontius and Wolf, 1990) ; let's remind that fast plasma flows and DFs can be related to a global scale substorm

activity or appear as isolated structures.

2.3.1 DFs generated by magnetic reconnection

The collisionless magnetic reconnection is one of the fundamental processes in the Earth's magnetosphere. When occurring in the magnetotail, this process can generate divergent fast plasma flows associated with the reconnection of anti-parallel magnetic field lines. A rough estimate based on mass and magnetic flux conservations gives an outflow velocity equals to the Alfvén velocity of the inflow region $B/\sqrt{\mu_0\rho}$ (where B is the magnitude of the magnetic field, μ_0 is the vacuum permeability, ρ is the plasma mass density, e. g., Cassak and Shay, 2007). It has long been shown that the kinetic tearing mode instability is a good candidate to produce magnetic reconnection in the magnetotail (Coppi et al., 1966). However, the rising time of this instability is longer than the particle bounce period along the magnetic field line and it was shown that the compressibility effect associated with the electron bounce motion can stabilise the tearing mode (e. g., Lembege and Pellat, 1982; Pellat et al., 1991). Further calculations have shown that, despite this stabilisation effect, a certain range of plasma parameters and conditions allow the growth of the tearing mode (e. g., Sitnov et al., 2019).

Thus, assuming an ongoing reconnection process, the fast flow moving earthward through the Earth's dipole can generate a DF and causes a significant energy dissipation and plasma transport from the reconnection region to the transition region where fast flows are thought to be braked (e. g., Shiokawa et al., 1997; Sitnov et al., 2009, 2014). However, it is necessary that the reconnection process

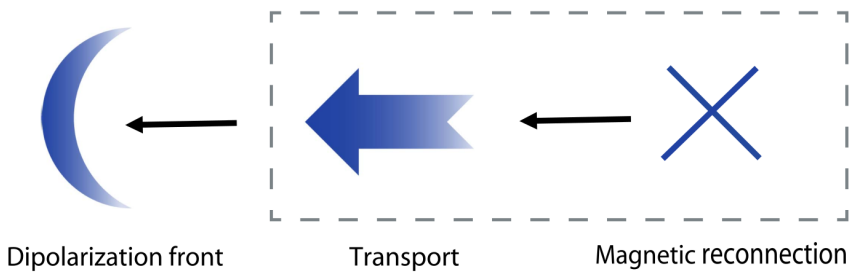

FIGURE 2.2 – A schematic presenting the DF formation from the magnetic reconnection process (adapted from Xu et al. (2018); Fu et al. (2020)).

is localized in the azimuthal direction (direction of the cross-tail current) and not invariant (as assumed for instance when one considers a tearing perturbation in the radial direction only) in order to explain the BBF/DF azimuthal width $\sim 3\ \mathrm{R}_E$. Otherwise, a secondary instability is required to fragment the large scale front of the reconnection jet.

2.3.2 DFs generated by kinetic ballooning interchange instability

In a plasma confined between magnetic mirrors, the curvature of the magnetic field lines can act as an effective gravitational force (directed away from the Earth) and excites a Rayleigh-Taylor type instability. In the magnetotail where the pressure gradient and curvature are directed earthward, the MHD/two fluid ballooning/interchange instability can grow and produce fast radial flows and magnetic reconfigurations (e. g., Ohtani and Tamao, 1993; Miura, 2004). Yet, as for the tearing mode, the frequency of this instability is smaller than the particle bounce frequency along the magnetic field line which makes the fluid treatment questionable. Indeed, in such conditions particles do not respond to the local electric field but to a non local bounce-averaged value which modifies the conditions of stability of the ballooning/interchange mode (e. g., Hurricane et al., 1995).

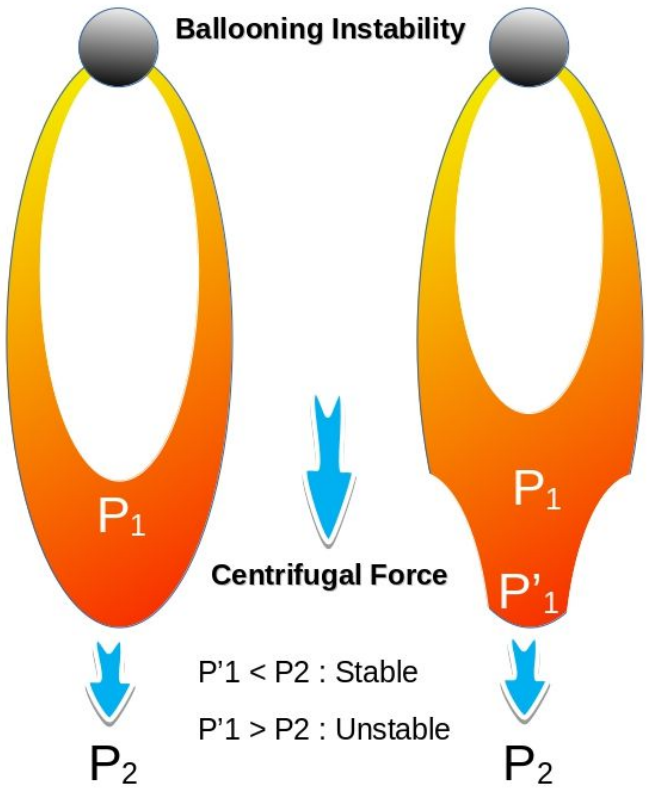

FIGURE 2.3 – A schematic presenting the ballooning instability (adapted from Ohtani and Tamao (1993)).

Considering a magnetotail equilibrium with a minimum of the northward component of the magnetic field along the radial direction and using large-scale

Three Dimension (3D) Particle In Cell (PIC) simulations, Pritchett and Coroniti (2010) showed that a kinetic ballooning/interchange mode becomes unstable in the region tailward of the minimum. The instability grows at wavelengths close to the ion Larmor radius and is able to generate fast flows and associated DFs in the non linear regime. Later, the same authors demonstrated that these results still hold even without a minimum of the northward magnetic field component as long as this latter is slowly decreasing with the distance down the tail (Pritchett and Coroniti, 2013).

2.3.3 DFs generated by low entropy magnetic flux tube instability

Pontius and Wolf (1990) proposed that density depleted flux tubes can be formed in the far magnetotail and named them "plasma bubbles". They showed that these bubbles can propagate earthward by an interchange process similar to the one described in the previous section as the earthward acceleration also occurs in the form of a buoyancy force. Later on, Birn et al. (2004) provided a more precise description of this process by introducing a measure of the entropy per unit magnetic flux of a thin flux tube pV^{γ} where p is the plasma pressure, assumed to be constant along a field line or thin flux tube, and V is the flux tube volume per unit magnetic flux, defined by $V = \int dl/B$ integrated along a field line. Using 3D MHD simulations, they showed that low entropy magnetic flux tubes ("bubbles") can move fastly through the magnetotail. Schindler and Birn (2004) demonstrated that MHD magnetotail equilibria having a pressure profile which decreases down the tail are stable when the entropy increases with the distance down the tail and unstable when it decreases. Thus in this process, the entropy reduction produces the fast earthward flow and its associated DFs but the origin of this reduction is attributed to an external process or to random fluctuations existing in the far tail.

Finally, all these different mechanisms can be coupled. Using 3D MHD simulations of magnetic reconnection in the magnetotail, Birn et al. (2011) showed that fast flows generated by reconnection correspond to magnetic flux tube with a depleted entropy ; they indicated that the onset of magnetic reconnection coincides with a strong reduction of the entropy. Furthermore they suggested that the magnetotail structure in the cross-tail direction is due to the growth of the ballooning/interchange mode. On the other hand, using large scale 3D PIC simulations Pritchett and Coroniti (2013) showed that to destabilise the kinetic ballooning/interchange mode, it is sufficient for the entropy to decrease with distance in the tail. Then the non linear evolution of the instability leads to the formation of fast flow channels (finger-like) and interchange heads (including DF) that propagate earthward. Then onset of localised magnetic reconnection and disruption of the plasma sheet resulted of the impact of the heads with the plasma of the inner

magnetosphere.

Regardless of the formation mechanism, as fast-moving 3D multi-scale structures, DFs play a key role in mass, energy and magnetic flux transport as well as in energy conversion/transfer processes.

2.4 DF modellings using MHD

Numerical MHD modellings allow us to investigate the DF propagation through the magnetotail from the region of their formation to the inner magnetosphere where they are thought to be decelerated and stopped (the braking region) by the strong Earth's magnetic field. They also provide a first estimate of their spatial scales.

Guzdar et al. (2010) using Two Dimension (2D) ideal MHD model and Lu et al. (2013a,b) using 2D MHD-Hall model have compared their results with DF observations provided by the THEMIS mission. They found that the general characteristics and modulation in the dawn-dusk direction of DFs can be described by the MHD interchange instability of the magnetotail.

However, only Lu et al. (2013a,b) were able to show the ion decoupling occurring at the DF due to the ion inertial length scale of the front. Also, they showed that both Hall electric field and electron pressure gradient contribute to produce a dawnward electric drift which modifies the shape of the front. Inside the DF, they found that ions are mainly decoupled by the Hall electric field, pressure gradient effects being smaller. Thus in order to better understand the structure and dynamics of DF and to be able to compare the results with the in-situ measurements provided by the multi-satellite missions (Cluster, THEMIS and MMS) from fluid to electron scales, it is essential to extend previous ideal MHD modellings to Hall-MHD and kinetic numerical modellings.

However, from 3D global MHD simulations (e. g., Ashour-Abdalla et al., 2011; Pan et al., 2014; Fu et al., 2014), the DF scale in the dawn-dusk direction has been estimated ~ 3 R_E in the near Earth's magnetotail consistent with the values around $\sim 3.2 - 3.6$ R_E of the Cluster observations (e. g., Nakamura et al., 2004; Huang et al., 2015).

Lapenta and Bettarini (2011) also performed 3D MHD simulations of magnetic reconnection in the magnetotail to study the DF formation. They showed that flux ropes are created by the reconnection process in 3D after the formation of the divergent reconnection jets and their associated DFs. Then these flux ropes are found unstable against a kink like instability (a current driven instability with long wavelengths compared with the Larmor radius) which is able to structure the flow in the cross-tail direction with a wavelength ~ 0.5 R_E. When these kink unstable flux ropes reach the DF, they are able to excite and select an interchange mode related to the density gradient at the front with a wavelength ~ 1 R_E a bit smaller than estimates from observations.

2.5 DF properties at ion and electron scales

As mentioned in the previous sections, DFs are commonly related to reconnection jets or fast flows/BBFs (e. g., Runov et al., 2009; Fu et al., 2012a; Huang et al., 2015) and are observed from ~ 10 to ~ 30 R_E in the near-Earth magnetotail. Standard thicknesses of DFs along the normal direction estimated from different missions (Cluster e. g., Fu et al., 2012a; Schmid et al., 2011; Xiao et al., 2017), (THEMIS, e. g., Liu et al., 2013) and (MMS e. g., Le Contel et al., 2016; Alqeeq et al., 2022)) vary from ~ 1.7 to ~ 4 ion inertial lengths. Such an ion scale thickness of DFs limits the validity of the results obtained from ideal MHD modelling and requires at least a MHD model including the Hall electric field. Furthermore, the sharp density gradient at DF can lead to the growth of electron scale instability capable to produce some ripples of the front and to modify the current density structures and energy conversion processes as discussed in the next sections. Another important question is about the possible existence of an electron scale current sheet embedded in the ion scale front which could play an important role in the dissipation of energy (e. g., Angelopoulos et al., 2013).

2.6 Wave measurements in the vicinity of DFs

Waves measured around DFs are very important because they contain information about the mechanism of propagation of fronts in the magnetotail, their impact on the structure of these fronts, how particles and fields interact and finally how energy can be exchanged between plasma and fields. In multiple previous studies, different waves associated with DFs were discussed such as : whistler waves (WW) detected before, during and after the DFs (e. g., Huang et al., 2012; Viberg et al., 2014; Li et al., 2015a; Grigorenko et al., 2020), Lower Hybrid Waves (LHW) (e. g., Sergeev et al., 2009; Greco et al., 2017) and Lower Hybrid Drift Instability (LHDI) (e. g., Divin et al., 2015a; Khotyaintsev et al., 2017; Le Contel et al., 2017; Pan et al., 2018; Nakamura et al., 2019a; Li et al., 2020; Hosner et al., 2022), Electrostatic Solitary Waves (ESW) (e. g., Liu et al., 2019; Li et al., 2020) and Electromagnetic Solitary Waves (EMW) (e. g., Andersson et al., 2009; Tao et al., 2011; Le Contel et al., 2017), and more recently the Electromagnetic Ion Cyclotron (EMIC) waves (e. g., Li et al., 2020). However in this section, we will only focus on the wave and particle interactions associated with lower hybrid drift waves.

LHW occurring at DFs have been already studied using data from Cluster, THEMIS and MMS by (e. g., Sergeev et al., 2009; Zhou et al., 2009; Divin et al., 2015a; Greco et al., 2017; Le Contel et al., 2017; Hosner et al., 2022). LHWs are quasi-electrostatic waves in the same frequency range of whistler waves $f_{ci} \leq f_{LH} \ll f_{ce}$, with $f_{LH} = f_{ci} + f_{pi}/\sqrt{1 + f_{pe}^2/f_{ce}^2}$, where f_{ci} and f_{ce} are the ion and electron cyclotron frequencies respectively, f_{LH} is the lower hybrid frequency

and f_{pi}, f_{pe} are the ion and electron plasma frequencies respectively. As in the magnetotail we can assume $(f_{pe}/f_{ce})^2 \gg 1$, f_{LH} becomes $\sim \sqrt{f_{ce}f_{ci}}$. In the context of DF, the free energy source generating LHWs is provided by the sharp density gradient via the LHDI. LHWs propagate at quasi-perpendicular angle with respect to the ambient magnetic field and the LH wavelengths range between the electron and ion thermal gyroradius ($\rho_{i,e} = v_{th,i,e}/(2\pi f_{c,i,e})$ with $v_{thi,e} = (2T_{i,e}/m_{i,e})^{1/2}$ the ion and electron thermal velocities and $T_{i,e}$ the ion and electron temperatures) depending on the plasma conditions (e. g., Huba et al., 1977; Cairns and McMillan, 2005).

LHWs have strong electric field fluctuations perpendicular to the ambient magnetic field and can lead to an effective particle acceleration and/or heating. Zhou et al. (2009) reported on multiple DFs located at the leading edge of earthward propagating plasma bubbles propagating in the near-Earth magnetotail during a substorm observed by THEMIS. They found that the majority of the wave activities at DF were associated with energetic electron flux enhancements and large fluctuations from below the lower hybrid frequency to above the electron cyclotron frequency. They showed that the LHWs can be generated by a diamagnetic current due to the temperature and density gradients present at DF in agreement with the LHDI.

Later, Le Contel et al. (2017) reported on intense LHWs associated with two ion scale DFs detected off-equator (large B_x) by MMS during a substorm period on 10th of August 2016 in the Earth's magnetotail. They showed that the first DF event was associated with a fast dawnward flow and intense LHWs propagating dawnward with a perpendicular phase speed close to the electric drift and the ion thermal velocity consistent with a LHDI. They suggested a possible acceleration of electrons parallel to the background magnetic field caused by the LHW interaction (Cairns and McMillan, 2005). For the second DF event associated with a reversal flow, a much smaller LHW activity was found. Furthermore, Pan et al. (2018) showed in a case study using MMS data that some electron scale ripples propagating along the DF were consistent with the growing of the LHDI with wavelength close to the electron Larmor radius. More recently, Hosner et al. (2022) carried out a statistical investigation of electric field fluctuations in the LH frequency range based on MMS data from 2017 to 2018 in the Earth's magnetotail. They showed that all DF events are associated with a peak of the power of electric field fluctuations integrated over the LH frequency range and with density and pressure gradients confirming the LHDI as the source of these waves. In addition, they showed that the wave power is related to the magnetic flux transfer rate produced by the DFs.

2.7 Energy conversion processes at DFs

Angelopoulos et al. (2013) suggested that DFs could play an important role in the global energy conversion process due to their large-scale propagation through the Earth's magnetosphere. Based on THEMIS data, they showed that energy conversion occurs within an electron scale current sheet (1-10 electron inertial lengths) generated by the DF propagation. Integrated all along the propagation mostly along X_{GSM} direction and assuming a transverse $Y - Z$ section of about 10 R_E^2, the authors suggested that DFs are able to provide a macroscopic energy conversion. Therefore the analysis of the energy conversion at DFs is crucial to understand the global energy cycle in the Earth's magnetosphere. This question is also fundamental for the fast flow propagation itself. Indeed, as the fast flow propagates, the fraction of energy that it can lose due to various energy conversion processes contributes to its braking. Using THEMIS data Chaston et al. (2012) suggested that kinetic Alfvén waves continually radiated toward the auroral region by fast flows during their earthward propagation can extract the total kinetic energy from the flows. Later Hamrin et al. (2014) found indications of fast flow decelerations in the range $-25 < X < -15$ R_E and investigated the related energy conversion processes by computing the $\mathbf{J} \cdot \mathbf{E}$ term (where $\mathbf{J}$ is the current density and $\mathbf{E}$ the electric field in the spacecraft frame). Thanks to a superposed epoch analysis applied on Cluster data, they showed that fast flows with a velocity peak behind the front (equivalent to a growing Flux Pileup Region (FPR) as introduced by Fu et al. (2012b)) are decelerated and that energy is radiated i.e. converted from particles to fields (generator) whereas, when the velocity peak is detected ahead or at DF (decaying FPR as introduced by Fu et al. (2012b)), no braking signature is detected and energy is transferred from fields to particles (dissipation or load). Still from statistical analysis of 2003 Cluster data corresponding to an average subproton scale spacecraft separation of 200 km, Huang et al. (2015) concluded that the energy was significantly transferred from the fields to the plasma at DFs. More recently, using data gathered during the MMS commissioning phase and with a better time resolution for particle measurements (150 ms for ions, 30 ms for electrons), Yao et al. (2017) showed that electron contribution to the DF current density is significant (60% of ions) and produced by the diamagnetic effect. With regards to the energy conversion, they found that the field energy is transferred to the plasma (dissipation) in the spacecraft frame though the velocity peak is detected behind the DF. In the fluid frame (ion or electron), they pointed out that the energy transfer is from particles to fields. Later Liu et al. (2018) showed that ion scale DFs can be also associated with electron scale current sheets. They specify that although their DF event corresponded primarily to an energy transfer from fields to particles, the electron scale currents could also lead to radiating the plasma energy. As mentioned in the previous subsection, such electron scale DF substructures were also reported in previous studies and attributed to the

LHDI growing in the density gradient region (e. g., Sergeev et al., 2009; Divin et al., 2015a; Le Contel et al., 2017; Yang et al., 2017a) leading to ripples on the DF (Pan et al., 2018). Later, these results were confirmed by a statistical study carried out by Zhong et al. (2019) based on 122 DF events detected by MMS in the magnetotail. The contribution of broad band high-frequency waves (with frequencies between the electron gyrofrequency and the plasma frequency) was also investigated and shown to be up to 10% of the total energy conversion at DF (Yang et al., 2017a). Finally, Zhang et al. (2020) suggested that both Joule dissipation via parallel and perpendicular currents as well as radiated energy by kinetic Alfvén waves contribute to the fast flow slowdown. Energy conversion processes have also been investigated recently by 3D kinetic PIC simulations. The role of the LHDI rising at DFs was also investigated and pointed out as significant element of the DF dynamics (Divin et al., 2015b). Later, comparing 3D PIC simulation results and Cluster observations Khotyaintsev et al. (2017) concluded that the energy dissipation in the satellite (Earth) frame was mainly due to the motional electric field and the ion contribution to the current suggesting that LHDI was not contributing to the energy conversion process. They found almost no energy conversion in the DF frame (defined by using the ion velocity at the DF). Using recent theoretical developments in turbulence studies by Yang et al. (2017b), which allow to disentangle ion and electron contributions, Sitnov et al. (2018) showed that ions are heated at and ahead of DFs whereas electrons are heated at and behind due to the long-wavelength LHDI ; therefore both contributions lead to an important energy dissipation. Finally, Nakamura et al. (2019b) also carried out 3D PIC simulations and reported that energy is dissipated in the electron frame at DFs within the density gradient layer due to the LHDI. Their numerical results were shown to be in good agreement with the recent MMS observations described by Liu et al. (2018) although the energy conversion term was estimated in the electron frame for the simulations and in the satellite frame for the observations.

2.8 Current density structures associated with DFs

We have already mentioned that DFs are formed ahead of fast flows/BBFs or can be detected embedded in these flows. BBFs have been shown to be associated with a dynamic current wedge (e. g., Palin et al., 2015) which closes in the ionosphere via the formation of the Field-Aligned Currents (FACs) see Figure 2.4 adapted from Hamrin et al. (2011). It has been suggested that substorm onset could be due to the braking of multiple BBFs in the near-Earth magnetotail and formation of their associated FACs establishing the global substorm current wedge which couples the magnetotail to the auroral regions (e. g., Shiokawa et al., 1998; Yao et al., 2012).

In Figure 2.4, the magenta current circuit connects the auroral region to the magnetotail via FACs generated by the shear and twisting of the magnetic field

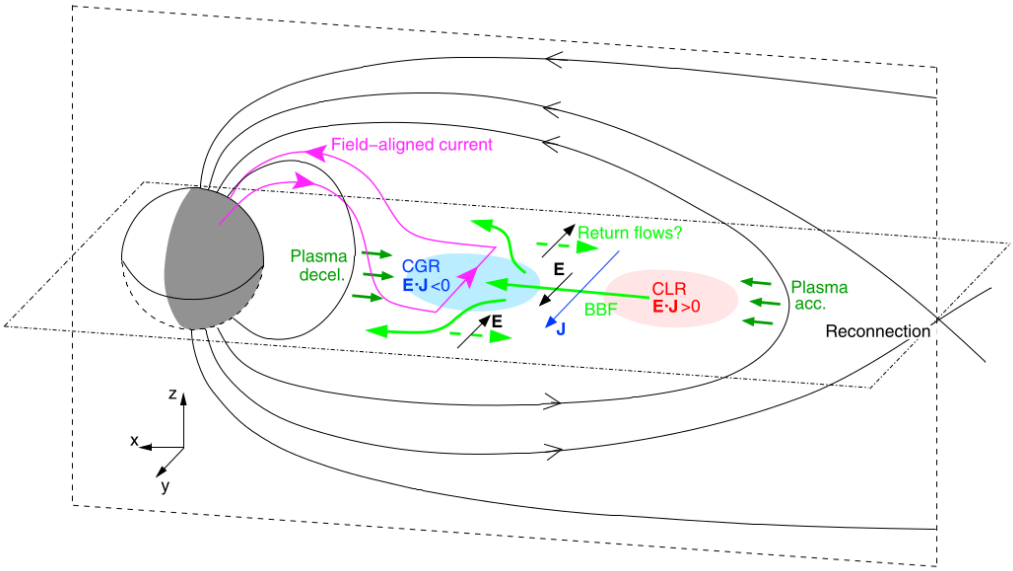

FIGURE 2.4 – Schematic image representing the association between Energy Conversion Regions (ECRs) and BBFs in the equatorial plane (adapted from Hamrin et al. (2011)).

at the flanks of the BBF and leading to a reversal of the cross-tail current ahead of the BBF (see also Birn et al., 2004). In this model, the BBF is produced by the magnetic reconnection occurring farther in the tail. Then two different regions of energy conversion processes (load and generator) are formed due to the BBF propagation and its associated current wedge. In the BBF as mentioned in the previous subsection, the energy is mostly dissipated in the Concentrated Load Region (CLR) while ahead of the BBF the plasma energy is transferred to the electromagnetic fields in the Concentrated Generator Region (CGR) contributing to the flow deceleration

Using Cluster data, Hwang et al. (2011) analysed six DFs and showed that they could be related to the interchange instability at the central current sheet in Earth's magnetotail. Average earthward/dawnward DF velocities were between 160–335 km/s and their front thicknesses were estimated of several ion inertial lengths in agreement with other studies. They showed that enhanced FACs, measured after the DF crossing, are associated with large amplitude fluctuations of the X and Y magnetic field components with 1-2 min (therefore longer than the ion gyroperiod, which is about 10 s at the edge of the current sheet $B_x \sim 10$ nT) and propagating duskward in the frame of the DFs as expected for an interchange instability (e. g., Nakamura et al., 2002; Guzdar et al., 2010; Pritchett and Coroniti, 2010).

Later, Sun et al. (2013) investigated FAC structures associated with 25 DF events observed by Cluster in the Earth's magnetotail from 15 to 20 R_E. Using

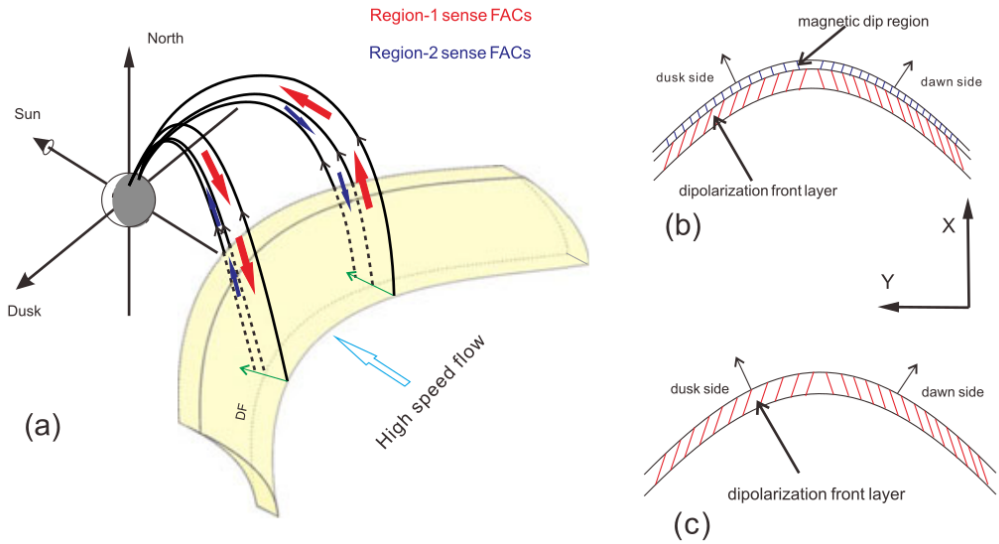

FIGURE 2.5 – Schematic presenting the FAC structures associated with the DF with (b) a magnetic dip in the current sheet plane as region 1 and (c) without a magnetic dip as region 2 (adapted from Sun et al. (2013)).

the curlometer technique, they showed that two different parallel current densities $J_{\|}$ can be distinguished for DFs with B_z dips ahead of the front : one measured before the front (in the dip) $\sim 5-10$ nA/m^2, a second measured through the front (at the sharp increase of B_z) $\sim 10-20$ nA/m^2. Conversely, DFs without magnetic dips have only FACs at the front, see Figure 2.5. It has been shown from 3D PIC simulations that all these off-equator FACs can contribute significantly to the energy conversion processes discussed in the previous subsection (e. g., Pritchett et al., 2014). However from the point of view of in-situ measurements, the lack of simultaneous measurements at different scales (fluid and kinetic) prevents us from carrying out a complete study of these 3D multi-scale structures.

Regarding the cross-tail current structures associated with DFs, Yao et al. (2015) carried out a statistical study of the compressed region formed by the DF arrival using THEMIS observations from the 2007 to 2011 tail seasons. They showed that the plasma pressure gradient ahead of the DF produces the redistribution of the cross-tail current and locally modifies the Earth's magnetotail current system. Notably, this effect is able to produce the magnetic dip observed before the DF. However, they pointed out that the total current density change is one order smaller than the typical total current associated with a moderate substorm current wedge.

Still using THEMIS observations in the near-Earth magnetotail ($X \sim 12$ R$_E$), Lu et al. (2016) showed that the cross-tail current density is significantly reduced near the neutral plane ahead of DFs. In addition, using 2D PIC simulations,

they showed that ion reflection and acceleration at the front create a positive charge density excess. As a consequence, a vertical electric field (E_z) is generated. Electrons being magnetized at DF, conversely to ions, they drift duskward due to this electric field ($E_z \times B_x > 0$) and reduce the total cross-tail current.

From these different previous studies carried out using Cluster, THEMIS or MMS data, we see that fast flows/BBFs and DFs are associated with complex current density structures coupling physical processes at large (ionosphere/magnetosphere) and kinetic (DF) scales. In the present study, I will mainly investigate the perpendicular current density. The complete understanding of the full current wedge associated with DF is out of the scope of this study and would still require further investigations using 3D numerical simulations and simultaneous in-situ measurements at different scales.

2.9 Summary

In section 2.2, the general DF properties have been reviewed and can be summarised as follows. When observed near the magnetic equator, DFs are characterised by a sharp increase of the northward component of the magnetic field and can be preceded by a dip of the same component. They correspond to a transition layer (tangential discontinuity) from a cold dense plasma at rest to a hot tenuous fast earthward moving plasma. When observed off the equator, the density jump can be reversed as the satellite transitions from the lower density edge of the plasma sheet to the dense central plasma sheet. The differences between localised and transient DF signatures and global and more persistent dipolarisation associated with substorms have also been summarised. In section 2.3, I have briefly described the main mechanisms for generating DFs in the Earth's magnetotail as : reconnection jets produced by the collisionless magnetic reconnection (triggered by tearing mode), the kinetic ballooning interchange instability and low entropy magnetic flux tube instability. Then different DF modellings have been reviewed in section 2.4 and the need of two-fluid and kinetic descriptions has been pointed out due notably to the ion scale DF thickness in section 2.5. An important type of waves, named LHD waves associated with DFs have been described in section 2.6 and their interaction with electrons leading to pitch-angle diffusion or parallel acceleration has been discussed. LHD waves could have also an important impact on DF shapes by generating ripples at electron scales. The possible role of DF in the energy conversion processes through the magnetotail has been discussed in section 2.7. In the spacecraft frame and due to their motion through the magnetotail, DF is thought to strongly contribute to the energy dissipation (mostly due to the convective electric field and the enhancement of the cross-tail current at the front). In the plasma frame, recent case studies have suggested that the energy could be transferred from the plasma to the electromagnetic fields (dynamo/generator). Finally, the current density structures associated with DFs have been

discussed in section 2.8. DFs and fast flows generate FACs during their earthward propagation and couple the magnetotail to the auroral region. Auroral signatures associated with DFs and energy conversion processes produced by FACs are still investigated. Increase of the cross-tail current produced by the DF motion has been related to the increase of the pressure ahead of the front and attributed to a diamagnetic effect mostly supported by ions. While this review shows the wealth of physical processes associated with DFs, it also shows that further investigations are required to better understand their role in the global dynamics and energy cycle of the Earth's magnetosphere. Using recent MMS data gathered at electron scales in the magnetotail, the next chapters propose to shed light on the energy conversion processes that occur in the vicinity of DFs.

Chapitre 3

The MMS mission and methods of space data analysis

"Whoever travels without a guide, needs two hundred years for a two-day journey."

Rumi, *Mathnavi translated by William Chittick, p.122-123*

Contents

3.1 Introduction **28**
3.2 The MMS mission **28**
3.2.1 Orbit and mission phases 29
3.2.2 The spacecraft 33
3.2.3 Data Products 39
3.3 Discontinuity analysis **39**
3.3.1 Minimum Variance Analysis (MVA) 39
3.3.2 Timing analysis (a multi-satellite method) 41
3.3.3 Gradient estimate (a single-satellite method) 42
3.4 Current density computations **42**
3.4.1 Current density computation using particle (FPI) measurements 44
3.4.2 Current density computation using the curlometer (multi-satellite) technique and the magnetic field (FGM) measurements 44
3.4.3 Diamagnetic current density estimates 46
3.5 Superposed epoch analysis (SEA) **46**

3.1 Introduction

The section 3.2 of this chapter provides a presentation of the MMS mission and a brief description of the main instruments used throughout the thesis. In particular, orbit and data products are described as well as the following instruments : the Spin-Plane Double Probe (SDP) and the Axial Double Probe (ADP) providing electric field measurements, the FluxGate Magnetometer (FGM) providing DC and low-frequency magnetic field measurements, the Fast Plasma Investigation (FPI), providing electron and ion Velocity Distribution Functions (VDF) and their moments, and the Hot Plasma Composition Analyzer (HPCA) measuring the 3D ion VDFs for different ion species.

The section 3.3 displays the analysis techniques that are used for the observational study reported in Chapter 4, and for the statistical study reported in Chapter 5. The first part of this section provides a description of a single spacecraft method named Minimum Variance Analysis of the Magnetic field (MVAB) which allows to analyse magnetic field discontinuities. In the second part, different multi-spacecraft methods are presented such as the Timing Analysis (TA) and the curlometer technique. Finally, the Superposed Epoch Analysis (SEA) used to perform a statistical study is described.

3.2 The MMS mission

In March 2015, NASA has launched the MMS mission. It is constituted of four identical satellites evolving in a tetrahedral formation separated at electron scales. The instrument suite and the tetrahedral configuration have been designed to reach time and spatial resolutions at electron scales, in near-Earth space. Before the MMS mission, ESA launched the Cluster mission in 2000 (Escoubet and Goldstein, 2001). Cluster, still operating, with its four identical satellites has led to significant advances in understanding some fundamental processes in the Earth's magnetic field environment such as the magnetic reconnection process or DF dynamics. The tetrahedral configuration of the MMS and Cluster missions can allow us to distinguish the temporal from the spatial variations and to compute the spatial gradients. However, important assumptions are required : the structures have to be considered as planar at the scale of the tetrahedron and stationary at least during the tetrahedron crossing time.

The main objective of the MMS mission beyond those achieved by Cluster is to study the fundamental plasma processes such as magnetic reconnection, plasma jet, turbulence, shock, ... at electron scales. Therefore the range of spacecraft separation has been chosen from 7-10 km (equivalent to a few electron inertial lengths at the magnetopause) to about 40-60 km (equivalent to a few electron inertial lengths in the magnetotail around apogee). Characteristical values of electron and ion inertial lengths and Larmor radii at the magnetopause and in the magnetotail are

given in Table 3.1.

The most distinctive feature of the MMS mission compared to the previous magnetospheric missions is that it has a 20 s spin period. Such a slow spin period allows to implement long electric field antennas along the spin axis (Ergun et al., 2016) providing the 3D electric field (not available onboard Cluster) and to perform particle measurements with a high-time resolution independently from the spin period thanks to rapid deflectors (Pollock et al., 2016). Thus, while onboard Cluster, the particle measurement is obtained every 4 s for ions and 2 s for electrons, MMS ion and electron VDFs are obtained every 150 ms and 30 ms respectively.

TABLE 3.1 – Characteristical values (in km) of electron and ion inertial lengths and Larmor radii at the magnetopause and in the magnetotail.

Comparison	Magnetopause	Magnetotail
Plasma conditions	n=10 p/cm^3, B=20 nT, T_e=30 eV, T_i=100 eV	n=0.2 p/cm^3, B=8 nT, T_e=1300 eV, T_i=5k eV
Electron inertial length	1.7	12
Ion inertial length	72	509
Electron Larmor radius	0.7	15
Ion Larmor radius	58	1277

3.2.1 Orbit and mission phases

While the THEMIS mission with its five identical probes has been designed to investigate large scale plasma and energy transports across the magnetosphere in particular related to magnetospheric substorms, Cluster tetrahedral configuration was targetting plasma processes such as magnetic reconnection, plasma jets and related DFs at fluid and ion scales. MMS has been designed to extend these investigations to electron scales and especially to identify the DR where electrons are thought to decouple from the magnetic field.

In order to study in detail the very localised EDR, MMS have to cross as many times as possible reconnection sites in the Earth's magnetotail as well as at the dayside magnetopause. For this purpose, MMS has an equatorial elliptical orbit with a perigee of 1.2 R_E and a varying apogee from 12 R_E to 25 R_E. MMS started the prime mission from Sept. 2015 to Sept. 2017, containing two phases (see Figure 3.1) : phase 1(a, b) to survey the dayside magnetopause and phase 2 to survey the Earth's magnetotail, respectively. The plasma density and the magnetic field being larger at the dayside magnetopause than in the mid-magnetotail, ion and electron scales given by inertial length and gyroradius are consequently smaller. Therefore, the distance between satellites has to be adjusted accordingly in the different regions. During phase 1a, satellite separation has been resized from 160 km to 10 km whereas phase 1b maintained the electron scale satellite separation at

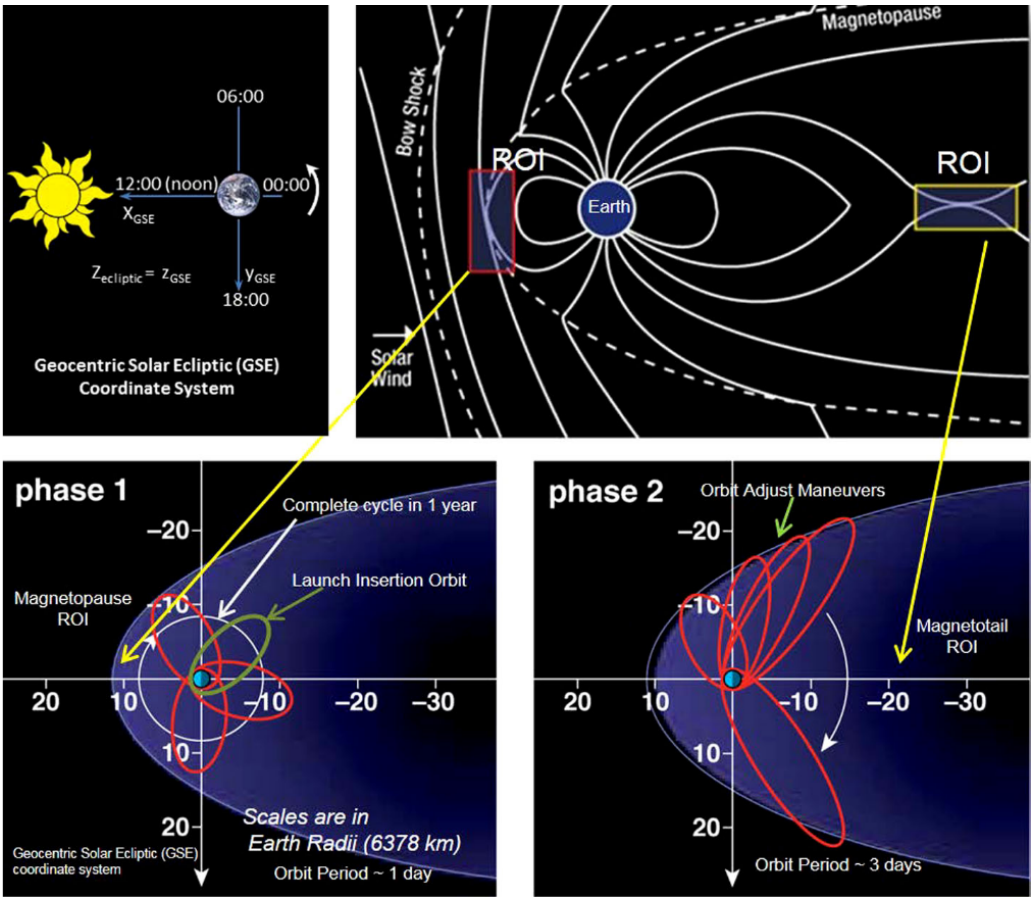

FIGURE 3.1 – MMS orbital geometry and science Region of Interest (ROI). Adapted from Tooley et al. (2016).

10 km. Then, during the phase 2a along the dawn flank, the apogee was raised from 12 to 25 R_E and the separation distance increased from 10 to 40 km. These parameters were maintained during the phase 2b investigating the magnetotail reconnection process.

After the achievement of the nominal mission, MMS has been already extended two times based on reports from senior reviews organized by NASA. The phase 3 from Sep. 2017 to Sep. 2018 preserved the same apogee at 25 R_E and perigee. Therefore on the dayside, MMS spent more time in the solar wind to investigate magnetic reconnection, current sheets, turbulence, interplanetary shocks. Then the apogee has been increased again from 25 to 29 R_E during the phase 4 (Sept. 2018 to Sept. 2019) of the extended mission in order to obtain even more observations in the pristine solar wind farther from perturbations produced by the Earth's bow shock. Since these last changes, MMS orbit parameters have remained the same while different intersatellite separations have been scanned. This chronology is

Table 3.2 – MMS mission phases

Phase	Period of time	Apogee (R_E)
Phase 0 (commissioning)	15/03/2015 – 30/08/2015	12
Phase 1a (dayside)	01/09/2015 – 15/03/2016	12
Phase 1x (nightside)	15/03/2016 – 27/09/2016	12
Phase 1b (dayside)	27/09/2016 – 21/02/2017	12
Phase 2a (dawnside)	21/02/2017 – 28/04/2017	apogee raising to 25
Phase 2b (nightside)	28/04/2017 – 28/08/2017	25
Phase 3	28/08/2017 – 27/09/2018	25
Phase 4	28/09/2018 - 29/09/2019	2nd apogee raising to 29
Phase 5	30/09/2019 - 02/10/2020	29
Phase 6	06/10/2020 - 10/10/2021	29
Phase 7	06/10/2021 - 10/10/2022	29

summarized in Table 3.2.

The Region of Interest (ROI), is the orbital part (located around the apogee, see Figure 3.1) with the highest probability to observe the magnetic reconnection process at the magnetopause or in the magnetotail. Along the ROI, high-time resolution for all instruments and high-quality of tetrahedron are maintained (Fuselier et al., 2016). Along its orbit, MMS uses three data acquisition rates as fast, slow and burst. Within the ROI, MMS only produces data with fast and burst rates which are stored onboard each satellite. All slow and fast rate data are transferred to the ground as opposed to burst data which are beyond the capabilities of the MMS telemetry transmission system. Figure 3.2 shows that around 75% of the telemetry bandwidth has allocated to burst data downlink although only 1–2% of these data are selected for transmission (Baker et al., 2016). Indeed, although MMS has an onboard repository with a large capacity, it is still limited compared to the data volume produced by high-time resolution instrument data rates. To manage this issue, MMS has a partially automatic data selection process (see Table 3.3 for a list of selection criteria) supervised by scientist at ground. Thus, collected data are evaluated before being downlinked and combined to deliver a Figure Of Merit (FOM) allowing a ranking of detected events. The most interesting data with regards to the main MMS objectives receive higher FOM and are downlinked in priority for investigations and analysis (Baker et al., 2016). This ranking is ensured by the Scientist-in-the-Loop (SITL) in charge of the data selection and of checking/modifying the automatically set FOM. By adjusting the FOM, the SITL decides which data have to be saved, directly downlinked or deleted. In addition, the SITL prepares a detailed report with every selection and percentage of its importance and the related physical phenomenon observed in each selected time segment (Baker et al., 2016). Category 1 corresponding to the highest significance of the FOM is recorded as (150–199) and attributed to best magnetic

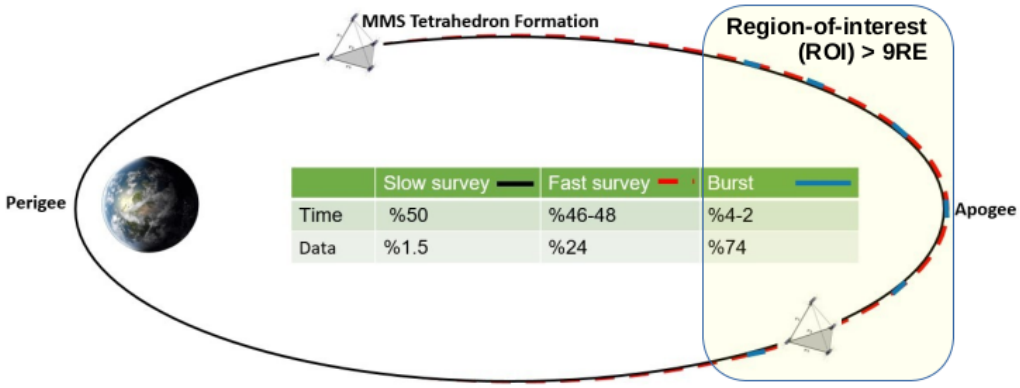

FIGURE 3.2 – A day in the life of MMS orbit indicates the region of interest in light yellow (ROI).

reconnection events detected by MMS when it is close or within the EDR or to active (acceleration, waves) DF events in the magnetotail, Category 2 (100-149) corresponds for instance to exhaust region of magnetic reconnection regions, shock or fore shock events, fast flows in the magnetotail. Category 3 data (60-90) allow to select secondary objectives like high-speed jets in the magnetosheath or pristine SW turbulence. Finally, Category 4 allows to select all other interesting events but with a high probability to be overwritten by more interesting events therefore to be never downlinked to the ground. During this thesis, I participated in these SITL activities when MMS apogee was located on the dayside (from 24 Jan. to 7 Feb. 2021) as well as on the nightside (from 15 to 23 Sep. 2020 and from 4 to 11 Jul. 2022).

TABLE 3.3 – Top level burst-mode parameters. Adapted from Burch et al. (2016)

Physical signature	Trigger parameter
Reconnection jets	Ion flow reversals
Magnetopause and neutral sheet detection	Large B variations
Large flows surrounding reconnection sites	Large E
Magnetopause and neutral sheet detection	Large electron currents
Particle acceleration produced by reconnection	Electron and ion beams
Electron diffusion region	$E_{\parallel}$ to B

3.2.2 The spacecraft

MMS is constituted of four identical spacecraft with an octagonal form. Below we limit our review of the MMS instrument suite to the main instruments used to perform our studies. Firstly, we review the main instruments measuring the magnetic and electric fields :

- ⊙ The Electric field Double Probe (EDP) measures the 3D electric field in the frequency range DC–100 kHz. It is formed by the Axial Double Probes (ADP, Ergun et al., 2016) and the Spin-plane Double Probes (SDP, Lindqvist et al., 2016).
- ⊙ The Fluxgate Magnetometer (FGM) is constituted by the Digital Fluxgate (DFG) and the Analog Fluxgate (AFG). FGM measures the magnetic field at a sampling frequency of 128 s^{-1} in burst mode and at 8 s^{-1} in survey mode ; with an accuracy of around 0.1 nT for the DC field (Russell et al., 2016).

Secondly, the instruments measuring particles are :

- ⊙ The Fast Plasma Investigation (FPI) instrument formed by four Dual Ion Spectrometers (DIS) and four Dual Electron Spectrometers (DES) per spacecraft. FPI measures the 3D VDF of ions and electrons in the energy range from 10 eV to 30 keV with a time resolution of 150 ms and 30 ms respectively (Pollock et al., 2016).
- ⊙ The Hot Plasma Composition Analyzer (HPCA) delivering the ion composition in the energy range from 1 eV to 40 keV. HPCA provides the 3D VDFs of He^{++}, He^{+}, H^{+} and O^{+} with a time resolution of 10 s (Young et al., 2016).

Each satellite is also equipped by an Active control of the spacecraft potential (ASPOC), energetic ion and electron detectors (EPD, Mauk et al., 2016) and electron drift instrument (EDI, Torbert et al., 2016a) providing additional perpendicular electric field measurements and magnitude of the magnetic field useful for intercalibrations. Data from these instruments have been examined only occasionally. Figure 3.3 illustrates how the instruments are positioned on each spacecraft.

Electric field measurements

EDP instrument measures the 3D electric field over the frequency range DC-100 kHz along (ADP) and perpendicularly (SDP) to the spin axis of the spacecraft. EDP is the outcome of a coordinated collaboration between the University of New Hampshire, the KTH Royal Institute of Technology (KTH), the Swedish Institute of Space Physics (IRFU), the Laboratory for Atmospheric and Space Physics (LASP) of the University of Colorado. ADP measures the electric field from the variation of the potential between two probes positioned on top of antennas, which have a

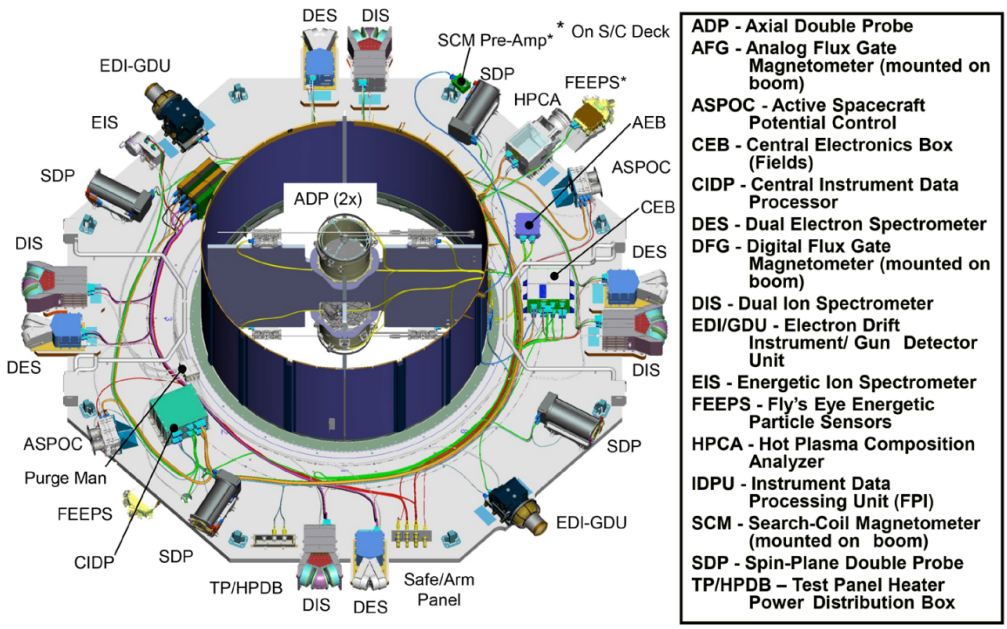

FIGURE 3.3 – FIELDS sensors on the MMS spacecraft. Adapted from Burch et al. (2015)

length of 30 m tip-to-tip, directed along the spin axis (z-axis of the spacecraft). SDP measures the electric field along two perpendicular directions in the spin plane from the difference of potential between two spherical (8 cm diameter) titanium-nitride electrodes mounted at the end of wire booms of 60 m length. Their accuracies are ∼1 mV/m for ADP and ∼0.5 mV/m for SDP, over the frequency range from DC to 100 kHz.

Magnetic field measurement

Magnetic field measurements are provided using two triaxial fluxgate magnetometers (DFG and AFG). Both magnetometers are mounted at the end of a 5 m boom. The DFG was delivered by the Space Research Institute of the Austrian Academy of Sciences, and the AFG was delivered by the University of California, Los Angeles, with dissimilarities in the electronic unit to which they are connected (Russell et al., 2016). The FluxGate Magnetometer (FGM) data product provides the magnetic field at a sampling frequency of 16 s^{-1} from AFG measurements and 128 s^{-1} from DFG in the survey and burst modes, respectively. Both AFG and DFG have the same sensor. It consists of two ferromagnetic ring cores around which are wrapped two coils : the sense coil and the drive coil (see Figure 3.4). A simple idea of FGM measurement can be given as follows : an alternating current is injected in the drive coil saturating the ring core while the sense coil measures

the time variation of the magnetic flux in the core (produced by the ambient field). This signal is used to inject a current into a feedback coil in order to cancel the ambient magnetic field. Finally, the resulting sense signal is checked until a minimum is reached. "The field strength reported to the ground is the feedback coil-generated field strength required to cancel the ambient field at the sensor" (Russell et al., 2016).

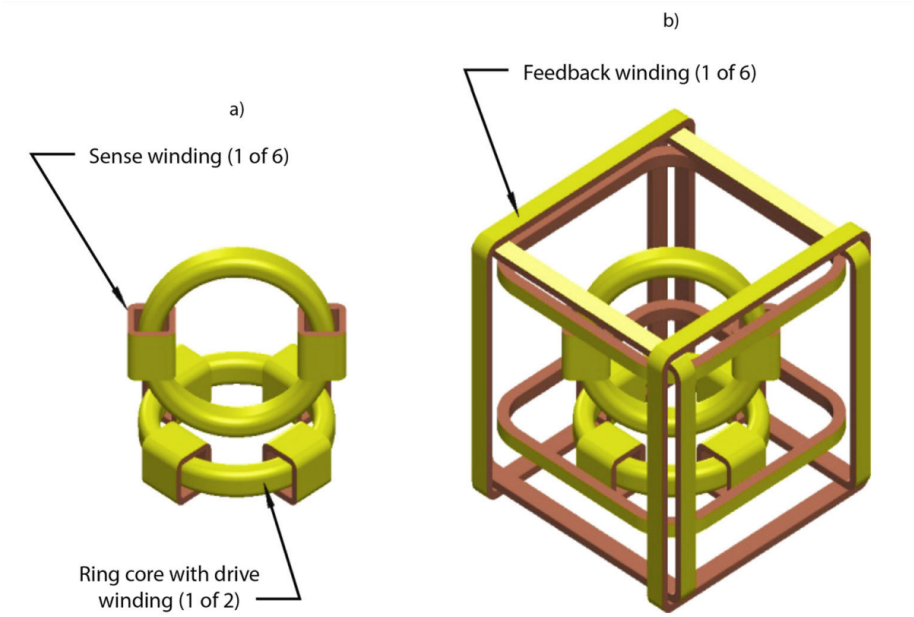

FIGURE 3.4 – (a) The magnetic ring cores, with their drive windings, the sense windings, and their relative positions and orientations. (b) The elements are shown in part (a) situated within a set of feedback windings. Adapted from Russell et al. (2016)

The Fast Plasma Investigation (FPI)

The FPI measures the 3D VDF of thermal (10 eV to 30 keV) ions and electrons. The novelty of this thermal plasma measurement compared with previous magnetospheric missions, is that the full azimuthal sampling of MMS does not dependent on the spacecraft spin. Indeed for both ions (DIS) and electrons (DES) eight top hat spectrometers (or equivalently 4 dual heads) positioned at 90° angles onboard the spacecraft allow to measure the full (4π steradians) VDF without waiting for an azimuthal rotation of the satellite as for Cluster or THEMIS missions for instance. The FPI was a result of the collaboration between Meisei Electric in Gunma-Japan that built the DIS, the Institut de Recherche en Astrophysique et Planetologie (IRAP) that has procured and tested the MicroChannel

Plates (MCPs) and Goddard Space Flight Center (GSFC)-USA as the Lead Co-Investigator institution.

The DIS and DES have identical designs, every sensor comprises two deflectors types ; a Multi-channel plate (MCP) detector with an anode coil underneath and an Electrostatic analyzer (ESA). Depending on the energy/charge of the particles, the reflectors change their path before they reach the electrostatic analyzer. In addition, the electrostatic energy/charge delivered the sampling of the energy between 10 eV/q to 30 keV/q. The ESA uses a classical top hat geometry to select and count the particles with a characteristic velocity direction and an energy/charge. DIS and DES have two sensors that have their own detector system comprised of admission of the MCP stack group, 16 discrete anodes (see Figure 3.6), and shield grids, each one has a charge-sensitive preamplifier discriminator (see Figure 3.5).

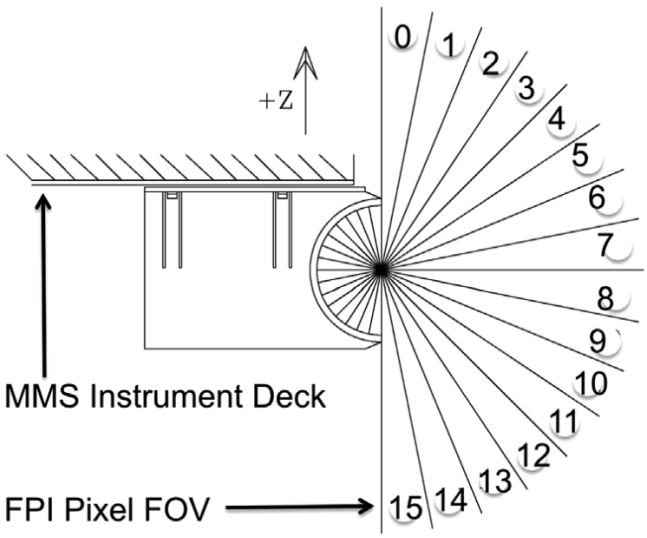

FIGURE 3.5 – Each FPI 180° polar angle top hat is mounted so that the 180° fan spans from the spacecraft spin axis to the anti-spin axis. Each sensor is oriented so that the 16 pixels (each nominally 11.25° wide) of its 180° Field Of View (FOV) are viewing radially in velocity space, spanning the 180° pole-to-pole range in the spinning spacecraft reference frame, Adapted from Pollock et al. (2016).

Plasma particles pass through the ESA to the detector set via the grid above the MCP stack. The filter receives incoming particles having a certain speed and direction and then allows them to reach the sensor plate. The instrument detects the event when those incoming particles reach the sensor. However, due to the very low density in the magnetotail (< 0.05 p.cm^{-3}), we have used the electron partial moments provided by the FPI team for which the integration of the distribution function starts at the minimum energy of ~ 100 eV which allows to remove photo-

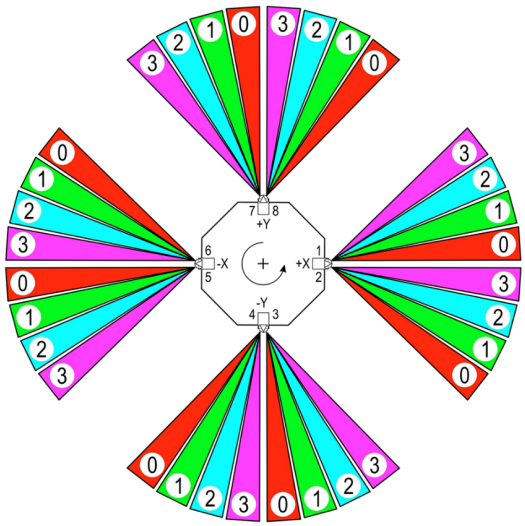

FIGURE 3.6 – To meet temporal requirements, thirty-two azimuthal fields of view using eight spectrometers (four dual spectrometers) are deployed around each MMS observatory perimeter. Nominally identical fields of view are provided for electrons and for ions. Eight spectrometers for each species, each exercising four deflected fields of view, yields thirty-two azimuth samples for each species, Adapted from Pollock et al. (2016).

electrons and obtain reliable moment calculations. Furthermore, in order to reduce even more the noise on electron moments, we have time-averaged the electron data at 0.3 s. Such a time averaging, while it reduces the noise on the particle moments, it still allows to keep a time resolution 10 times better than THEMIS (3 s) or Cluster (4 s). Furthermore, it corresponds to a time scale much longer than the electron gyroperiod which is about 4 ms, using an average value of B$\sim$ 8 nT.

Hence all results shown in this study are based on data with 0.3 s time resolution. Note that background noise produced by energetic electrons penetrating the ion detectors has been subtracted from ion FPI measurements as recommended by the FPI team (Gershman et al., 2015). Furthermore, the upper energy limit of FPI being 30 keV, ion moment calculations can be still inaccurate in the magnetotail where ions can be more energetic, as we will see by comparing them with the particle measurements from the HPCA instrument which has a higher energy cutoff and a time resolution of 10 s as described in the next subsection.

Hot Plasma Composition Analyser (HPCA)

HPCA comprises an electrostatic energy analyzer and a carbon-foil-based time-of-flight analyzer (see Figure 3.7). The HPCA design has the advantage of an

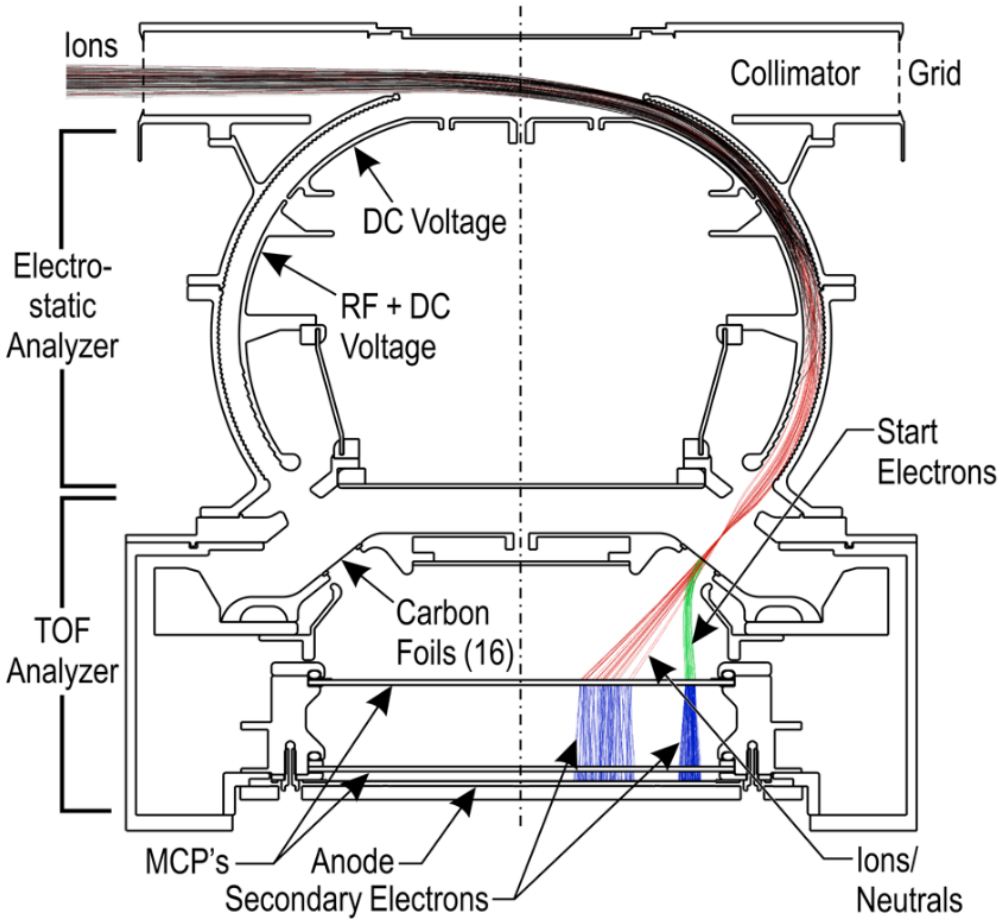

FIGURE 3.7 – Schematic drawing of the HPCA sensor showing the main optical design elements together with characteristic ion and electron trajectories. The ion trajectories through the ESA are shown with the RF field operating to deflect protons (black trajectories) while transmitting O+ (red trajectories), Adapted from Young et al. (2016).

adjustable voltage to match the energy and arrival angles of the incoming ions penetrating the two concentric toroids with the internal torus in the instrument. Using an ultra-thin carbon foil an ion entry is detected via the generation of secondary electrons. HPCA applied an electric field to accelerate these electrons to typical energy before they reach the MCP sensor. After the start signal has been recorded, a stop pulse is caused corresponding to the Time of Flight when

the ion hits the stop sensor. Thus, from ESA energy of ions is determined then measuring the Time of Flight and knowing the size of the chamber the ion velocity is estimated. Knowing the energy and the velocity, ion mass is obtained.

3.2.3 Data Products

MMS have three levels of data : level 1,2, and 3. Level 1 data are raw data in spacecraft frame at full resolution but produced by fast and simplified processing algorithms after some hours from the reception at ground. Using these L1 data, MMS science operation centre produces QuickLooks which provide a basic scientific vision without the final calibration improvements. As we have seen, they are used by SITL to perform the selection of the best burst periods having the highest time resolution. The calibrated version of L1 data moved in a geocentric frame (such as GSE or Geocentric Solar Magnetospheric coordinate system (GSM)) corresponds to L2 data available in open-access after 1 month and ready for science publications (Baker et al., 2016). Mission-level data is called Level 3 data with the highest improvement of the treatment and possible combination of two or more different instrument data sets. Level 3 data are only created on an event basis so they are not available for all events. Thus, only level 2 burst and survey data have been used throughout this thesis and were downloaded from the MMS Science Data Center (SDC) (https://lasp.colorado.edu/mms/sdc/public/) or the Laboratory of Plasma Physics (LPP) MMS mirror base (https://mms.lpp.upmc.fr/)

3.3 Discontinuity analysis

This section is largely based on different articles in Analysis Methods for Multi-Spacecraft Data book edited by G.Paschmann, P.W. Daly (Sonnerup and Scheible, 1998; Harvey, 1998; Chanteur and Harvey, 1998).

3.3.1 Minimum Variance Analysis (MVA)

The Minimum Variance Analysis (MVA) is a single satellite method used to determine the normal direction to a planar (at the scale of the satellite) transition layer. It is usually applied on the magnetic field vector (MVAB) measured by one single satellite crossing the transition layer although other physical quantities can be also used as for example the Maximum Variance Analysis of the Electric field (MVAE). Note that for multi-satellite missions with a tetrahedral configuration such as Cluster or MMS, a global normal can be determined by applying the MVA on the four satellite average of the magnetic field data. Then this global normal can be compared with each single-satellite normal determination in order to check the planarity and stationarity assumptions at the scale of the tetrahedron. The MVA method is based on the fundamental assumption that for a One Dimension (1D)

transition layer there are no variations in the two tangent directions to the surface layer (x and y) which implies that the normal component B_z does not vary along the normal direction z due to the divergence-free nature of the magnetic field ($\nabla \cdot \mathbf{B} = \partial B_z/\partial z = 0$). Then from Faraday's law, we get that B_z is also constant in time. The unit vector $\hat{\mathbf{n}}$, whose direction, depending on our reference frame, is directed along the $\hat{z}$ axis, $\hat{n} = \hat{z}$. Based on these assumptions, we only need three magnetic field values to determine the unit vector $\hat{\mathbf{n}}$. First, one $\mathbf{B}_2$ is taken close to the layer, while $\mathbf{B}_1$ and $\mathbf{B}_3$, are taken at opposite ends of the layer. Then as B_z is constant, we can write :

$$\mathbf{B}_1 \cdot \hat{\mathbf{n}} = \mathbf{B}_2 \cdot \hat{\mathbf{n}} = \mathbf{B}_3 \cdot \hat{\mathbf{n}} \rightarrow 0 = \hat{\mathbf{n}} \cdot (\mathbf{B}_2 - \mathbf{B}_3) = \hat{\mathbf{n}} \cdot (\mathbf{B}_1 - \mathbf{B}_2) \tag{3.1}$$

Therefore both $(\mathbf{B}_2 - \mathbf{B}_3)$ and $(\mathbf{B}_1 - \mathbf{B}_2)$ are orthogonal to $\hat{\mathbf{n}}$ and tangential to the layer. Through this we can define $\hat{\mathbf{n}}$:

$$\hat{\mathbf{n}} = + - \frac{(\mathbf{B}_2 - \mathbf{B}_3) \times (\mathbf{B}_1 - \mathbf{B}_2)}{|(\mathbf{B}_2 - \mathbf{B}_3) \times (\mathbf{B}_1 - \mathbf{B}_2)|} \tag{3.2}$$

This formulation makes it apparent that the two vectors of the observed magnetic field must not be parallel, that is, in most study cases, selecting values from the two different sides of the layer should bypass this issue. However, high-time resolution magnetometers together with high telemetry rates allow us to generalize this basic idea using hundred or thousands magnetic field values to get a more reliable result and without assuming an idealized 1D transition layer. Considering that variations of $\mathbf{B}$ are smallest along the normal direction and $\hat{\mathbf{n}}$ being a unit vector ($|\hat{\mathbf{n}}^2| = 1$), we can define the measure that we want to minimize (using the method of Lagrange multipliers) as :

$$\partial n_i \left[\frac{1}{M} \sum_{m=1}^{M} |(\mathbf{B}_m - < \mathbf{B} >) \cdot \hat{\mathbf{n}}|^2 - \lambda(|\hat{\mathbf{n}}|^2 - 1) = 0 \right] \tag{3.3}$$

with $i = x, y, z$, M measured values of the magnetic field and where $< \mathbf{B} >$ is the average of the magnetic field over M measurements. After performing the differentiation, the set of equations can be written in a matrix form as

$$\Sigma_{j=1,3} M_{ij} n_j = \lambda n_i \tag{3.4}$$

with the matrix of magnetic variance defined as

$$M_{ij} = \langle \mathbf{B}_i \mathbf{B}_j \rangle - \langle \mathbf{B}_i \rangle \langle \mathbf{B}_j \rangle \tag{3.5}$$

So allowed λ values correspond to eigen values of the magnetic variance matrix. Since this matrix is symmetric all eigenvalues are real and corresponding eigen vectors are orthogonal. A preferable ordering corresponds to $\lambda_1 < \lambda_2 < \lambda_3$ identifying directions of maximal, intermediate and minimal variances respectively. Therefore,

the normal to the transition layer is given by v_3 which is the eigenvector of the direction of the minimum variance and λ_3 represents the variance of the magnetic field component along this estimated normal. The two other eigenvectors are tangential to the transition layer and allow to build a convenient local coordinate system to investigate physical processes in the vicinity of the transition layer.

As we have already indicated earlier, most of the time MVAB analysis provides three distinct eigenvalues. However in some cases, two or three eigenvalues of the variance matrix can be equal or substantially equal ; in that cases the matrix is said to be degenerate. There are three possible types of degeneracy : $\lambda_1 \approx \lambda_2 \approx \lambda_3$, $\lambda_1 \approx \lambda_2$ and $\lambda_2 \approx \lambda_3$. When $\lambda_1 \approx \lambda_2$, the normal direction is still correctly identified as long as $\lambda_3 \ll \lambda_1 \approx \lambda_2$. When $\lambda_2 \approx \lambda_3$, the normal cannot be determined but the eigen vector v_1 of the maximum variance is tangent to the discontinuity provided that $\lambda_1 \gg \lambda_2 \approx \lambda_3$. For the last case of degeneracy $\lambda_1 \approx \lambda_2 \approx \lambda_3$, $\lambda_1 \approx \lambda_2$, neither the normal nor the tangent to the layer can be determined.

3.3.2 Timing analysis (a multi-satellite method)

The timing analysis (TA) is relevant when the studied structure can be assumed as a plane layer moving with a constant velocity at the scale of the crossing of the tetrahedron. We have to choose a physical quantity such as the magnitude or one component of the magnetic field, then determine the reference point by plotting the same quantity for all spacecraft [MMS1, MMS2, MMS3, MMS4] which of course have some differences that are due to the difference in the respective position of each spacecraft.

Let's give more details about the computation of the timing analysis. We define t_n as the time when each spacecraft n=[2, 3, 4] crosses the discontinuity (MMS1 being arbitrary chosen as the reference) and $\mathbf{r}_n$ as the spacecraft position, (see Figure 3.8). Assuming that the studied structure moves along the boundary normal with a constant structure velocity V_{SS}, we can write

$$(\mathbf{r}_n - \mathbf{r}_1) \cdot \hat{\mathbf{n}} = V_{SS}(t_n - t_1) \tag{3.6}$$

We introduce the vector $\mathbf{N} = \hat{\mathbf{n}}/V_{SS}$ so the linear system becomes :

$$\begin{bmatrix} \mathbf{r}_{21} \\ \mathbf{r}_{31} \\ \mathbf{r}_{41} \end{bmatrix} \cdot \mathbf{N} = \begin{bmatrix} t_{21} \\ t_{31} \\ t_{41} \end{bmatrix} \tag{3.7}$$

Then the normal is obtained by inversing the matrix of the separation vectors which yields to :

$$\mathbf{N} = L^{-1}\mathbf{T} \tag{3.8}$$

where we have defined L as

$$L = \begin{bmatrix} r_{21,x} & r_{21,y} & r_{21,z} \\ r_{31,x} & r_{31,y} & r_{31,z} \\ r_{41,x} & r_{41,y} & r_{41,z} \end{bmatrix} \tag{3.9}$$

and T as

$$T = \begin{bmatrix} t_{21} \\ t_{31} \\ t_{41} \end{bmatrix} \tag{3.10}$$

This method is valid if all spacecraft are not co-planar then L^{-1}, the inverse of L, exists.

Based on the equation 3.8, the accuracy of the normal and velocity estimates depends on errors in : the spacecraft separation vectors and the crossing times. Actually, timing errors are usually below 1% therefore we can consider that most of the error comes from the separation vector uncertainty.

3.3.3 Gradient estimate (a single-satellite method)

Although any physical gradient can be estimated from four satellite measurements, some specific plasma conditions such as a very small plasma density in the magnetotail can make the moment values very noisy and the gradient calculations not reliable. In such conditions, it is useful to get back to a single satellite method to estimate particle density or pressure gradient (e. g., Fu et al., 2012a; Yao et al., 2017).

First, we estimate the normal to the boundary and the velocity along the normal using the timing analysis described in the previous section. Second, we assume that the time variations of the scalar quantity (density, pressure or temperature) are mostly due to the motion of the boundary along the gradient direction. Therefore, knowing the velocity of the boundary, the gradient can be obtained from the time derivative measured onboard the satellite. For instance, for the pressure gradient, we get :

$$\frac{\partial P_{i,e}}{\partial N} \approx \frac{1}{V_{SS}} \frac{\partial P_{i,e}}{\partial t} \tag{3.11}$$

3.4 Current density computations

An important step at the beginning of the space data investigation must be to ensure the correctness and accuracy of the current density calculations. Indeed these quantities are fundamental in order to have a good understanding of the plasma dynamics and the current system we are studying. In this section, we discuss two types of computations of the current density : (1) $\mathbf{J_{part}}$ is the current density computed from the particle measurements, (2) $\mathbf{J_{curl}}$ is the current density computed from the curlometer technique. Furthermore, as we have seen in subsection 3.2.2, the plasma conditions (very low density < 0.05 p.cm^{-3}) in the magnetotail can make difficult particle moment measurements. One way to verify the reliability of these measurements is to compare the current densities computed

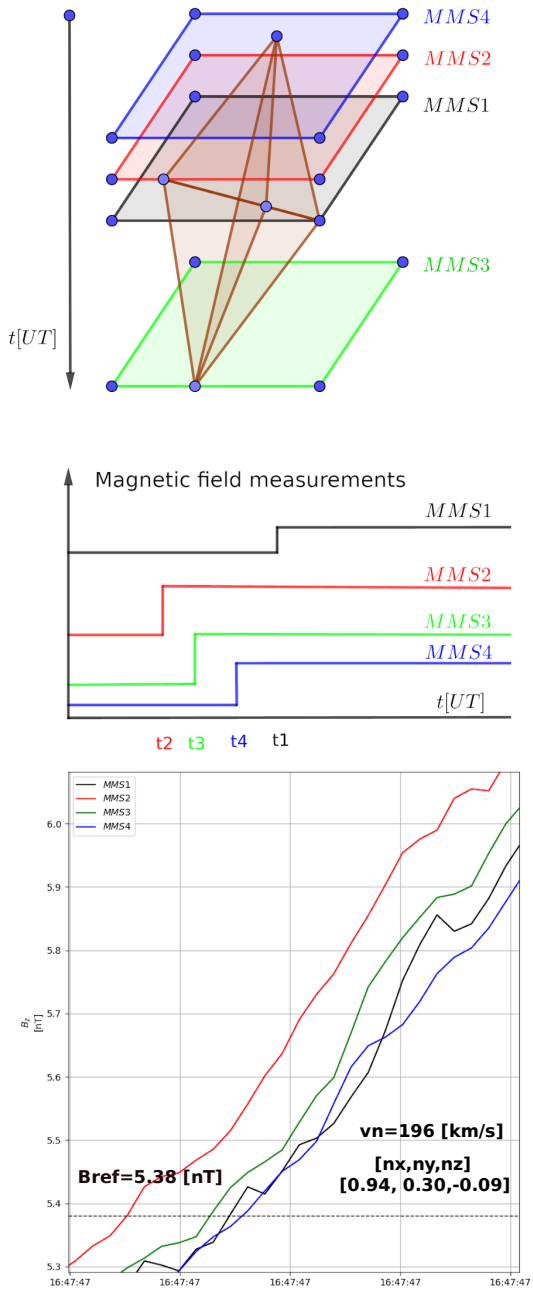

FIGURE 3.8 – Detection of measurements by MMS, the magnetic field measurements are marked by a plane moving with time, that is, the different magnetic field populations are seen as a change in the time series, and all spacecraft are assumed to be planar on the scale of the tetrahedron.

from ion and electron moments averaged over the four individual spacecraft with those estimated independently from the magnetic field data at the same time resolution (~ 0.3 s) thanks to the curlometer technique.

3.4.1 Current density computation using particle (FPI) measurements

The current density computed from particle measurements is given by :

$$\mathbf{J}_{part} = en_e(\mathbf{v}_i - \mathbf{v}_e) \tag{3.12}$$

where $\mathbf{v}_{i,e}$ are respectively the ion and the electron velocities and n_e is the electron density. We have assumed $n_i = n_e$ as the plasma can be considered in a quasi neutrality state for any structure having a spatial scale larger than the Debye length. Furthermore, as described in subsection 3.2.2, ion density measurements in the magnetotail provided by FPI have some limitations and electron density measurements (after having removed the photo-electrons) are more reliable. Yet, in order to reduce the noise due to the low plasma density, all these particle moments have been time averaged at 0.3 s. Then, ion velocity data are linearly interpolated on electron data. Finally, the four individual current densities can be averaged in order to be compared with the current density obtained from the curlometer technique described in the next section. To estimate the uncertainty of the current density produced from FPI measurements we used the following expression :

$$\mathbf{J}_{part} = e \cdot (\Delta N_e) \cdot (\mathbf{V}_i - \mathbf{V}_e) + e \cdot N_e \cdot (\Delta \mathbf{V}_i + \Delta \mathbf{V}_e) \tag{3.13}$$

while ΔN_e, ΔV_i, and ΔV_e are provided by the FPI team within each data file.

3.4.2 Current density computation using the curlometer (multi-satellite) technique and the magnetic field (FGM) measurements

The curlometer technique allows us to compute directly the current density at the barycenter of a tetrahedron by using four-point magnetic field measurements, (see Figure 3.9). The current density estimate $\mathbf{J}$ is obtained from the Ampère's law (where the displacement current can be neglected for slowly time varying structure with small phase speed compared to the speed of light) given by

$$\mathbf{J_{curl}} = \frac{\nabla \times \mathbf{B}}{\mu_0} \tag{3.14}$$

The curlometer technique is an estimate of the current density in the perpendicular direction on every face of the tetrahedron, (see Figure 3.9). The main assumption of this technique is that the current density is stable on all surfaces of the tetrahedron

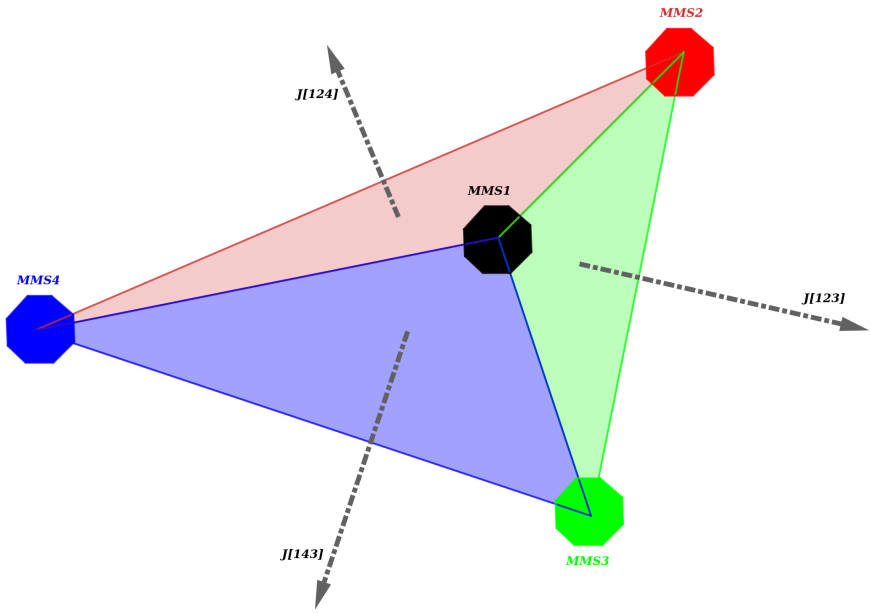

FIGURE 3.9 – Schematic representation of the current density estimation using the Curlometer technique.

and the magnetic field varies very slowly at the scale of the crossing time of the tetrahedron ; thus, the current density $\mathbf{J}_{(i,j,k)}$ normal to the surface defined by spacecraft (i, j, k) can be evaluated through the integral form of Ampère's law (Dunlop et al., 2002) :

$$\mu_0 \mathbf{J}_{(i,j,k)} \cdot (\Delta \mathbf{r}_{ik} \times \Delta \mathbf{r}_{jk}) = \Delta \mathbf{B}_{ik} \cdot \Delta \mathbf{r}_{jk} - \Delta \mathbf{B}_{jk} \cdot \Delta \mathbf{r}_{ik} \tag{3.15}$$

The positions and magnetic field data are in cartesian coordinates where (i, j, k) are indexes of the three independent faces of the tetrahedron, $\Delta \mathbf{r}_{ik} = \mathbf{r}_i - \mathbf{r}_k$ and $\Delta \mathbf{B}_{ik} = \mathbf{B}_i - \mathbf{B}_k$ are the position and magnetic field difference between spacecraft i and k, respectively.

From equation 3.15, we can compute $\mathbf{J}_{124}, \mathbf{J}_{143}, \mathbf{J}_{123}$ and $\mathbf{J}_{234}$ flowing through each surface of the tetrahedron. Finally, after projecting each current vector normal to the three surfaces into cartesian coordinates, an estimate of the total current density in the tetrahedron $\mathbf{J}_{curl}$ is obtained.

To estimate the uncertainty of the curlometer technique it has been tested to check the value of $\nabla \cdot \mathbf{B}$ which, due to the solenoidality of the magnetic field, should be 0. Non-zero results can come from the neglected nonlinear gradients in B (assuming that the error measurement is weak by respect to the error due to the nonlinear gradients). Therefore, usually, $\nabla \cdot \mathbf{B}/|\nabla \times \mathbf{B}| \ll 1$ is considered as a quality indicator to evaluate the reliability of the curlometer technique.

However, further error sources can be considered as the relative measurement error $\delta\mathbf{J}/|\mathbf{J}|$ caused by uncertainties of the positions and magnetic field measurements. Therefore both $\nabla \cdot \mathbf{B}/|\nabla \times \mathbf{B}|$ and $\delta\mathbf{J}/|\mathbf{J}|$ are useful to monitor the reliability of the current density estimate. A significant value of the former indicates possible non-linear gradient effects while the latter provides the measurement accuracy (Robert et al., 1998).

3.4.3 Diamagnetic current density estimates

The equation of motion for each particle species i,e writes :

$$\rho_{i,e}\frac{d\mathbf{v}_{i,e}}{dt} = -\nabla \cdot \mathbf{P}_{i,e} + \frac{q_{i,e}}{m_{i,e}}\rho_{i,e}(\mathbf{E} + \mathbf{v}_{i,e} \times \mathbf{B}) \tag{3.16}$$

Neglecting the inertial terms and performing the cross product with $\mathbf{B}/B$, we can obtain the total perpendicular drift velocity of the fluid :

$$\mathbf{v}_{\perp,i,e} = \frac{(\mathbf{E} \times \mathbf{B})}{B^2} - \frac{1}{q_{i,e}n_{i,e}B^2}(\nabla \cdot \mathbf{P}_{i,e} \times \mathbf{B}) \tag{3.17}$$

The first right-hand side term $\mathbf{v}_E = (\mathbf{E} \times \mathbf{B})/B^2$ corresponds to the electric drift motion, while the second term $\mathbf{v}_{dia,i,e} = -(\nabla \cdot \mathbf{P}_{i,e} \times \mathbf{B})/(q_{i,e}m_{i,e}B^2)$ is the diamagnetic drift motion.

As $\mathbf{v}_{dia}$ depends on the sign of the charge, ions and electrons have opposite drift direction leading to diamagnetic current density as

$$\mathbf{J}_{dia,i,e} = -\frac{\nabla \cdot \mathbf{P}_{i,e} \times \mathbf{B}}{B^2} \tag{3.18}$$

Assuming an isotropic pressure and using single spacecraft method results about the pressure gradient estimate at a boundary layer in a Local Boundary Normal Coordinate System (LMN) frame, we can write

$$J_{dia,M} = \frac{B_L}{B^2}\nabla_N(P_i + P_e) \tag{3.19}$$

then :

$$J_{dia,M} = \frac{B_L}{B^2}\frac{1}{V_{SS}}\frac{\partial(P_i + P_e)}{\partial t} \tag{3.20}$$

3.5 Superposed epoch analysis (SEA) : A useful tool for statistical studies

The superposed epoch analysis is a general technique used for carrying out statistical studies. It is often used to demonstrate an effect relative to some repeatable phenomenon. It allows to analyze data of some observable phenomenon in a coherent state over time, i.e. a time series (Chree, 1908).

In chapter 5, we will see that we have reorganized the time series by setting the maximum of the magnetic field as a reference for the measurements t0 and the duration of time period (t0-160,t0+160), (see Figure 3.10). then I have used State Estimation and Analysis in Python (SeaPy) to obtain the SEA of my database of DF events, and through it, I have shown the mean, the median and the interquartile range. Note that the median measure is less impacted by departures from normality (Morley et al., 2014).

To make an accurate and correct SEA, the most important steps that we must follow are :

1. Import time series dataset for various events based on what your study requires.
2. Define the reference point t0 for each event individually [e.g., maximum, minimum,... etc] and determine the duration of time intervals.
3. Perform any scientific or physical calculations on the dataset and then rename the outputs based on the quantities produced.
4. Reconstruct the dataset based on the resulting quantities to include all events together, so that each quantity has its own set of data, e.g., by using the Python package "pandas.DataFrame".
5. Finally use SeaPy from SpacePy to plot your SEA results.

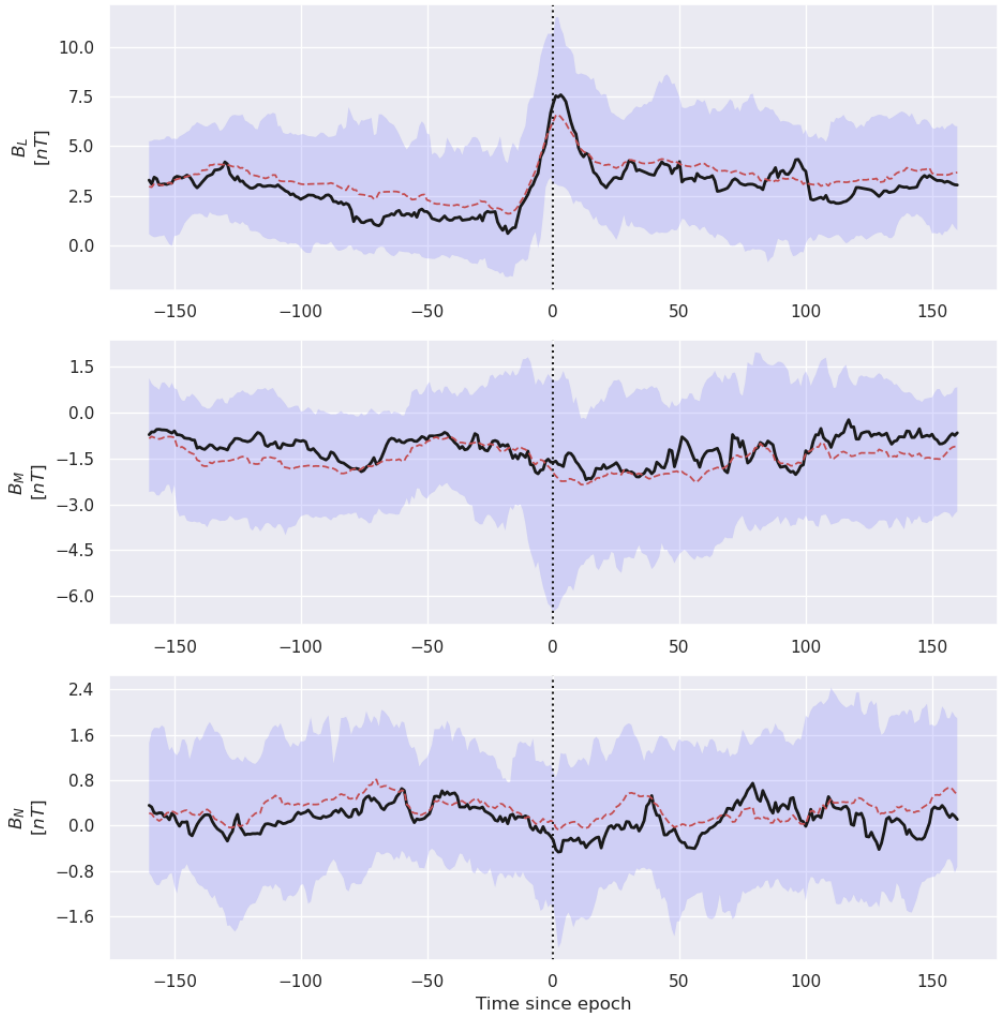

FIGURE 3.10 – Example of SEA using MMS dataset for DF events. The black line marks the superposed epoch median, the red dashed line marks the superposed epoch mean, and the blue fill marks the range.

Chapitre 4

Investigation of the homogeneity of energy conversion processes at DFs from MMS measurements

"The stars had only one task : they taught me how to read. They taught me I had a language in heaven and another language on earth."

Mahmoud Darwish, *Unfortunately, It Was Paradise : Selected Poems, 2013.*

Contents

4.1 Data and Methods 50
4.2 Overview of classical DF properties 50
4.3 Current density and Hall electric field comparisons . . 54
4.4 Analysis of Ohm's Law 56
4.5 Energy conversion processes at the DF 60
4.6 Discussion and summary 68

4.1 Data and Methods

In this chapter, we analyse the various physical quantities related to DFs with the same treatment (data noise reduction, time averaging, LMN frames, current density calculation both from particle and magnetic field measurements, pressure gradient in the normal direction from single spacecraft method, ...) as described in chapter 3.

Data were gathered by MMS on the 23rd of July 2017 when the constellation was located on the dusk side of the magnetotail [X=-23.9, Y=5.8, Z=5.4] Earth radii (R_E) in the GSE. The average spacecraft separation was about 15 km i.e. close to the scale of the average electron Larmor radius in the magnetotail during this period (in average between 40 and 60 km).

Between 16 : 45 and 17 : 15 UT, MMS detected successive fast earthward flows which occurred during a substorm period as indicated by the Auroral electrojet -Auroral Electrojet (AE) index $\sim$ 400 nT (courtesy of Kyoto World data Center for Geomagnetism http://wdc.kugi.kyoto-u.ac.jp/ae_provisional/201707/index_20170723.html). The AE index is built from geomagnetic field variations measured at ground in a geomagnetic latitude range of 61°-70° in the northern hemisphere (Davis and Sugiura, 1966). Sudden increase of the AE index is a good proxy of substorm onset. In section 4.2, an overview of six DF signatures embedded in these fast flows are described. Section 4.3 presents the results related to the current density calculations and to the Hall electric field. Section 4.4 and section 4.5 discuss the generalised Ohm's law and the energy conversion processes in the vicinity of DFs respectively. Finally, section 4.6 summarises my results presented in this chapter followed by a discussion. Note that for the sake of clarity, only DF1 figures are shown in this chapter whereas figures related to DF2 up to DF6 are presented in Appendix B.

4.2 Overview of classical DF properties

In this section, we describe the global properties of six DF events, each one embedded in a fast earthward flow detected by MMS between 16 : 45 and 17 : 15 UT.

Figures [4.1,B.1,B.2,B.3] show these six DF events denoted DF1, DF2a,b, DF3a,b, and DF4, respectively, in their respective LMN frame obtained from the MVAB. For each event, the MVAB results are summarized in Table 4.1 and the time period used is indicated. From these MVAB results, we define L, M, and N vectors as maximum, intermediate, and minimum variance directions respectively. We have verified that the ratio between the three corresponding eigenvalues, $\lambda_1, \lambda_2, \lambda_3$ are sufficiently large ($>$ 10 in average though three ratios are between 2 and 10) to indicate that the three directions are well separated (see Table 4.1). Note that in accordance with the propagation direction given by timing analysis,

the orientation of the N vector of the MVAB was set to be positive (earthward) and L always oriented northward leading to M directed dawnward. Table 4.2 shows the components of the normal estimated by a timing analysis as well as the velocity along the normal in GSE. Normal directions obtained from the two methods are qualitatively consistent and indicate that DFs are mainly oriented earthward (along X GSE), some DF normals having a significant duskward component (along $+Y$ GSE) and southward component (along -Z GSE). DF normal velocities range from 135 to 481 km/s. As the angle between the DF2a and DF2b normals (respectively DF3a and DF3b) is $\sim 12.7°$ (resp. $\sim 22.2°$) and for the sake of simplicity, only DF2a and DF3a LMN frames are used for plotting DF2 and DF3 periods. We checked that similar results are obtained when individual LMN frames are used. The estimated thickness δ of each DF event is also given in Table 4.2 (in km and in d_i, the ion inertial length estimated based on the plasma sheet density prior to respective DF arrival) by multiplying the normal DF velocity with the time interval between the minimum and maximum of B_L, (Khotyaintsev et al., 2017).

The estimated thickness δ obtained from different missions ranges from 0.98 to 3.78 d_i. For instance from THEMIS data, Runov et al. (2009) found $\delta \sim 500$ km considering a DF passing time of around ~ 1.70 s and a measured ion velocity of ~ 300 km/s. Using timing analysis from Cluster data Khotyaintsev et al. (2011) estimated the speed of the DF to be about 450 km/s and with a DF passing time of about ~ 1.33 s, they found $\delta \sim 600$ km. Fu et al. (2012a) considering a DF passing time of about ~ 2.1 s and a DF speed of ~ 197 km/s found $\delta \sim 420$ km. Using the minimum directional derivative (MDD) technique (Shi et al., 2005) and Spatio-temporal difference (STD) method (Shi et al., 2006) to estimate the propagating speed of the DF, Yao et al. (2013) found a speed of about 100 km/s and for a DF passing time of 6 s ; they estimated $\delta \sim 600$ km. More recently, using timing analysis with MMS data, Khotyaintsev et al. (2017) found a DF speed of about 370 km/s and obtained $\delta \sim 575$ km for a DF passing time of ~ 1.55 s. Finally, using the STD method or classical timing analysis with MMS data, (Yao et al., 2017) found a DF speed $\sim 130 - 150$ km/s and estimated $\delta \sim 520 - 600$ km for a DF passing time of around 4 s.

Figures [4.1,B.1,B.2,B.3] display ion scale properties of these six DFs, respectively. Magnetic field components and magnitude are plotted in Figures [4.1,B.1,B.2,B.3]A, FPI ion velocity components and the N component of the HPCA velocity (V_{H+}) in Figures [4.1,B.1,B.2,B.3]B, ion and electron temperatures in Figures [4.1,B.1,B.2,B.3]C, electron density in Figures [4.1,B.1,B.2,B.3]D, and finally ion and electron pressure variations in Figures [4.1,B.1,B.2,B.3]E. These six DF events are identified by a vertical red dashed line (maximum of the B_L component). Vertical black dashed lines indicate possible signatures of flux ropes (large increase of the total magnetic field due to an increase of the cross-tail M component, associated with a bipolar signature of another component) ahead of these DF signatures. The detailed description of these flux ropes is beyond the scope of this study. They are mentioned

TABLE 4.1 – Minimum Variance Analysis (MVAB) Results : Eigenvalue ratios and vectors (in GSE).

DF	UT	$\frac{\lambda_M}{\lambda_N}$	$\frac{\lambda_L}{\lambda_N}$	L	M	N
DF1	16 :47 :45/16 :47 :50	5.69	450.62	0.14,0.63,0.76	0.13,-0.78,0.62	0.98,0.01,-0.19
DF2a	16 :55 :10/16 :55 :25	75.67	813.54	0.06,0.47,0.88	0.64,-0.70,0.33	0.77,0.54,-0.34
DF2b	16 :55 :35/16 :55 :36	19.6	14218.5	0.08,0.72,0.69	0.60,-0.59,0.54	0.8,0.37,-0.48
DF3a	17 :01 :03/17 :01 :09	42.25	103.88	0.01,0.59,0.81	0.61,-0.64,0.47	0.79,0.49,-0.36
DF3b	17 :02 :18/17 :02 :19	29.62	186.86	0.6,-0.52,0.61	-0.20,-0.83,-0.52	0.78,0.19,-0.60
DF4	17 :09 :45/17 :09 :52	58.12	581.82	0.32,0.06,0.95	0.77,-0.61,-0.22	0.56,0.79,-0.24

as they can drive their own energy conversion processes as we will see in the next sections.

The six DF signatures can be considered to belong to category A, the most common category, of the DF classification established from a statistical study based on 303 events detected by the Cluster mission (Schmid et al., 2015, see also next chapter). Indeed, Schmid et al. (2015) created four large categories to which DF are linked according to their magnetic field, ion density, velocity, temperature and pressure variations during the DF crossing. Category A, the most common, corresponds to DFs with a density decrease (see Figures [4.1,B.1,B.2,B.3]D) and a temperature increase (see Figures [4.1,B.1,B.2,B.3]C) consistent with the transition between a relatively cold dense plasma at rest with respect to a hot tenuous fast earthward moving plasma. Note that HPCA V_N velocity is always much larger than FPI V_N (see Figures [4.1,B.1,B.2,B.3]B), confirming that FPI instrument underestimates the velocity of the earthward flow due to its limited upper energy. Moreover, the maximum of the V_N component of the ion velocity is always located after the DF associated with the maximum of B_L (except for DF4) which, according to Hamrin et al. (2014) results should therefore correspond to decelerated DFs with a significant part of the energy being radiated. Furthermore, in such conditions, Fu et al. (2011) showed that these DFs correspond to a growing magnetic flux pile-up region (innermost flux tubes being pushed by faster outermost flux tubes leading to the compression of the magnetic field) causing the acceleration of electrons by betatron effect. Finally, from Figures [4.1,B.1,B.2,B.3]E one can see that for both ions and electrons, the DF always corresponds to a transition between high pressure to a low-pressure region at fluid scale whereas at the kinetic scale it mostly corresponds to a transient pressure reduction except for DF4. Therefore at the DF crossing, the particle pressure gradients vary fastly.

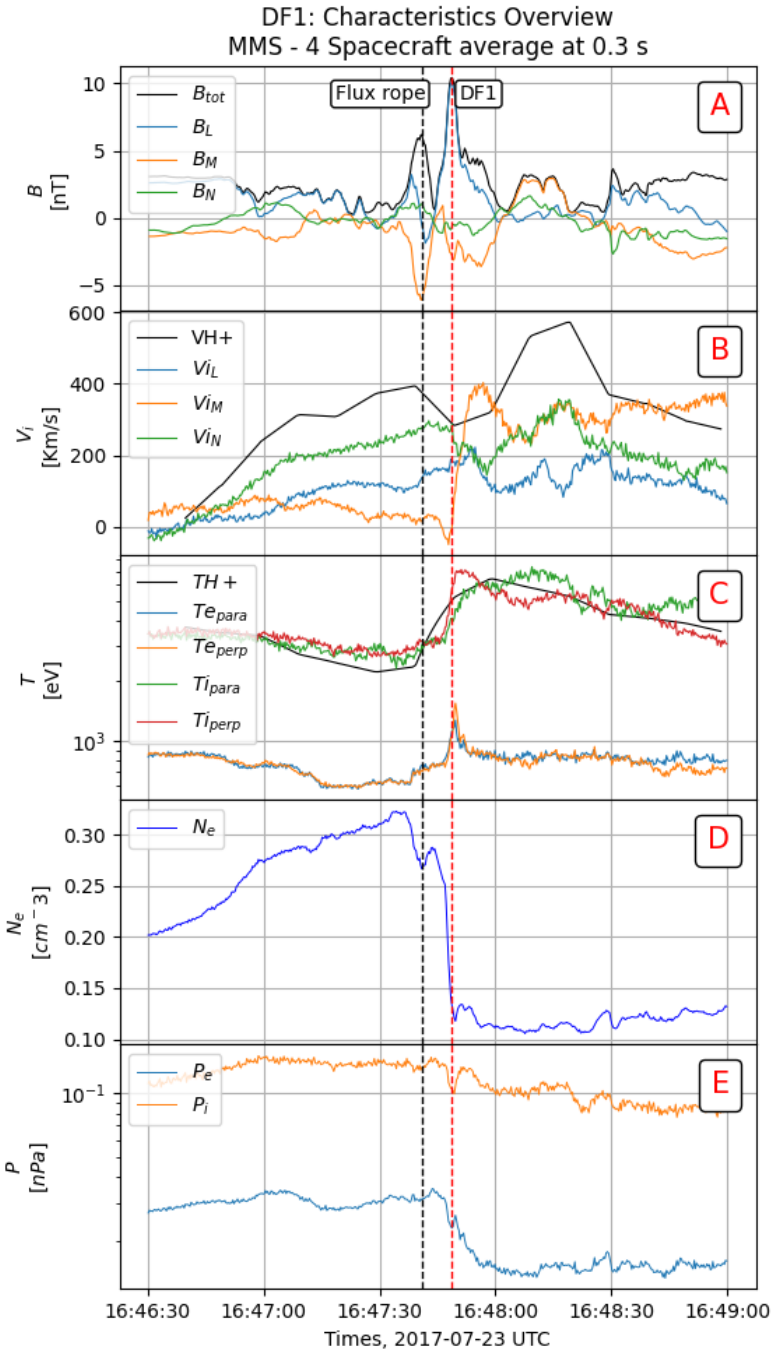

FIGURE 4.1 – DF1 signature in LMN frame, all data are averaged over the four satellites then time averaged at 0.3 s. Panel (A) shows the magnetic field components and its magnitude, (B) the components of ion velocity from FPI and the N component of the V_{H+} HPCA velocity, (C) the electron and ion temperatures from FPI with the isotropic proton temperature from HPCA, (D) the electron density, (E) the ion and electron pressures from FPI. Vertical black dashed lines indicate possible flux rope signatures (see text).

TABLE 4.2 – Timing analysis Results : Normal vectors and velocity (in GSE) with estimated DF thickness δ.

DF	UT	[n_x, n_y, n_z]	[Vn_x,Vn_y,Vn_z]	Vn [km/s]	δ [km]	δ [d_i]
DF1	16 :47 :45/16 :47 :50	0.95,0.30,-0.09	186,59,-18	196	588	1.34
DF2a	16 :55 :10/16 :55 :25	0.95,0.27,-0.13	129,36,-17	135	811.98	1.63
DF2b	16 :55 :35/16 :55 :36	0.86,0.17,-0.48	241,49,-135	281	561.42	0.98
DF3a	17 :01 :03/17 :01 :09	0.60,0.72,-0.35	289,345,-169	481	1924.92	3.78
DF3b	17 :02 :18/17 :02 :19	0.34,0.30,-0.89	124,111,-327	367	587.536	0.81
DF4	17 :09 :45/17 :09 :52	0.54,0.83,-0.14	251,390,-63	468	1871.72	3.67

4.3 Current density and Hall electric field comparisons

For each DF event in their own LMN frame, Figures [4.2,B.4,B.5,B.6] display comparisons between current densities ($\mathbf{J}_{part} = en_e(\mathbf{v}_i - \mathbf{v}_e)$ computed from the particle measurements and $\mathbf{J}_{curl} = (\nabla \times \mathbf{B})/\mu_0$) computed from the magnetic field measurements as described in section 3.4.1. They also display the Hall electric fields ($\mathbf{J}_{part} \times \mathbf{B}/(ne)$ and $\mathbf{J}_{curl} \times \mathbf{B}/(ne)$) calculated using the different current densities.

Figures [4.2,B.4,B.5,B.6]A,B, and C for each event demonstrate good agreement between the two current density measurements within an accuracy < 10 nA/m^2. Indeed, considering the accuracy of 0.1 nT for the magnetic field measurement (Russell et al., 2016), the accuracy of the current density measurements from the curlometer with a spacecraft separation of 15 km can be roughly estimated to 5 nA/m^2. The current density accuracy from the particle measurement is estimated to 8 nA/m^2 (see section 4.5 for more details). In a similar manner, Figures [4.2,B.4,B.5,B.6]D,E, and F confirm that Hall fields estimated from both currents are in good agreement, within an accuracy ~ 1 mV/m. However, a large discrepancy between the two Hall field calculations can be found in the low-density region and when current densities are smaller than or close to their error bars and oscillate around 0. In such conditions, the error on the current density measurement is amplified by the low density and leads to a large error in the Hall field calculation (e.g., Figure [B.6]E).

Furthermore, we can identify each DF with their negative peak in J_M (an increase of cross-tail duskward current) associated with the bipolar signature of the N component of the Hall electric field. This latter is mostly produced by the reversal of J_M just behind the DF, B_L remaining positive (see Figures [4.2,B.4,B.5,B.6]B and [4.1,B.1,B.2,B.3] A). This Hall field is expected due to the ion inertial scale of the DF which leads ions to be decoupled from the magnetic field.

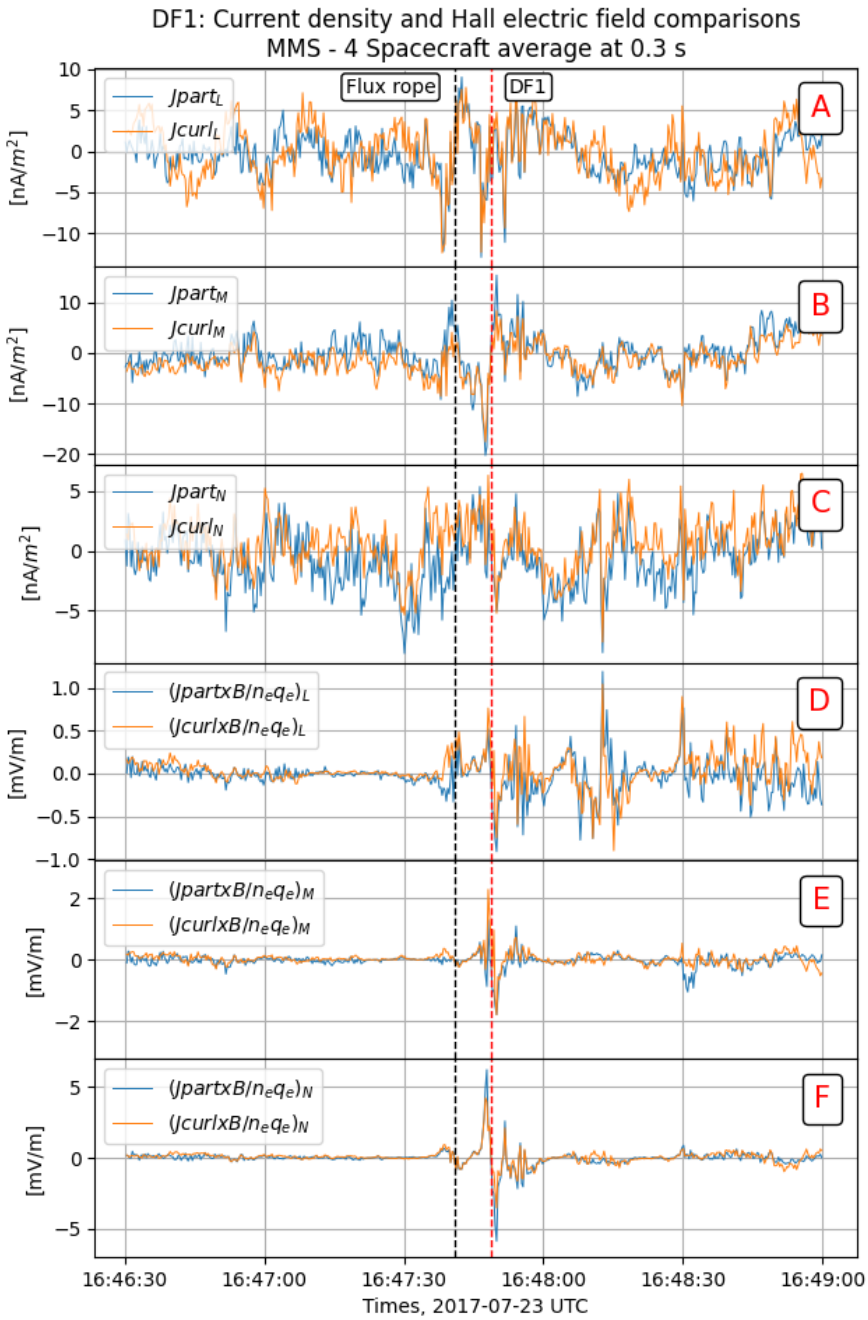

FIGURE 4.2 – DF1 LMN frame, comparison between current densities calculated from $\mathbf{J}_{part} = en_e(\mathbf{v}_i - \mathbf{v}_e)$ and $\mathbf{J}_{curl} = \nabla \times \mathbf{B}/\mu_0$: (A) along L, (B) along M, (C) along N, and Hall electric field comparison between two computations $\mathbf{J}_{part}/(en_e)$ and $\mathbf{J}_{curl}/(en_e)$: (D) along L, (E) along M, (F) along N.

4.4 Analysis of Ohm's Law

The precise analysis of all terms in the generalized Ohm's law, estimated from in-situ measurements, allows us to identify the regions where kinetic effects become important. Then by computing the curl of the equation, which corresponds to Faraday's law, we could in principle also determine where the plasma decouples from the magnetic field. It also leads to a better understanding of which term plays the most important role in the energy conversion process. Previous analyses related to fast plasma flows in the magnetotail have been carried out using measurements from the four Cluster satellites (4 s time resolution, e.g., Lui et al., 2007). The authors suggested that the anomalous resistivity term arising from electromagnetic field fluctuations and the Hall term played a dominant role in the breakdown of the frozen-in condition. Using both single and multi-satellite methods, it was confirmed that Hall and electron pressure gradient terms contribute to ion decoupling at DF although the Hall term was indeed dominant (Fu et al., 2012a). High time and spatial MMS resolutions allow analysis of Ohm's law at kinetic scales which are relevant at DF (e. g, Yao et al., 2017; Liu et al., 2018). Assuming a possible anomalous resistivity η for collisionless plasmas, the generalized Ohm's law is written as :

$$\mathbf{E} + \mathbf{v_e} \times \mathbf{B} = -\frac{1}{en}\nabla \cdot \mathbf{P_e} - \frac{m_e}{e}\frac{d\mathbf{v_e}}{dt} + \eta\mathbf{J} \tag{4.1}$$

where $\mathbf{v_e}, \mathbf{P_e}$ are the electron velocity and pressure tensor respectively. One writes equivalently

$$\mathbf{E} + \mathbf{v_i} \times \mathbf{B} = \frac{\mathbf{J} \times \mathbf{B}}{en} - \frac{1}{en}\nabla \cdot \mathbf{P_e} - \frac{m_e}{e}\frac{d\mathbf{v_e}}{dt} + \eta\mathbf{J} \tag{4.2}$$

where $\mathbf{v_i}$ is the ion velocity.

In the dayside region, where the plasma density is on average larger than in the magnetotail and at the vicinity of the electron diffusion region, all terms can be estimated with good accuracy and the validity of the Ohm's law can be tested. Pressure gradient and inertial terms are found to have significant contributions without excluding the existence of an anomalous resistivity term due to high-frequency electric field fluctuations (Torbert et al., 2016b). In the low-density magnetotail (< 1 part.cm^{-3}) and in the vicinity of DFs, electron pressure gradient and inertial terms are difficult to estimate and quite noisy even after time averaging (Liu et al., 2018). For each DF event, we have computed both terms. The inertial term is negligible whereas the divergence of the electron pressure tensor is larger, but still very noisy. Therefore, in the rest of the study, only convective and Hall terms are shown. No anomalous resistivity will be considered, yet the electron pressure gradient term will be estimated by the single satellite method described in section 3.3.3. All data are averaged over the four satellites.

As mentioned previously, the decoupling of ions or electrons from the magnetic field occurs when the curl of the ideal term ($\mathbf{E} + \mathbf{v}_{i,e} \times \mathbf{B}$) is not equal to $\mathbf{0}$.

Therefore the electron decoupling due to the electron pressure gradient term could happen when $\nabla \times [(\nabla P_e)/n_e] = -1/(n_e^2)[\nabla n_e \times \nabla P_e]$ does not vanish which can be the case when the density is not homogeneous. However, if we assume that the electron pressure is a function of n_e only (as for instance with a polytrope law $P_e \propto n_e^\gamma$) this term goes to 0 and electrons remain coupled to the magnetic field even for an unhomogeneous density (e. g., Sittler and Scudder, 1980). Therefore, when we suggest in the following sections that the electron gradient pression term could cause the decoupling of electrons from the magnetic field, we implicitly assume a more complex equation of state for electrons.

Figures [4.3,B.7,B.8,B.9] show the comparison between the ideal ion frozen-in ($\mathbf{E}+\mathbf{v}_i \times \mathbf{B}$) and the Hall electric field ($\mathbf{J}_{part} \times \mathbf{B}/(en)$) terms in LMN coordinates. For all events, ions are decoupled in the vicinity of the DF by the Hall electric field. However, the difference between the two terms can exceed 2 mV/m, which suggests that the electron pressure gradient term is not negligible in these regions despite the difficulty to estimate it from the four satellite measurements.

Figures [4.4,B.10,B.11,B.12] show the comparison between the ideal electron frozen-in term ($\mathbf{E}+\mathbf{v}_e \times \mathbf{B}$) and the ideal ion frozen-in plus the Hall term computed from curlometer ($\mathbf{E} + \mathbf{v}_i \times \mathbf{B} - \mathbf{J}_{curl} \times \mathbf{B}/(en)$). One can see that electrons are mostly magnetized as the ideal frozen-in term does not exceed $1.7 - 2$ mV/m, which is the order of the error bar of the E' measurement (see the next section for details about the error bars). However, at the DF this term is very close to or exceeds the error bar. This suggests that electrons could be decoupled from the magnetic field assuming that $\nabla \times [(\nabla P_e)/n_e]$ term is non zero. It is difficult to confirm that this decoupling is due to the term of the divergence of the electron pressure tensor at DF since the calculation of this term is very noisy for such low-density plasma conditions (e. g., Yao et al., 2017; Liu et al., 2018).

Figures [4.3,B.7,B.8,B.9]C and Figures [4.4,B.10,B.11,B.12]C show the contribution of the electron pressure term using the single spacecraft method described in section 3.3.3 (green line) based on four spacecraft averaged quantities. These figures confirm that the electron pressure gradient term is small but not negligible compared to the ideal frozen-in and Hall field terms. Note that for DF2a and DF2b (resp. DF3a and DF3b), we have used the smallest estimated V_N. Therefore the gradient term is overestimated for the fastest DFs (see Table 4.2). At the vicinity of the DF crossing and along the normal direction, this raw estimate allows us to suggest that the electron pressure gradient term must be taken into account for the Ohm's law of ions (Figures [4.3,B.7,B.8,B.9]C) and electrons (Figures [4.4,B.10,B.11,B.12]C) to be satisfied.

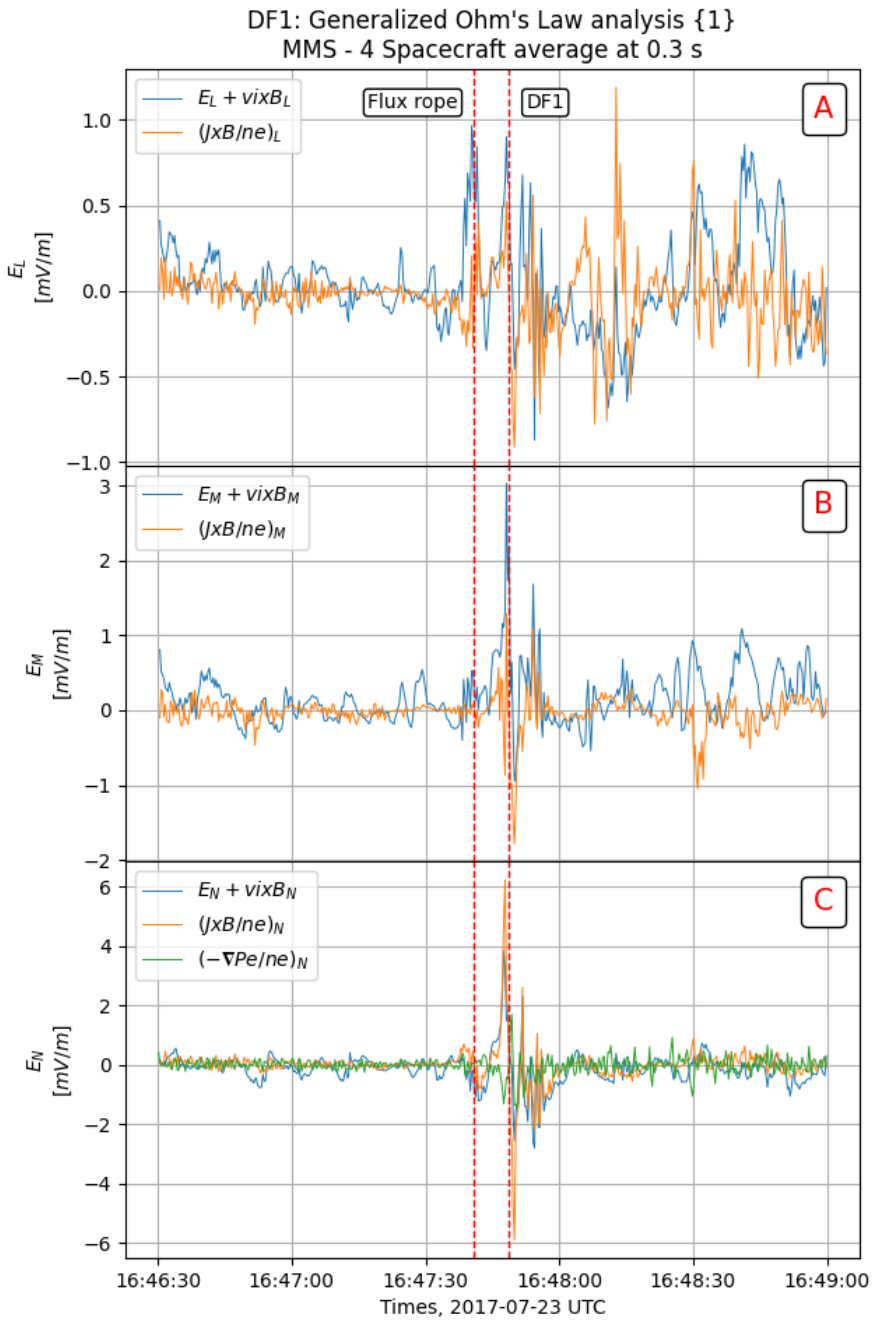

FIGURE 4.3 – Panels A, B, and C show L, M, N components of Ion Ohm's Law terms respectively : $\mathbf{E} + \mathbf{v_i} \times \mathbf{B}$ (blue line), $(\mathbf{J}_{part} \times \mathbf{B})/(ne)$ (orange line). Panel C also includes electron pressure gradient term along N (green line).

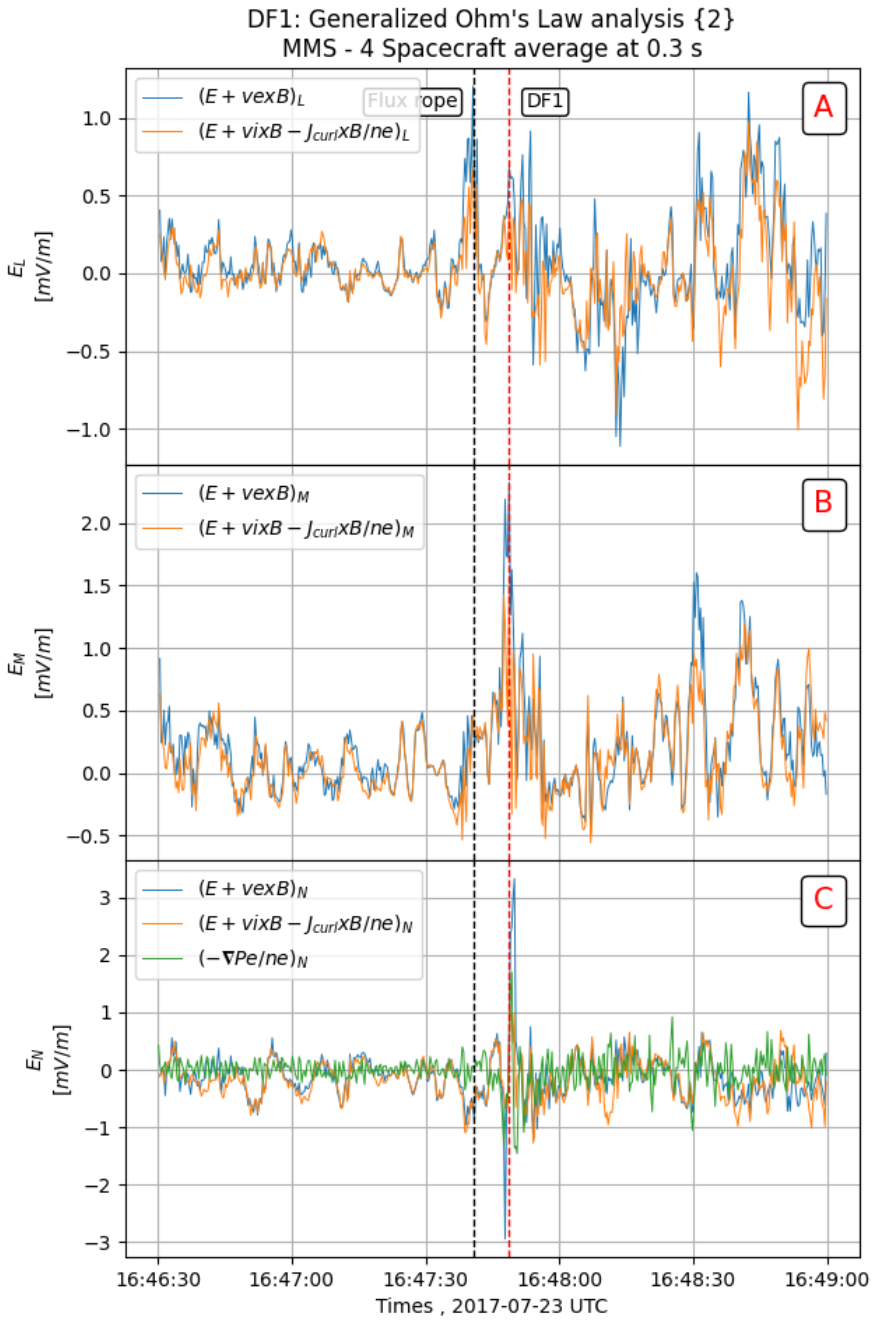

FIGURE 4.4 – Panels A, B, and C shows L, M, N components of electron Ohm's Law terms respectively : $\mathbf{E} + \mathbf{v_e} \times \mathbf{B}$ (blue line), and $\mathbf{E} + \mathbf{v_i} \times \mathbf{B} - (\mathbf{J}_{curl} \times \mathbf{B})/(ne)$(orange line). Panel C also includes electron pressure gradient term along N (green line).

4.5 Energy conversion processes at the DF

The conservation of the electromagnetic energy or Poynting theorem writes (e g., Birn and Hesse, 2005) :

$$\frac{\partial}{\partial t}\left[\frac{\epsilon_0 \mathbf{E}^2}{2} + \frac{\mathbf{B}^2}{2\mu_0}\right] = -\nabla \cdot (\frac{\mathbf{E}\times\mathbf{B}}{\mu_0}) - \mathbf{j}\cdot\mathbf{E} \tag{4.3}$$

where ϵ_0 is the vacuum permittivity, $(\mathbf{E}\times\mathbf{B})/\mu_0$ is the Poynting vector describing the electromagnetic energy flow and $\mathbf{j}\cdot\mathbf{E}$ is the energy conversion term. Then we can neglect the electric field energy density on equation 4.3 to be consistent with the neglect of the displacement current in Ampere's law accompanied by the assumption of quasi-neutrality, valid for transport and wave speeds well below the speed of light. Therefore the equation becomes the conservation of the magnetic energy :

$$\frac{\partial}{\partial t}\left[\frac{\mathbf{B}^2}{2\mu_0}\right] = -\nabla \cdot (\frac{\mathbf{E}\times\mathbf{B}}{\mu_0}) - \mathbf{j}\cdot\mathbf{E} \tag{4.4}$$

Finally, by rewriting the equation 4.4 using the electric field in the ion or electron frames, $\mathbf{E}^{'} = \mathbf{E} + \mathbf{v}_{i,e}\times\mathbf{B}$, we get :

$$\frac{\partial}{\partial t}\left[\frac{\mathbf{B}^2}{2\mu_0}\right] = -\nabla \cdot (\frac{\mathbf{E}\times\mathbf{B}}{\mu}) - \mathbf{v}_{i,e}\cdot(\mathbf{j}\times\mathbf{B}) - \mathbf{j}\cdot\mathbf{E}^{'} \tag{4.5}$$

where $\mathbf{E}^{'}$ is given by the ion (equation 4.2) or electron (equation 4.1) expressions of the Ohm's law. Figures [4.5,B.13,B.14,B.15] show the magnetic and the electric field components, the current density components computed from particle measurements and the corresponding energy conversion $\mathbf{j}\cdot\mathbf{E}$ term for each DF event. For all DF events, the DF is associated with a positive $\mathbf{j}\cdot\mathbf{E}$ slightly ahead or at the DF therefore to an energy transfer from fields to the plasma (dissipation or load region) in the spacecraft frame. However, a negative value with an equivalent amplitude is measured immediately behind the front, indicating an energy transfer from the plasma to the electromagnetic field (dynamo or generator region). When we calculate separately the three terms of the scalar product using the LMN coordinates, we can see that the main contribution comes from the cross-tail current and electric field components ($J_M \cdot E_M$, see Figures [4.6,B.16,B.17,B.18]). Furthermore, the negative part of the energy conversion term is mostly due to the local reversal of the J_M component while E_M related to the flow motion remains positive. Note that the large variations of E_N at the DF do not lead to any energy conversion as they correspond to the Hall field therefore are perpendicular to the main component of the current density. Regardless of the sign, energy conversion values range from -0.02 to +0.02 nW/m^3 except for a maximum negative value of -0.04 for DF1. Finally, one can notice that the possible flux rope signatures are

associated with positive or negative energy conversion terms comparable to those associated with DFs.

For each DF, Figures [4.8,B.22,B.23,B.24]A, B and C display four spacecraft averaged values of ($\mathbf{j}_{curl} \cdot (\mathbf{E}+\mathbf{v}_e \times \mathbf{B})$) and ($\mathbf{j}_{curl} \cdot (\mathbf{E}+\mathbf{v}_i \times \mathbf{B})$) using the current density estimated from the curlometer and ($\mathbf{j}_{part} \cdot (\mathbf{E}+\mathbf{v}_e \times \mathbf{B})$) from the particle measurements. We can therefore verify that the energy conversion term is equal in the ion and electron frames, attesting to the reliability of the energy conversion term calculation. Indeed mathematically, we have $\mathbf{j} \cdot (\mathbf{E}+\mathbf{v}_i \times \mathbf{B}) - \mathbf{j} \cdot (\mathbf{E}+\mathbf{v}_e \times \mathbf{B}) = \mathbf{j} \cdot (\mathbf{j} \times \mathbf{B})/(ne) = 0$. In the fluid frames, the four spacecraft average of the energy conversion term is mostly negative (from -0.02 to -0.01 nW/m^3) just ahead of the DF and corresponds to an energy transfer from the plasma to the electromagnetic fields (generator or wave radiation) in accordance to a previous MMS single event study (Yao et al., 2017). One can notice that, when the curlometer is used, some discrepancies between calculations in ion and electron frames can be seen for DF4. This is due to the fact that some of the current density components are smaller or close to their error bars (e.g., J_N in Figure [B.6]C for DF4) as mentioned in section 4.3. Figures [4.7,B.19,B.20,B.21] show separately the different contributions of $\mathbf{j} \cdot \mathbf{E}'$. We can see that the largest contribution still comes from the $J_M E'_M$ term which is now negative (panel E). It is worth noticing that the $J_N E'_N$ contribution is consistent with the contribution computed from the electron pressure gradient term $-J_N.\nabla P_e/(en)$ (see green line and black line in Figure [4.7]E). Assuming that this agreement exists also for the M component, we can suggest that the energy conversion process in the fluid frame would be controlled by the electron pressure gradient in the azimuthal or cross-tail (M) direction. Thus, the significant negative values of the energy conversion term in the fluid frame confirms the crucial role of the electron pressure gradient term in energy conversion processes. In addition to allowing the decoupling of the electrons from the magnetic field lines, the electron pressure gradient constitutes the free energy for radiating waves or more generally to generate electromagnetic fields in the fluid frame at DF.

For each DF event, Figures [4.8,B.22,B.23,B.24]C show the energy conversion term for each individual satellite in electron frames. These single satellite calculations indicate that the energy conversion process is not homogeneous at the scale of the tetrahedron (electron scales). Indeed, strong variations of the sign and the amplitude of the energy conversion term are seen from one satellite to another and can differ significantly from the four spacecraft average values. Such variations suggest that a physical process is going on at the electron scales while the DF is propagating earthward.

For a better understanding of the origin of the non-homogeneity of the energy conversion at the electron scales, we estimated the standard deviation for each component of the current density and the electric field in the fluid frame ($\mathbf{E}' = \mathbf{E} + \mathbf{v}_e \times \mathbf{B}$) normalized by their respective error bar :

$$SD(X)/\Delta X = \sqrt{\Sigma_{i=1}^{4}(X_i - < X >)^2/4}/\Delta X \tag{4.6}$$

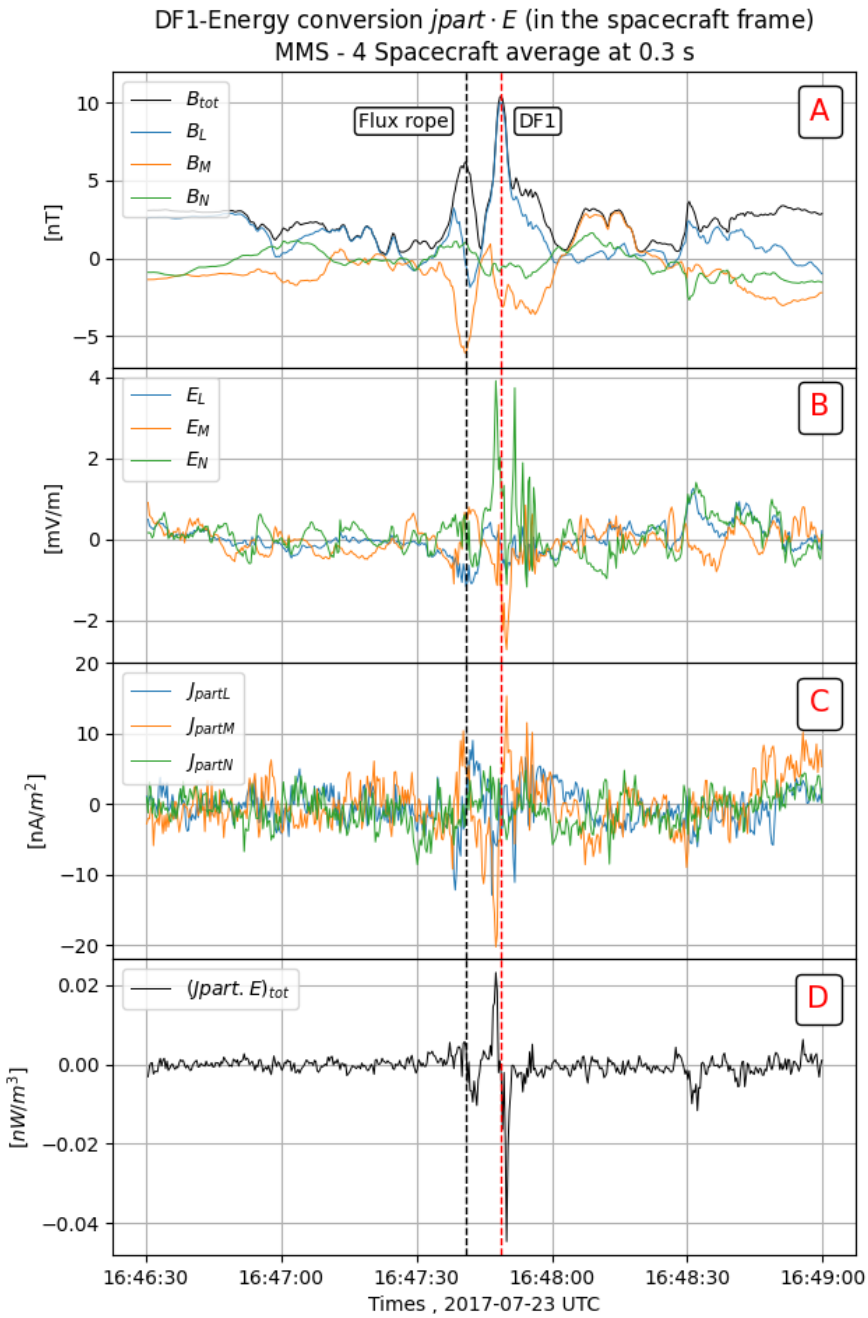

FIGURE 4.5 – For DF1 event and in LMN frame : (A) Magnitude and components of the magnetic field, (B) Electric field components, (C) Current density components using $\mathbf{J}_{part}$, (D) Energy conversion $\mathbf{j}_{part} \cdot \mathbf{E}$ (in the spacecraft frame).

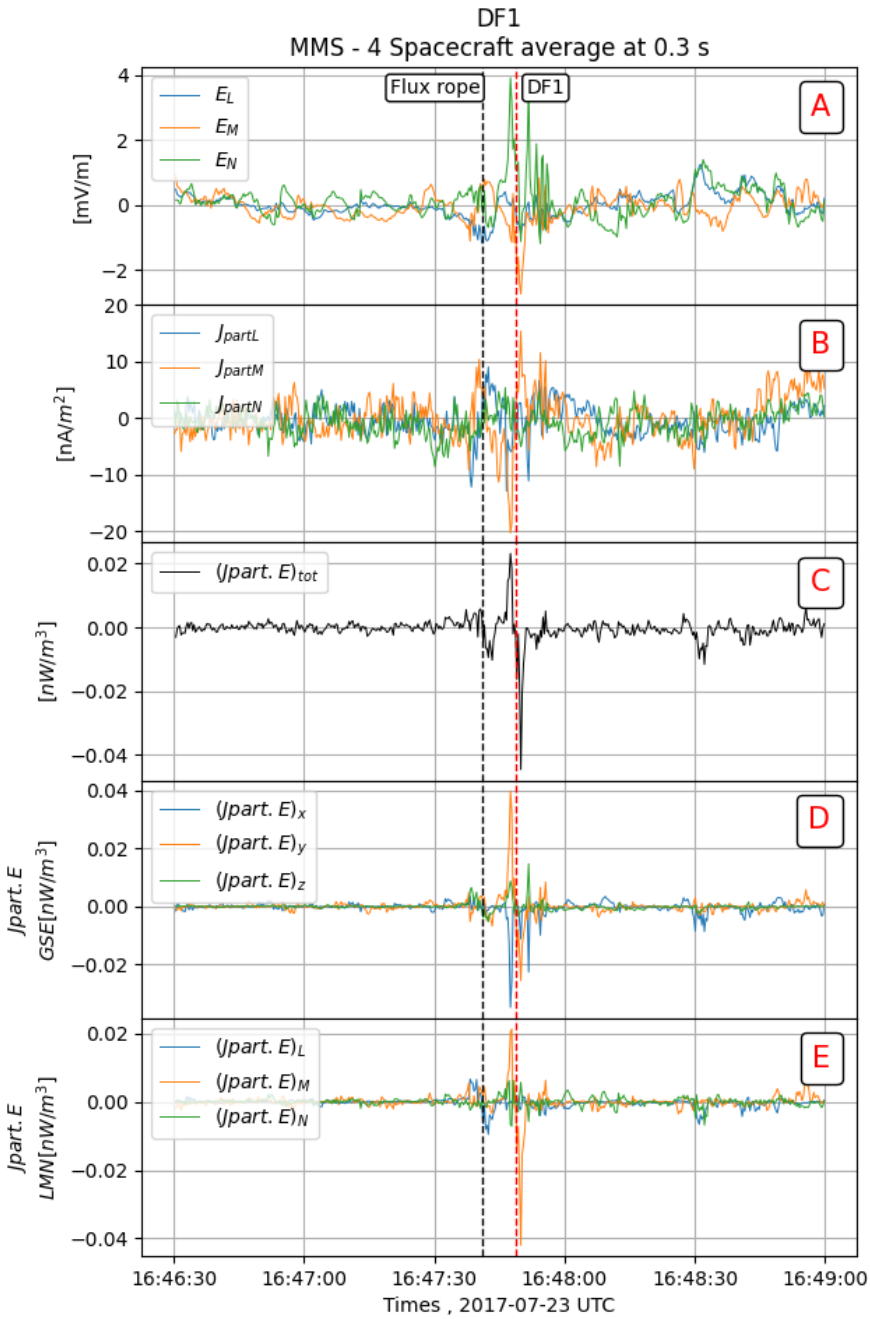

FIGURE 4.6 – For DF1 event and in LMN frame : (A) Components of the Electric field, (B) Current density components using $\mathbf{J}_{part}$, (C) Energy conversion $\mathbf{j}_{part} \cdot \mathbf{E}$ (in the spacecraft frame), (D) Separate contributions of energy conversion term $\mathbf{j}_{part} \cdot \mathbf{E}$ (GSE) and , (E) Separate contributions of energy conversion term $\mathbf{j}_{part} \cdot \mathbf{E}$ (LMN).

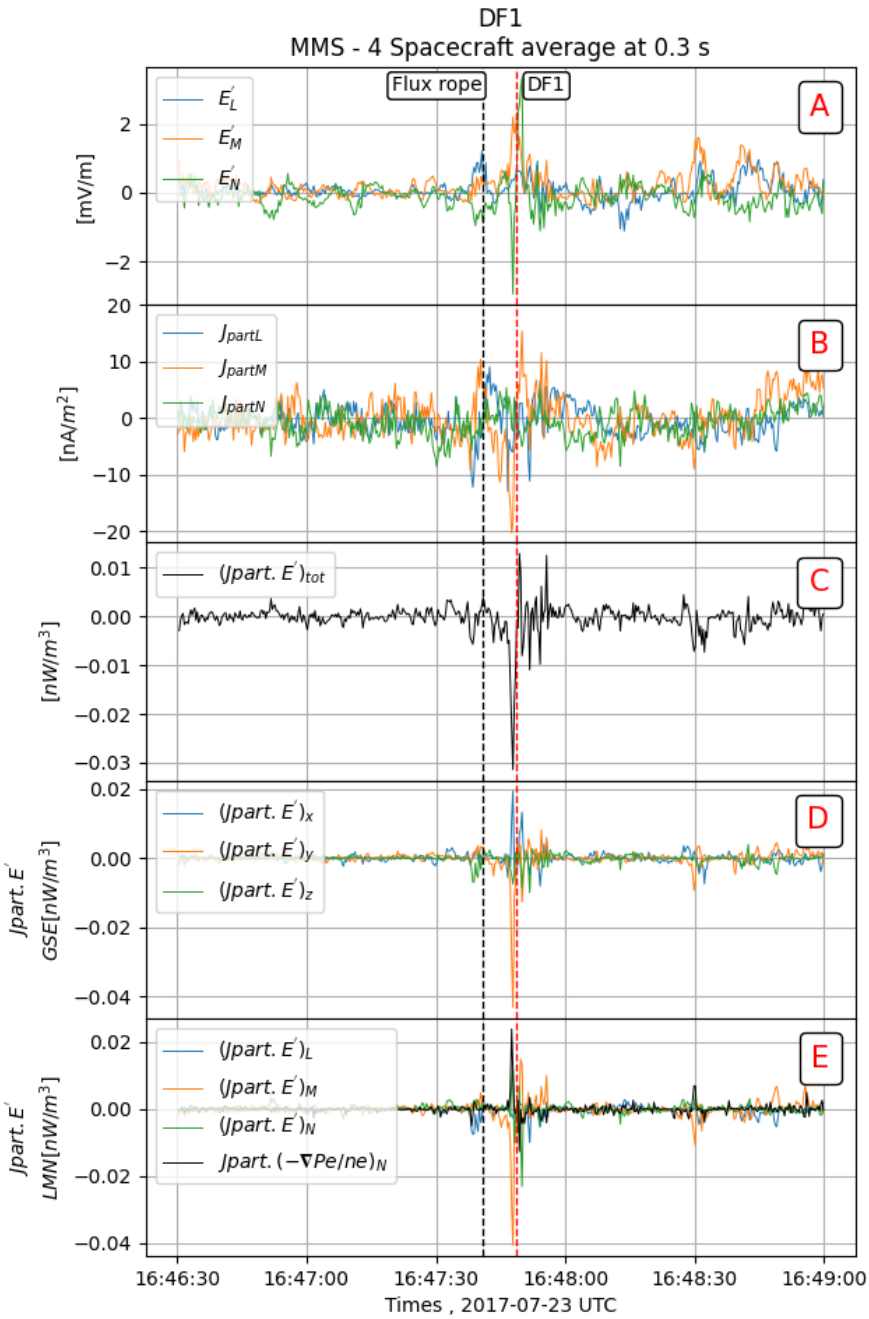

FIGURE 4.7 – For DF1 event and in LMN frame : (A) Components of the electric field in the electron frame ($\mathbf{E}' = \mathbf{E} + \mathbf{V}_e \times \mathbf{B}$), (B) Current density components using $\mathbf{J}_{part}$, (C) Energy conversion $\mathbf{j}_{part} \cdot \mathbf{E}'$ (in the fluid frame), (D) Separate contributions of energy conversion term $\mathbf{j}_{part} \cdot \mathbf{E}'$ (GSE) and (E) Separate contributions of energy conversion term $\mathbf{j}_{part} \cdot \mathbf{E}'$ (LMN) including the contribution of the electron pressure gradient ($-J_N.\nabla P_e/(en)$).

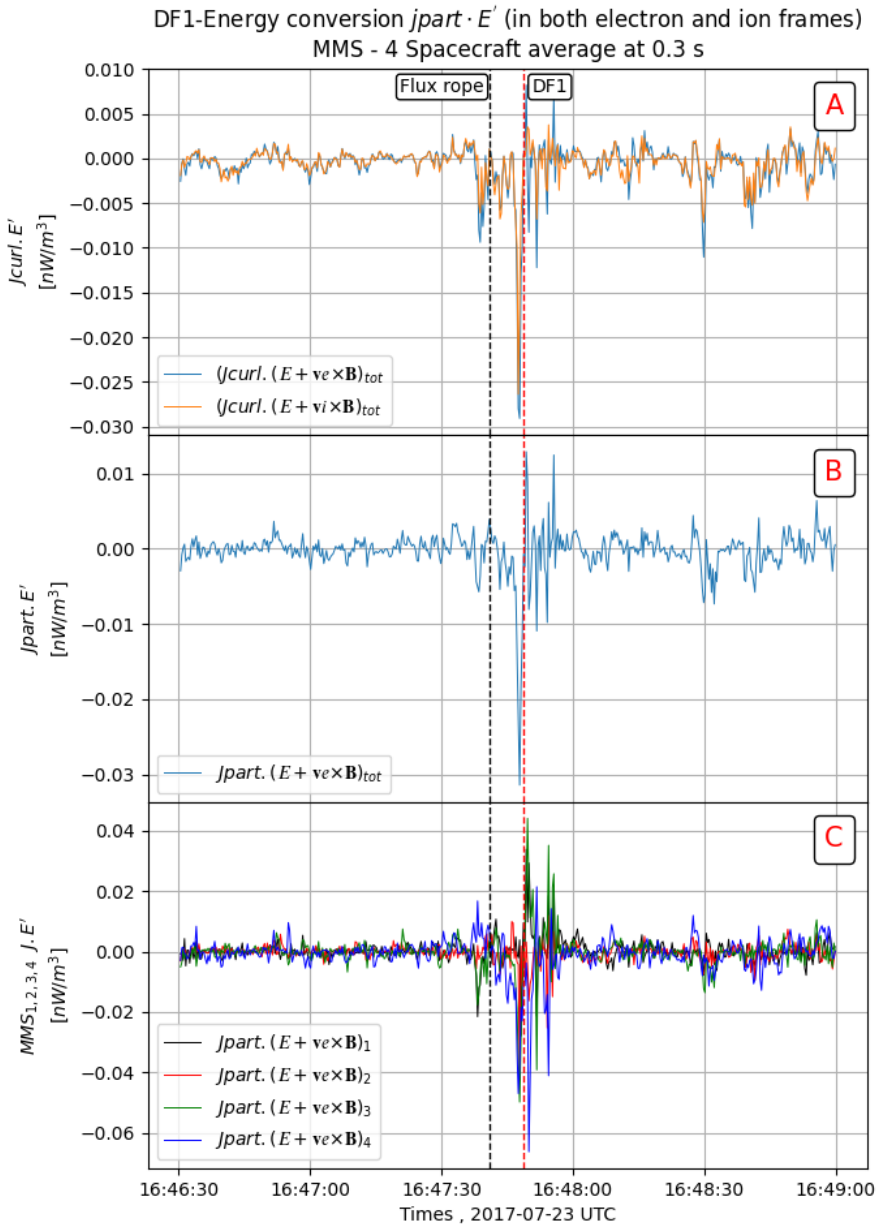

FIGURE 4.8 – Comparison of the energy conversion term in both electron and ion frames. (A) Four spacecraft average of the energy conversion using $\mathbf{J}_{curl}$, (B) Four spacecraft average of the energy conversion using $\mathbf{J}_{part}$, (C) Energy conversion using $\mathbf{J}_{part}$ for MMS1 (black), MMS2 (red), MMS3 (green), and MMS4 (blue).

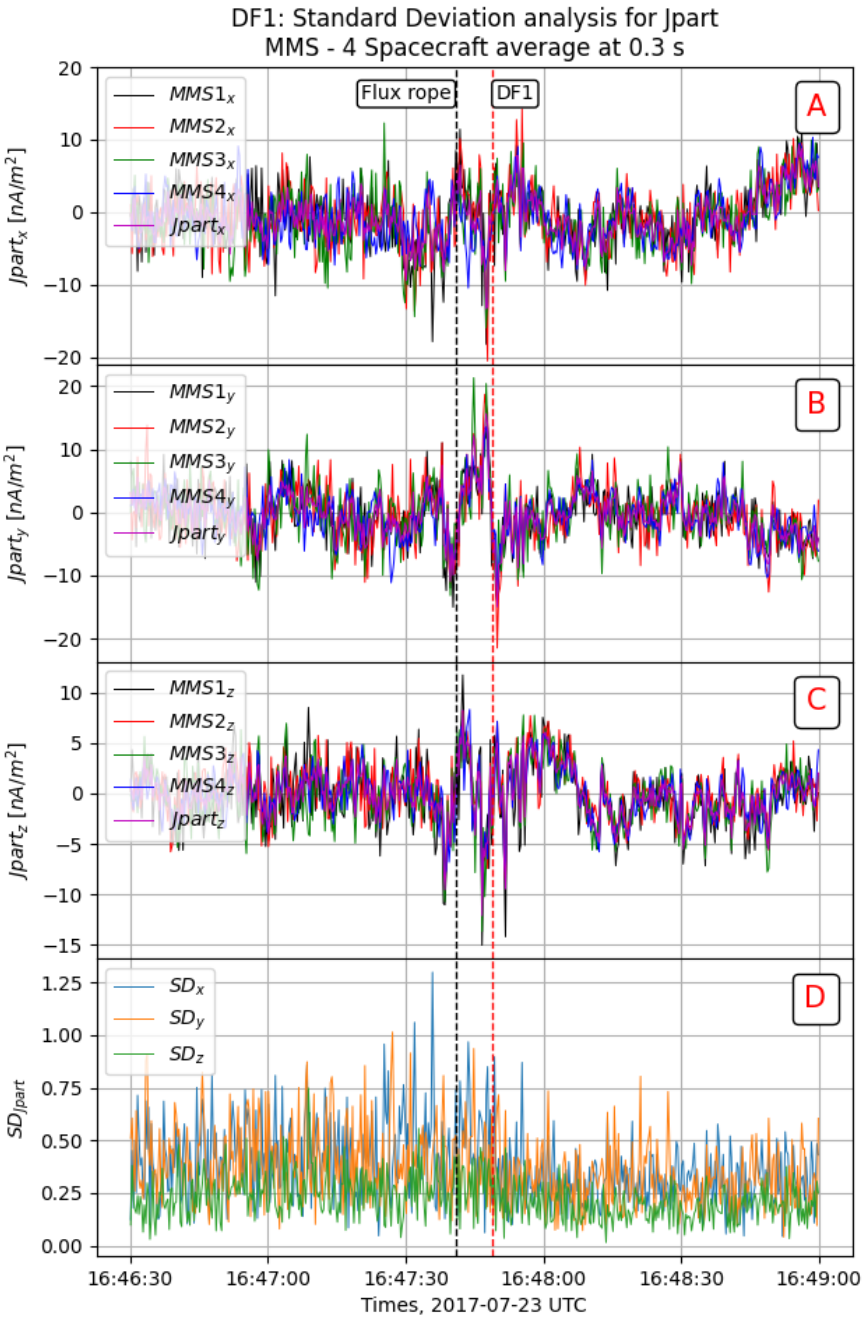

FIGURE 4.9 – Components of the current density obtained from FPI in *GSE* for each MMS satellite and the four spacecraft average (panels A, B and C). Panel D shows the standard deviation SD(**j**) of each component of the current density. Panel E shows the SD(**j**) normalized by the current density error bar, see text for details.

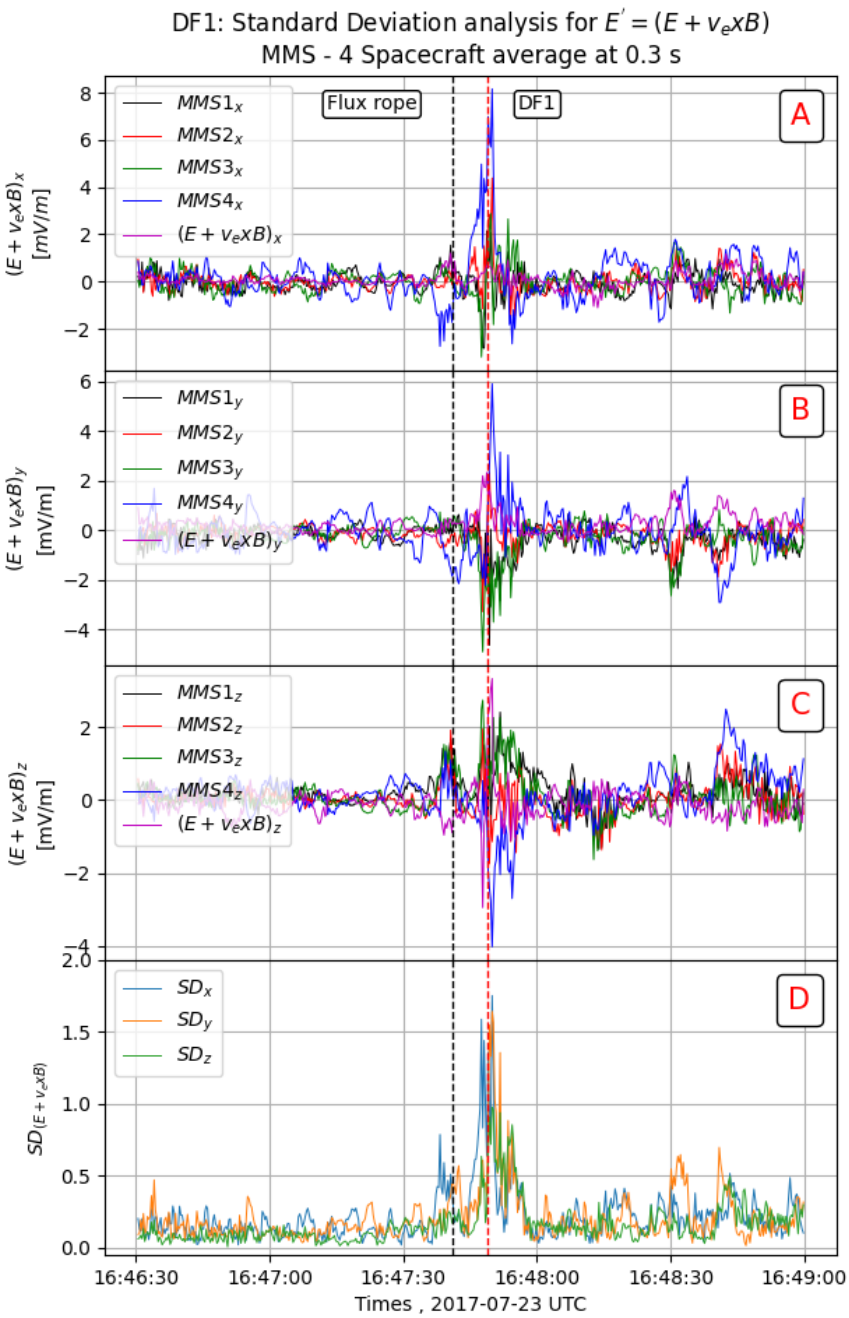

FIGURE 4.10 – Same as Figure 4.9 for the electric field in the electron frame ($\mathbf{E}' = \mathbf{E} + \mathbf{V}_e \times \mathbf{B}$). Panel E shows the standard deviation normalized by the error bar of $\mathbf{E}'$, see text for details.

where $< X >$ being the four spacecraft average of the X component and ΔX its respective estimated error bar. For the electric field, we use the error bar provided by the EDP team ($\Delta E \sim 1$ mV/m, Lindqvist et al., 2016) whereas for the electron convective term the error is estimated as $(\Delta V_e B + V_e \Delta B)$ with $\Delta B = 0.1$ nT (Russell et al., 2016) and using the moment error bars provided by the FPI team (Gershman et al., 2015). Thus we found that the error bar of E' averaged over each DF period is $\sim 1.7 - 2$ mV/m. For the error bar of the current density $\Delta J_{part} = e \cdot (\Delta N_e) \cdot (V_i - V_e) + e \cdot N_e \cdot (\Delta V_i + \Delta V_e)$, we got an average value ~ 8 nA/m^2. Let us remember that in the present study, we use the partial moments which allow us to deal with smaller errors.

Figures [4.9,B.25,B.26,B.27]A-C, and [4.10,B.28,B.29,B.30]A-C show for each DF, the three components of the current density and the electric field ($\mathbf{E}'$) respectively. Figures [4.9,B.25,B.26,B.27]D-E and [4.10,B.28,B.29,B.30]D-E display the raw and normalized SD of the corresponding quantity. One can see that at DFs the normalized SD of the electric field ($\mathbf{E}'$) is usually greater (≥ 1) than the normalized SD of the current density (<1). These results are consistent with the fact that the dispersion between the four curves measured by the four satellites is usually smaller for the current density than for the electric field ($\mathbf{E}'$) (Figures [4.9,B.25,B.26,B.27]A-C and [4.10,B.28,B.29,B.30]A-C). Therefore, the non-homogeneity of the energy conversion process seems to be caused mainly by the electric fluctuations having electron scales. Conversely, the current density remains more homogeneous at the scale of the MMS tetrahedron, which suggests that the origin of the electric field fluctuations are mostly electrostatic as we will discuss in the next section.

4.6 Discussion and summary

Six DF events embedded in fast earthward flows and detected during a large-scale substorm event have been analysed in this chapter. These DF events belong to the most common category corresponding to a decrease of the density and an increase of the temperature (Schmid et al., 2015) therefore they are characterised by a transition between a cold dense plasma at rest to a hot tenuous accelerated plasma moving earthward. We analysed each front orientation using the MVAB method as well as a timing analysis and found that all DFs are mostly moving earthward with some DFs having a significant duskward and southward motions. We have pointed out that the HPCA V_N velocity is always much larger than FPI V_N, confirming that FPI instrument underestimates the velocity of the earthward flow in the magnetotail due to its low upper energy. This caveat is quite common during substorm events as the plasma is energised due to the global magnetotail reconfiguration. Moreover, the maximum of the V_N component of the ion velocity is always located behind the DF (except for one event) associated with the maximum of B_L (forming a growing field pile-up region) which, according to a statistical study

based on Cluster data, should correspond to decelerated DFs with a significant part of the energy being radiated (in the spacecraft frame) (e, g., Hamrin et al., 2014; Fu et al., 2011).

In order to have more confidence on the particle moment measurements, we have compared the current densities obtained from the particle instruments (using partial moment for electrons) with those obtained from the curlometer technique. Despite relatively small values (< 20 nA/m^2) associated with the DF crossing, we found a good agreement between the two types of current density estimates. Then to better understand ion and electron dynamics at the DF crossing, we analysed Ohm's law. Near the DF crossing, we found that ions are decoupled from the magnetic field due to the Hall field. A clear bipolar signature of the Hall field is present normal to the DF (along N) mostly related to a reversal of the cross-tail current just behind the DF. However, the Hall field does not seem to be sufficient to balance the $\mathbf{E} + \mathbf{v} \times \mathbf{B}$ term. The electron pressure gradient term needs to be also considered. Due to the low plasma density, we could not compute the divergence of the electron pressure tensor with a sufficient reliability. Instead, we used a single satellite method (applied to the four spacecraft averaged data) to estimate the electron pressure gradient along the normal direction (e, g., Fu et al., 2012a; Yao et al., 2017). For most of DF events, we found that the signature of the electron pressure gradient along the normal is significant and could account for the departure between the ideal ion frozen-in term ($\mathbf{E} + \mathbf{v}_i \times \mathbf{B}$) and the Hall field. Electrons are magnetised most of the time. However at the DF crossing, the departure between the electron ideal frozen-in term ($\mathbf{E} + \mathbf{v_e} \times \mathbf{B}$) is very close to or exceeds the error bar which also suggests, as for ions, that the electron pressure term along the normal needs to be considered and could take part in the electron decoupling (assuming that the electron pressure does not depend only on the density so $\nabla \times ((\nabla Pe)/ne \neq \mathbf{0})$. In the other directions (L and M), it is not possible to estimate the gradient by the same technique. However, the results obtained along the normal, suggest that the decoupling along M could also involve the electron pressure term whereas along L (along the background magnetic field) the gradient seems to be smaller and so the spatial scale larger.

In order to investigate the energy conversion process at the DF, we have estimated the $\mathbf{j} \cdot \mathbf{E}$ term (e. g., Angelopoulos et al., 2013; Hamrin et al., 2014; Huang et al., 2015; Yao et al., 2017; Yang et al., 2017a; Liu et al., 2018; Xu et al., 2021). For all DFs in the spacecraft frame, we found that the energy is transferred from the electromagnetic field to the plasma (dissipation or loading region) at or just ahead of the DF and from the plasma to the electromagnetic field behind the DF (wave radiation or generator region). The amplitudes of the positive and negative peaks have similar values (± 0.02 nW.m^{-3}) which do not allow us to draw conclusions about a net energy transfer between fields and particles, despite the fact that the normal velocity peak is detected behind the front (e.g., Hamrin et al., 2014; Fu et al., 2011). This reversal of the energy conversion is mostly related to the reversal of the cross-tail current component (J_M) just behind the front. Such

a current reversal at the DF has been already mentioned by Yao et al. (2013) based on 2003 Cluster data (subproton scale spacecraft separation $\sim$ 200 km) but only related to DFs preceded by a dip of the magnetic field. It has been also recently mentioned by Liu et al. (2018) in a previous MMS single DF case study event leading to a negative $\mathbf{j} \cdot \mathbf{E}$ behind the DF. The origin of this reversal is not fully understood and could be due to a current density shear at an electron scale between the main front and the front trailing part. Another possibility could be the formation of substructures such as electron vortices driven by the current carried by electrons within the front region which could contribute locally to the increase of the total magnetic field (Stawarz et al., 2018). Such substructures could be also related to the propagation of the nonlinear kinetic-ballooning heads described by Panov et al. (2022) as we will discuss in the next chapter. Whatever the origin of these current density reversals, these results suggest that DFs have complex substructures that make difficult to draw conclusions about the net energy transfer in the spacecraft frame and question their contribution in the global energy cycle of the magnetosphere.

To better understand this energy conversion process, we have carried out the computation in each fluid frame (ion and electron) using four spacecraft average value of $\mathbf{E}'$ and $\mathbf{j}$. Equality of the calculation in both ion and electron frames has been used as a reliability test. In these fluid frames, the $\mathbf{j} \cdot \mathbf{E}'$ just ahead of the DF is negative most of the time indicating a net transfer from the plasma to the electromagnetic fields as also found in a previous MMS single DF event (Yao et al., 2017). Therefore the energy would be radiated and this process should lead to the deceleration of the fast plasma flow. Note that this negative term cannot be related to the electron pressure gradient along the normal since this latter is perpendicular to the main current J_M. However, as we mentioned in section 4.4, the electron decoupling along M could also be due to the electron pressure gradient along this direction and leads to negative $\mathbf{j} \cdot \mathbf{E}' \sim J_M.E'_M = -J_M.|\nabla P_e|_M/(en)$. Therefore the electron pressure term would play a crucial role not only in the electron decoupling but also as a free energy source for radiating waves and decelerating fast flows.

Furthermore, we have analysed the homogeneity of this energy conversion process by computing the $\mathbf{j} \cdot \mathbf{E}'$ term for each satellite. We found that the energy conversion is not homogeneous at the scale of the tetrahedron i.e. at the electron scales. By computing the standard deviation of $\mathbf{E}'$ and $\mathbf{j}$ normalized by their respective error bars, we showed that the non-homogeneity of the energy conversion process comes mostly from the electric field fluctuations while the contribution of current density fluctuations is smaller. As mentioned above, these electric field fluctuations should be related to the electron pressure gradient. This result is consistent with previous studies which identified large-amplitude electric field fluctuations related to lower-hybrid drift waves from space observations (e. g., Sergeev et al., 2009; Divin et al., 2015a; Le Contel et al., 2017; Yang et al., 2017a; Liu et al., 2018). We should notice that in order to reduce the noise of particle

measurements, we have time averaged all data over 0.3 s which correspond to filter-out the high frequency part of the LHD waves. Yet, we have verified that the calculation of $\mathbf{j} \cdot \delta\mathbf{E}$ using unfiltered electric field data gives the same sign.

This result is also consistent with 3D PIC simulations (e. g., Divin et al., 2015b; Sitnov et al., 2018; Nakamura et al., 2019b). These waves with frequencies between ion and electron gyrofrequencies ($f_{ci} < f < f_{ce}$) are expected to be generated by the large density gradient ($n_e/\nabla n_e \sim c/\omega_{pi}$) at DF and are known to have wavelengths on the order of the electron Larmor radius for the fastest growing mode (e. g., Davidson and Gladd, 1975; Huba et al., 1978). These electron-scale wavelengths correspond to the average spacecraft separation for these events and the period of the LHD waves are much smaller than the DF crossing time. These waves are able to generate ripples on the front at the electron scales which can lead to the non-homogeneity of the energy conversion process (Pan et al., 2018). Indeed, these waves are considered as "quasi-electrostatic" waves. Due to their frequency range, ions can be assumed unmagnetized whereas electrons are magnetized (Huba et al., 1978). Therefore electron drift in the electric field of the waves produces small perpendicular (to the background magnetic field) currents and a parallel magnetic field perturbations causing the ripple of the front at electron scales. These currents are much smaller than the current associated with the front. Thus, regarding the energy conversion process in the fluid frame ($\mathbf{J} \cdot \mathbf{E}'$), the dominant term corresponds to the product between the ion-scale current associated with the front ($\mathbf{J}_0$) and the electron-scale electric field associated with the LHD waves ($\delta\mathbf{E}'$). The energy conversion ($\delta\mathbf{J} \cdot \delta\mathbf{E}'$) due to currents generated by LHD waves ($\delta\mathbf{J}$) is smaller and can be considered as a second order contribution compared to the former term. This can be summarized as $\mathbf{J} \cdot \mathbf{E}' \simeq \mathbf{J}_0 \cdot \delta\mathbf{E}'$ with $\delta\mathbf{J} \cdot \delta\mathbf{E}' << \mathbf{J}_0 \cdot \delta\mathbf{E}'$. The non-linear evolution of these waves could generate electron scale vortices (Chen et al., 2020) that could explain the current density reversal at the DF and the negative part of $\mathbf{j} \cdot \mathbf{E}$ although the low non homogeneity of the current density at the scale of the tetrahedron is not in favour of this interpretation.

However, from their 3D PIC simulations Nakamura et al. (2019b) found an oscillating $\mathbf{j} \cdot \mathbf{E}'$ which once integrated along the cross-tail direction leads to a non zero positive term corresponding to an energy dissipation. In the following chapter, I present the results of a statistical analysis in order to investigate the significance of these results obtained from 6 DFs.

Chapitre 5

A statistical study of DFs observed by MMS

The work presented in this chapter will be submitted JGR, 2023.

"Ignorance leads to fear, fear leads to hatred, and hatred leads to violence. This is the equation."

Ibn Rushd, Averroes : Antologia (1126-1198).

Contents

5.1 Introduction **74**
5.2 Data, Methods and Event Selection **74**
5.2.1 Data 74
5.2.2 Selection criteria 74
5.2.3 Methods 75
5.3 Statistical overview of classical DF properties **77**
5.4 Current density structures associated with DF **81**
5.5 Statistical analysis of the Ohm's Law **82**
5.6 Energy conversion at DF **84**
5.7 Discussion and summary of the DF statistical study . **88**
5.8 The nature of the class II DFs **91**

5.1 Introduction

In this chapter, I will show that most of the results obtained in my 6 DF case study are confirmed by a statistical analysis carried out using MMS data of the full 2017 magnetotail season. In particular, the non homogeneity of the energy conversion processes at electron scales is confirmed. Moreover, thanks to this statistical investigation I will show that two subclasses of DF can be distinguished depending on the magnetic field profile and sign of the energy conversion term. Data and methods are described in section 5.2. Following the same plan as for the case study, an overview of the statistical DF properties is presented in section 5.3. In section 5.4, we present a cross validation of current density calculations. Ion and electron dynamics are investigated thanks to the Ohm's law in section 5.5 then the energy conversion processes in the vicinity of DFs are scrutinized in section 5.6. Finally global results of this statistical study are summarised and discussed in section 5.7.

5.2 Data, Methods and Event Selection

5.2.1 Data

For the present statistical study, I have performed the same treatment (data noise reduction, time averaging, LMN frames, current density calculation both from particle and magnetic field measurements, pressure gradient in the normal direction from single spacecraft method, ...) as described in chapter 3.

5.2.2 Selection criteria

I have selected DFs using burst FGM and FPI (DIS and DES) nominal L2 data in GSE from the full magnetotail season of 2017 (end of April to end of August). In order to automatically identify DF signature, I have used an Artificial Intelligence for heliophysics Data Analysis (AIDA)py routine (Lapenta and AIDA H2020 Team, 2019) based on difference between maximum and minimum values of physical quantities (n, Vi, B, ...) computed within a 60 s sliding window. A typical DF signature is defined by :

- an increase of the northward B_z component of the magnetic field > 6 nT,
- an increase of the X component of the ion velocity > 150 km/s,
- an increase of both parallel and perpendicular temperatures of ions ($>$ 5 keV) and electrons (> 1 keV),

- a decrease of both ion and electron densities (only corresponding to negative value of the difference between maximum and minimum values without specific threshold value).

After this first automatic selection step which has provided 857 DF events, the following constraints are checked manually :

- electron partial moment data have to be available at least 60 s before and 60 s after DF crossing. DF crossing time t_0 is defined by the maximum of B_z in the selected time interval.
- only DFs near the Earth's magnetotail equator are kept using the following constraint $|B_x|$<5 nT.

Due to these constraints, the new DF list is reduced to 132 DF events. These criteria are quite similar to those used in previous DF statistical studies (e. g., Zhong et al., 2019; Li et al., 2015b; Liu et al., 2013). For instance, Zhong et al. (2019) limited their DF selection by considering only plasma densities between 0.2 to 0.9 p.cm^{-3} and burst mode data available at least 15 s before and 30 s after the DF. On the other hand, Liu et al. (2013) considered just the measurements in the magnetotail region defined by -6 R$_E$ < X_{GSM} <-30 R$_E$ whereas Li et al. (2015b) investigated the region defined by X_{GSM} ≤-8 R$_E$ and $|Y_{GSM}| \leq$ 10 R$_E$.

My selection criteria are applied to each spacecraft and only events observed by all four MMS satellites are kept. Finally, all selected DF events have been individually validated by visual check.

From Figures 5.1A and B, we can see that all selected DFs are located in the region satisfying $-25 \leq X_{GSE} \leq -10$ R$_E$ and $|Y_{GSE}| \leq 15$ R$_E$. The DF distribution is quite symmetric in the equatorial plane while it is shifted toward the north due to the MMS orbit inclination (see Figure 5.2A and B). The external limit at $X_{GSE} \sim -25$ R$_E$ corresponds to the MMS apogee in 2017 (see Table 3.2). The internal limit at $X_{GSE} \sim -10$ R$_E$ is a bit farther from the Earth than the beginning of the fast survey mode associated with the ROI (X_{GSE}<9 R$_E$). Therefore the outer and inner limits are related to the MMS apogee and ROI and do not mean that DF cannot be detected nearer or farther from the Earth.

5.2.3 Methods

As explained in chapter 3 about methods and used in chapter 4, DF signatures are usually displayed in a local coordinate system obtained from a Minimum Variance Analysis (Sonnerup and Scheible, 1998) applied on magnetic fields data MVAB of a single spacecraft (e. g., Huang et al., 2015; Liu et al., 2018) and/or from a timing analysis in case of multi-spacecraft missions (e. g., Fu et al., 2012b).

In the present study, MVAB is applied on the four spacecraft average of the magnetic field during the time period corresponding to the sharp increase of northward component B_z (defined as the period between the minimum and the maximum values) for all selected DF events. As MMS satellites are separated at electron scales, MVAB applied on each single spacecraft magnetic field data gives

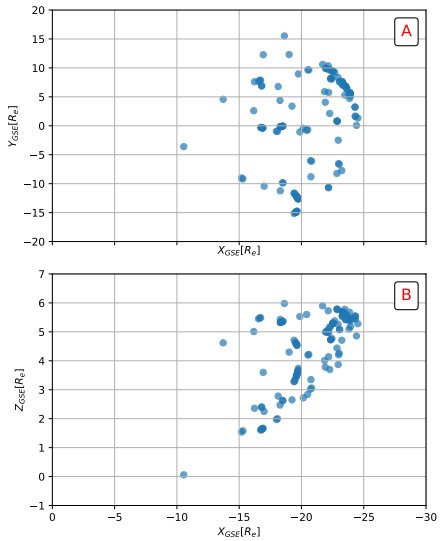

FIGURE 5.1 – An overview of all DFs events that match the selection criteria. Panels (A) XY and (B) XZ position of MMS during the observations of the 132 DF events in GSE.

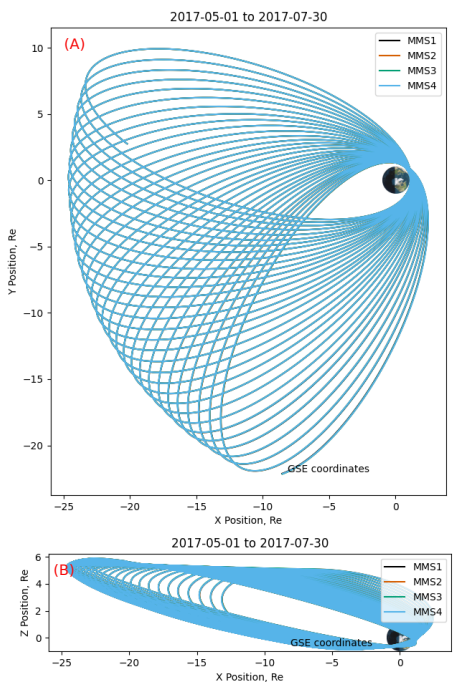

FIGURE 5.2 – MMS orbit regarding the magnetotail season of 2017 (1st of May to end of July in GSE frame. Panel (A) show MMS orbit in XY plane and (B) in XZ plane.

similar LMN frames. LMN coordinates are well defined and correspond to L directed northward, M approximately directed dawnward, and N approximately directed Earthward. The time period used to perform MVAB and its results are summarized in Tables [C.3,C.4,C.5] provided in Annex C.

From these MVAB results, we define L, M, and N vectors as maximum, intermediate, and minimum variance directions respectively. We have verified that the ratio between the three corresponding eigenvalues, $\lambda_1, \lambda_2, \lambda_3$ are sufficiently large (average values of the ratio $\lambda_M/\lambda_N \sim 22.034$ and of the ratio $\lambda_L/\lambda_N \sim 420.13$, lowest ratio value is 2.) to consider that the three directions are well separated.

Tables [C.6,C.7,C.8] show the components of the normal estimated by a timing analysis as well as the speed along the normal. Note that in accordance with the propagation direction given by timing analysis, the orientation of the N vector of the MVAB was set to be positive (earthward) and L always oriented northward leading to M directed dawnward. Figures 5.3A, B, C and D show the histogram for each component of the normal (from TA and MVAB methods) as well as the magnitude of the normal speed obtained by TA. While all DFs are propagating earthward, percentages indicate that duskward/dawnward and northward/southward DF propagations are relatively balanced with no specific statistically significant direction. Figure 5.3 D shows a peak of the speed histogram around 200 km/s. The smallest values below 50 km/s correspond to a normal orientation almost perpendicular to the X axis when DFs are crossed through their flanks. In such a configuration, the DF speed can be much slower than the radial fast flow propagation. The normal speed results are summarized in Tables [C.6,C.7,C.8].

5.3 Statistical overview of classical DF properties

In this section, I describe the results obtained using a SEA described in section 3.5. Let's just remind that we defined the representative time series by setting the maximum of B_L component of the magnetic field as a time reference for the measurements and we kept 180 s of data on each side of this time reference. Furthermore, each DF data is time-averaged at 0.3 s in order to remove all fluctuations which are not consistent with the phenomenon time scale.

After a first SEA using the full set of DFs, I have realised that an important dispersion was due to the existence of two different types of magnetic signatures satisfying the DF selection criteria. From this observation, I decided to split the DF set into two different classes and to perform two separated SEAs. Thus, the statistical characteristics of DF events for these two different classes are shown separately reducing the dispersion for each class.

Figure 5.4 shows SEA results in order to illustrate ion scale properties for both DF classes in their respective LMN frame obtained from MVAB. Figure 5.4A presents the most important DF characteristics namely a sharp increase of the northward component of the magnetic field B_L showing a small decrease (dip) just

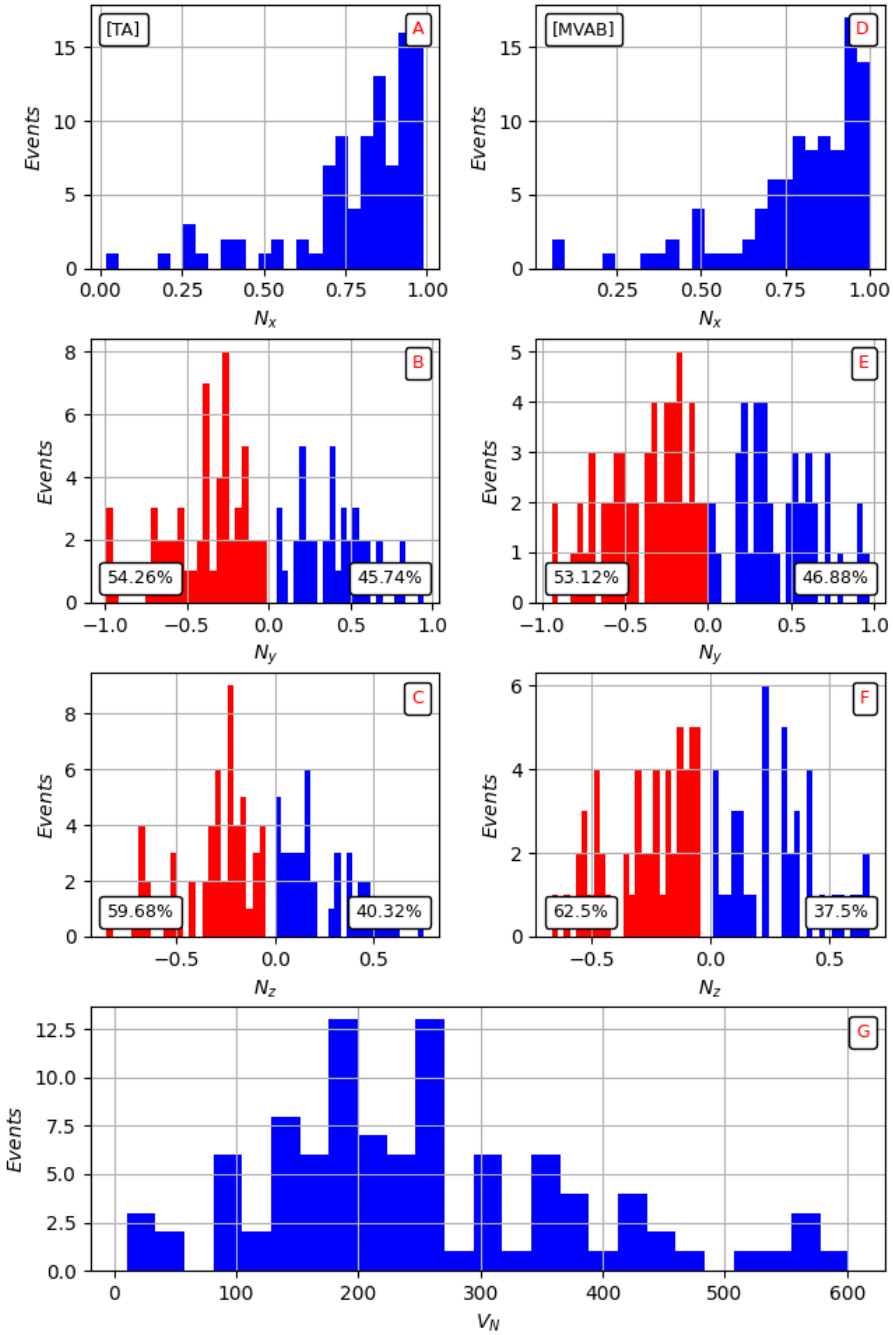

FIGURE 5.3 – Histograms of the normal components in GSE, from TA panels (A), (B) and (C) and from MVAB panels (D), (E), and (F). Panel (G) shows the magnitude of the normal velocity obtained by TA.

before the front as reported by previous studies. Figure 5.4B shows the decrease of the electron density N_e until 0.21 p.cm^{-3}. Figures 5.4C, D display electron and ion pressure variations respectively. One can see that for electrons as well as for ions, the DF crossing always corresponds to a transition between a high pressure to a low pressure region on the largest scale (fluid). Figures 5.4F, G present the perpendicular electron and ion temperatures from FPI data in order to compare with proton temperature from HPCA data Figure 5.4E. Let's remind that due to their different upper energy limit 40 keV (resp. 30 keV) for HPCA (resp. for FPI-DIS), FPI-DIS ion moments although having a faster time resolution can be underestimated. Indeed, comparison of Figures 5.4G, E confirm that isotropic HPCA proton temperature is much larger than FPI perpendicular ion temperature (adding the parallel ion temperature to compute the isotropic FPI temperature does compensate the discrepancy, not shown). For the same reason, HPCA proton velocity $V_{H^+,N}$ is much larger than FPI ion velocity V_N as shown in Figures 5.4H, I. The V_N decreases shown by FPI-DIS within the front when ions are energised can also be considered as an artefact caused by this limited upper energy and not as a real reduction of the fast flow velocity.

Class I corresponds to 74.4% of selected DFs and has the typical DF properties reported so far by previous studies. This DF class displays a slow decrease of the magnetic field after the front (see Figure 5.4(class I-[A])) and is associated with a smaller ion velocity than class II (see Figures 5.4(class I-[H]&class II-[H])). They seem to propagate through a hotter plasma as ion and electron temperatures are higher before the front than for class II (see Figures 5.4(class I-[E,F,G]& class II-[E,F,G])). Ion perpendicular temperature increase is smaller whereas a significant ($\sim$ 50%) electron perpendicular temperature increase is present. Yet, both pressures decrease monotonously at the DF (Figures 5.4(class I-[C,D]). This class is very similar to the Decaying field pile-up event defined by Fu et al. (2012b) although it is not clear that the peak of the velocity is colocated with the DF.

Class II corresponds to 25.6% of selected DFs. This new DF class has the same time scale for the rising and the falling of B_L (like a bump) (see Figure 5.4(class II-[A])) associated with minimums of density and (ion and electron) pressures (see Fig.5.4(class II-[B-D])). In addition to the pressure minimums at DF crossing, compressional fluctuations with smaller amplitudes are present. This DF class has faster velocity than class I (see Figure 5.4(class II-[H] and [I])). As the $V_{H^+,N}$ maximum is located behind the front, this class could correspond to the growing field pile-up event defined by Fu et al. (2012b). As already mentioned, these DF events seem to propagate through a colder plasma than class I as ion and electron temperatures before the front are smaller. Finally, both ion and electron perpendicular temperatures increase significantly ($\sim$ 50%). It is worth noting that this DF class is mostly detected on the duskside and includes all six DF events analysed in chapter 4 (see Figure 5.5(class II)). Substorm onsets being also more frequent in this region, it could suggest a possible link between the two phenomena.

Figure 5.5 displays an overview of the class I and class II events that match

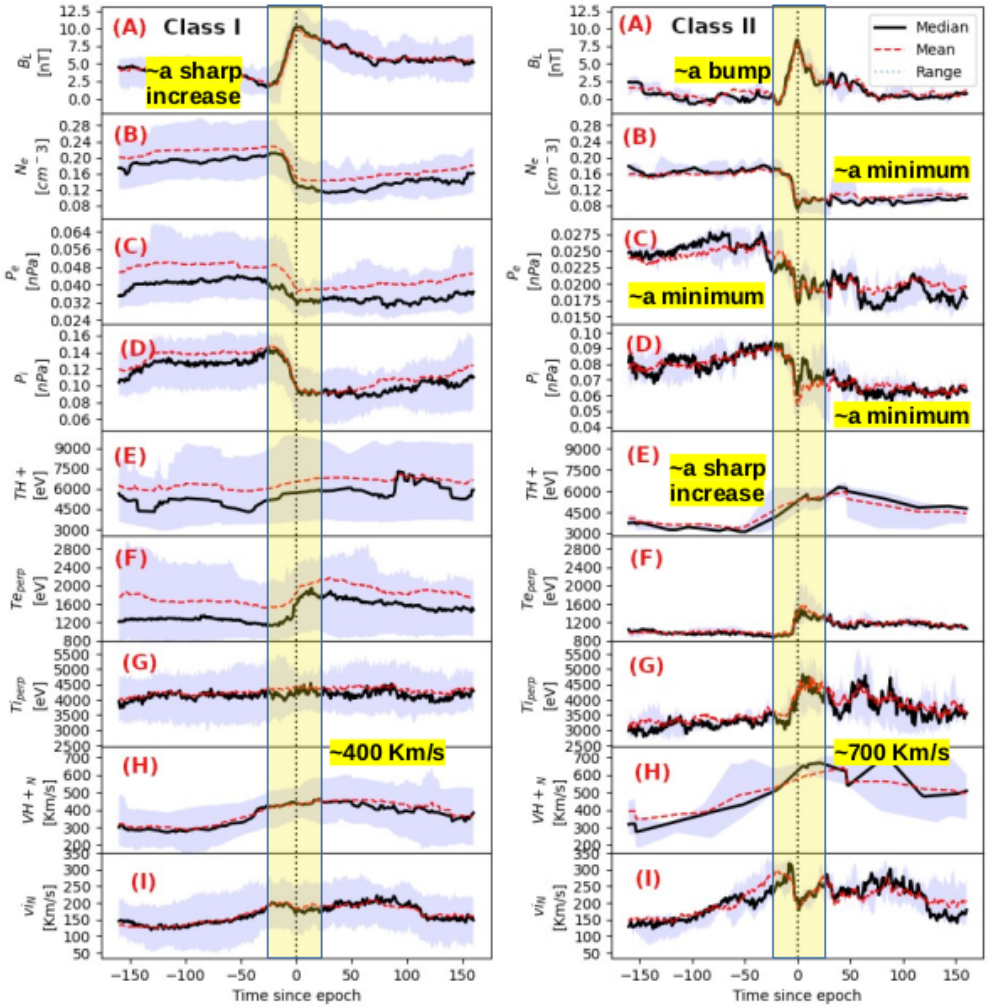

FIGURE 5.4 – Superposed epoch analysis plots of DF signatures using 132 DFs, in their respective LMN frame, all data being time averaged at 0.3 s. In each panel, the black line marks the superposed epoch median, the red dashed line marks the superposed epoch mean, and the blue fill marks the interquartile range. (A) Magnetic field B_L, (B) electron density N_e, (C) and (D) electron and ion pressures from FPI, (E) HPCA proton temperature T_{H^+}, (F) and (G) perpendicular electron T^e_{perp} and ion T^i_{perp} temperatures from FPI, (H) HPCA normal proton bulk velocity $V_{H^+_,N}$, (I) FPI normal ion bulk velocity vi_N.

the selection criteria. The colors represent the change in the northward magnetic field component $< B_z >$ averaged over the full DF time interval, the arrows represent the DF normal velocity perpendicular to the boundary (obtained by TA) projected onto the X/Y plane in GSE. While for class I, locations and propagations are relatively random, class II DFs have preferentially duskward locations and propagations with larger velocities.

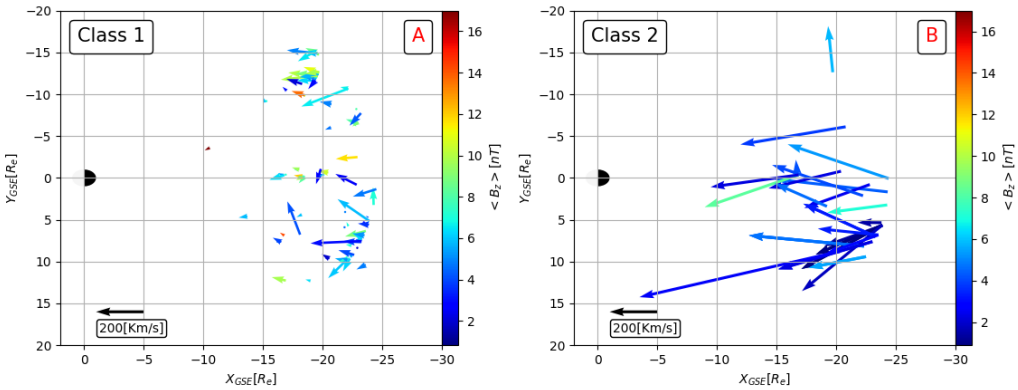

FIGURE 5.5 – An overview of the class I and class II events that match the selection criteria. The colors represent the change in the northward magnetic field component $< B_z >$ time averaged over the full DF time interval, and the arrows represent the DF velocity perpendicular to the boundary (obtained by TA), projected onto the XY plane in GSE.

5.4 Current density structures associated with DF

Following the same approach as for analysing the first 6 DF events described in chapter 4 and using methods already described in section 5.2, I have compared the current densities computed from ion and electron moments averaged over the four individual spacecraft with those estimated independently from the magnetic field data at the same time resolution (0.3 s) using the curlometer technique.

Figure 5.6 shows the SEA of the current densities computed from particle measurement $\mathbf{J}_{part} = en_e(\mathbf{v}_i - \mathbf{v}_e)$ (panel E) and computed from the magnetic field $\mathbf{J}_{curl} = (\nabla \times \mathbf{B})/\mu_0$ (panel D) estimated for each DF event in their own LMN frame. For both categories, the comparisons demonstrate good agreements between the two current density measurements although the values are quite small (~ -6 nA/m^2). Note that each DF can be identified by its negative peak in J_M (increase of cross-tail duskward current).

In addition to these measured current densities, one can obtain, from two-fluid theory, the diamagnetic current densities computed from the electron and

ion pressure gradient terms estimated by a single satellite method described in chapter 3. The M component of the total (perpendicular) diamagnetic current density becomes $J_{dia-tot,M} = B_L/B^2\nabla_n(P_e + P_i)$ and can be compared with the two other current densities. Figure 5.6 shows (A) the electron diamagnetic current $J_{dia-e,M} = B_L/B^2\nabla_n P_e$, (B) the ion diamagnetic current $J_{dia-i,M} = B_L/B^2\nabla_n P_i$, and (C) the total diamagnetic current $J_{dia-tot} = B_L/B^2\nabla_n(P_e + P_i)$.

From the comparison between ion and electron diamagnetic currents, we see that for both classes the ion contribution is dominant and constitutes $\simeq 72$ % of the total diamagnetic current. Furthermore, for both classes the total diamagnetic current along M is highly consistent with the curlometer and particle measurements indicating that the diamagnetic effect is the main source of the current. More importantly, the reversal in the current density pointed out in (Alqeeq et al., 2022) as the cause of the reversal of the energy conversion process for the 6 analysed DF events is confirmed by this statistical study as being a common signature of class II events. Finally, this statistical study demonstrates that the reversal of the current density for class II events is mainly due to the reversal of the ion pressure gradient or in other words by the ion diamagnetic current. Although the electron density gradient follows the same behaviour, the electron pressure gradient is smaller mainly due to their smaller temperature. Therefore for both DF classes, the perpendicular current density structure of DF is governed by the diamagnetic current density dominated by the ion gradient pressure produced by the propagation of the fast flow through the magnetotail.

5.5 Statistical analysis of the Ohm's Law

In this section, I reproduce the analysis of the different terms of the generalised Ohm's law for our two different DF classes as explained in chapter 4. Figure 5.7 shows for both categories the SEA of the ideal ion frozen-in ($\mathbf{E}^{'\mathbf{i}} = \mathbf{E} + \mathbf{v}_i \times \mathbf{B}$) and the Hall electric field ($\mathbf{J}_{part} \times \mathbf{B}/(en)$) terms in LMN coordinates. One can notice that for both classes the ideal ion frozen-in condition is mostly broken along the N axis ($E'^i_N \sim 3$ mV/m, panels D) whereas in contrast it is still well satisfied along L ($|E'^i_L| < 0.6$ mV/m, panels B). This behaviour is consistent with the idea of a front structure having a smaller (ion) scale in the direction of propagation (N) perpendicular to the background magnetic field than along it (L). However, a significant peak of ($E'^i_M \sim 1.8$ mV/m, right-hand panel C) is obtained for class II. This field is in the opposite direction of the M component of the Hall field (median value ~ -1.6 mV/m, right-hand side panel F) suggesting that the contribution from the electron pressure gradient would be quite large ($\sim$ 3.4 mV/m). As the median and mean values have opposite signs due to 2 extreme events, if we use the mean value ($\sim +0.8$ mV/m), the contribution of the electron pressure gradient would be only (~ 1 mV/m). This significant value of the electron pressure gradient along M could suggest that class II DFs have a smaller azimuthal scale

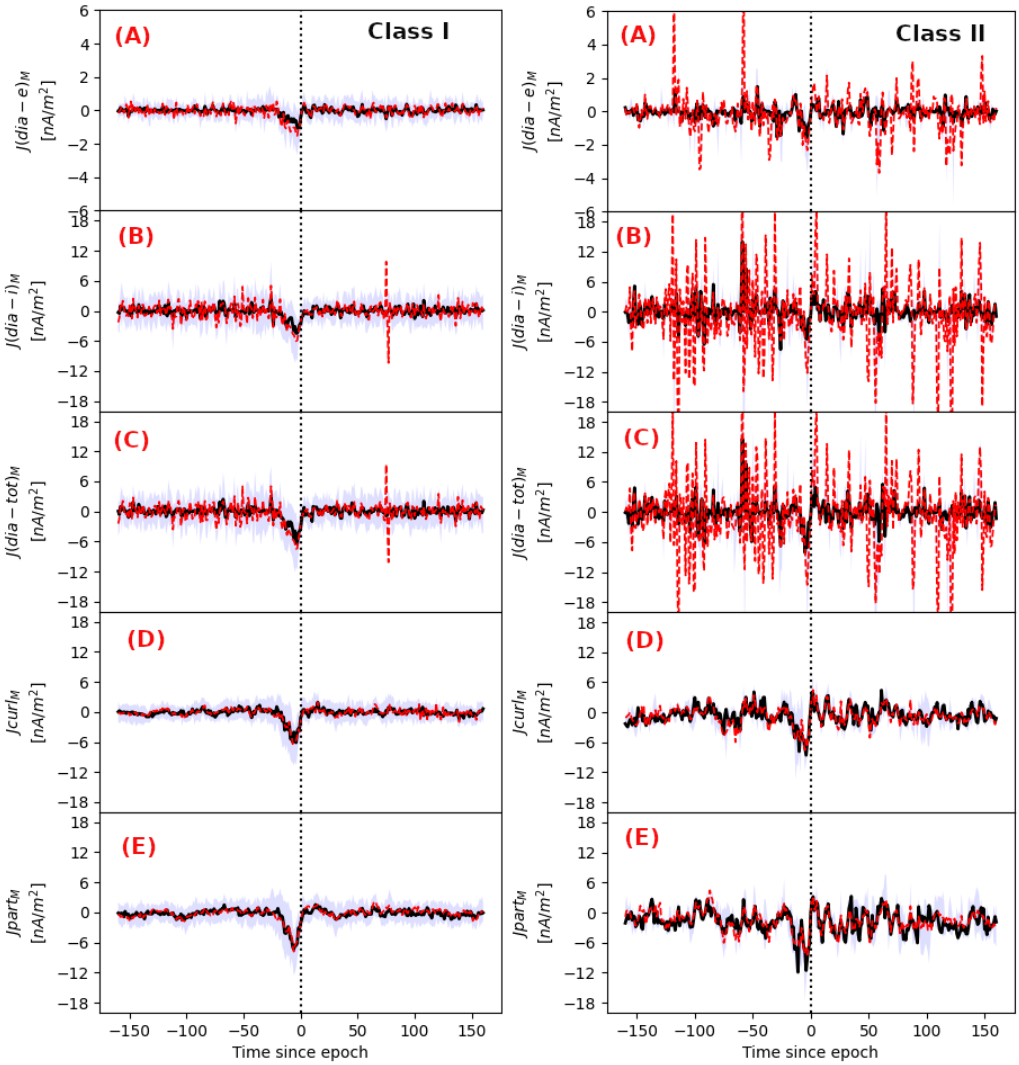

FIGURE 5.6 – For both categories, superposed epoch analysis of the current densities along M calculated by using : (A) $J_{dia-e} = B_L/B^2\nabla_n P_e$, (B) $J_{dia-i} = B_L/B^2\nabla_n P_i$, (C) $J_{dia-tot} = B_L/B^2\nabla_n(P_e + P_i)$, (D) $\mathbf{J}_{curl} = (\nabla \times \mathbf{B})/\mu_0$, (E) $\mathbf{J}_{part} = en_e(\mathbf{v}_i - \mathbf{v}_e)$. Same color code as Figure 5.4.

(cross-tail direction) along M than class I DFs. Thus for both classes, in the N direction, ions are decoupled mostly by the Hall electric field shown in panels G. However, for class II and in the M direction, the electron pressure gradient could contribute significantly to the ion decoupling. Furthermore, even in the N direction, the discrepancy between the two terms (ideal term and Hall field) can exceed $\simeq 1$ mV/m which statistically confirms that electron pressure gradient term is not negligible and reduce the positive Hall electric field along N despite the difficulty to estimate it from the four satellite measurements, see Figure 5.7(A).

Figure 5.8 shows for both categories, the SEA of the ideal electron frozen-in term ($\mathbf{E}^{'\mathbf{e}} = \mathbf{E} + \mathbf{v}_e \times \mathbf{B}$) in LMN coordinates. As for ions, electrons are mostly magnetised along the L direction (panels B) as the ideal frozen-in term $|E'^e_L| < 0.8$ mV/m close the electric field error bar although class II DFs are associated with larger fluctuations. In the N direction for class II DFs, electrons could be decoupled from the magnetic field as the departure to frozen-in condition ($E'^e_N \sim -1.6$ mV/m, right-hand side panel D) is consistent with the estimated electron pressure gradient term (right-hand side panel A) and assuming a non-zero curl of the electron pressure gradient term $-(\nabla P_e)/(en_e)$. This agreement is also found for class I DFs showing a bipolar signature but with smaller values ($E'^e_N \sim \pm 0.8$ mV/m, left-hand side panels D and A). In the M direction for which we are not able to estimate the electron pressure gradient, a larger departure to the ideal frozen-in condition is found for class II than for class I which suggests, as from ion Ohm's law, that class II DFs could be more localised in the azimuthal (cross-tail) direction due to larger electron pressure gradients. Thus electrons could be decoupled from the magnetic field at DF by their pressure gradient term in the N direction and probably also in the M direction although it is not possible to confirm it using a single Spacecraft (s/c) method. Note that the estimate of the electron pressure gradient along M using the mean values from the ion Ohm's law ($E'^i_M - \mathbf{j} \times \mathbf{B}/(ne) \sim 0.7$ mV/m) agrees with the estimate from the electron Ohm's law using the mean value ($E'^e_M \sim 0.7$ mV/m).

5.6 Energy conversion at DF

In this section, I present the results from the SEA of the energy conversion processes. Let's remind that positive $\mathbf{j} \cdot \mathbf{E}$ values correspond to an energy load or dissipation whereas negative values correspond to a generator or dynamo effect (e. g., Torbert et al., 2016a; Huang et al., 2015; Birn and Hesse, 2005; Alqeeq et al., 2022). Figure 5.9 shows the results of the SEA of the energy conversion processes for our two DF categories. Figure 5.9(A) displays the magnetic B_L, Figure 5.9(B) the cross-tail electric field E_M, Figure 5.9(C) the energy conversion term in s/c frame $\mathbf{j} \cdot \mathbf{E}$, Figure 5.9(D) the energy conversion term in the electron frame $\mathbf{j} \cdot \mathbf{E}'$, and Figure 5.9(E) the current density $Jpart_M$ computed from particle measurements shown again for reference. For both categories, the SEA shows that in the spacecraft

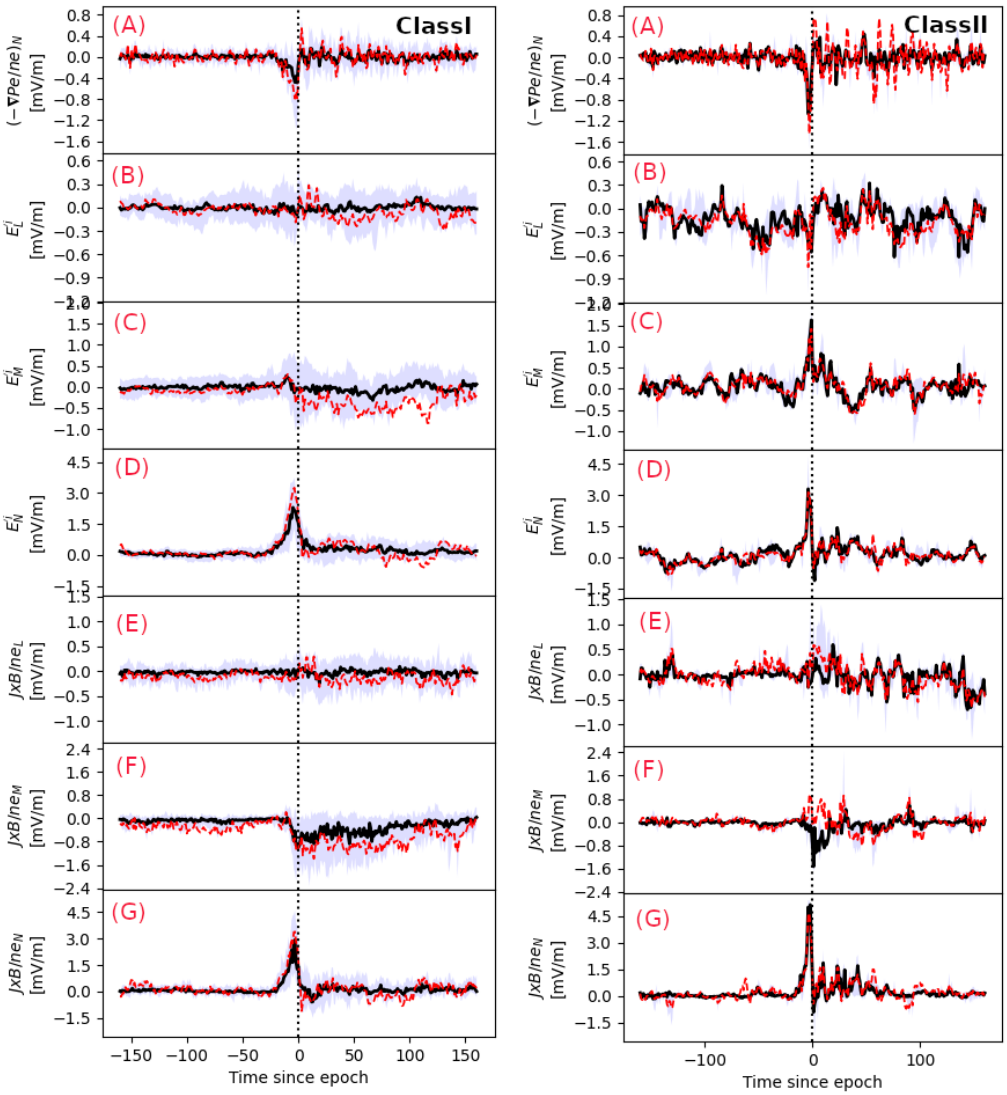

FIGURE 5.7 – Superposed epoch analysis of the ion generalized Ohm's law comparison between different terms. Panel (A) includes the electron pressure gradient term along N. Panels (B), (C) and (D) shows L, M, N components of the electric field $\mathbf{E}' = \mathbf{E} + \mathbf{v_i} \times \mathbf{B}$ and panels (E), (F) and (G) shows L, M, N components of the Hall electric field $\mathbf{J}_{part}/(en_e)$, all data being time averaged at 0.3 s. Same color code as Figure 5.4.

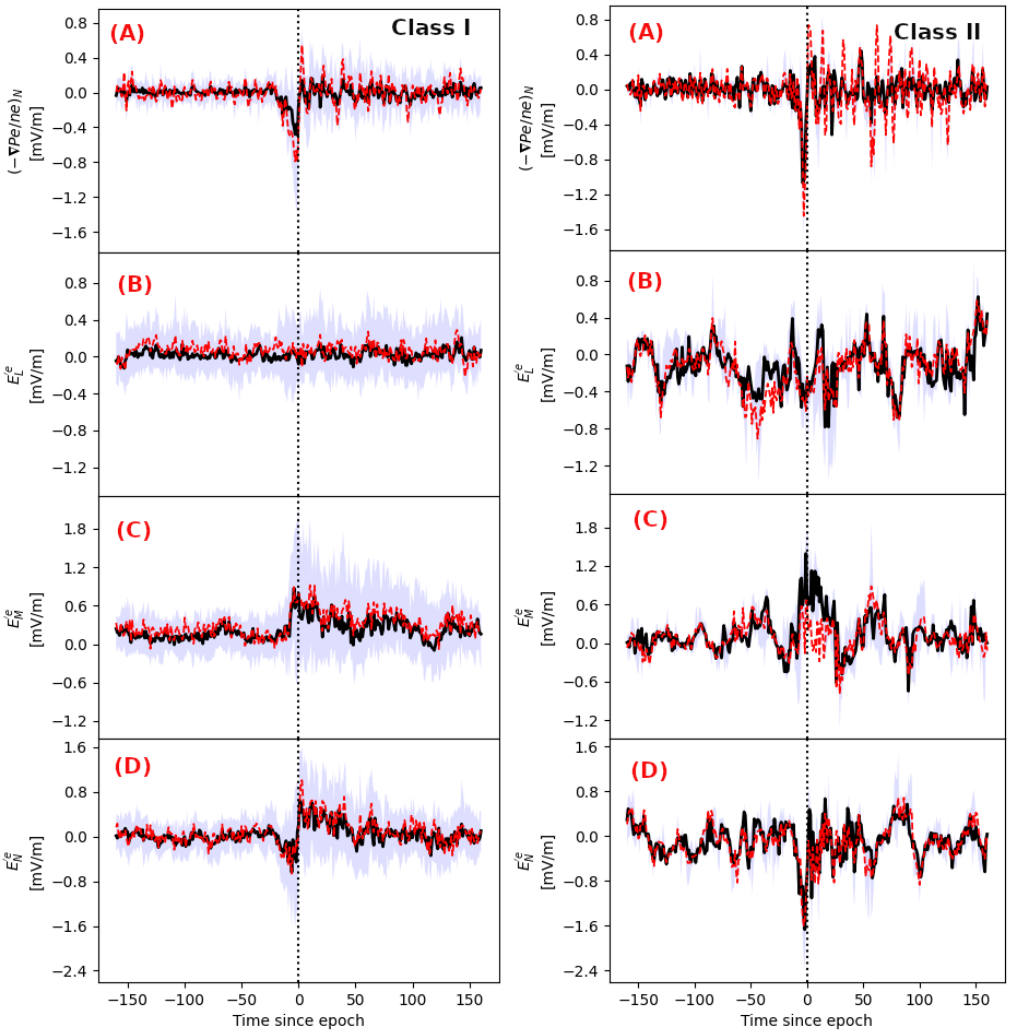

FIGURE 5.8 – Superposed epoch analysis of the electron generalised Ohm's law comparison between different terms. Panel (A) includes the electron pressure gradient term along N. Panels (B), (C) and (D) shows L, M, N components of the electric field $\mathbf{E}' = \mathbf{E} + \mathbf{v_e} \times \mathbf{B}$, all data being time averaged at 0.3 s. Same color code as Figure 5.4.

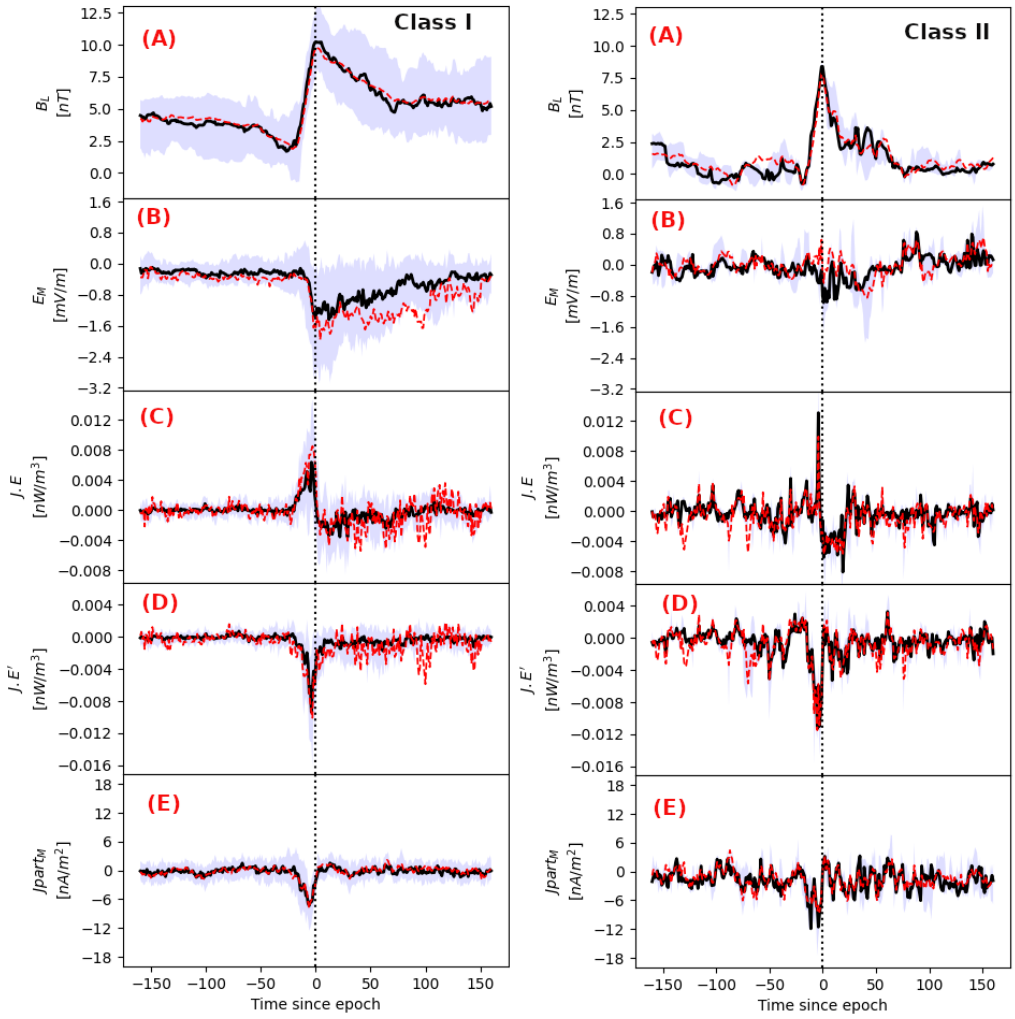

FIGURE 5.9 – Superposed epoch plots of the energy conversion processes. (A) the magnetic field B_L, (B) the electric field E_M, (C) the energy conversion term in s/c frame $\mathbf{j} \cdot \mathbf{E}$, (D) the energy conversion term in electron frame $\mathbf{j} \cdot (\mathbf{E} + \mathbf{v}_e \times \mathbf{B})$, and (E) the current density $Jpart_M$. Same color code as Figure 5.4.

frame Figure 5.9(C), the energy is transferred from the electromagnetic fields to the plasma ($\mathbf{j} \cdot \mathbf{E} > 0$) ahead or at DF. This result is consistent with all previous DF studies. However, for class II as found for the 6 DF events by Alqeeq et al. (2022), a reversal of the energy conversion process is found behind the front. The energy is transferred from the plasma to the electromagnetic fields ($\mathbf{j} \cdot \mathbf{E} < 0$) due to the reversal of the ion diamagnetic current which has been confirmed in the previous section. Indeed, as we can see in Figure 5.9(B), the M component of the electric field related to the fast convective earthward plasma motion does not change sign. Therefore, for both classes the energy conversion processes in the vicinity of DFs seems to be governed by the ion pressure gradient generated by the flow propagation.

In the fluid frame Figure 5.9(D), as found for the 6 DFs, the statistical study confirms that for both classes the energy is transferred from the plasma to the electromagnetic fields ($\mathbf{J} \cdot \mathbf{E}^{'} < \mathbf{0}$, generator or dynamo) due to the contribution of the electron pressure gradient in the Ohm's law and could lead to the slow down process of DFs during their earthward motion.

Then as in our 6 DF event study, I investigated the homogeneity of the energy conversion processes in the fluid frame observed around the DF. Indeed, from the 6 DF analysis which, as a matter of fact, all belong to class II, we have shown that the energy conversion process is not homogeneous at the scale of the tetrahedron (electron scales). We have found strong variations of the sign and the amplitude of the energy conversion term obtained from one satellite to another. Such variations suggested that a physical process is going on at the electron scales while the DF is propagating earthward. Based on our estimates of the SD (see equation 4.6) for each component of the current density and the electric field in the fluid frame, we have shown that the non homogeneity was caused mainly by the electric field fluctuations as discussed in chapter 4 in detail. The SEA of the normalised SD of the electric field and the current density shown in Figure 5.10 confirms the dominant role of the electric field fluctuations in the variability of the energy conversion term. Indeed, for both classes SD of electric fields is about 1 for x and y components (panels A and B) whereas the SD of current densities is always smaller than 1 for all components.

5.7 Discussion and summary of the DF statistical study

In this chapter, I have reported on a statistical study based on 132 DFs detected by the MMS mission during the full magnetotail season of 2017 (end of April to end of August). We found that the 132 events can be subdivided into two categories mostly according to their DF-shape (magnetic field profile) : class I with 98 events (74.4%) for which the DF-shape shows a slow decrease of the magnetic field after the

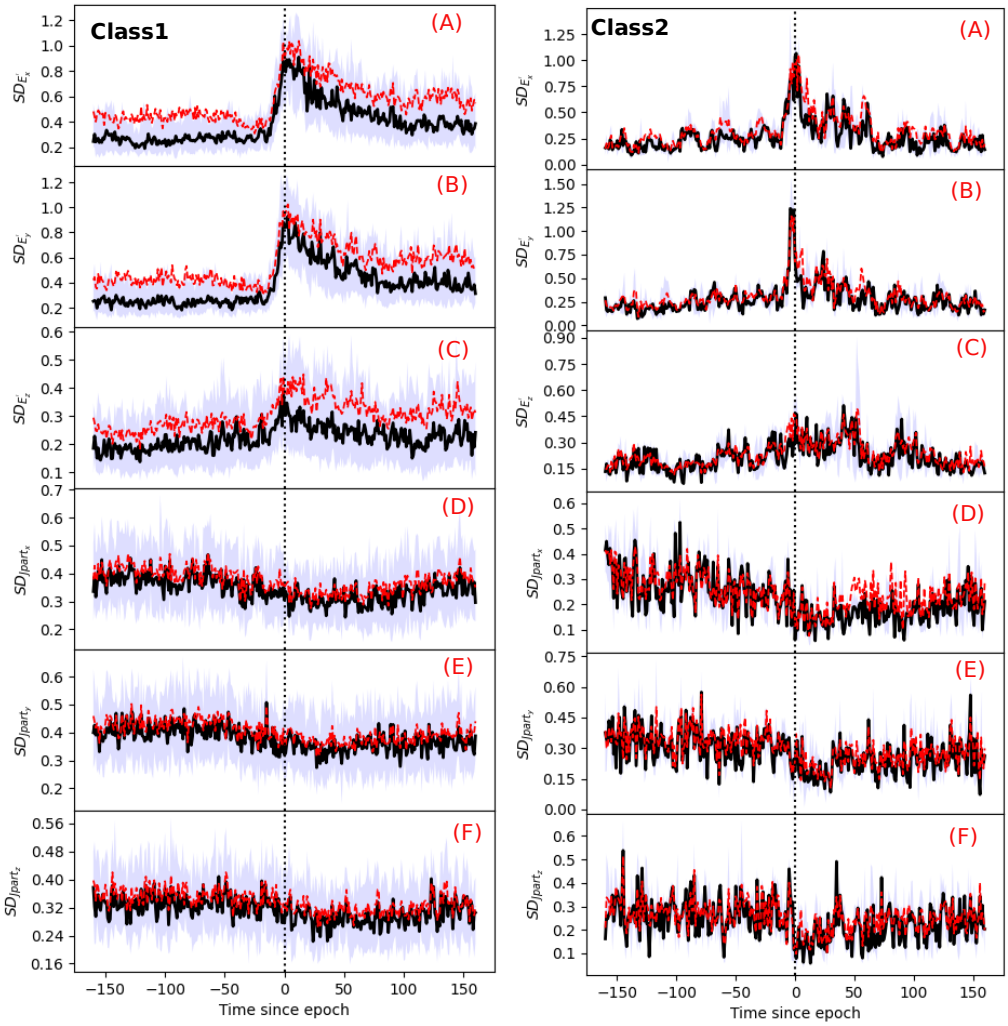

FIGURE 5.10 – Superposed epoch analysis of the SD of class I and class II for each component of the current density and the electric field in the fluid frame ($\mathbf{E}' = \mathbf{E} + \mathbf{v}_e \times \mathbf{B}$) in GSE, all data being time averaged at 0.3 s. For context, panel (A) the SD(E'_x), and (B) the SD(E'_y), and (C) the SD(E'_z),(D) the SD($Jpart_x$), (E) the SD($Jpart_y$), (F) the SD($Jpart_z$). Same color code as Figure 5.4

.

DF and is associated with smaller ion velocity, class II with 34 events (25.6%) for which the DF-shape shows the same time scale for the rising and the falling of the magnetic field (a bump) associated with minimums of ion and electron pressures and faster velocity as shown in Alqeeq et al. (2022) for 6 DF events. This new DF subcategory (class II) is mostly detected on the duskside. For both categories, using a single s/c method we found that along the cross-tail current direction ($-M$), the ion diamagnetic current density contribution to the total diamagnetic current is dominant ($\sim$ 72%). For both categories, the enhancement of the ion pressure gradient ahead of the DF leads to an increase of the diamagnetic cross-tail current and an energy dissipation ($\mathbf{J} \cdot \mathbf{E} > 0$) in the spacecraft frame i.e. an energy transfer from the electromagnetic field to the plasma. This result related to the DF contribution to the global energy dissipation process in the magnetosphere is consistent with previous statistical analysis (e. g., Zhong et al., 2019; Song et al., 2020; Wang et al., 2020). However, for our new class II, we have found a reversal of the energy conversion term. This reversal is mainly produced by the reversal of the ion pressure gradient i.e. a reversal of their diamagnetic current as the main component along M of the electric field due to the fast earthward plasma motion does not change sign. Therefore for class II DF events, the energy is transferred from the plasma to the electromagnetic field behind the front ($\mathbf{J} \cdot \mathbf{E} < 0$, dynamo effect). This reversal of the energy conversion term with similar values raises the question of a net contribution to the energy dissipation from this class of DF which still represents about 1/4 of the DF events. It raises also the question about the cause of this different behaviour compared with class I.

In the fluid frame and for both categories, I found that the energy is mostly transferred from the plasma to the electromagnetic field ($\mathbf{J} \cdot \mathbf{E}^{'} < 0$) ahead or at the DF which could contribute to the deceleration of the flow. As we have seen from the generalised Ohm's law analysis, the non-ideal electric field comes from the electron pressure gradient. The latter, although contributing little to the total diamagnetic current due to the lower temperature of electrons, could lead to the electron decoupling at the front and to a net energy conversion toward the electromagnetic field. Thus, the energy conversion process in the vicinity of DF seems to be mainly controlled by the particle pressure gradients : in the spacecraft frame, the contribution of the ion pressure gradient to the diamagnetic cross-tail current is dominant and determines the nature of the conversion process (dissipation versus dynamo) ; in the fluid frame the electron pressure gradient, although weaker than that of the ions due to the lower temperature of electrons, could be sufficient to lead to the decoupling of electrons and to a net energy transfer from the plasma to the electromagnetic field. This transfer could result to the slow down of the fast flows.

Indeed, I have shown that the SEA of the generalised Ohm's law for all events confirms that the ideal frozen-in condition is broken for ions mostly due to the Hall electric field ($\mathbf{J} \times \mathbf{B}/(en)$). We have seen that this field is produced by the enhancement of the cross-tail current caused by the ion pressure gradient at DF and

the corresponding diamagnetic current but electron pressure gradient although smaller also contributes. Therefore electrons remain almost always magnetised except at the front where a significant electron pressure gradient is found. Finally, I have statistically examined the homogeneity of the energy conversion processes in the fluid frame by estimating the standard deviation of the current density and of the electric field measurements. For both categories, we found that the non homogeneity comes from the variations of the electric field which occur at electron (tetrahedron) scales. These variations are produced by variations in the electron pressure gradient which should be caused by a kinetic scale process. From the 6 DF analysis, we have suggested that this process could be identified as the lower-hybrid drift instability whose the source lies in the enhancement of the pressure gradient ahead of the front.

5.8 The nature of the class II DFs

The identification of the class II DFs raises many new questions :

— Why and how are they produced compared with the typical class I ?
— Why are they mostly detected on the duskside ?
— Why are they less often observed ?
— What is their net contribution to the global circulation of magnetospheric energy ?

We do not pretend here to answer all these new questions but we just want to suggest some clues. The duskside near-Earth magnetotail (pre-midnight sector) has been known for a long time to be a preferential location for substorm onset (e. g., Nagai et al., 1998; Baumjohann et al., 1999; Angelopoulos et al., 2008, 2013) or/and magnetotail reconnection (e. g., Sitnov et al., 2009; Zhou et al., 2011; Runov et al., 2012; Fu et al., 2013; Drake et al., 2014). Therefore, class II DF events could be directly related to onset events although it has been shown that fast flows and DF can be detected without substorms (e. g., Lui, 2001; Runov et al., 2009, 2011). Class II DFs would be detected near the substorm onset with an higher probablility in the pre-midnight sector but with a lower probability than fast flow detection anywhere across the magnetotail. This conjecture could be tested in the future by investigating the occurrence of substorm onset with regards to class II events.

Recently combining THEMIS observations and 3D PIC simulations, Panov et al. (2022) identified ion gyroradius scale structures associated with the propagation of heads produced by the non linear evolution of the kinetic Ballooning-Interchange Instability (BICI). The head structures were detected by the three THEMIS near-Earth probes when they were located between -7.5 and -7.9 R_E therefore much closer to the Earth than DFs detected by MMS. Their measurements were performed in a stronger magnetic field ($\sim$ 60 nT) and farther from the equator ($B_x \sim$ 40 nT). Furthermore, the heads were moving dawnward while on each

head side plasma was moving tailward leading to a flow reversal during the head crossing by the probes. However, some properties pointed out by Panov *et al.* could have some similarities with properties of class II DFs. The BICI head crossing is associated with a density trough and a hump of the ion temperature in addition to the classical DF signature (B_z increase up to 40 nT preceded by a negative dip and $V_x \sim 400$ km/s) as for class II. It is worth noticing that the authors used the spacecraft potential with a time resolution of $1/128 \sim 0.008$ s to estimate the density and to show the density trough. So a time resolution even better than the 0.3 s time resolution used in our MMS statistical study. Moreover, while from THEMIS measurements the authors showed that the ion temperature increases by a factor 2 on the duskside of the head, in our MMS measurements we found only an increase $\sim 50\%$. They attributed the enhancement of the ion temperature on the duskside of the head to the penetration of the suprathermal ions from the dawnside across the head to the duskside. This process could be also investigated in the future from our DF database. Despite these differences, BICI head crossing appear to be a good candidate to interpret our class II DFs. However taking into account the different locations between THEMIS and MMS observations, class II DFs could correspond to BICI head crossings in the early stages of their development before they were slowed down and broadened closer to the Earth due to the interaction with the stronger dipole field.

Chapitre 6

Conclusions and outlook

Old Man's Advice to Youth : "Never Lose a Holy Curiosity"

Albert Einstein, *LIFE Magazine (2 May 1955) p. 64*

Contents

6.1 Summary of main results **93**
6.2 Further works **96**

6.1 Summary of main results

Since their unambiguous identification by the THEMIS mission with its five radially separated probes, DFs have been widely studied. Throughout my thesis, I have aimed to obtain a better understanding of the energy conversion processes associated with DF signatures based on in-situ observations of particles and fields from the MMS spacecraft. This observational study has been carried out in two classical steps : (1) A case study (including 6 DFs) and (2) a statistical analysis in order to extend the case study results.

In Chapter 4, I have investigated six DF events observed by MMS in the Earth's magnetotail on July 23, 2017. I have shown that the current density estimates obtained independently from the magnetic field and the particle measurements were in good agreement. By analysing the different terms of the Ohm's law, ions have been found decoupled from the magnetic field in the direction normal to the front (N), mostly due to the Hall electric field although electron pressure gradient obtained (by a single satellite method) could also contribute. This electron pressure gradient could be also responsible for the electron decoupling at DF. In the azimuthal direction (M), it has not been possible to estimate the electron

pressure gradient using the single spacecraft method and suggest its possible role in the particle decoupling from the magnetic field although this is very likely (as E'_M is larger than the E field error bar). The energy conversion processes have been analysed based on the calculation of the $\mathbf{J} \cdot \mathbf{E}$ term. I have found that in the frame of the satellite, the energy is dissipated (dissipation or load region) ahead of the DF but transferred from the plasma to the field behind the front (dynamo or generator region). This inversion is caused by the inversion of the diamagnetic current dominated by the ion pressure gradient. This mechanism has been already mentioned by Yao et al. (2013) but only in the case of DFs preceded by a dip of the magnetic field. In the fluid frame, the energy is transferred from the plasma to the fields as also found in a previous MMS single DF event (Yao et al., 2017). This dynamo region could contribute to the slow down of the fast flow. Then, by calculating the standard deviation of the current density and the electric field measurements from the four satellites, I have found that this energy conversion is not homogeneous at the electron scale due to the electric variations produced by the electron pressure gradient. The LHD waves have been suggested as a possible source of these electric field variations although due to the time averaging of all data (0.3 s) the high-frequency part of the spectra was filtered out. These waves are expected to be generated by the large density gradient at DF (e. g., Sergeev et al., 2009; Divin et al., 2015a; Le Contel et al., 2017; Yang et al., 2017a; Liu et al., 2018) generating ripples on the front at the electron scales and thus leading to the non-homogeneity of the energy conversion process (Pan et al., 2018).

In order to extend these case study results, I have carried out a statistical analysis over the full 2017 magnetotail season (chapter 5). From the analysis of 132 DF events and based on their magnetic profile visualised using a SEA, I have proposed to define two separate categories. Class I with 98 events (74.4%) shows a gradual decrease in the magnetic field after the DF and corresponds to the classical signature of DF previously reported by various studies. Class II with 34 events (25.6%) is a new category and is characterised by a bump in the magnetic field related to a minimum of ion and electron pressures and faster velocity than class I events. It turns out that all 6 DF events analysed in chapter 4 and in (Alqeeq et al., 2022) belong to class II. While class I events are randomly distributed in the XY GSE plane, class II events are located preferentially in the pre-midnight sector and could be related to substorm onsets.

Case study results about current density comparison, ions and electron decoupling from the Ohm's law analysis are confirmed for both categories. Furthermore, in the spacecraft frame and for both categories, I found that the energy is dissipated ($\mathbf{J} \cdot \mathbf{E} > 0$) ahead or at the DF due to the increase of the diamagnetic cross-tail current dominated by the enhancement of the ion pressure gradient ($\sim 72\%$ of the total current). On the other hand, class II events are associated with a reversal of the energy conversion process caused by a reversal of the diamagnetic current also mostly dominated by the ion pressure gradient although electron pressure gradient follows the same trend. Therefore, for class II events the energy is first

dissipated from the electromagnetic fields into the plasma but then transferred from the plasma to the electromagnetic fields behind the DF. Thus whatever the sign of $\mathbf{j} \cdot \mathbf{E}$, for both categories, ion pressure gradient drives the energy conversion process. In the fluid frame, both categories show an energy transfer from the plasma to the electromagnetic fields (dynamo or generator region) which could contribute to the deceleration of the fast flow by radiating waves. As for the 6 DFs, this energy conversion process caused by the electron pressure gradient has been shown to be not homogeneous at the electron scale. Both classes appear as 2D structures with significant electron pressure gradients along M and N directions. Class II events could be a bit more localised than class I as their electron pressure gradients (or E'_M and E'_N) seem to be a bit stronger. A summary of respective class I and class II signatures is given in Table 6.1.

The possible link between this process and the LHD waves propagating along M with a wavelength $\sim \rho_e$ and including the electron pressure gradient still needs to be demonstrated theoretically although a recent statistical study by Hosner et al. (2022) showed the ubiquitous presence of LHD waves at DF and kinetic simulations have shown their importance in the energy conversion process (Divin et al., 2015b; Nakamura et al., 2019b).

Finally, I have suggested that class II event could correspond to the crossing of head structures produced by the kinetic ballooning-interchange instability and recently identified in THEMIS data closer to the Earth by Panov et al. (2022).

TABLE 6.1 – Summary of class I and class II signatures

Physical quantity	**Class I**	**Class II**
B_z or B_L	fast increase then slow decrease	fast increase then fast decrease "bump"
$P_{i,e}$ & $N_{i,e}$	monotonous decrease	minimum or "hole"
$\mathbf{J} \cdot \mathbf{E}$ (s/c frame)	>0 dissipation	>0 dissipation then <0 dynamo
$\mathbf{J} \cdot \mathbf{E}'$ (fluid frame)	<0 dynamo	<0 dynamo
Geometry	2D $E'_N \sim E'_M \sim$ |0.8| mV/m	2D $E'_N \sim E'_M \sim$ |1.2| mV/m
Homogeneity at electron scales SD(E')	No (>1)	No (>1)
Flux rope signatures	sometimes relevant	frequently observed

6.2 Further works

An obvious follow-up of this study is an extension over all magnetotail seasons of the MMS mission. However, the capacity of electron measurements onboard MMS4 have been reduced due to a failure of a subsystem (optocoupler) since the 5th of June 2018 on MMS4 preventing from high time resolution measurements for electrons moments.

In addition to in situ measurements, I would like to briefly present possible follow-up studies, actually already started, of DFs generated by magnetic reconnection based on 3D kinetic simulations using the Smilei PIC code.

Thanks to a collaboration with the Smilei team of Maison de la simulation at Paris-Saclay (initiated during a SMILEI training formation), Young Dae Yoon from Pohang Accelerator Laboratory, Jérémy Dargent from Ruhr-Universität Bochum and Emanuele Cazzola from LPP, a parameter setting for running a simulation of the DFs in the Earth's magnetotail has been discussed. Then, I started to run a fully kinetic simulation of symmetric magnetic reconnection based on the Earth's magnetotail conditions in a two-dimensional (2-D) geometry using a parameter setting adapted from the one used by Dargent et al. (2017).

A 3D version of this kinetic simulation, that could be run at Polytechnique mesocenter, should allow me to compare the present MMS measurements with numerical results. In particular, two questions could be addressed. Following Divin et al. (2015b) and Nakamura et al. (2019b) studies, the role of LHD waves at DF could be investigated and the effect of electron pressure gradient at electron scale could be better understood. The possible link between class II events and head structures produced by kinetic ballooning-interchange instability could be investigated.

Annexe A

Programming Environments

A.1 PYSPEDAS

The Space Physics Environment Data Analysis Software (SPEDAS) (https://github.com/spedas/pyspedas) is a powerful library of codes written in Interactive Data Language (IDL) and aims at visualising and analysing all kind of data from different space missions (Angelopoulos et al., 2019). Its conversion into python language is ongoing and already includes data loading, some data analysis and data plotting tools for various scientific space missions.

A.2 AIDApy

AIDApy (https://www.aida-space.eu/AIDApy_AIDAdb) is a new open-source software written in Python and capable of collecting, combining and correlating data from different space missions funded by the European Commission (Lapenta, 2022). AIDApy wants to replace mission-specific tools written for costly languages (such as IDL or Matlab) that exclude many scientists, students and amateur space enthusiasts from exploring the data, with a much-needed single platform where methods are shared and continuously improved by the whole community.

AIDA project focuses on analysing large data sets from different space missions [e.g., THEMIS, Cluster, MMS, ...], from high-performance computing simulations and from statistical investigations using statistical and machine learning techniques (Lapenta, 2022). The most important advantage of the AIDA project is its use of Machine learning (ML), Deep learning (DL) and Artificial Intelligence (AI) via Python language. Thus, it allows to access and manages more space data using lots of Python tools made available for the space weather community, Lapenta (2022). The main difference between the AIDA project and any space data analysing project is that AIDA is intertwined with many different research tools [e.g., Data Engine, HelioPy, Xarray, Sunpy, Astropy, ML Engine, Visualization Engine, ...].

Thus, AIDA operates as an assignment environment in which all the different research projects are integrated, which can facilitate a lot of investigations for scientists in this field. As an example, the statistical investigation described in Chapter 5 has required a treatment of a huge amount of data. Search of DF events that would need to develop some complex tools or to do it by eyes have been performed using the Event Search subpackage included in AIDApy saving a lot of time and effort.

A.3 SpacePy

Tools for Space Science Applications (SpacePy), a python based library of tools for the space sciences, (https://spacepy.github.io/) is also a new package written in Python to investigate the space plasma observations, to produce basic data analysis and visualizations. The project aims to encourage accurate and open research standards by providing open-source software development. SpacePy has supplied a considerable benefit thanks to its package pycdf, a Python interface for reading the Common Data Format (CDF) files ; many NASA missions have data files in such a format. Furthermore, SpacePy has provided a useful and simple technique analysis in Python to perform superposed epoch analysis which has been used in Chapter 5 to carry out my statistical study.

A.4 Github

All my data analysis can be found online on Github (https://github.com/Sobohalqeeq) and is organized as follows : the Reference List (RL) that includes basic observations of DF using MMS data, a comparison between different current density computations, calculation, analysis of generalized Ohm's law, analysis of the energy conversion processes, DF normal computations using the timing analysis (TA) method and the Minimum Variance Analysis (MVA), routine to plot professional figures. Also, it can be found an example code with its description for conducting statistical studies using spacecraft data [e.g., MMS] by incorporating some of the previously mentioned scientific tools.

Annexe B

Supplementary materials of Chapter 4

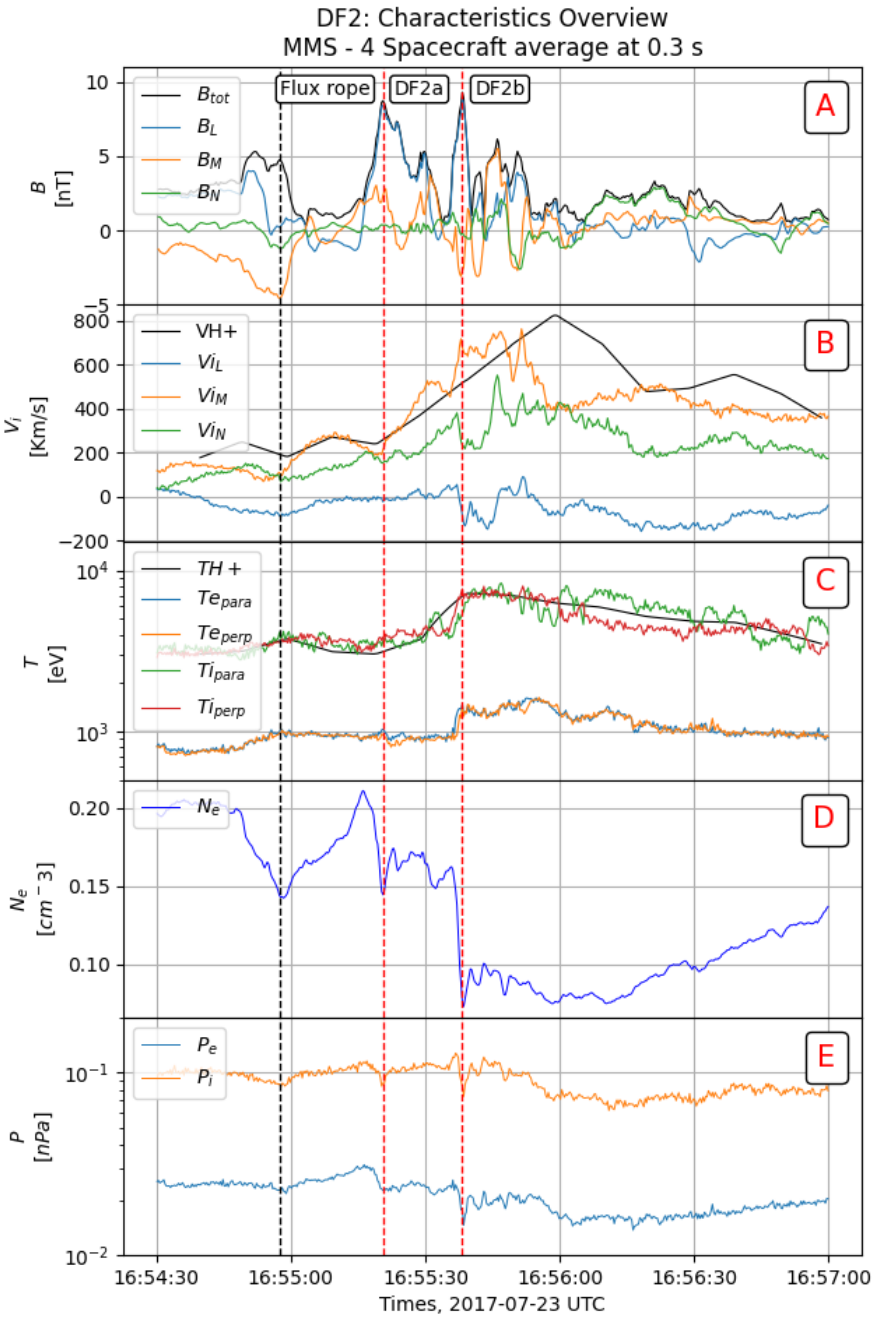

FIGURE B.1 – Same as Fig. 4.1 for DF2a,b signatures.

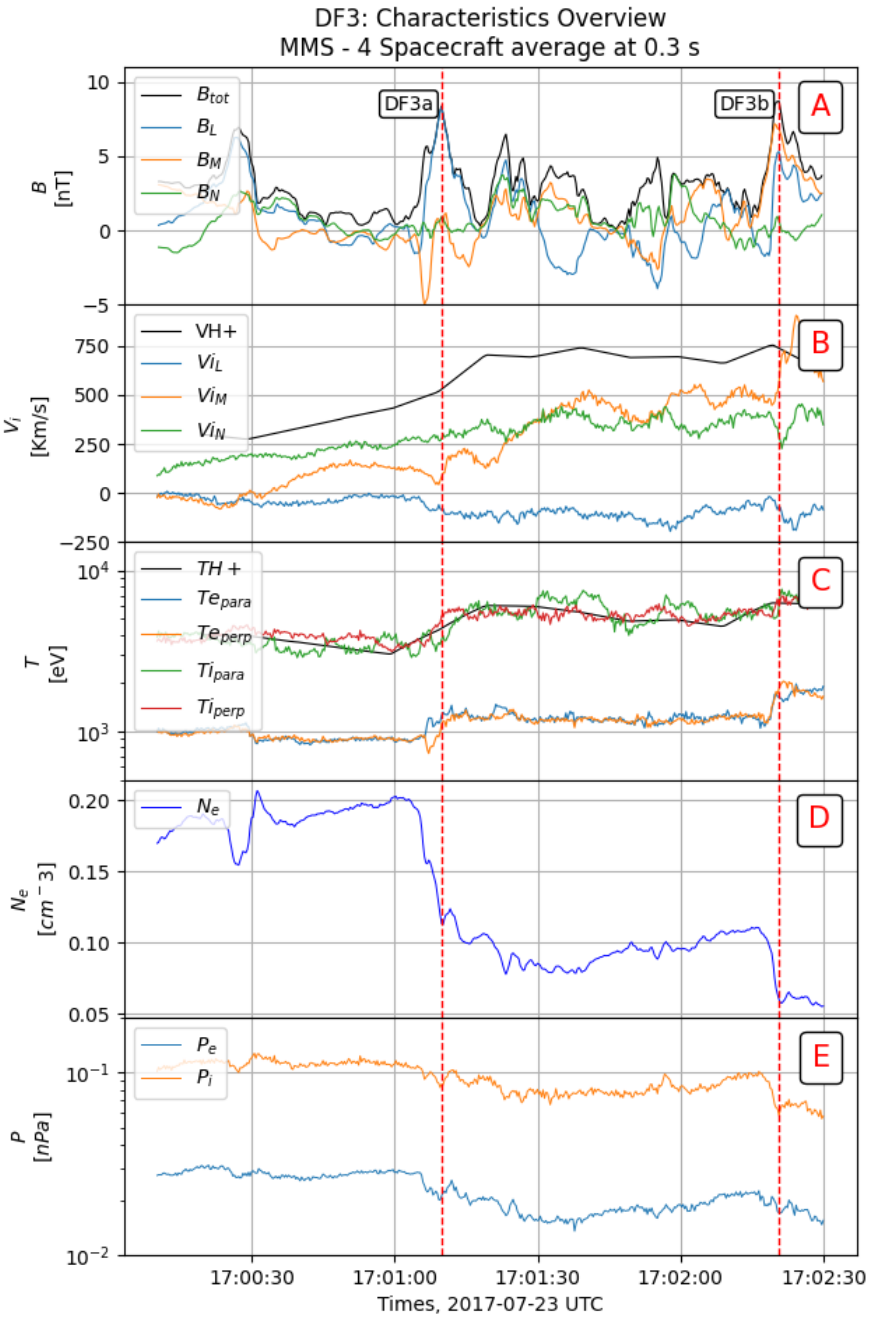

FIGURE B.2 – Same as Fig. 4.1 for DF3a,b signatures.

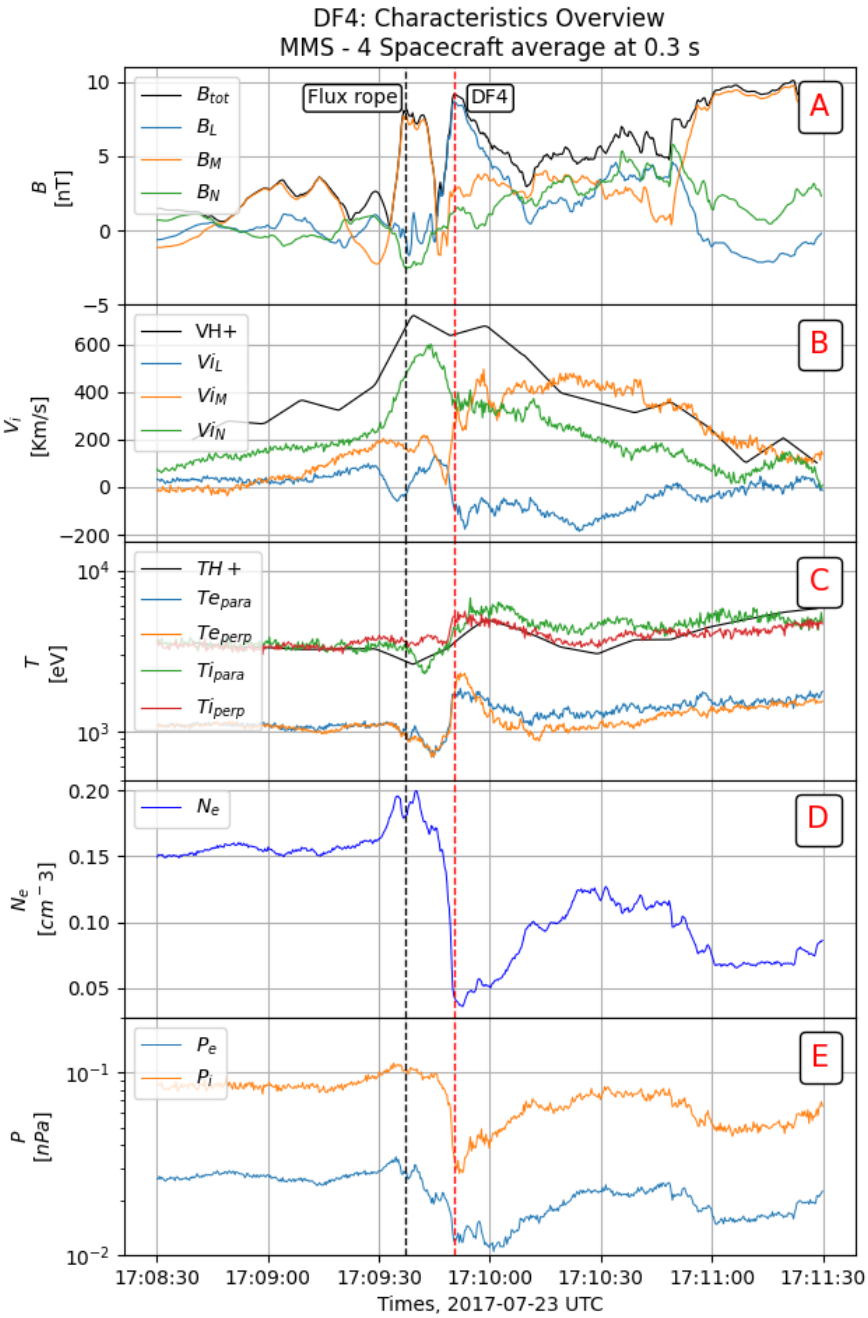

FIGURE B.3 – Same as Fig. 4.1 for DF4 signature.

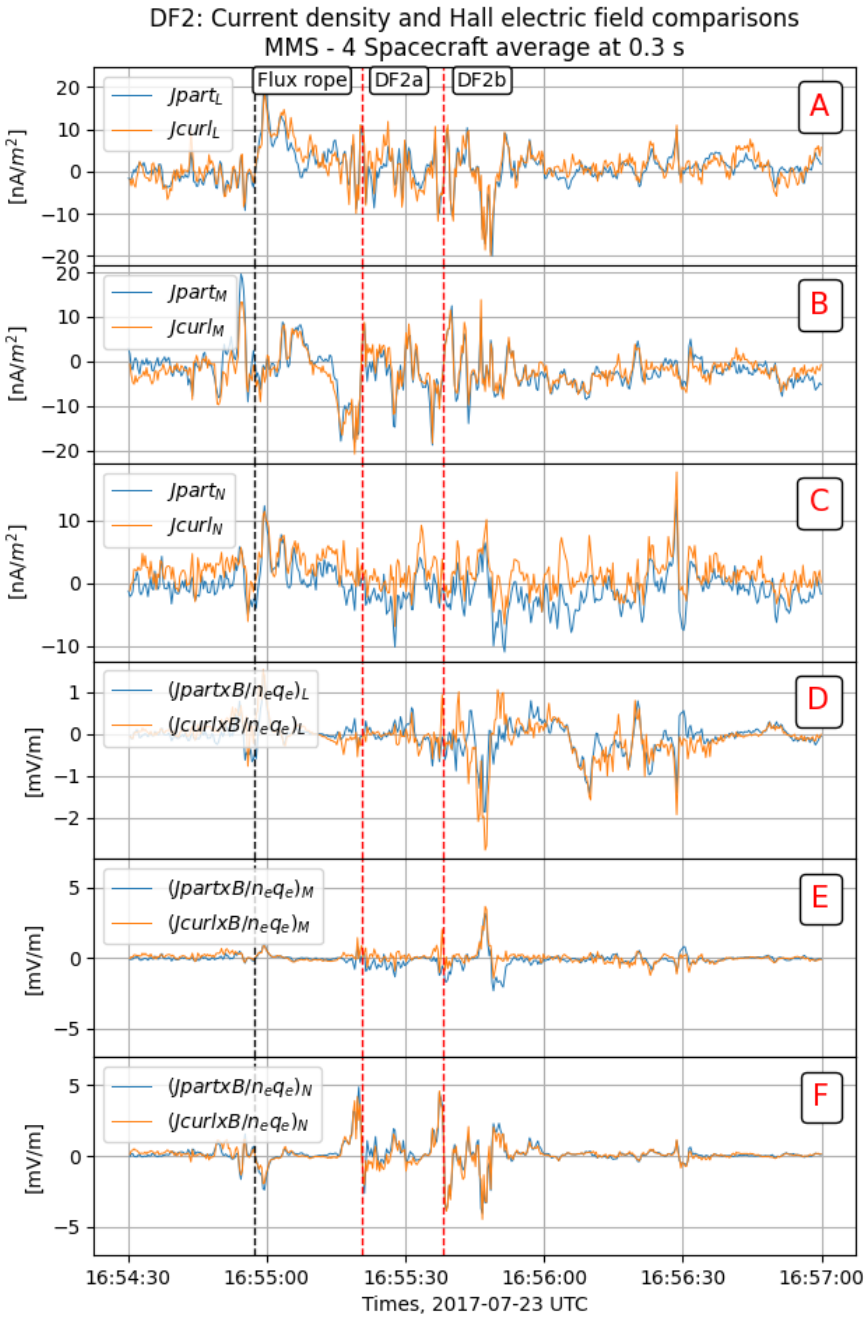

FIGURE B.4 – Same as Fig. 4.2 for DF2a,b signatures.

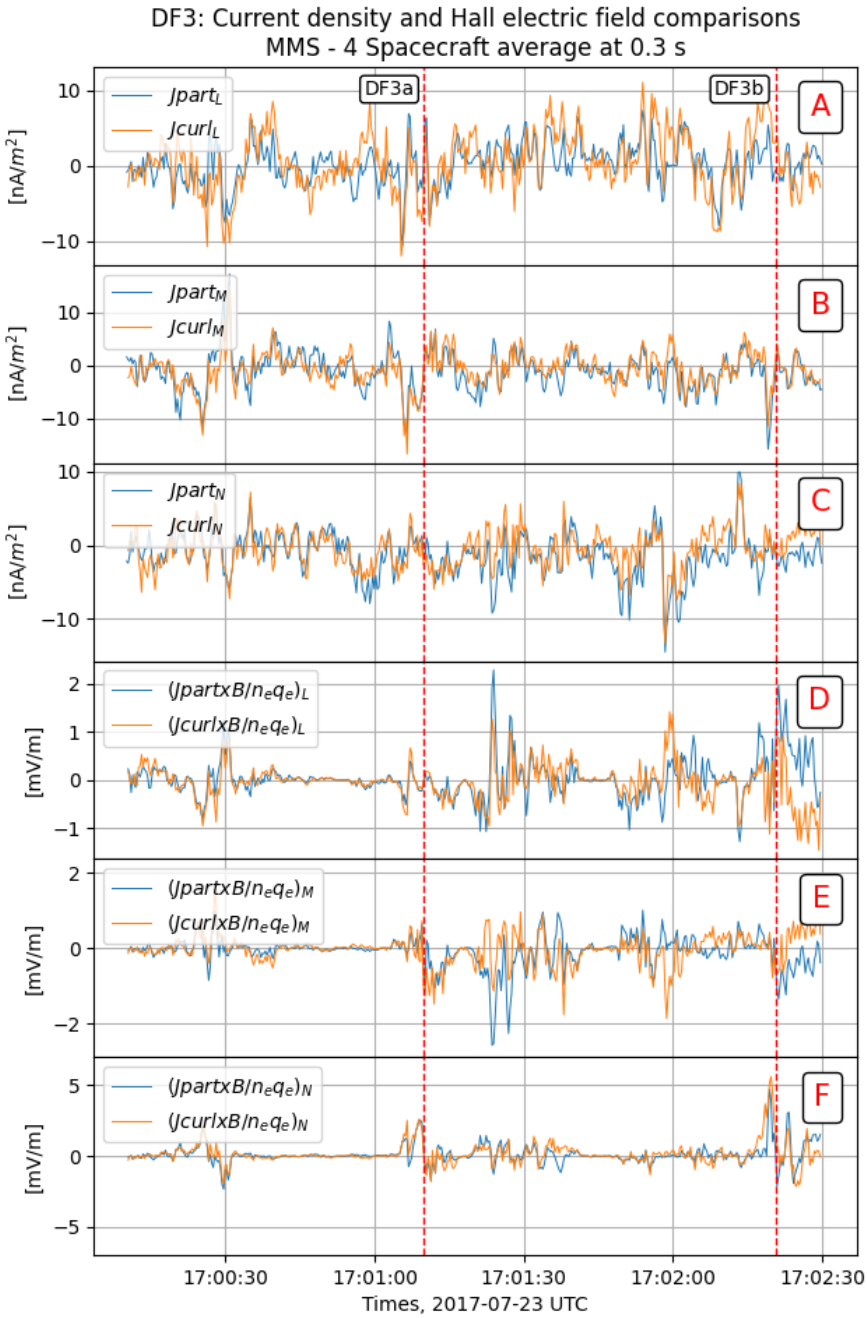

FIGURE B.5 – Same as Fig. 4.2 for DF3a,b signatures.

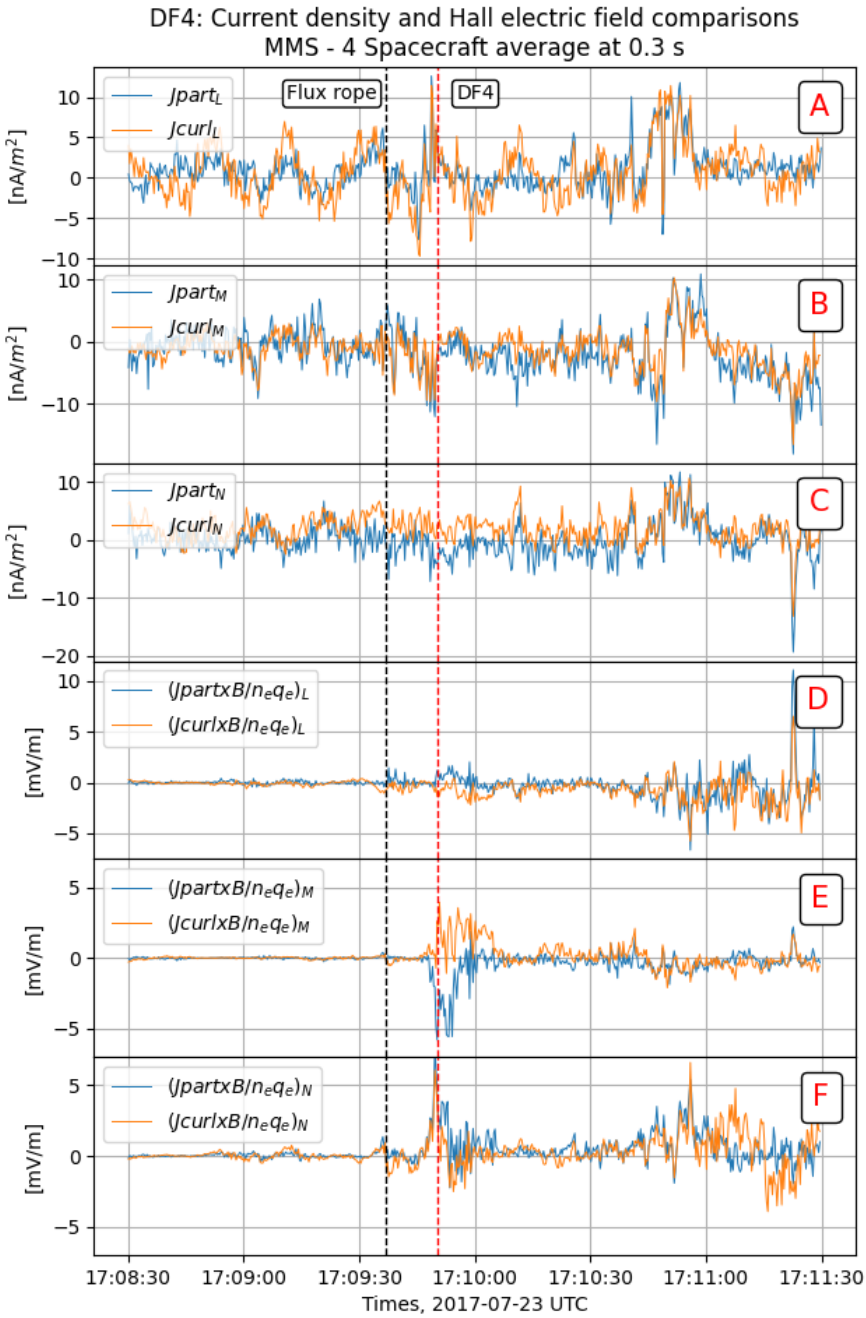

FIGURE B.6 – Same as Fig. 4.2 for DF4 signature.

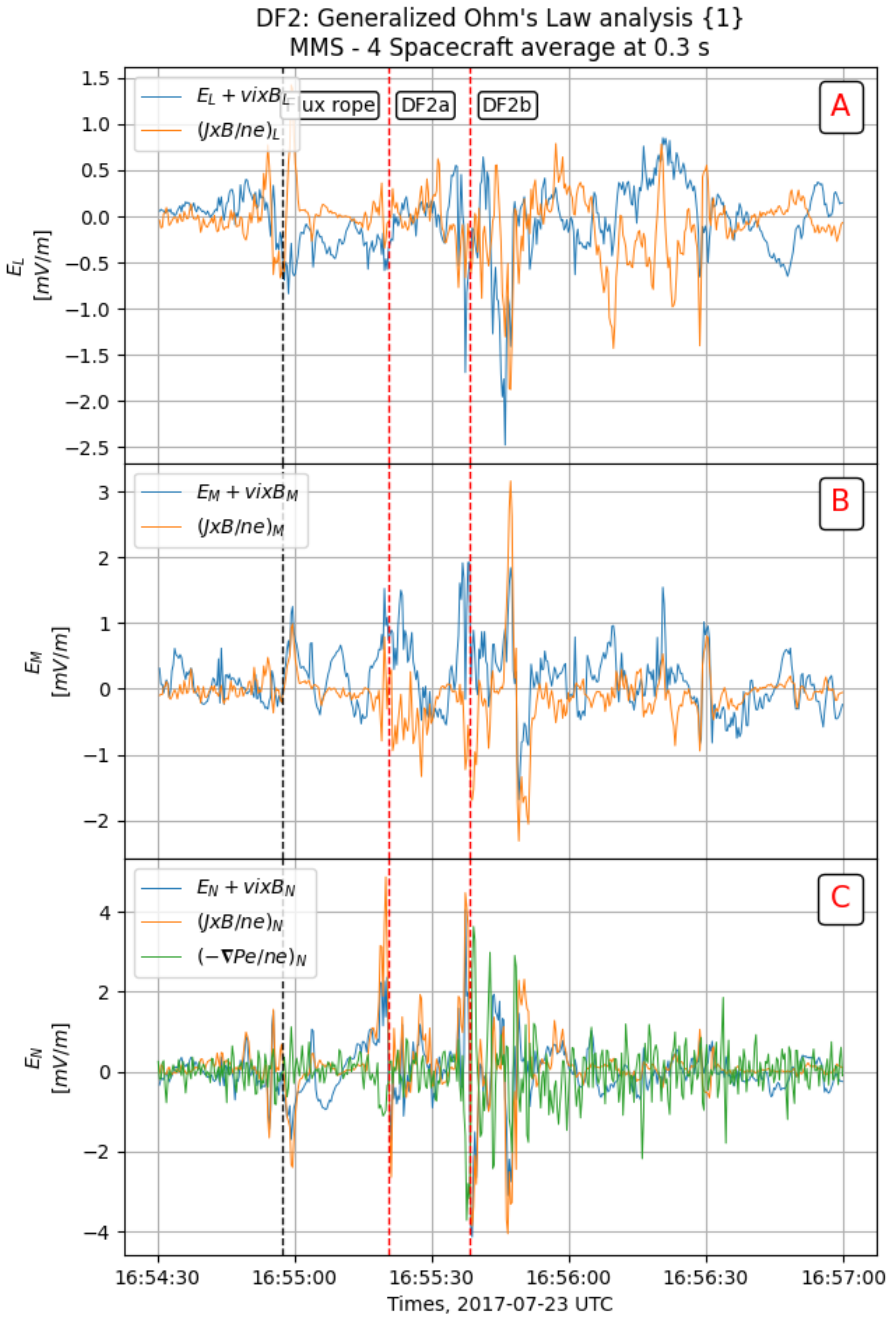

FIGURE B.7 – Same as Fig. 4.3 for DF2a,b.

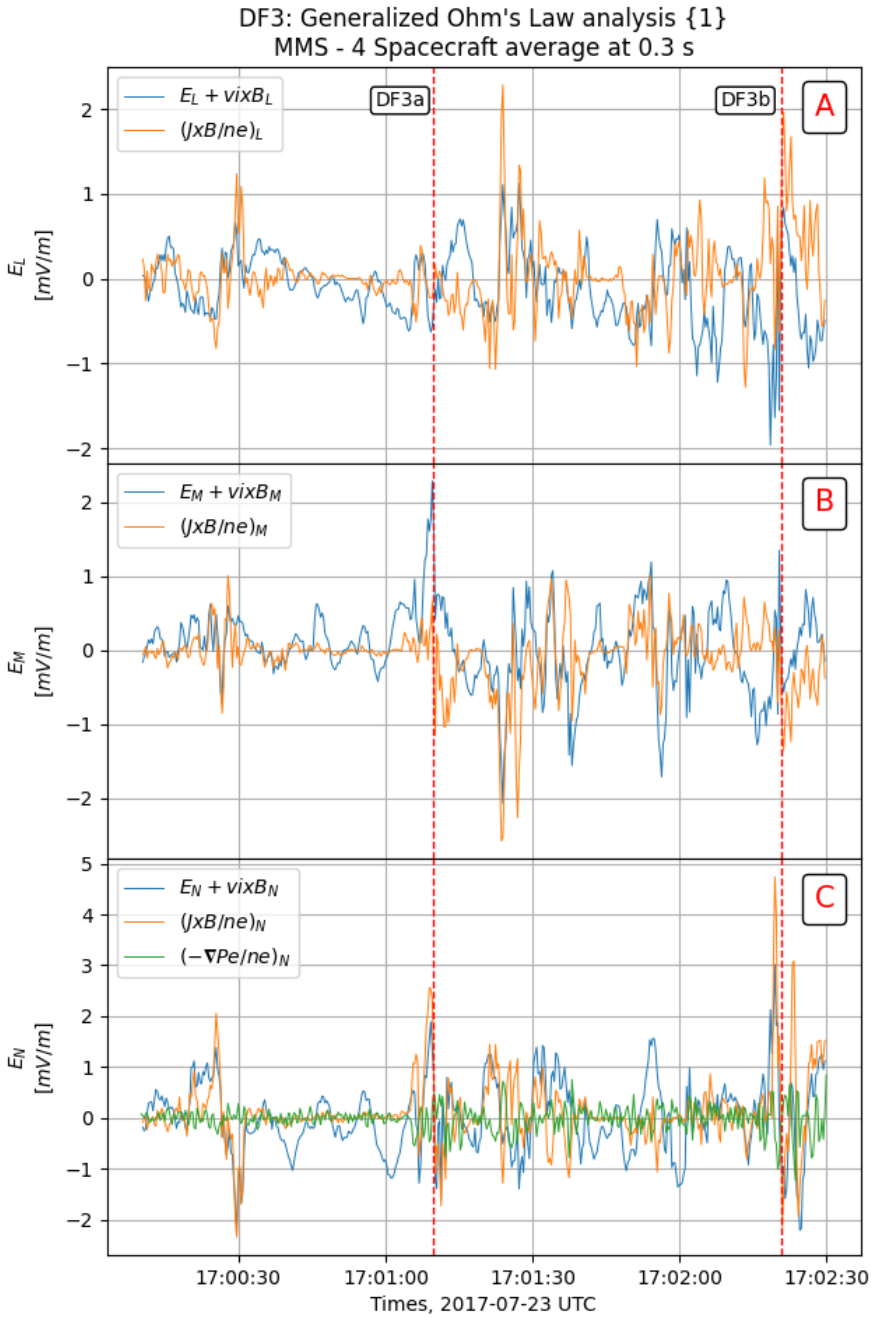

FIGURE B.8 – Same as Fig. 4.3 for DF3a,b.

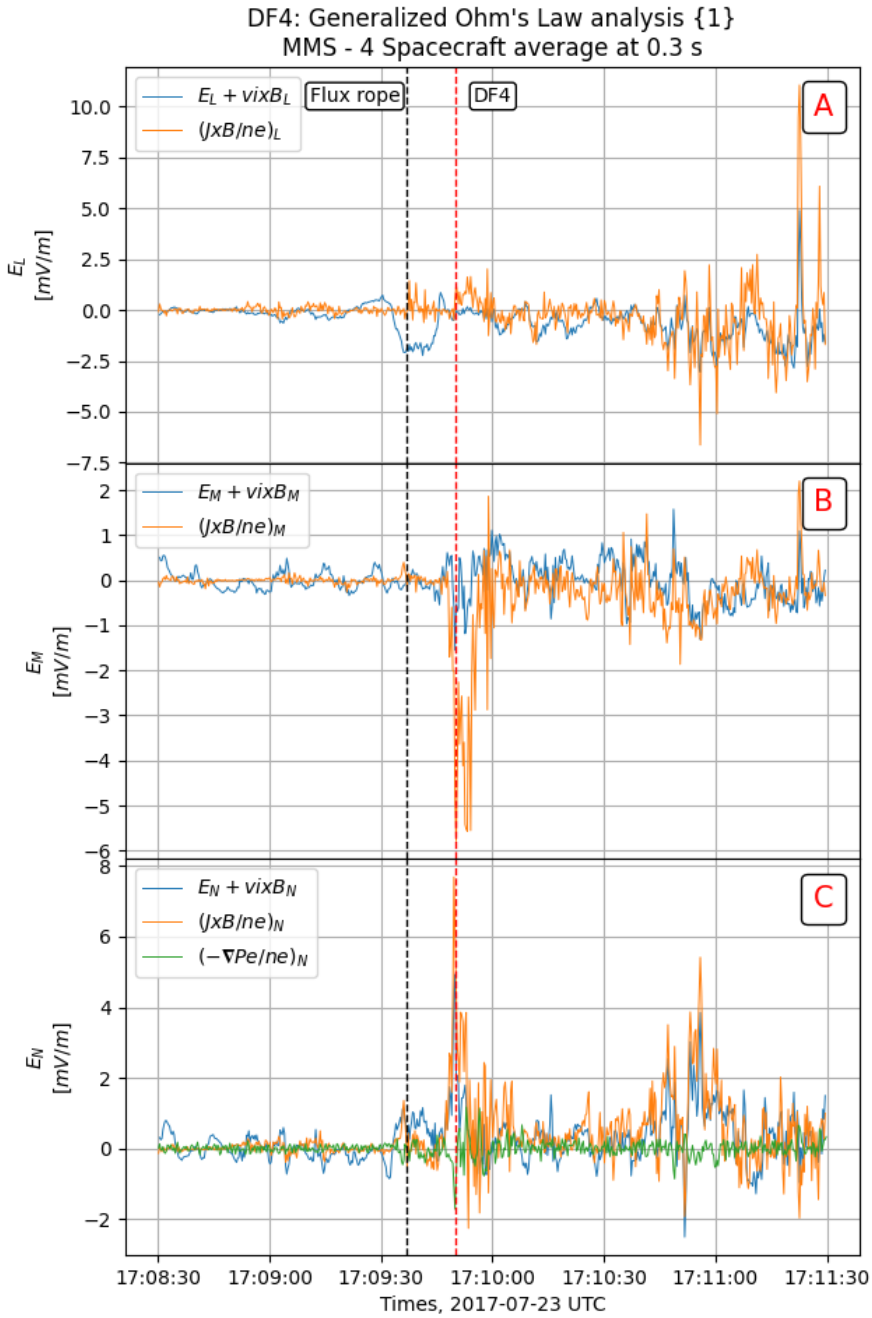

FIGURE B.9 – Same as Fig. 4.3 for DF4.

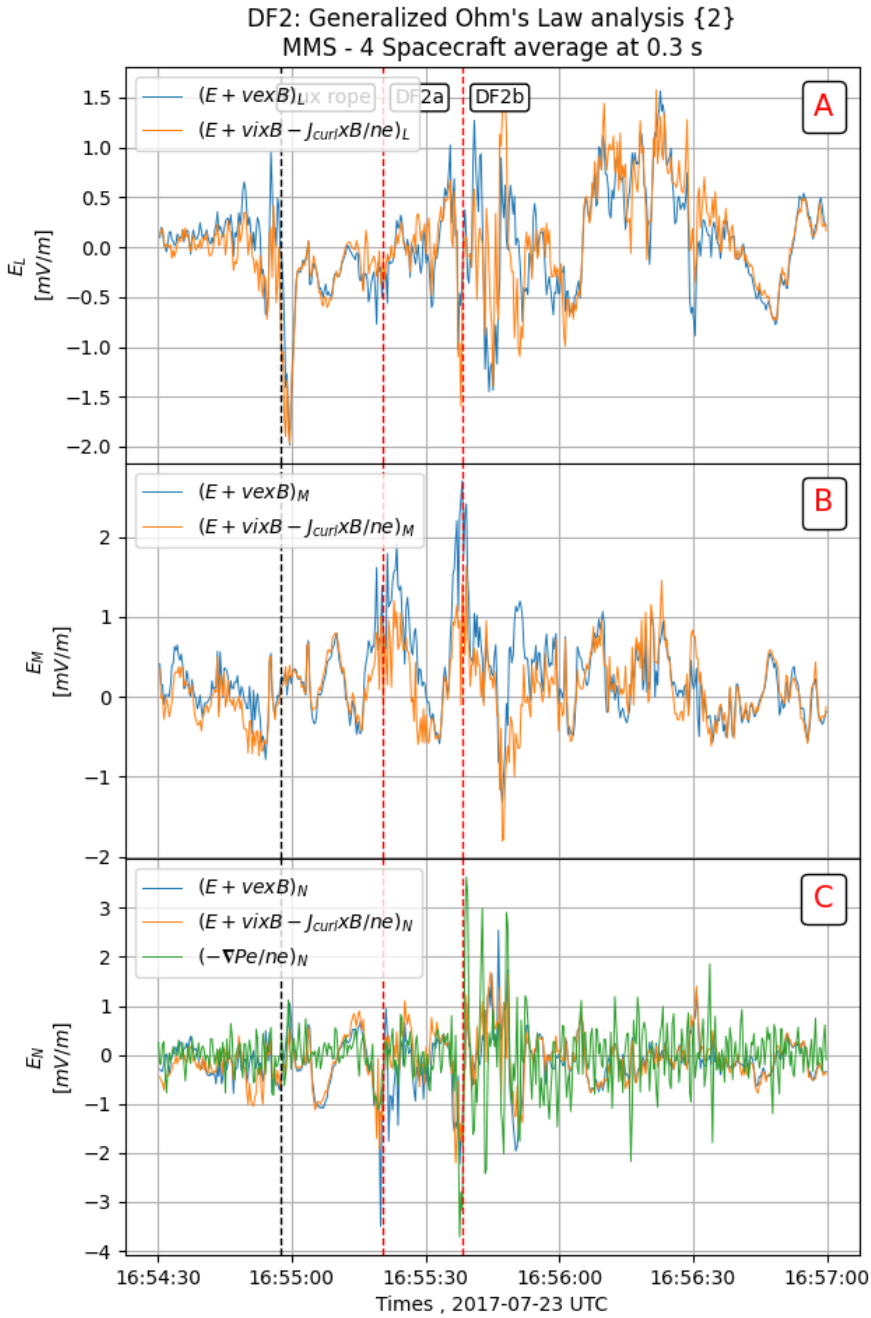

FIGURE B.10 – Same as Fig. 4.4 for DF2a,b.

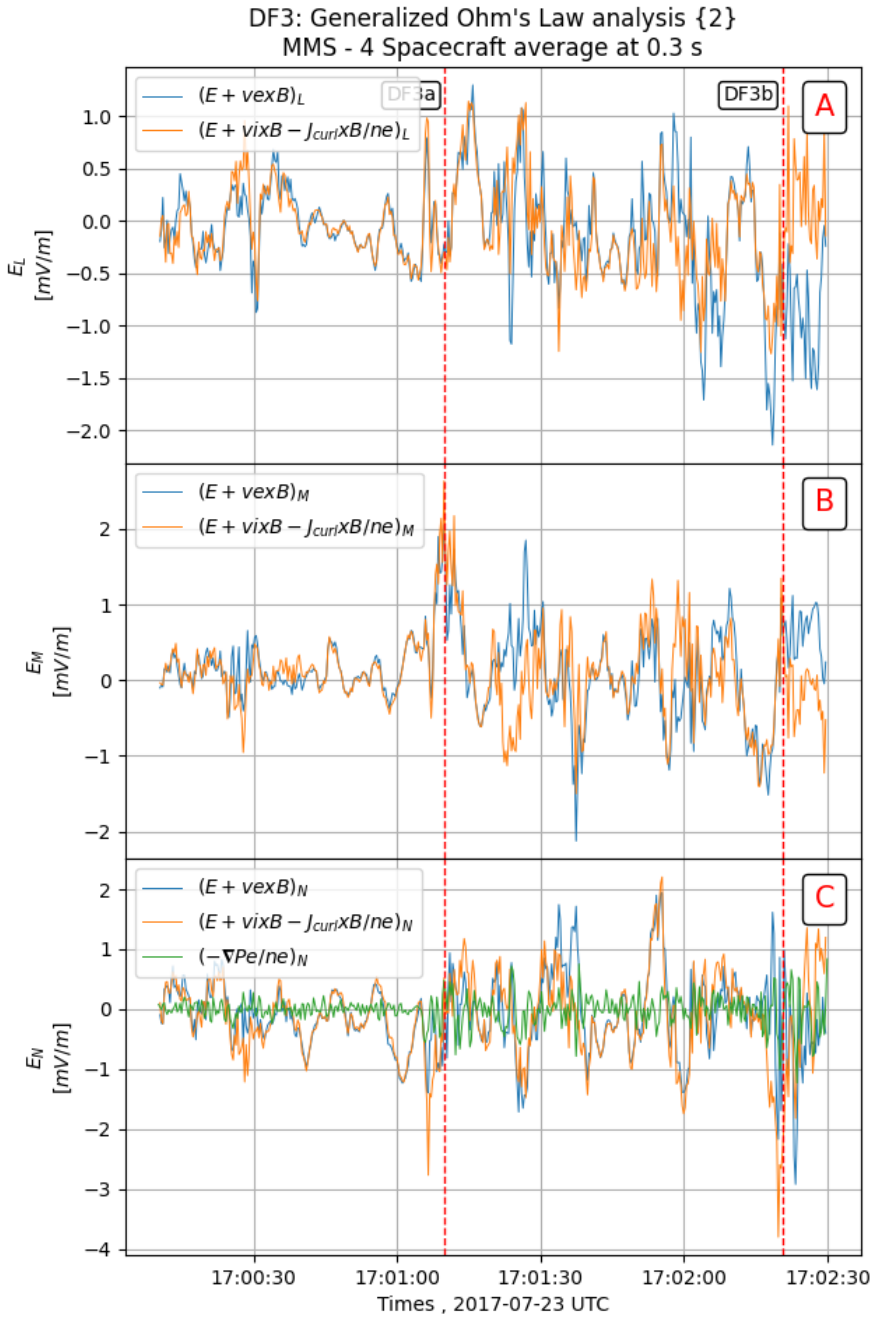

FIGURE B.11 – Same as Fig. 4.4 for DF3a,b.

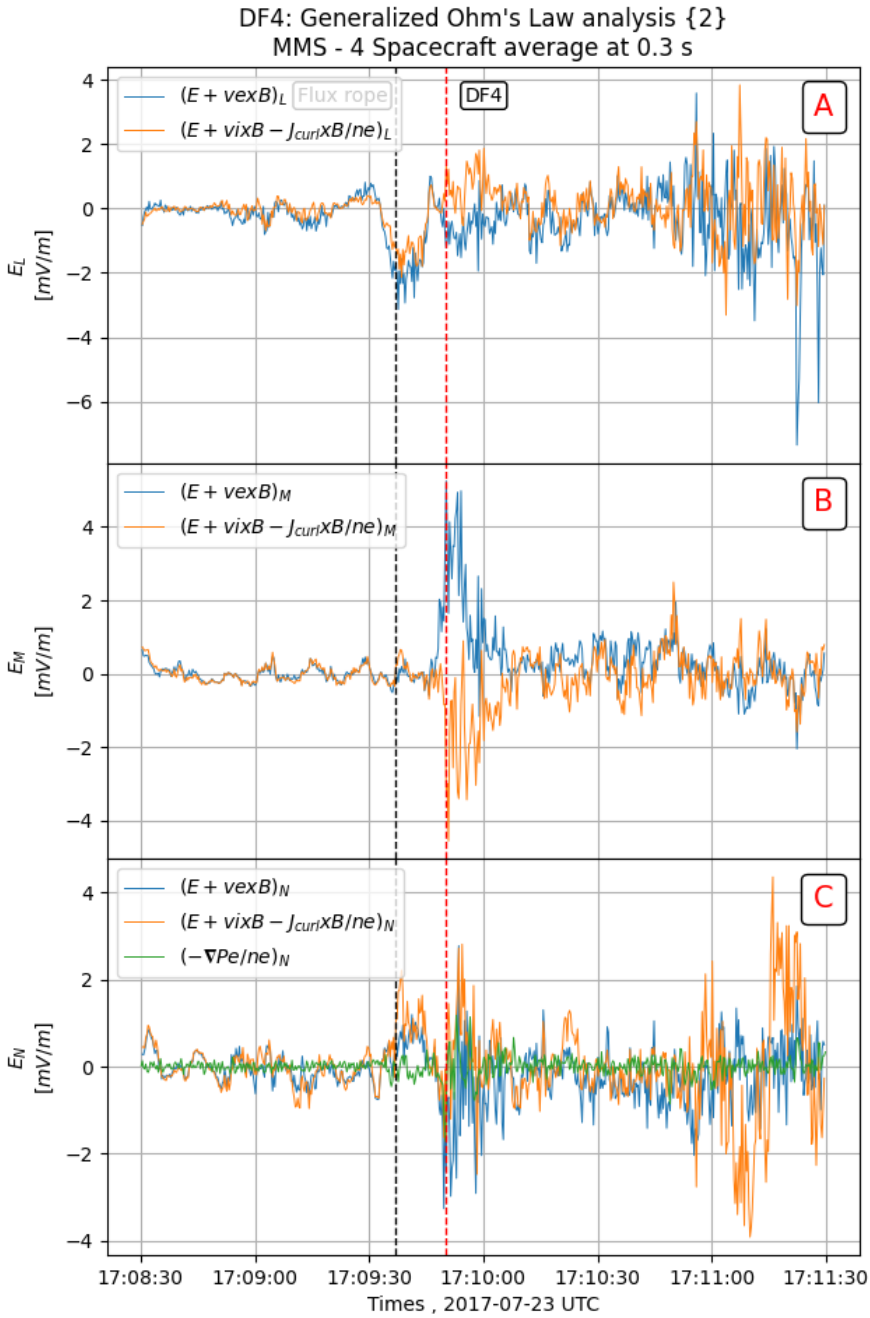

FIGURE B.12 – Same as Fig. 4.4 for DF4.

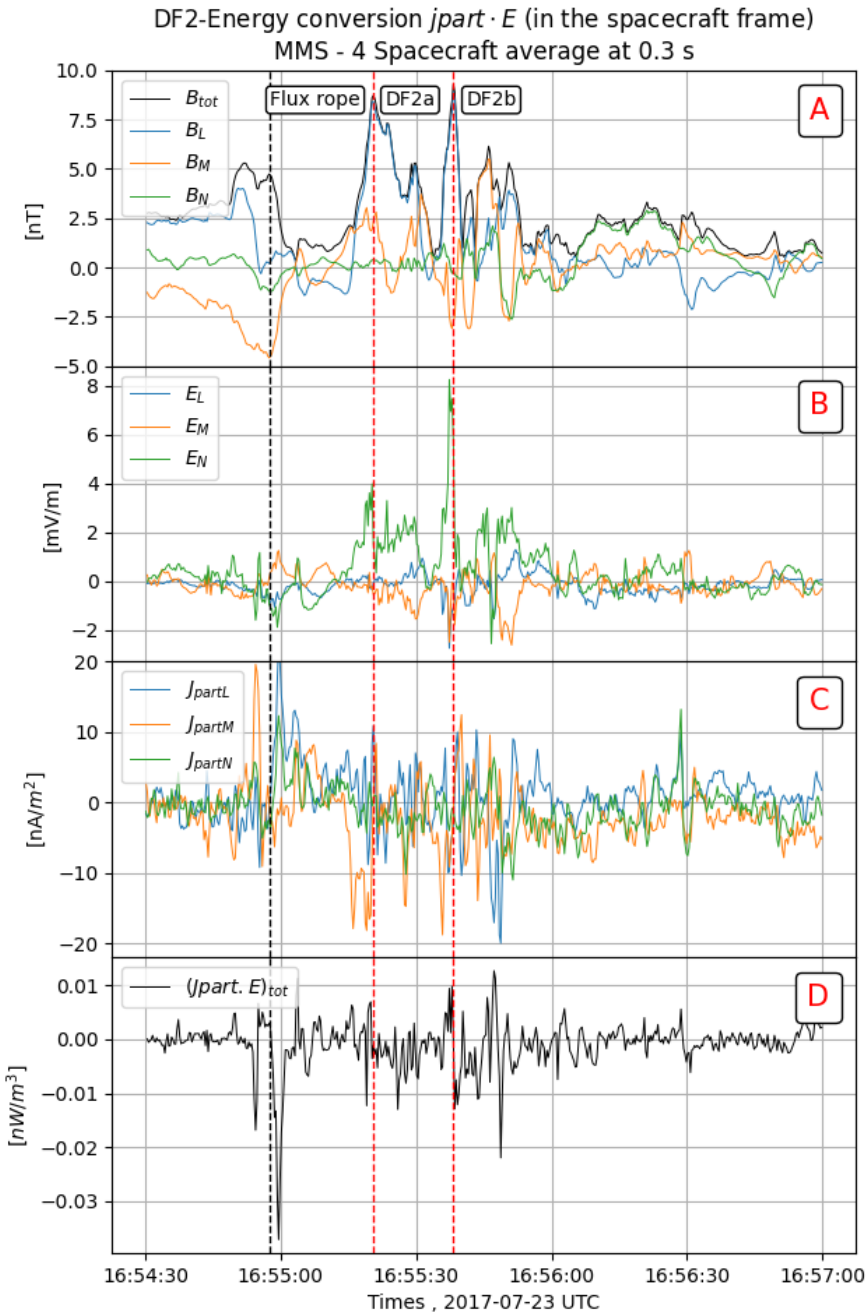

FIGURE B.13 – Same as Fig. 4.5 for DF2a,b.

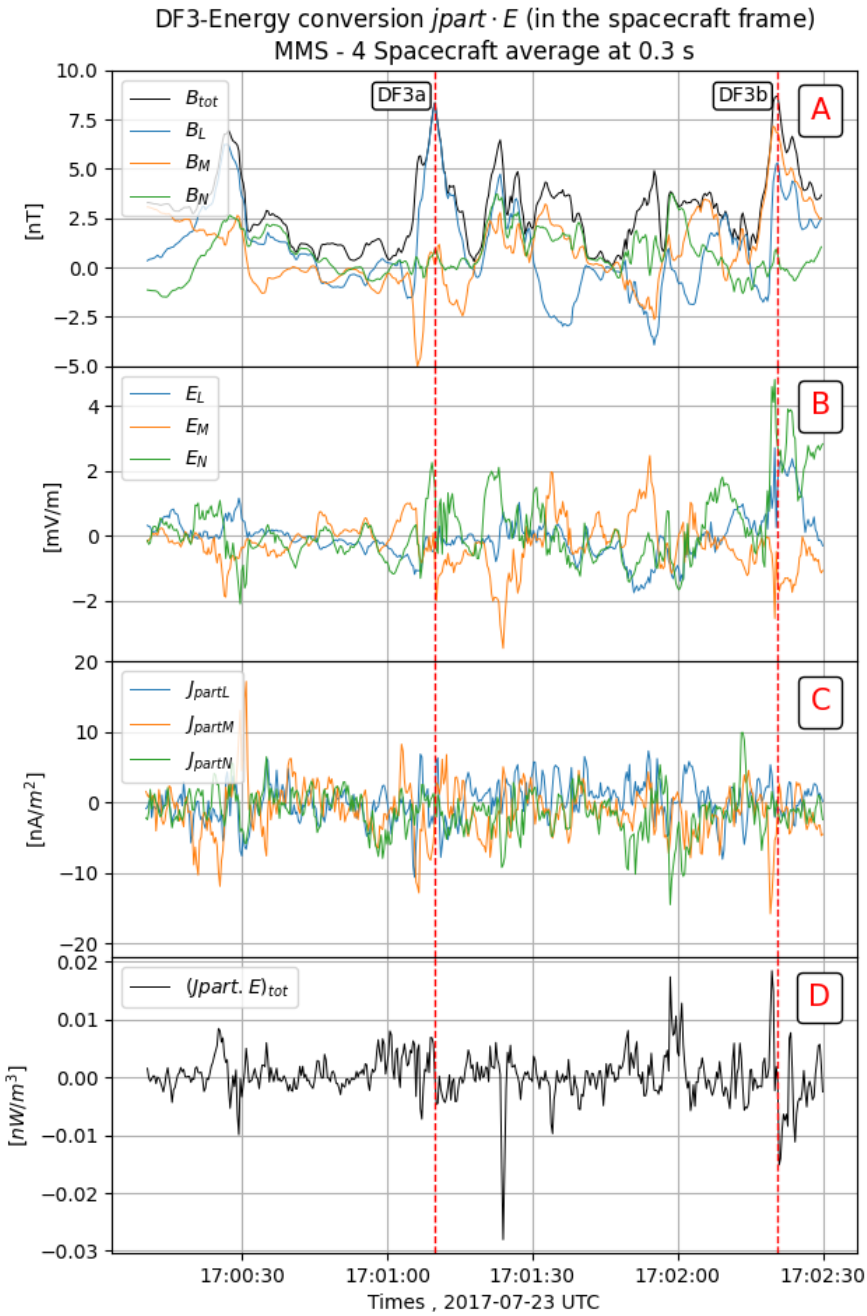

FIGURE B.14 – Same as Fig. 4.5 for DF3a,b.

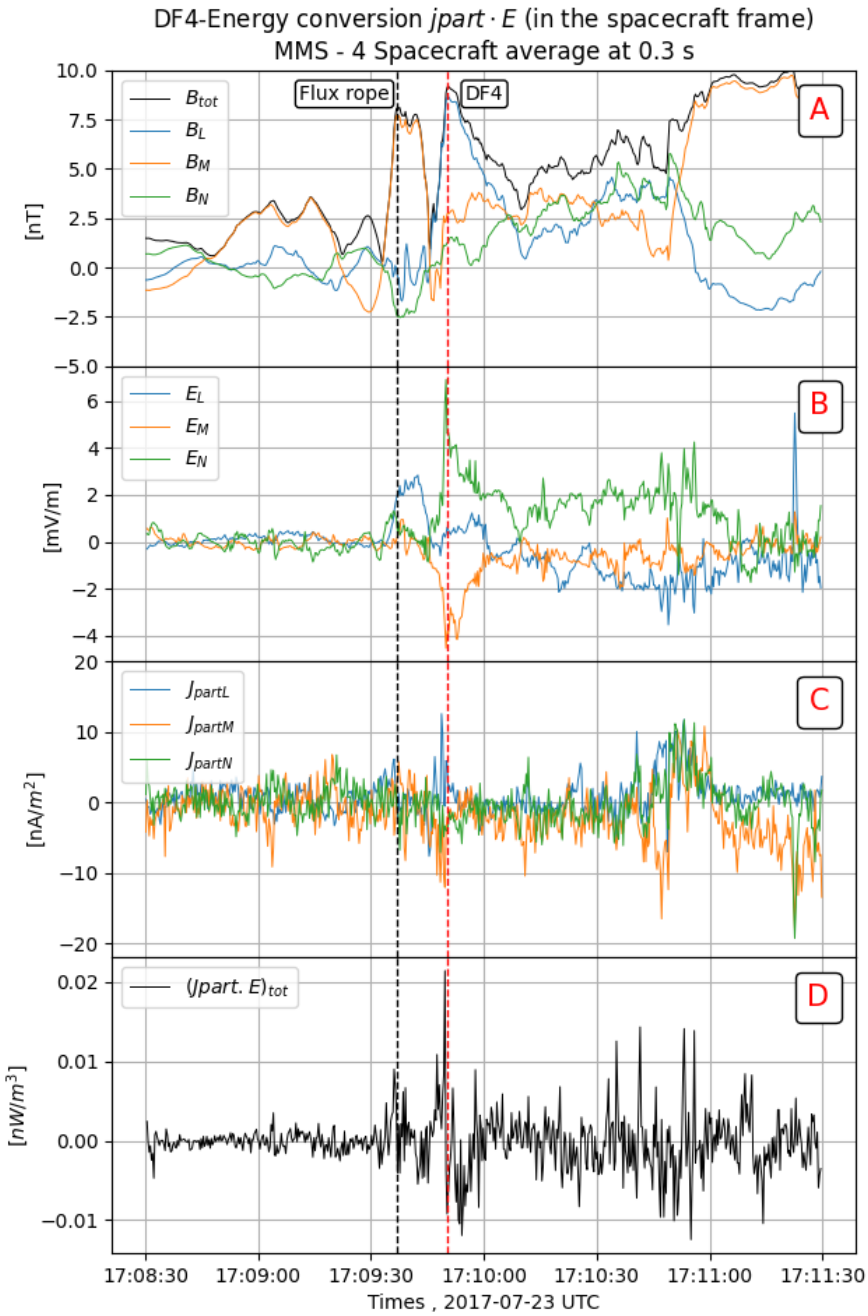

FIGURE B.15 – Same as Fig. 4.5 for DF4.

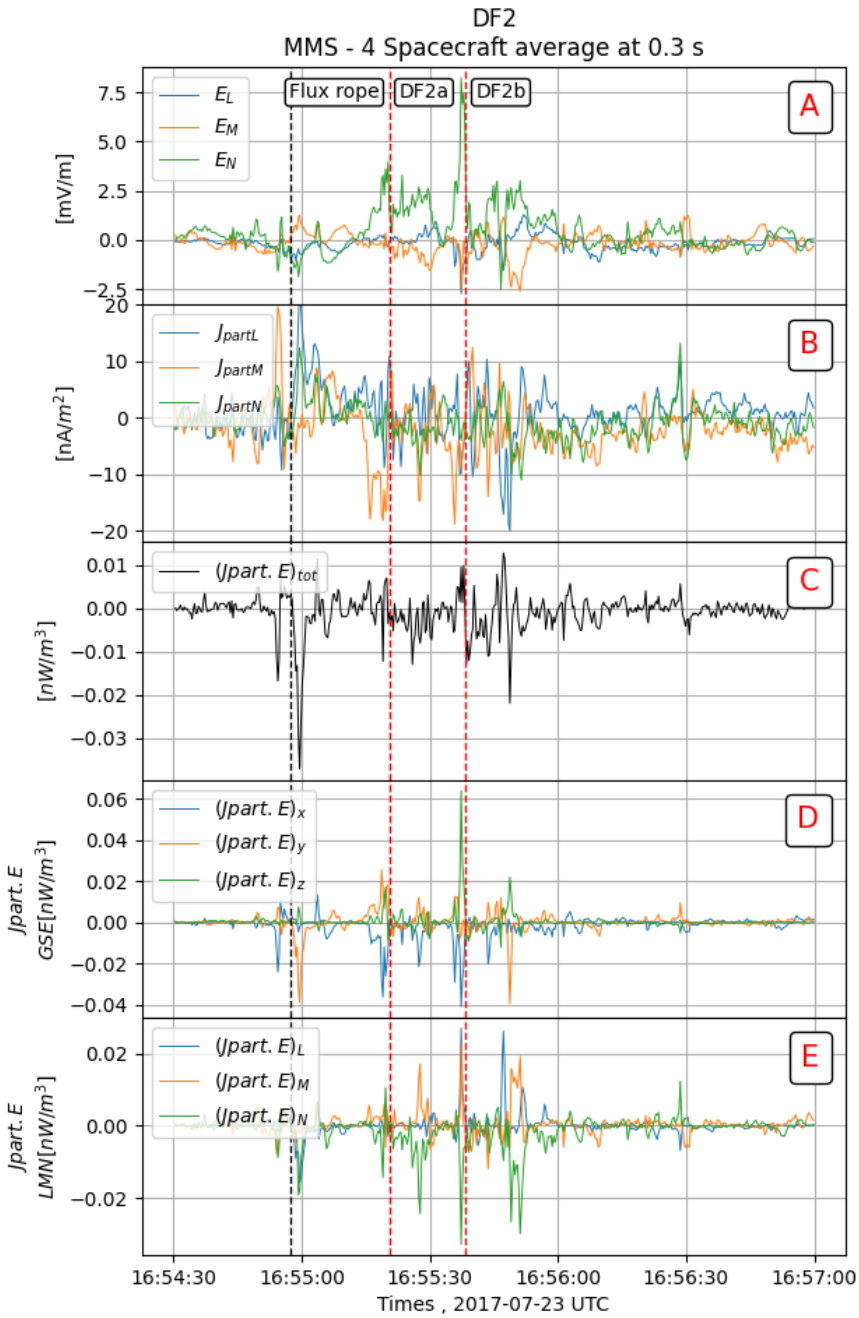

FIGURE B.16 – Same as Fig. 4.6 for DF2a,b.

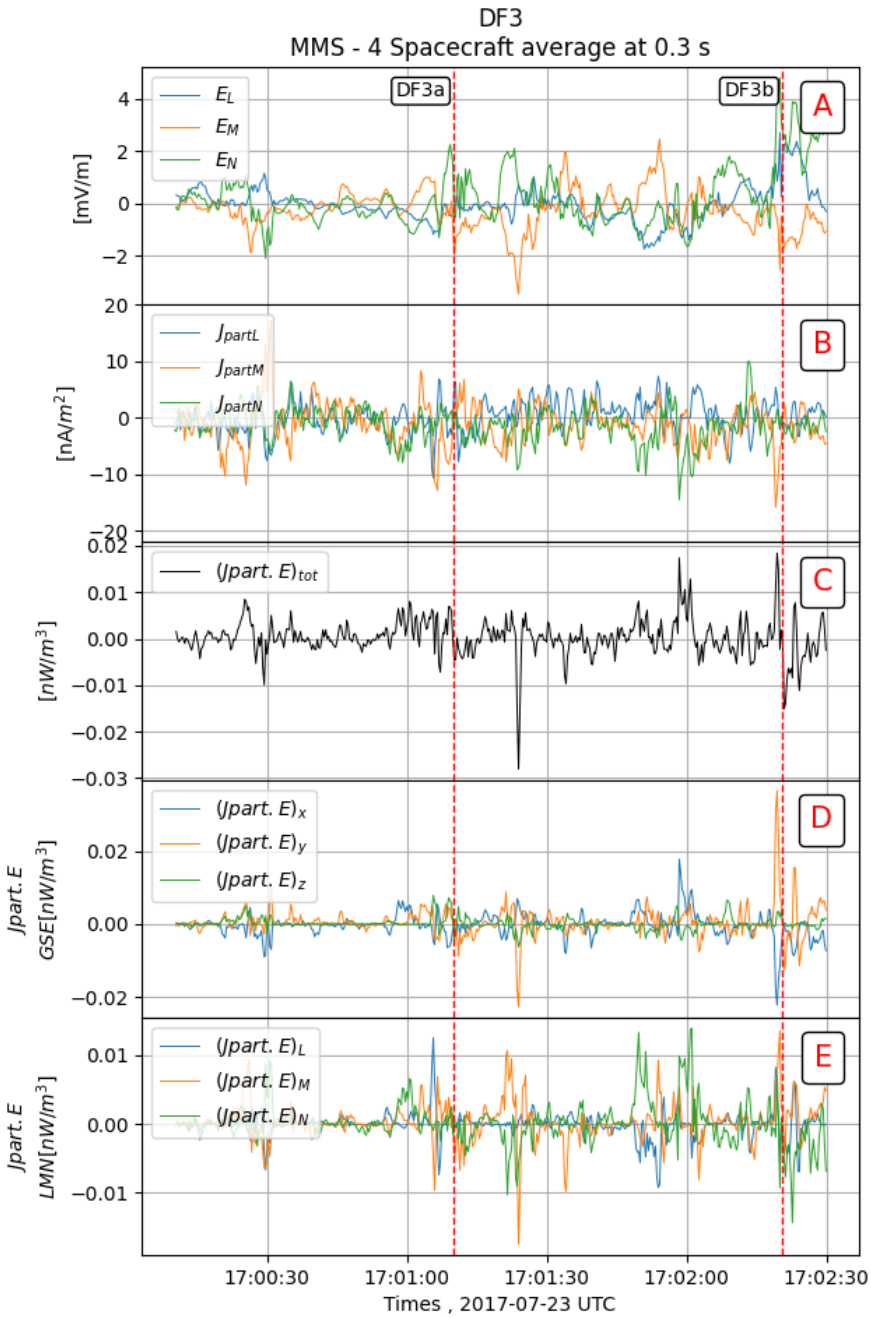

FIGURE B.17 – Same as Fig. 4.6 for DF3a,b.

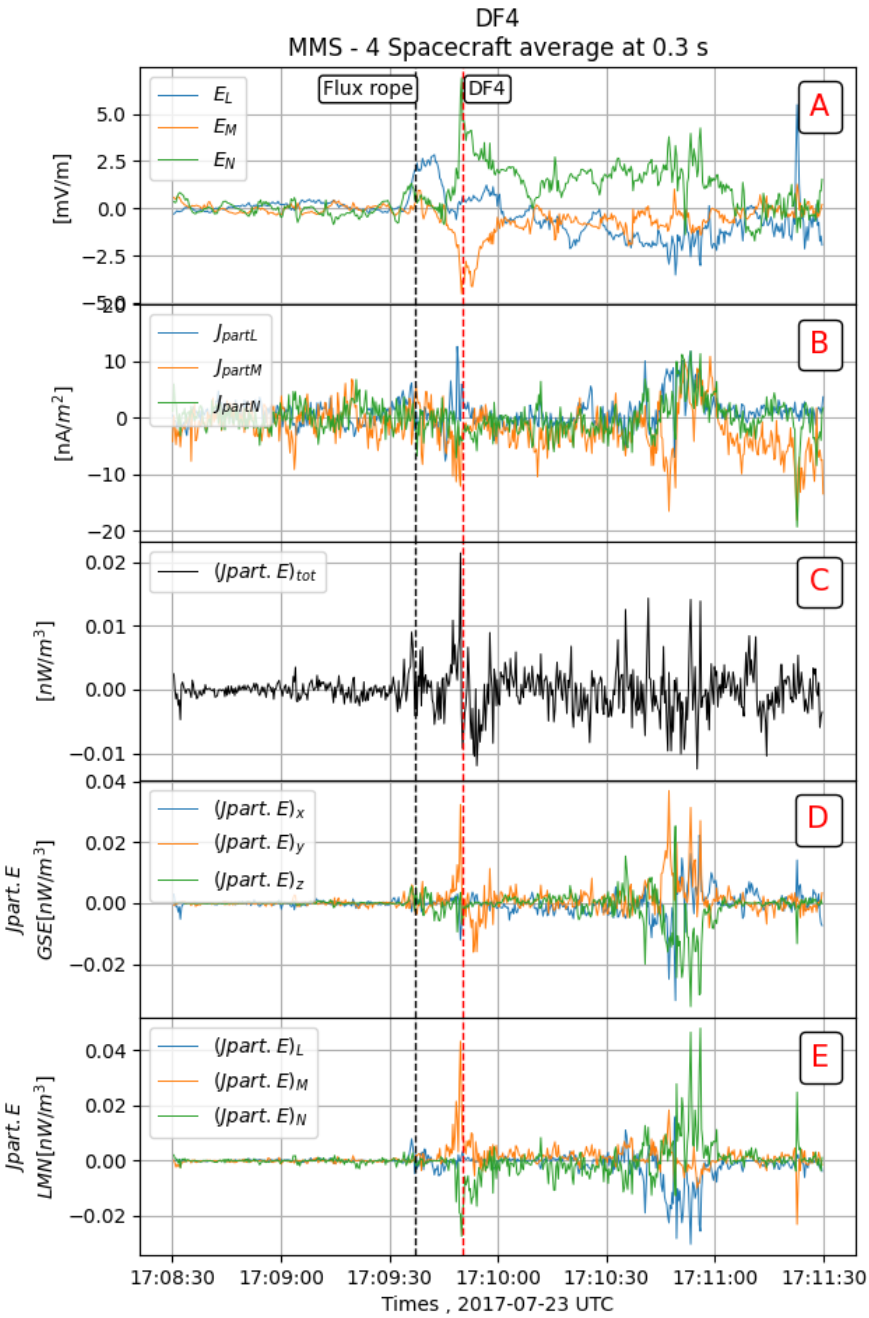

FIGURE B.18 – Same as Fig. 4.6 for DF4.

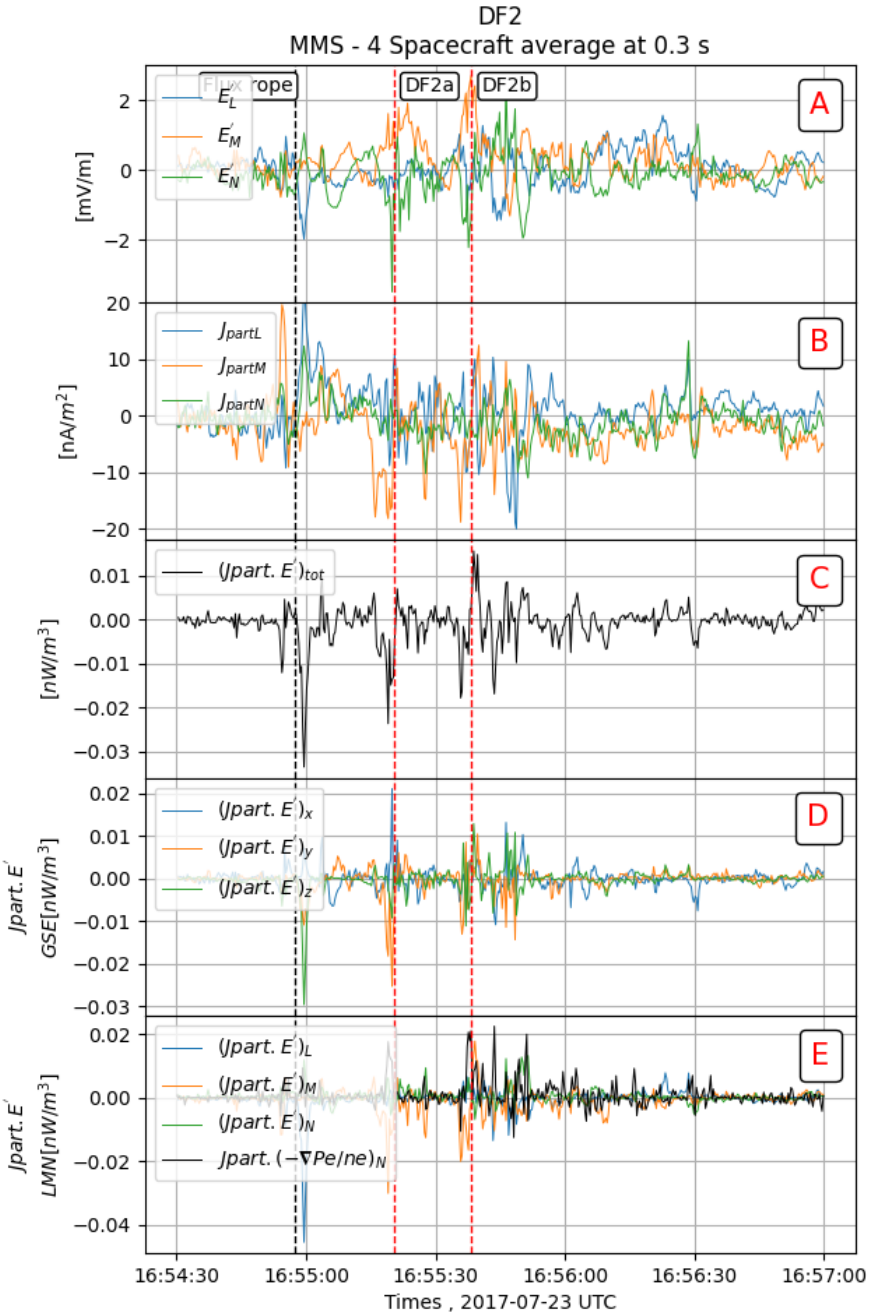

FIGURE B.19 – Same as Fig. 4.6 for DF2a,b.

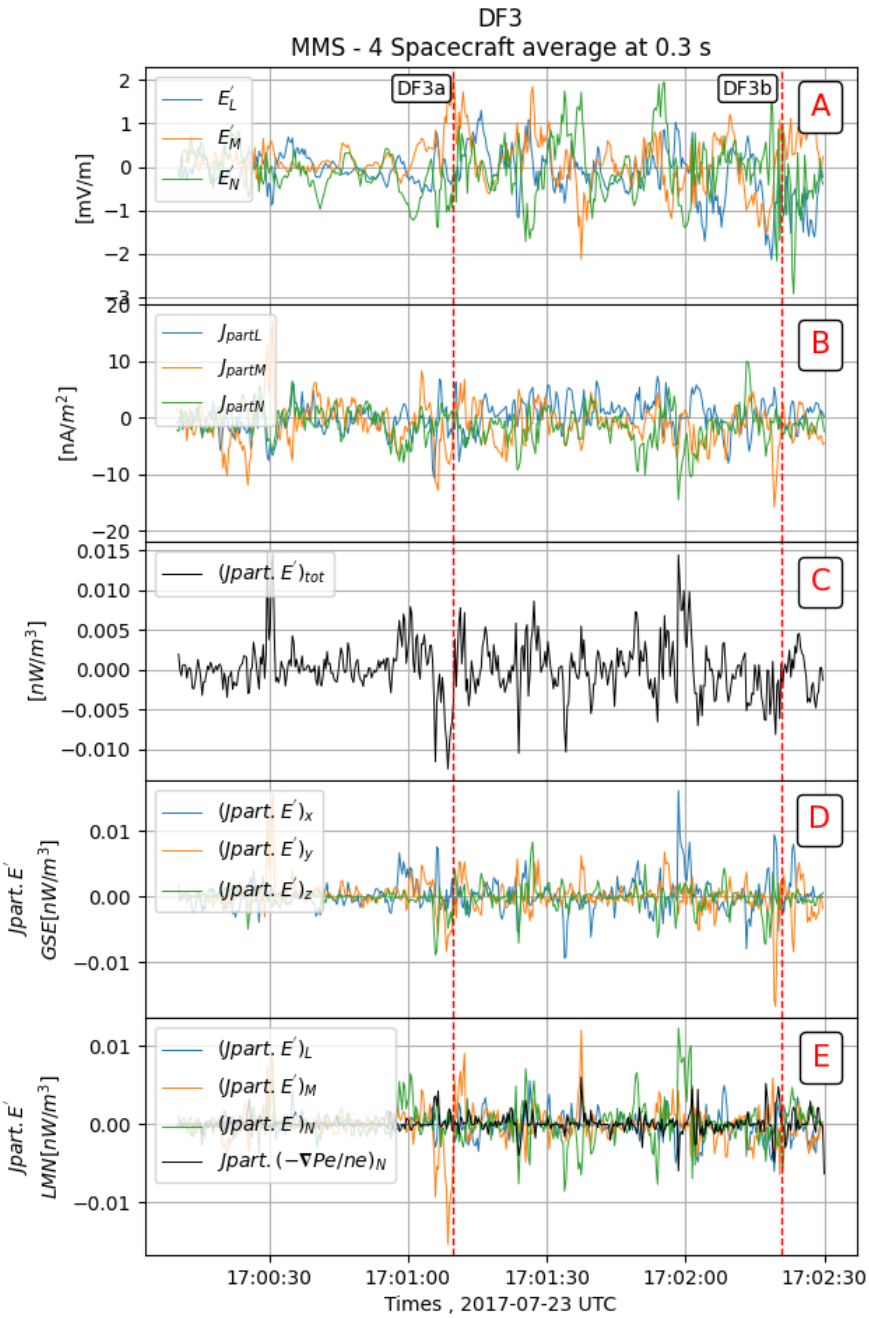

FIGURE B.20 – Same as Fig. 4.6 for DF3a,b.

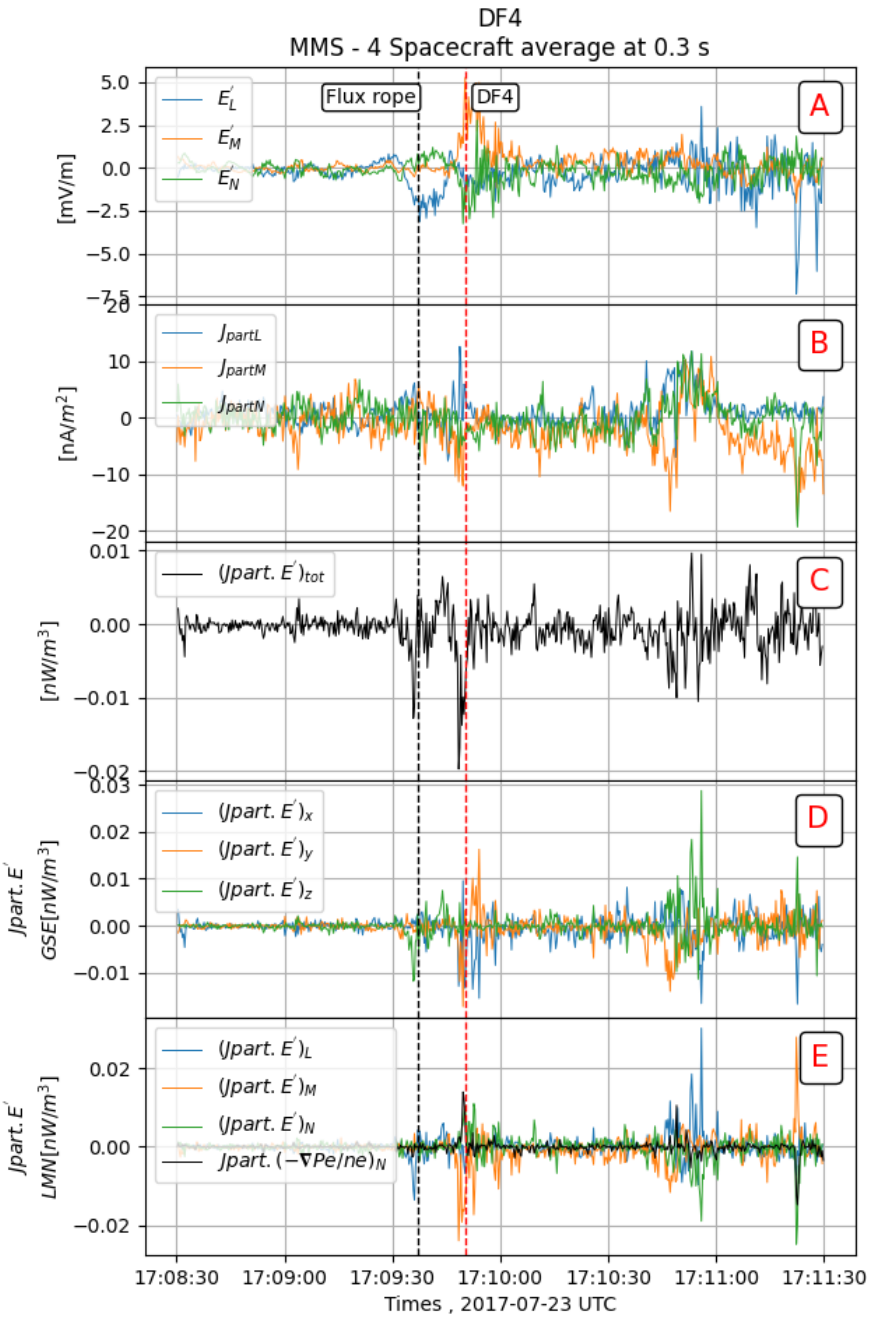

FIGURE B.21 – Same as Fig. 4.6 for DF4.

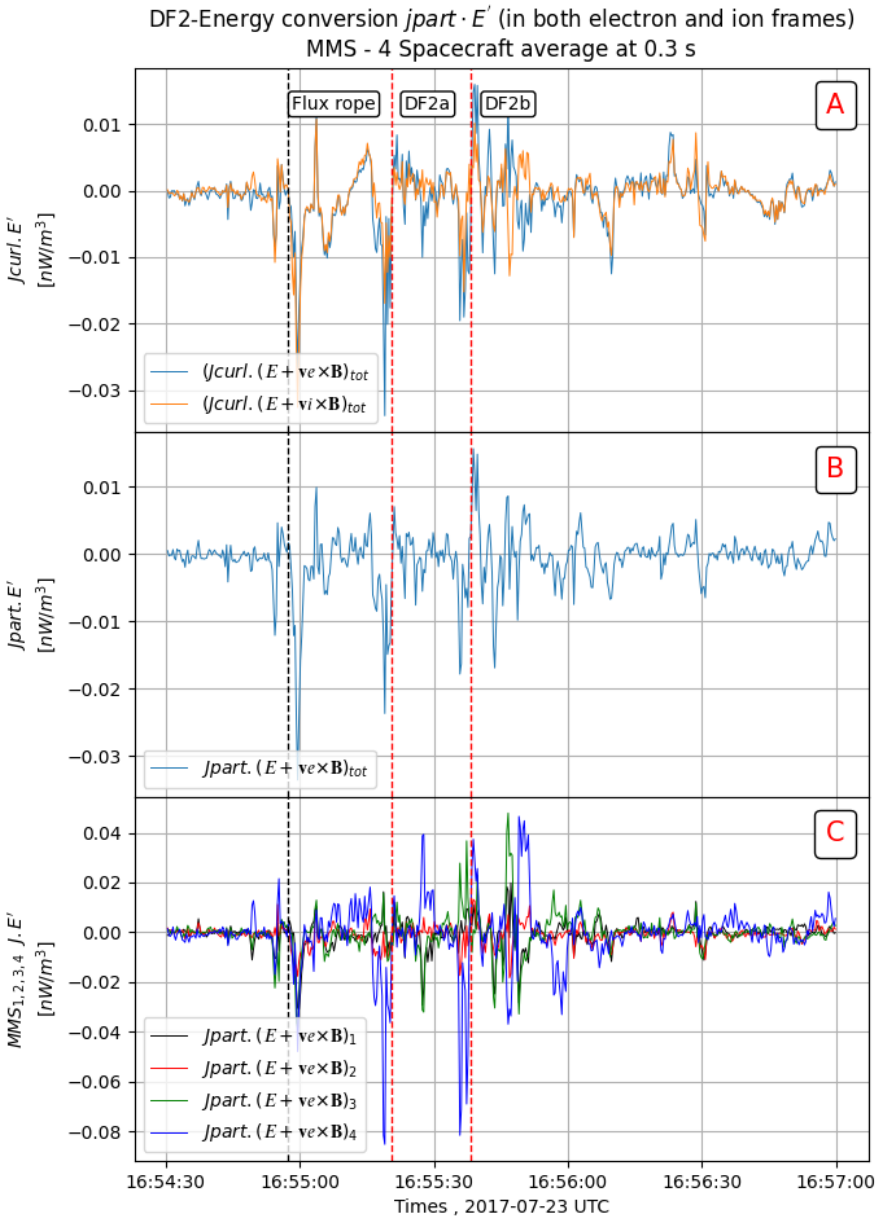

FIGURE B.22 – Same as Fig. 4.8 for DF2a,b.

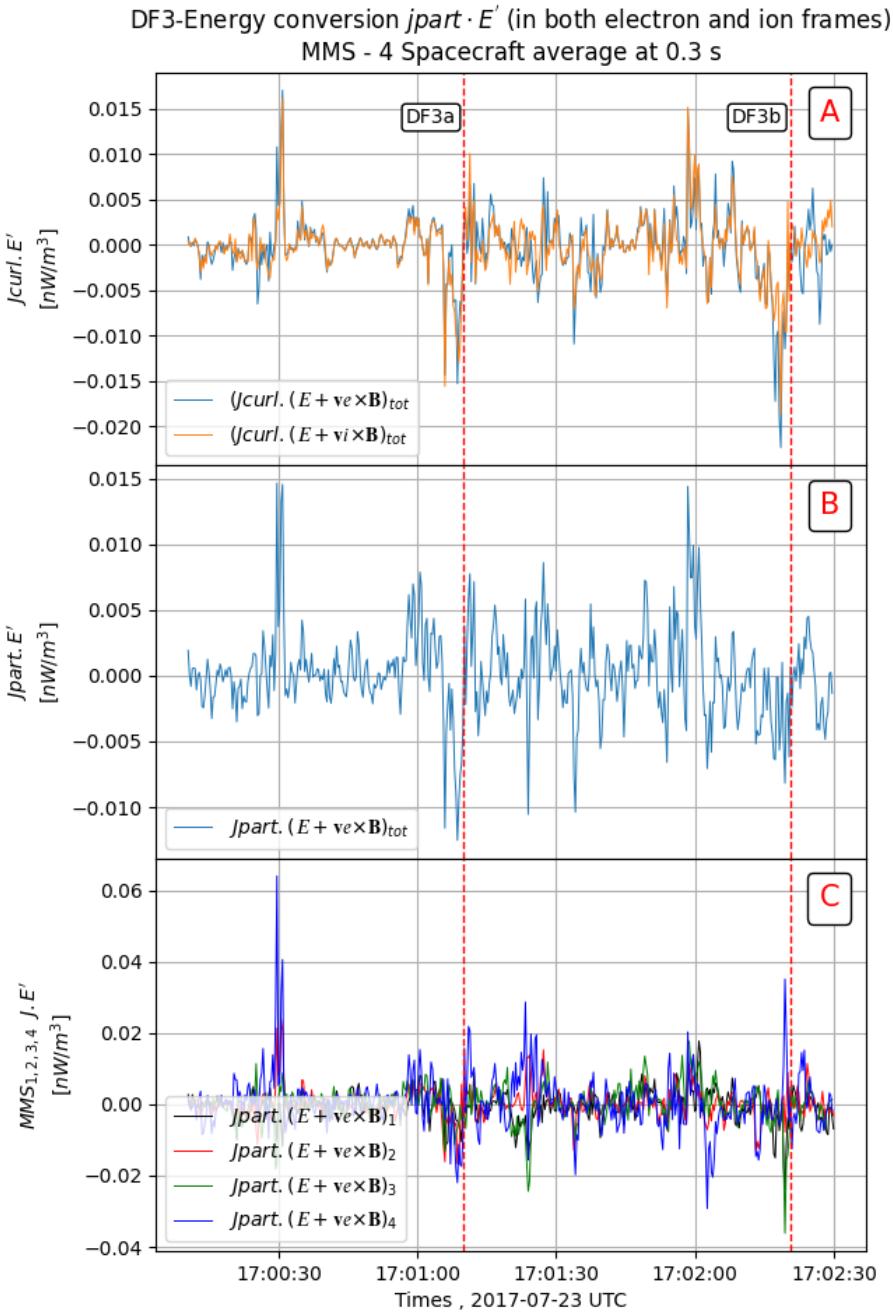

FIGURE B.23 – Same as Fig. 4.8 for DF3a,b.

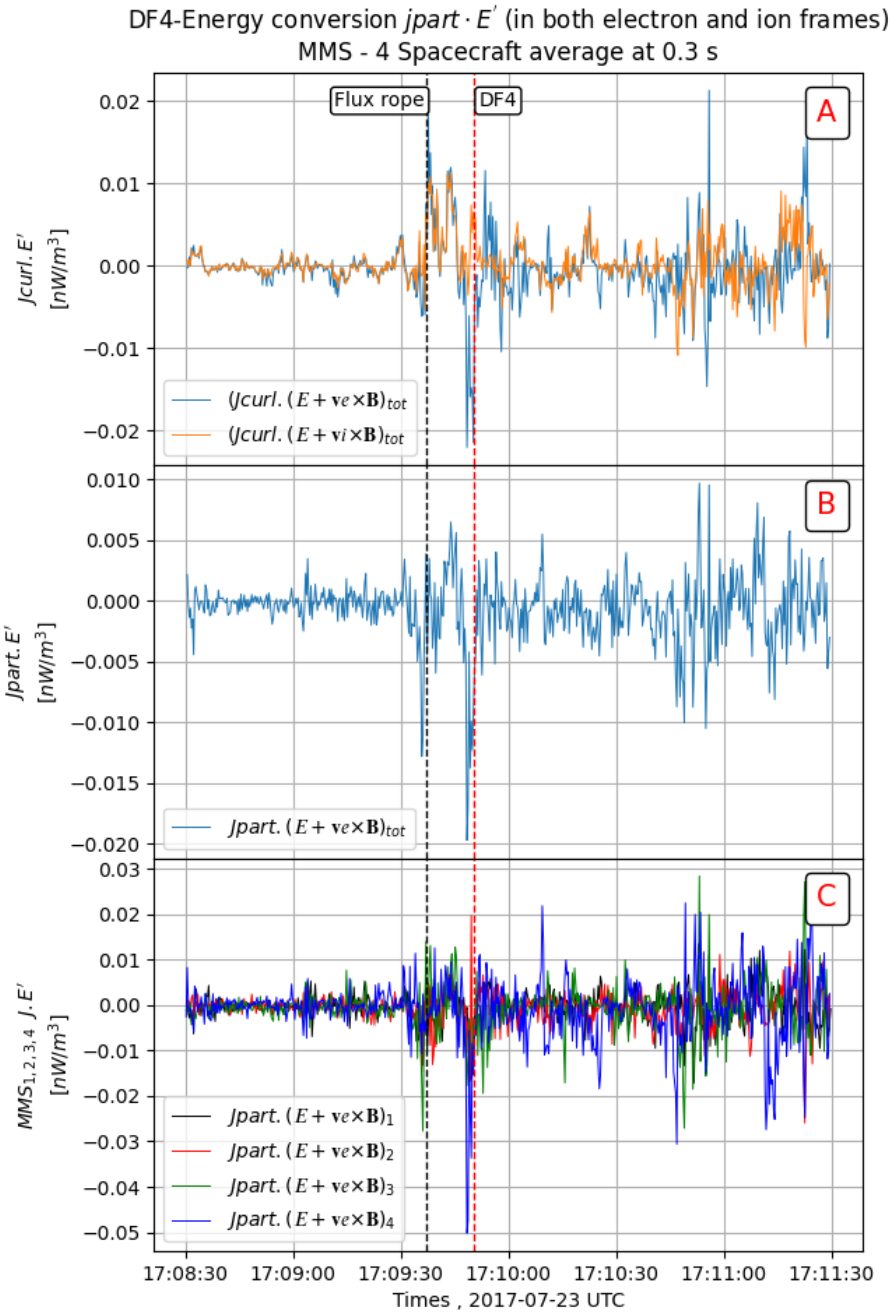

FIGURE B.24 – Same as Fig. 4.8 for DF4.

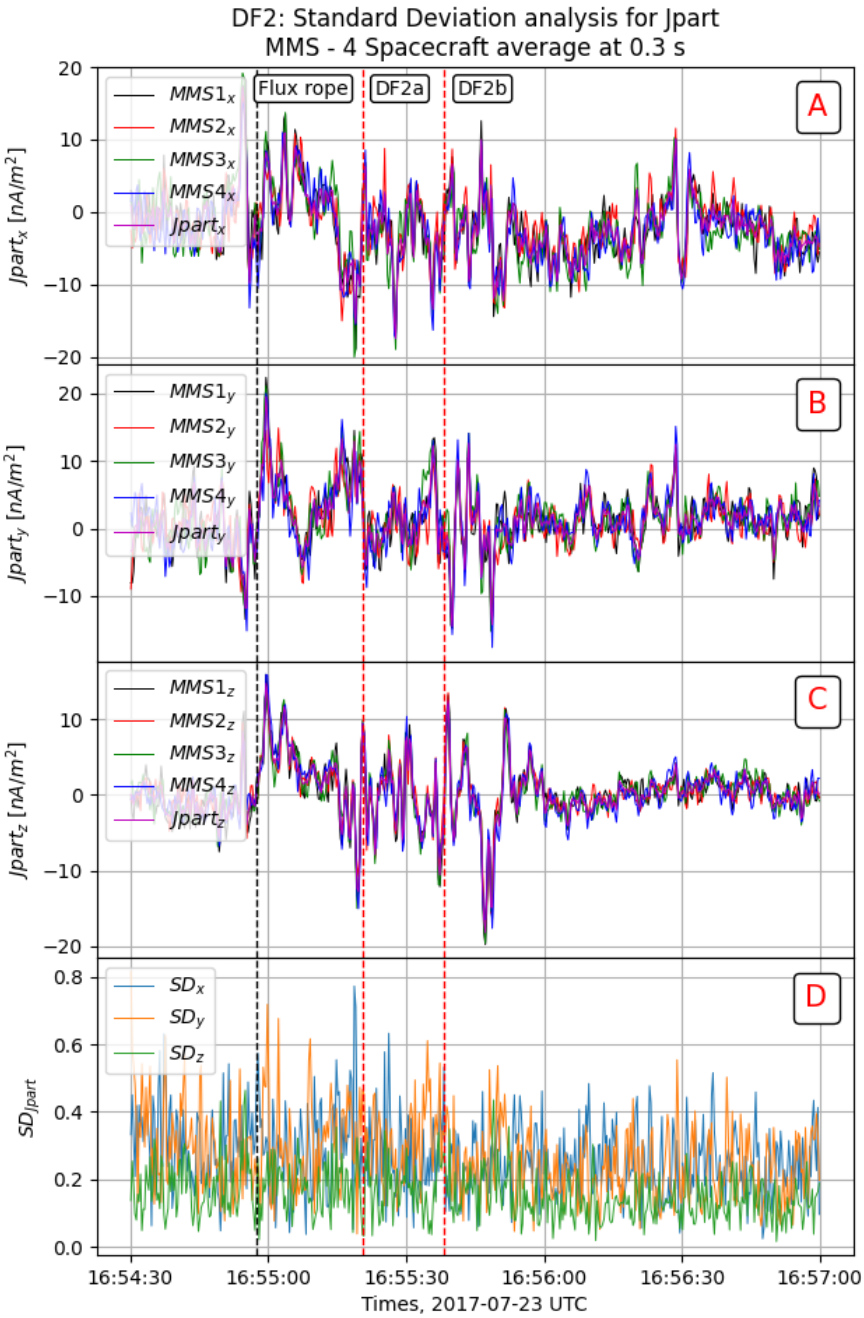

FIGURE B.25 – Same as Fig. 4.9 for DF2a,b signatures.

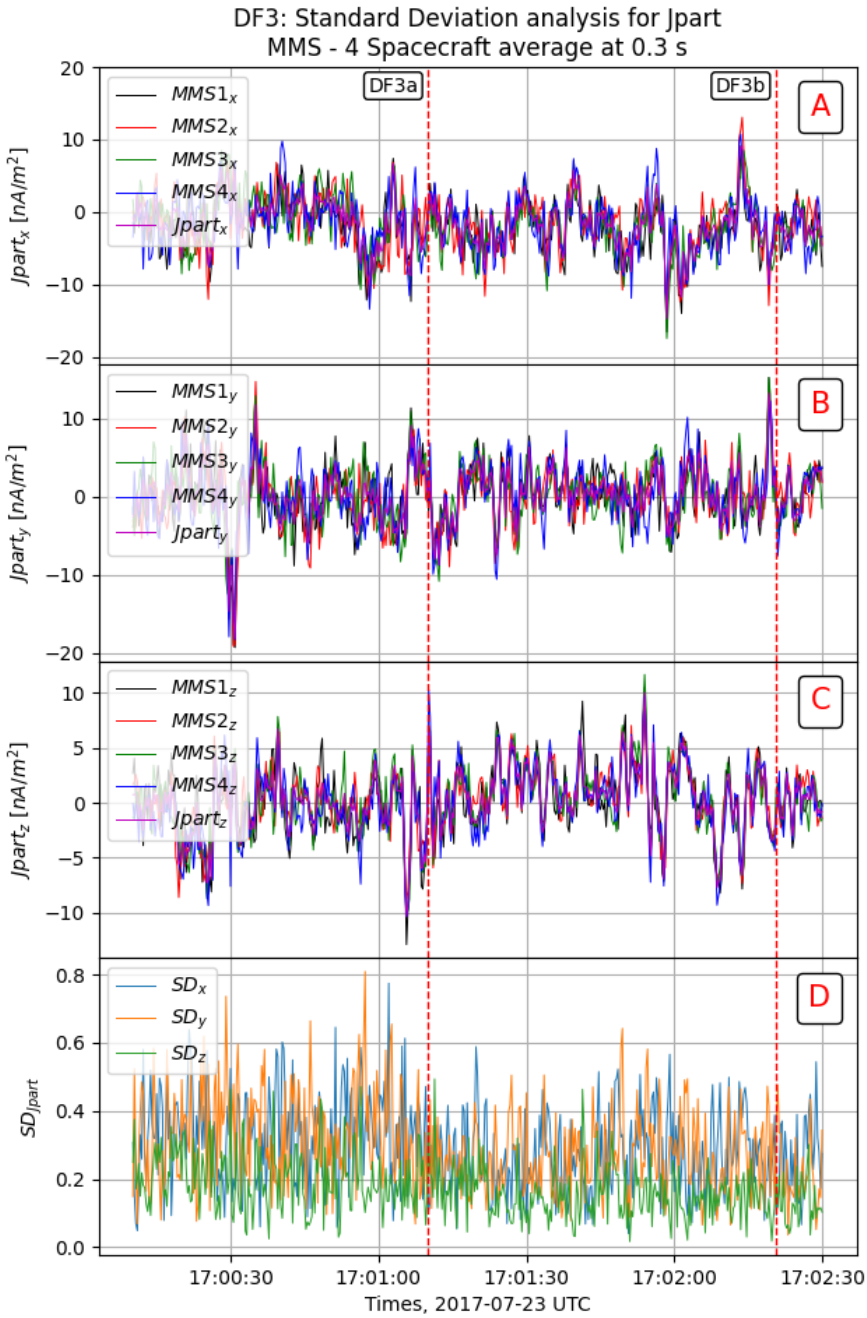

FIGURE B.26 – Same as Fig. 4.9 for DF3a,b signatures.

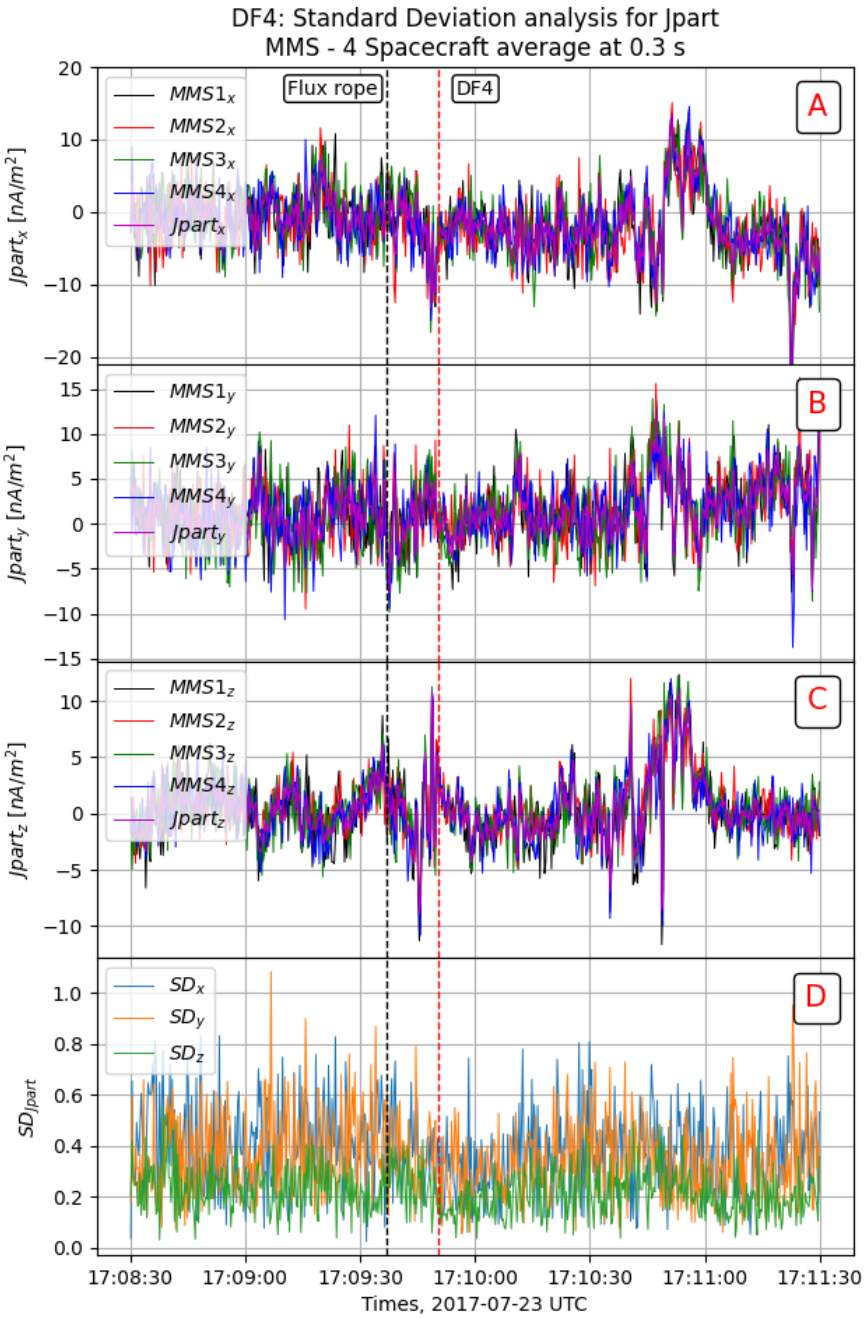

FIGURE B.27 – Same as Fig. 4.9 for DF4 signature.

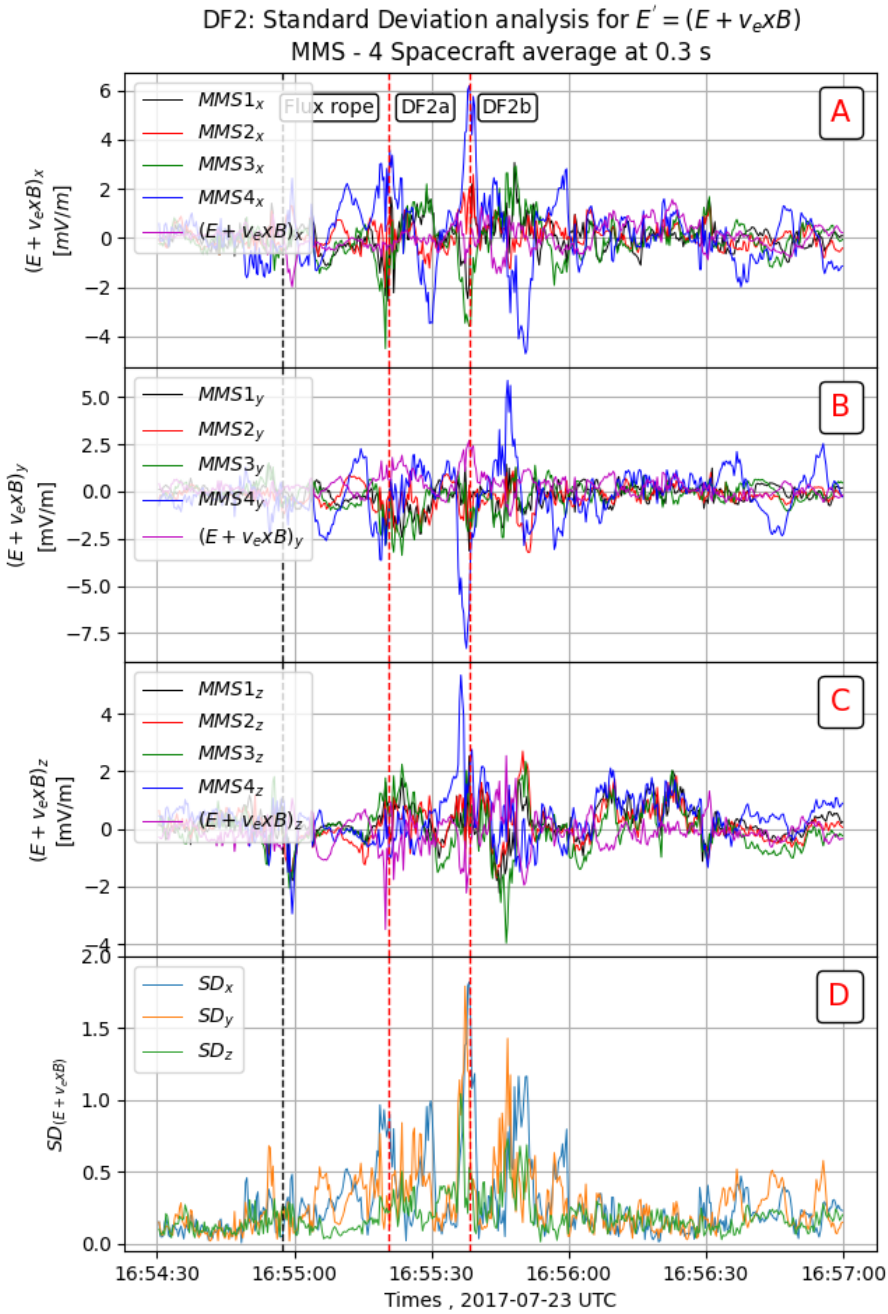

FIGURE B.28 – Same as Fig. 4.10 for DF2a,b.

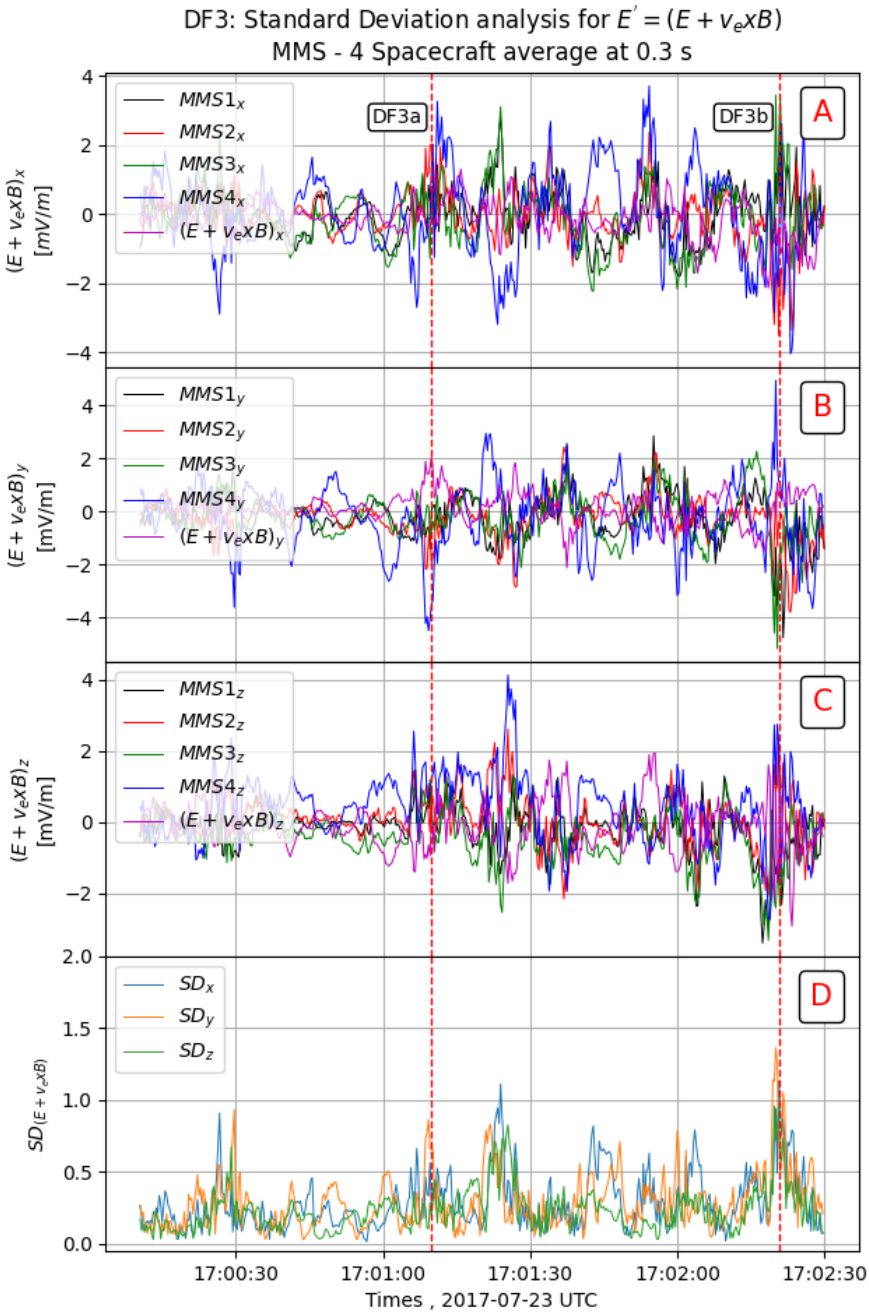

FIGURE B.29 – Same as Fig. 4.10 for DF3a,b.

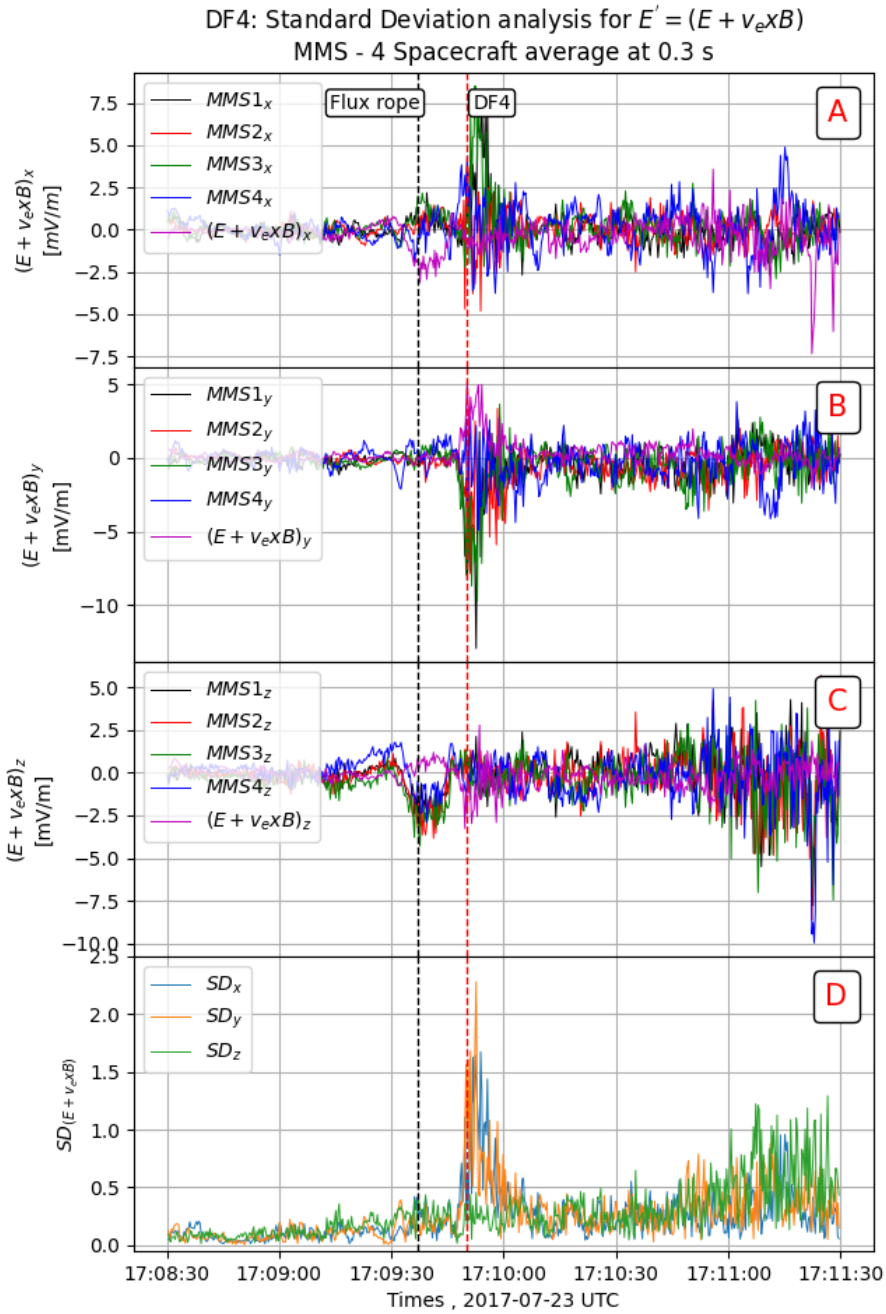

FIGURE B.30 – Same as Fig. 4.10 for DF4.

Annexe C

Supplementary materials of Chapter 5

Table C.1 – MMS located RE [GSE]

#	day	UT	R_E (X,Y,Z)	#	day	UT	R_E (X,Y,Z)
1	05-19	03 :06 :42	-10.55,-3.6,0.06	51	07-26	11 :31 :44	-23.54 , 6.85 , 5.42
2	05-19	09 :46 :58	-15.19,-9.03,1.54	52	07-28	20 :00 :06	-20.52 , 9.66 , 4.2
3	05-19	10 :00 :53	-15.3,-9.18,1.58	53	07-28	20 :10 :46	-20.59 , 9.65 , 4.22
4	05-22	08 :29 :35	-17.04 , -10.49 , 2.25	54	07-29	08 :16 :50	-23.29 , 7.55 , 5.56
5	05-28	00 :35 :14	-18.49 , -9.84 , 2.62	55	07-29	09 :22 :55	-23.32 , 7.28 , 5.63
6	05-28	00 :39 :00	-18.51 , -9.87 , 2.63	56	07-31	20 :57 :39	-21.95 , 9.91 , 5.0
7	05-28	04 :35 :40	-19.41 , -11.64 , 3.28	57	07-31	22 :33 :00	-22.3 , 9.64 , 5.17
8	05-28	04 :39 :08	-19.42 , -11.67 , 3.29	58	07-17	06 :03 :30	-16.81 , 6.89 , 2.4
9	05-28	05 :03 :00	-19.49 , -11.83 , 3.35	59	07-17	07 :52 :30	-18.13 , 6.78 , 2.78
10	05-28	05 :43 :18	-19.58 , -12.09 , 3.45	60	07-17	14 :51 :20	-21.86 , 5.9 , 4.01
11	05-28	05 :54 :14	-19.6 , -12.16 , 3.48	61	07-17	15 :40 :30	-22.18 , 5.77 , 4.14
12	05-28	06 :02 :32	-19.62 , -12.22 , 3.5	62	07-18	03 :43 :30	-24.3 , 3.23 , 5.45
13	05-28	06 :05 :13	-19.62 , -12.23 , 3.51	63	07-18	13 :03 :03	-22.88 , 0.82 , 5.78
14	05-28	06 :29 :40	-19.67 , -12.39 , 3.57	64	07-20	00 :54 :03	-16.23 , 7.61 , 2.36
15	05-28	06 :34 :02	-19.68 , -12.42 , 3.58	65	07-20	19 :15 :39	-23.94 , 5.15 , 5.19
16	05-28	06 :44 :07	-19.69 , -12.48 , 3.6	66	07-23	17 :18 :24	–23.9 , 5.57 , 5.46
17	05-28	07 :04 :30	-19.72 , -12.6 , 3.65	67	07-23	20 :44 :54	-23.86 , 4.72 , 5.68
18	05-28	14 :23 :19	-19.64 , -14.75 , 4.53	68	07-24	12 :48 :13	-18.53 , -0.05 , 5.37
19	05-28	14 :26 :48	-19.64 , -14.77 , 4.54	69	07-24	12 :54 :30	-18.47 , -0.08 , 5.35
20	05-28	15 :01 :00	-19.57 , -14.89 , 4.59	70	07-24	13 :02 :30	-18.38 , -0.12 , 5.34
21	05-28	15 :04 :00	-19.57 , -14.9 , 4.6	71	07-24	13 :07 :35	-18.32 , -0.15 , 5.33
22	05-28	15 :30 :18	-19.51 , -14.99 , 4.64	72	07-24	13 :07 :30	-18.32 , -0.15 , 5.33
23	05-28	07 :14 :30	-19.74 , -12.67 , 3.68	73	07-24	13 :09 :30	-18.3 , -0.16 , 5.33
24	05-28	14 :59 :00	-19.57 , -14.89 , 4.59	74	07-26	05 :11 :30	-22.45 , 8.09 , 4.77
25	05-28	16 :13 :40	-19.41 , -15.14 , 4.71	75	07-26	13 :40 :54	-23.65 , 6.34 , 5.57
26	06-11	17 :38 :35	-22.17 , -10.68 , 4.98	76	07-26	17 :40 :38	-23.48 , 5.31 , 5.78
27	06-19	03 :56 :26	-16.81 , -0.34 , 1.64	77	07-29	04 :36 :33	-22.93 , 8.36 , 5.26
28	08-21	13 :20 :50	-16.55 , 7.68 , 5.45	78	07-29	07 :46 :30	-23.26 , 7.67 , 5.53
29	06-24	23 :18 :06	-20.15 , -0.43 , 2.72	79	07-29	08 :35 :30	-23.3 , 7.48 , 5.58
30	06-05	14 :03 :11	-20.76 , -8.81 , 3.35	80	07-29	09 :23 :08	-23.32 , 7.28 , 5.63
31	06-11	01 :58 :23	-20.73 , -6.03 , 3.02	81	07-29	09 :48 :33	-23.33 , 7.17 , 5.66
32	06-11	17 :36 :34	-22.18 , -10.67 , 4.98	82	07-31	20 :57 :48	-21.95 , 9.91 , 4.99
33	06-14	06 :48 :18	-22.85 , -8.23 , 4.44	83	07-31	22 :33 :18	-22.3 , 9.64 , 5.17
34	06-15	02 :16 :10	-18.3 , -11.23 , 5.43	84	07-31	23 :46 :48	-22.52 , 9.41 , 5.29
35	06-16	23 :49 :21	-22.98 , -6.53 , 4.21	85	07-17	06 :03 :00	-16.81 , 6.89 , 2.4
36	06-17	00 :14 :00	-23.03 , -6.65 , 4.26	86	07-18	13 :03 :34	-22.87 , 0.82 , 5.78
37	06-17	04 :14 :17	-23.24 , -7.74 , 4.71	87	07-26	13 :30 :00	-23.64 , 6.39 , 5.56
38	06-19	03 :50 :31	-16.73 , -0.3 , 1.61	88	07-31	21 :40 :27	-22.11 , 9.79 , 5.07
39	06-19	04 :05 :24	-16.92 , -0.39 , 1.67	89	08-01	00 :48 :12	-22.67 , 9.2 , 5.38
40	06-19	05 :31 :14	-17.99 , -0.93 , 1.97	90	08-06	01 :20 :36	-16.93 , 12.27 , 3.6
41	06-19	05 :38 :17	-18.07 , -0.98 , 2.0	91	08-06	05 :34 :20	-19.01 , 12.31 , 4.3
42	06-24	23 :57 :17	-20.5 , -0.63 , 2.84	92	08-06	18 :56 :30	-22.15 , 10.37 , 5.73
43	06-25	06 :11 :39	-22.95 , -2.49 , 3.87	93	08-07	15 :56 :10	-16.17 , 2.6 , 5.01
44	07-08	21 :13 :03	-18.28 , 4.38 , 2.47	94	08-09	16 :55 :39	-21.7 , 10.6 , 5.9
45	07-11	23 :25 :23	-21.91 , 4.07 , 3.78	95	08-21	12 :58 :39	-16.72 , 7.89 , 5.49
46	07-12	11 :53 :20	-24.53 , 1.34 , 5.28	96	08-21	13 :06 :35	-16.66 , 7.82 , 5.48
47	07-18	20 :00 :42	-19.87 , -1.07 , 5.53	97	08-23	15 :37 :22	-18.63 , 15.52 , 5.98
48	07-24	12 :48 :03	-18.53 , -0.05 , 5.37	98	08-21	18 :10 :30	-13.7 , 4.58 , 4.62
49	07-24	12 :54 :43	-18.46 , -0.08 , 5.35				
50	07-24	13 :07 :04	-18.32 , -0.15 , 5.33				

Table C.2 – MMS located RE [GSE]

#	day	UT	R_E (X,Y,Z)	#	day	UT	R_E (X,Y,Z)
1	05-28	07 :09 :49	-19.73 , -12.63 , 3.66	18	07-26	04 :51 :30	-22.35 , 8.15 , 4.73
2	06-11	02 :10 :52	-20.81 , -6.11 , 3.06	19	07-26	04 :51 :30	-22.35 , 8.15 , 4.73
3	06-19	03 :53 :00	-16.76 , -0.31 , 1.62	20	07-26	04 :51 :30	-22.35 , 8.15 , 4.73
4	06-19	04 :01 :41	-16.88 , -0.37 , 1.65	21	07-26	11 :42 :30	-23.56 , 6.81 , 5.43
5	06-19	04 :00 :18	-16.86 , -0.36 , 1.65	22	07-29	10 :24 :00	-23.32 , 7.02 , 5.69
6	07-23	16 :46 :30	-23.88 , 5.69 , 5.42	23	07-29	10 :24 :00	-23.32 , 7.02 , 5.69
7	07-23	16 :54 :30	-23.88 , 5.66 , 5.43	24	07-31	23 :46 :48	-22.52 , 9.41 , 5.29
8	07-23	16 :54 :30	-23.88 , 5.66 , 5.43	25	07-31	23 :46 :48	-22.52 , 9.41 , 5.29
9	07-23	17 :00 :10	-23.89 , 5.64 , 5.44	26	07-31	23 :51 :20	-22.53 , 9.39 , 5.3
10	07-23	17 :00 :10	-23.89 , 5.64 , 5.44	27	07-31	23 :51 :20	-22.53 , 9.39 , 5.3
11	07-23	17 :08 :30	-23.9 , 5.61 , 5.45	28	07-06	09 :00 :00	-22.27 , 2.13 , 3.7
12	07-15	10 :20 :30	-24.34 , 1.67 , 5.54	29	07-06	17 :46 :07	-24.42 , 0.07 , 4.86
13	07-15	10 :38 :00	-24.31 , 1.6 , 5.55	30	07-26	07 :52 :28	-23.06 , 7.61 , 5.08
14	07-18	03 :43 :30	-24.3 , 3.23 , 5.45	31	07-26	07 :52 :28	-23.06 , 7.61 , 5.08
15	07-18	13 :10 :00	-22.84 , 0.79 , 5.78	32	07-26	11 :42 :24	-23.56 , 6.81 , 5.43
16	07-18	19 :01 :15	-20.42 , -0.8 , 5.6	33	07-06	03 :07 :41	-19.25 , 3.39 , 2.65
17	07-20	18 :23 :10	-23.82 , 5.35 , 5.1	34	07-25	22 :08 :45	-19.75 , 8.96 , 3.74

TABLE C.3 – The Minimum Variance Analysis Results For Class I (1)

#	$\frac{\lambda_M}{\lambda_N}$	$\frac{\lambda_L}{\lambda_N}$	L	M	N
1	10.7	105.7	0.6, 0.2, -0.7	0.02, 0.9, 0.3	0.8, -0.2, 0.6
2	16.7	43.2	0.08, 0.6, -0.7	-0.9, -0.09, -0.2	-0.2, 0.7, 0.66
3	2.9	17.8	0.01, 0.05, 0.9	-0.5, -0.8, 0.05	0.8, -0.5, 0.01
4	6.2	38.2	0.5, -0.2, 0.8	0.8, 0.2, -0.5	-0.06, 0.9, 0.3
5	11.3	52	0.5, 0.6, 0.7	-0.7, -0.1, 0.6	0.5, -0.8, 0.3
6	2.4	40.1	0.4, 0.3, -0.9	0.09, 0.9, 0.3	0.9, -0.2, 0.3
7	12.9	150.5	0.2, -0.5, 0.9	0.1, 0.9, 0.4	-0.9, 0.05, 0.2
8	3.9	69	0.2, 0.4, 0.9	-0.6, -0.7, 0.5	0.8, -0.6, 0.1
9	1.4	52.7	0.5, 0.2, 0.8	0.5, 0.7, -0.5	-0.6, 0.7, 0.2
10	13.7	94.9	0.5, 0.2, 0.9	0.4, 0.8, -0.4	-0.7, 0.6, 0.3
11	37.3	457	0.5, 0.3, 0.8	0.3, 0.8, -0.5	-0.8, 0.5, 0.3
12	6.2	37.4	0.3, -0.6, -0.8	0.8, -0.2, 0.5	-0.4, -0.8, 0.4
13	3.5	24.1	0.2, -0.05, 0.9	-0.5, 0.8, 0.1	-0.8, -0.5, 0.1
14	8.8	322.7	0.1, -0.6, 0.7	0.3, 0.7, 0.6	-0.9, 0.1, 0.3
15	33.9	159.9	0.2, -0.4, 0.9	0.6, 0.8, 0.2	-0.8, 0.5, 0.3
16	17.4	74.7	0.5, 0.01, -0.8	-0.2, 0.9, -0.1	0.8, 0.3, 0.5
17	5.9	32.4	0.3, 0.2, 0.9	0.1, 0.9, -0.3	-0.9, 0.2, 0.2
18	14.3	132.4	0.5, 0.03, -0.9	-0.8, 0.2, -0.5	0.2, 0.9, 0.1
19	26.8	68.8	0.2, -0.1, 0.9	0.9, 0.3, -0.2	-0.3, 0.9, 0.2
20	42.5	1143.3	0.4, 0.05, 0.9	0.05, 0.9, -0.08	-0.9, 0.08, 0.4
21	7.7	651.8	0.001,-0.6,-0.7	0.01,0.7,-0.6	0.9,-0.007,0.008
22	6.2	83.2	0.6, 0.3, 0.7	0.5, 0.42, -0.7	-0.6, 0.8, 0.05
23	7.5	151	0.02, 0.2, 0.9	-0.2, 0.9, -0.2	-0.9, -0.2, 0.07
24	10	65.3	0.4, 0.5, 0.8	-0.5, -0.5, 0.6	0.7, -0.6, 0.05
25	24.9	360.9	0.2, 0.6, 0.8	-0.2, 0.8, -0.5	-0.9, -0.008, 0.3
26	2.7	24.3	0.4, 0.5, 0.7	0.2, 0.7, -0.6	-0.9, 0.4, 0.2
27	3.2	64	0.3, -0.2, -0.9	0.2, 0.9, -0.1	0.9, -0.2, 0.3
28	254	560.5	0.05, -0.2, 0.9	0.08, 0.9, 0.2	-0.9, 0.07, 0.06
29	11.1	85.5	0.6, -0.2, -0.7	0.5, 0.8, 0.2	0.5, -0.5, 0.6
30	5.5	27.5	0.2, -0.08, 0.9	0.6, 0.7, -0.09	-0.7, 0.7, 0.2
31	35.5	6599.8	0.2, -0.3 -0.9	0.6, 0.8, -0.2	0.8, -0.5, 0.3
32	7.2	160.9	0.4, -0.4, 0.8	0.6, 0.8, 0.08	-0.7, 0.5, 0.5
33	8.1	57.5	0.6, 0.3, -0.7	0.2, 0.8, 0.5	0.8, -0.4, 0.4
34	8.2	84.6	0.2, -0.2, 0.9	0.3, 0.9, 0.1	-0.9, 0.3, 0.2
35	7.8	58.9	0.3, 0.6, -0.7	-0.8, 0.5, 0.1	0.5, 0.5, 0.6
36	56.7	613.9	0.02, -0.003,-0.9	-0.6, 0.8, -0.01	0.8, 0.6, 0.02
37	7.8	107	0.004, -0.7, -0.7	0.3, -0.67, 0.66	-0.9, -0.2, 0.2
38	4.6	22.5	0.6, -0.1, -0.8	0.1, 0.9, -0.02	0.8, -0.08, 0.6
39	1.5	93.5	0.4, -0.1, -0.9	-0.3, 0.9, -0.2	0.9, 0.3, 0.3
40	65.6	427.4	0.07, 0.19, -0.9	-0.4, 0.9, 0.15	0.9, 0.4, 0.14
41	9.1	136.5	0.05, 0.6, 0.8	-0.2, -0.8, 0.6	0.9, -0.2, 0.06
42	5.1	132.6	0.2, -0.19, 0.9	-0.2, 0.9, 0.22	-0.9, -0.2, 0.12
43	38.6	326.5	0.5, 0.008, 0.9	0.15, 0.9, -0.09	-0.9, 0.17, 0.5
44	27.1	129.8	0.3, -0.4, -0.9	0.2, 0.9, -0.3	0.9, -0.1, 0.3
45	4.8	30.8	0.1, -0.4, -0.9	0.68, 0.66, -0.2	0.7, -0.5, 0.4

Table C.4 – The Minimum Variance Analysis Results For Class I (2)

#	$\frac{\lambda_M}{\lambda_N}$	$\frac{\lambda_L}{\lambda_N}$	L	M	N
46	24.2	143.7	0.48, 0.27, 0.8	-0.29, 0.9, -0.1	-0.8, -0.17, 0.5
47	9.9	84.5	0.48, 0.41, 0.8	0.21, 0.79, -0.5	-0.84, 0.4, 0.3
48	2	7.1	0.38, 0.2, -0.9	0.4, 0.8, 0.4	0.8, -0.5, 0.2
49	10.6	41.3	0.16, 0.2, 0.9	-0.02, 0.9, -0.1	-0.9, 0.003, 0.17
50	7.5	92.3	0.2, -0.7, 0.67	0.5, 0.7, 0.5	-0.8, 0.2, 0.5
51	38.4	455.8	0.1, -0.5, 0.8	0.6, -0.6, -0.4	0.8, 0.6, 0.2
52	4	58.2	0.3, -0.2, -0.9	0.67, 0.7, 0.06	0.65, -0.63, 0.4
53	3.3	254.5	0.06, -0.07, -0.9	0.9, 0.4, 0.03	0.4, -0.9, 0.09
54	1.6	5.7	0.3, -0.65, 0.68	0.6, -0.4, -0.66	0.7, 0.6, 0.3
55	71.1	249.8	0.3, 0.3, -0.9	0.2, 0.9, 0.4	0.9, -0.3, 0.2
56	11.7	18.2	0.2 , 0.2, 0.9	-0.6, 0.8, -0.04	-0.8, -0.6, 0.2
57	6.5	52.9	0.1, -0.1, 0.9	0.9, -0.4, -0.2	0.4, 0.9, 0.1
58	15.3	22.7	0.2, -0.6, -0.7	-0.07, 0.74, -0.6	0.9, 0.2, 0.09
59	18.3	1023	0.3, 0.5, 0.8	0.09, 0.8, -0.5	-0.9, 0.2, 0.2
60	9.7	123.6	0.05, -0.2, 0.9	0.1, 0.9, 0.2	-0.9, 0.1, 0.07
61	42.3	999.1	0.3, 0.03, -0.9	0.2, 0.9, 0.08	0.9, -0.2, 0.3
62	15.2	161.1	0.5, 0.09, 0.9	-0.2, 0.9, 0.02	-0.9, -0.2, 0.5
63	8.6	1151.1	0.1, -0.002, 0.9	-0.3, 0.9, 0.04	-0.9, -0.3, 0.1
64	10.6	517.7	0.3, -0.034, 0.9	-0.7, 0.67, 0.2	-0.66, -0.73, 0.1
65	7.5	207.6	0.63, -0.4, 0.7	0.09, 0.9, 0.4	-0.8, -0.2, 0.6
66	6.9	62.6	0.2, -0.58, -0.8	0.57, 0.7, -0.4	0.8, -0.4, 0.5
67	8	190.4	0.06, 0.2, -0.9	-0.7, 0.6, 0.1	0.66, 0.70, 0.2
68	8.6	82.2	0.06, -0.09, 0.9	0.3, 0.9, 0.06	-0.9, 0.3, 0.08
69	5.9	38.3	0.2, 0.06, 0.9	0.3, 0.9, -0.1	-0.9, 0.3, 0.2
70	5.6	52.5	0.3, -0.4, 0.9	-0.2, 0.9, 0.5	-0.9, -0.3, 0.1
71	5.6	52.5	0.2, -0.4, 0.9	-0.3, 0.8, 0.5	-0.9, -0.4, 0.1
72	9.5	77.1	0.3, -0.6, 0.8	0.6, 0.7, 0.3	-0.7, 0.4, 0.6
73	14.3	163.4	0.3, 0.9, -0.3	-0.2, -0.3, -0.9	-0.94, 0.3, 0.06
74	1.6	10.2	0.004, 0.5, -0.9	-0.2, -0.9, -0.5	-0.9, 0.2, 0.1
75	52.2	410.9	0.5, 0.03, 0.9	-0.09, 0.9, 0.02	-0.9, -0.09, 0.5
76	4.9	19.7	0.1, -0.05, -0.9	0.8, 0.4, 0.09	0.5, -0.8, 0.1
77	104.4	384	0.43, -0.7, -0.6	0.7, -0.07, 0.6	-0.5, -0.7, 0.48
78	5	19.1	0.4, -0.2, 0.9	0.9, 0.04, -0.4	0.05, 0.9, 0.2
79	30.2	245.5	0.01, -0.430, 0.9	0.3, -0.85, -0.4	0.9, 0.27, 0.11
80	104.7	255.9	0.3, 0.05, -0.9	0.3, 0.9, 0.1	0.9, -0.3, 0.2
81	14.8	209.2	0.27, 0.3, -0.9	-0.7, 0.7, 0.03	0.7, 0.6, 0.4
82	3.2	16.2	0.4, -0.8, -0.3	0.26, -0.26, 0.9	-0.9, -0.5, 0.1
83	12.4	158	0.1, -0.3, 0.9	0.5, -0.8, -0.3	0.9, 0.5, 0.03
84	27.2	36	0.3, -0.9, 0.1	0.1, 0.2, 0.9	-0.9, -0.3, 0.2
85	2	56.7	0.04, -0.4, -0.9	0.2, 0.9, -0.4	0.9, -0.2, 0.1
86	6.1	76.2	0.1, -0.2, 0.9	0.008, 0.9, 0.2	-0.9, -0.01, 0.1
87	47.7	291	0.5, 0.2, -0.8	-0.03, 0.9, 0.2	0.8, -0.1, 0.5
88	2.7	25.9	0.4, -0.09, 0.9	-0.5, 0.8, 0.3	-0.8, -0.6, 0.2
89	43.8	212	0.05, 0.16, 0.9	-0.4, 0.9, -0.1	-0.9, -0.4, 0.1
90	8.4	218.5	0.08, 0.01, 0.9	-0.05, 0.9, -0.01	-0.9, -0.05, 0.08
91	12.9	122.4	0.2, 0.5, -0.8	-0.4, 0.8, 0.4	0.9, 0.2, 0.3
92	14.4	116.1	0.1, 0.1, 0.9	-0.2, 0.9, -0.1	-0.9, -0.2, 0.1
93	4.3	27.7	0.68, -0.3, 0.66	-0.1, 0.8, 0.57	-0.7, -0.5, 0.4
94	1.3	212.3	0.3, -0.5, 0.8	-0.3, 0.7, 0.6	-0.9, -0.5, 0.04
95	21.7	350.2	0.04, 0.009, 0.9	-0.3, 0.9, 0.005	-0.9, -0.3, 0.04
96	13.2	291.1	0.5, -0.06, 0.9	-0.2, 0.9, 0.2	-0.8, -0.3, 0.4
97	9.0	63.1	0.4, 0.2, -0.9	0.3, 0.9, 0.2	0.9, -0.4, 0.3
98	2	56.7	0.04, -0.4, -0.9	0.2, 0.8, -0.4	0.9, -0.2, 0.1

TABLE C.5 – The Minimum Variance Analysis Results For Class II

#	$\frac{\lambda_M}{\lambda_N}$	$\frac{\lambda_L}{\lambda_N}$	L	M	N
1	5.24	9.4	0.19,0.17,-0.96	-0.97,-0.04,-0.20	-0.07,0.98,0.15
2	2.7	24.3	0.4, 0.5,0.7	0.2, 0.7, -0.65	-0.8, 0.4, 0.2
3	4.7	856.8	0.21, 0.53, 0.81	-0.52, 0.77, -0.36	-0.82, -0.3, 0.4
4	8.8	11.9	0.48,-0.68,-0.54	-0.09,0.58,-0.80	0.87, 0.44, 0.22
5	33.6	18.7	0.14,-0.002,-0.98	-0.82,0.54,-0.12	0.54, 0.83,0.075
6	5.69	450.62	0.14,0.63,0.76	0.13,-0.78,0.62	0.98,0.01,-0.19
7	75.67	813.54	0.06,0.47,0.88	0.64,-0.70,0.33	0.77,0.54,-0.34
8	19.6	14218.5	0.08,0.72,0.69	0.60,-0.59,0.54	0.8,0.37,-0.48
9	42.25	103.88	0.01,0.59,0.81	0.61,-0.64,0.47	0.79,0.49,-0.36
10	29.62	186.86	0.6,-0.52,0.61	-0.20,-0.83,-0.52	0.78,0.19,-0.60
11	58.12	581.82	0.32,0.06,0.95	0.77,-0.61,-0.22	0.56,0.79,-0.24
12	10.1	11.9	0.05,0.86,-0.5	-0.1,-0.5,-0.8	-0.9,0.11, 0.07
13	10.1	11.9	0.05,0.86,-0.5	-0.1,-0.5,-0.8	-0.9,0.11, 0.07
14	3.3	30	0.4,-0.05,0.9	-0.16,0.97,0.12	-0.9,-0.2,0.38
15	1.8	18.1	0.01,0.34,-0.93	-0.85,0.5,0.17	0.5,0.8,0.3
16	1.8	9.9	0.01, 0.3, -0.9	-0.9, 0.5, 0.17	0.5, 0.8, 0.3
17	1.8	9.9	0.01, 0.3, -0.9	-0.9, 0.5, 0.17	0.5, 0.8, 0.3
18	8.2	21	0.15, 0.3, 0.9	-0.06, 0.9, -0.3	-0.9, -0.01, 0.2
19	8.2	21	0.15, 0.3, 0.9	-0.06, 0.9, -0.3	-0.9, -0.01, 0.2
20	8.2	21	0.15, 0.3, 0.9	-0.06, 0.9, -0.3	-0.9, -0.01, 0.2
21	6.3	136	0.2, -0.4, 0.9	0.4, 0.8, 0.3	-0.9, 0.3, 0.2
22	6.3	136	0.2, -0.4, 0.9	0.4, 0.8, 0.3	-0.9, 0.3, 0.2
23	6.3	136	0.2, -0.4, 0.9	0.4, 0.8, 0.3	-0.9, 0.3, 0.2
24	25.9	50	0.3, -0.42, 0.82	-0.17, 0.8, 0.5	-0.9, -0.32, 0.24
25	25.9	50	0.3, -0.42, 0.82	-0.17, 0.8, 0.5	-0.9, -0.32, 0.24
26	1.3	11.3	0.6, 0.2, -0.8	0.1, 0.9, 0.3	0.8, -0.2, 0.5
27	1.3	11.3	0.6, 0.2, -0.8	0.1, 0.9, 0.3	0.8, -0.2, 0.5
28	15.3	22.7	0.2, -0.6, -0.7	-0.08, 0.7, -0.6	0.9, 0.2, 0.09
29	20.5	62	0.4, 0.4, -0.8	0.3, 0.7, 0.6	0.8, -0.5, 0.1
30	62.4	596.8	0.2, 0.5, 0.8	-0.4, 0.8, -0.3	-0.9, -0.3, 0.4
31	62.4	596.8	0.2, 0.5, 0.8	-0.4, 0.8, -0.3	-0.9, -0.3, 0.4
32	254	560.5	0.05, -0.2, 0.9	0.08, 0.9, 0.17	-0.9, 0.07, 0.06
33	9.8	15.5	0.3, -0.4, 0.9	-0.4, 0.8, 0.4	-0.9, -0.5, 0.07
34	4.4	33.8	0.9, -0.4, -0.07	0.3, 0.8, -0.5	0.2, 0.4, 0.9

Table C.6 – The Timing analysis Results For Class I (1)

#	$[n_x, n_y, n_z]$	$[Vn_x, Vn_y, Vn_z]$	Vn
1	0.38 , -0.356 , -0.853	51.37 , -47.97 , -115.05	134.82
2	0.26 , -0.965 , 0.02	23.24 , -85.19 , 1.8	88.32
3	0.87 , -0.094 , 0.485	168.08 , -18.18 , 93.88	193.38
4	0.28 , -0.921 , -0.276	116.86 , -389.12 , -116.68	422.71
5	0.02 , -0.991 , 0.136	3.19 , -195.17 , 26.83	197.03
6	0.81 , -0.588 , 0.07	202.57 , -147.94 , 17.71	251.46
7	0.99 , 0.053 , -0.146	194.04 , 10.33 , -28.58	196.41
8	0.7 , -0.686 , 0.189	403.04 , -393.44 , 108.11	573.52
9	0.74 , -0.599 , -0.295	226.23 , -182.21 , -89.76	304.03
10	0.76 , -0.598 , -0.24	164.93 , -128.92 , -51.78	215.64
11	0.75 , -0.648 , -0.105	162.66 , -139.76 , -22.75	215.66
12	0.51 , 0.811 , -0.29	96.6 , 153.86 , -54.98	189.8
13	0.82 , 0.531 , -0.215	179.13 , 115.95 , -46.9	218.47
14	0.89 , -0.206 , -0.406	243.52 , -56.35 , -110.9	273.46
15	0.97 , 0.225 , 0.072	123.52 , 28.55 , 9.09	127.11
16	0.8 , 0.39 , 0.449	203.21 , 98.62 , 113.57	252.82
17	0.91 , -0.25 , -0.339	239.78 , -66.08 , -89.69	264.4
18	0.7 , 0.266 , -0.663	188.72 , 71.68 , -179.0	269.81
19	0.42 , 0.594 , -0.688	4.32 , 6.17 , -7.14	10.38
20	0.95 , -0.236 , -0.198	255.1 , -63.26 , -53.14	268.15
21	0.99 , -0.063 , 0.15	175.52 , -11.21 , 26.69	177.89
22	0.94 , -0.279 , -0.174	213.39 , -63.06 , -39.39	225.97
23	0.88 , 0.194 , 0.432	115.01 , 25.29 , 56.37	130.56
24	0.64 , -0.486 , 0.598	82.99 , -63.38 , 77.99	130.33
25	0.95 , -0.319 , -0.047	217.83 , -73.47 , -10.84	230.14
26	0.88 , 0.419 , -0.223	329.59 , 157.1 , -83.44	374.53
27	0.72 , -0.696 , 0.024	313.59 , -303.95 , 10.28	436.84
28	0.79 , 0.543 , -0.285	143.39 , 98.48 , -51.78	181.49
29	0.26 , -0.965 , 0.02	23.24 , -85.19 , 1.8	88.32
30	0.95 , -0.27 , 0.161	154.92 , -44.14 , 26.2	163.2
31	0.53 , -0.717 , 0.454	101.19 , -137.26 , 86.85	191.37
32	0.86 , -0.05 , -0.516	300.88 , -17.57 , -181.32	351.73
33	0.87 , -0.411 , -0.274	292.12 , -138.17 , -92.21	336.05
34	0.95 , -0.006 , -0.319	174.46 , -1.11 , -58.73	184.09
35	0.39 , 0.679 , 0.624	131.99 , 232.17 , 213.2	341.73
36	0.87 , -0.389 , 0.289	88.3 , -39.32 , 29.22	100.98
37	0.71 , 0.485 , -0.511	148.3 , 101.41 , -106.83	209.02
38	0.63 , -0.187 , 0.753	118.33 , -35.15 , 141.35	187.66
39	0.97 , -0.141 , 0.18	355.57 , -51.43 , 65.87	365.26
40	0.99 , 0.156 , 0.07	161.33 , 25.62 , 11.39	163.75
41	0.99 , -0.034 , 0.156	239.21 , -8.2 , 37.91	242.34
42	0.97 , 0.235 , 0.097	348.86 , 84.89 , 34.86	360.73
43	0.8 , -0.254 , -0.537	204.48 , -64.54 , -136.54	254.21
44	0.73 , -0.37 , 0.571	84.13 , -42.42 , 65.58	114.8
45	0.74 , -0.649 , -0.168	296.82 , -259.81 , -67.26	400.16

TABLE C.7 – The Timing analysis Results For Class I (2)

#	$[n_x, n_y, n_z]$	$[Vn_x, Vn_y, Vn_z]$	Vn
46	0.94 , -0.273 , 0.183	568.21 , -163.99 , 110.15	601.57
47	0.97 , -0.145 , -0.211	228.18 , -34.34 , -49.73	236.04
48	0.84 , -0.528 , -0.093	357.72 , -223.96 , -39.39	423.88
49	0.86 , 0.192 , -0.476	121.7 , 27.25 , -67.43	141.78
50	0.95 , -0.299 , -0.114	235.95 , -74.48 , -28.39	249.05
51	0.87 , 0.466 , 0.162	307.73 , 164.84 , 57.43	353.79
52	0.94 , -0.273 , -0.181	38.78 , -11.21 , -7.41	41.04
53	0.94 , -0.277 , -0.18	38.3 , -11.25 , -7.31	40.58
54	0.84 , -0.382 , 0.394	467.4 , -213.7 , 220.36	559.19
55	0.9 , -0.431 , -0.05	207.77 , -99.35 , -11.48	230.59
56	0.7 , 0.669 , -0.259	220.02 , 211.09 , -81.8	315.69
57	0.54 , 0.839 , -0.056	55.35 , 85.74 , -5.77	102.22
58	0.82 , -0.474 , 0.33	206.66 , -120.12 , 83.65	253.25
59	0.73 , -0.678 , 0.042	399.29 , -369.06 , 22.65	544.2
60	0.98 , -0.19 , -0.061	341.74 , -66.41 , -21.31	348.78
61	0.87 , -0.377 , 0.328	112.58 , -48.95 , 42.63	129.95
62	0.94 , -0.251 , -0.222	130.45 , -34.82 , -30.74	138.47
63	0.99 , 0.118 , 0.002	220.9 , 26.24 , 0.53	222.46
64	0.81 , 0.543 , -0.209	106.76 , 71.31 , -27.48	131.3
65	0.72 , 0.046 , -0.694	112.96 , 7.17 , -109.14	157.23
66	0.78 , 0.353 , 0.516	325.87 , 147.51 , 215.65	417.68
67	0.21 , 0.949 , -0.24	63.88 , 293.0 , -74.07	308.89
68	0.96 , -0.167 , -0.244	430.04 , -75.22 , -109.97	450.21
69	0.94 , -0.155 , -0.306	170.69 , -28.09 , -55.54	181.68
70	0.97 , 0.199 , -0.155	298.65 , 61.58 , -47.84	308.66
71	0.93 , -0.153 , -0.329	232.98 , -38.32 , -82.13	249.99
72	0.93 , -0.153 , -0.329	232.98 , -38.32 , -82.13	249.99
73	0.68 , -0.574 , 0.463	136.57 , -116.07 , 93.74	202.26
74	0.99 , 0.061 , -0.16	218.33 , 13.5 , -35.37	221.59
75	0.7 , 0.266 , -0.663	188.72 , 71.68 , -179.0	269.81
76	0.42, 0.594 , -0.688	4.32 , 6.17 , -7.14	10.38
77	0.3 , 0.804 , -0.511	59.35 , 157.6 , -100.15	195.94
78	0.85, -0.366 , 0.389	24.77 , -10.73 , 11.4	29.3
79	0.92 , -0.321 , -0.229	132.51 , -46.36 , -32.99	144.21
80	0.93 , -0.372 , 0.053	223.73 , -89.93 , 12.75	241.46
81	0.8 , 0.587 , 0.113	84.0 , 61.46 , 11.84	104.76
82	0.83 , 0.383 , -0.409	312.34 , 144.4 , -154.03	377.01
83	0.9 , 0.405 , 0.162	88.23 , 39.71 , 15.87	98.05
84	0.8 , 0.496 , -0.34	158.42 , 98.38 , -67.41	198.29
85	0.79 , -0.531 , 0.318	241.56 , -163.46 , 97.84	307.64
86	0.9 , 0.392 , -0.206	507.08 , 221.45 , -116.44	565.44
87	0.96, -0.291, 0.007	33.28, -10.13, 0.23	426.45
88	0.96,0.245,-0.142	357.51,91.52, -53.0	372.83
89	0.86 , 0.466 , -0.228	145.45 , 79.19 , -38.84	170.1
90	0.92 , -0.394 , 0.056	144.5 , -62.07 , 8.81	157.52
91	0.96 , 0.212 , 0.169	290.26 , 63.81 , 50.99	301.53
92	0.98 , 0.173 , -0.094	257.14 , 45.3 , -24.62	262.26
93	0.75 , -0.103 , -0.659	343.13 , -47.58 , -303.45	460.52
94	0.71 , 0.583 , 0.389	123.38 , 100.8 , 67.37	172.98
95	0.87 , 0.475 , 0.102	223.45 , 121.5 , 25.97	255.67
96	0.87 , 0.396 , -0.298	161.21 , 73.57 , -55.35	185.65
97	0.74 , -0.554 , 0.376	258.03 , -192.22 , 130.36	347.16
98	0.67 , 0.361 , -0.648	353.67 , 190.59 , -341.67	527.39

Table C.8 – The Timing analysis Results For Class II

#	$[n_x, n_y, n_z]$	$[Vn_x, Vn_y, Vn_z]$	Vn
1	0.73,0.669,0.144	123.0,112.86,24.36	168.71
2	0.97,-0.238,0.097	222.49,-54.7,22.25	230.19
3	0.14,-0.986,0.087	27.27,-192.72,16.91	195.37
4	0.95,0.22,-0.228	532.67,123.57,-128.22	561.65
5	0.86,0.302,0.416	537.49,189.28,260.74	626.67
6	0.95,0.30,-0.09	186,59,-18	196
7	0.95,0.27,-0.13	129,36,-17	135
8	0.86,0.17,-0.48	241,49,-135	281
9	0.60,0.72,-0.35	289,345, -169	481
10	0.34, 0.30,-0.89	124, 111, -327	367
11	0.54, 0.83,-0.14	251, 390, -63	468
12	0.83, -0.56 , -0.02	23.83 , -16.07 , -0.44	331.11
13	0.83,-0.56 , -0.02	23.83 , -16.07, -0.44	331.11
14	0.85 , -0.24 , 0.47	27.32 , -7.73 , 15.1	246.74
15	0.69 , -0.7 , -0.15	7.32 , -7.45 , -1.63	41.95
16	0.62 , -0.65 , -0.44	26.98 , -28.48,-19.33	164.03
17	0.47 , -0.87 , -0.17	14.56 , -26.94 , -5.36	36.72
18	0.951 , -0.167 , 0.261	5.42 , -0.95 , 1.49	451.28
19	0.951 , -0.167 , 0.261	5.42 , -0.95 , 1.49	451.28
20	0.951 , -0.167 , 0.261	5.42 , -0.95 , 1.49	451.28
21	0.94, 0.35 , 0.01	34.57 , 13.1 , 0.06	298.36
22	0.86, -0.27 , -0.44	22.66 , -7.18 , -11.64	273.7
23	0.86, -0.27 , -0.44	22.66 , -7.18 , -11.64	273.7
24	0.91, -0.39 , -0.11	6.98 , -3.02 , -0.84	195.27
25	0.91, -0.39 , -0.11	6.98 , -3.02 , -0.84	195.27
26	0.84, -0.53 , -0.13	21.52 , -13.74,-3.37	135.05
27	0.84, -0.53 , -0.13	21.52 , -13.74 , -3.37	135.05
28	0.86, 0.302 , 0.416	537.49 , 189.28 , 260.74	627
29	0.98, 0.002 , 0.197	142.15 , 0.26 , 28.63	145.01
30	0.72, 0.301 , 0.623	320.71 , 133.82 , 277.01	444
31	0.72, 0.301 , 0.623	320.71 , 133.82 , 277.01	444
32	0.935, 0.354 , 0.001	34.57 , 13.1 , 0.06	302.41
33	0.645, 0.062 , 0.762	14.84 , 1.43 , 17.52	199.46
34	0.85,0.308,-0.433	450.81 , 164.17 , -230.5	532.27

Annexe D

Publications and Communications

D.1 Publications

1. Alqeeq et al. (2022), Investigation of the homogeneity of energy conversion processes at dipolarization fronts from MMS measurements, Physics of Plasmas 29, 012906 (2022), (https://doi.org/10.1063/5.0069432).
2. Alqeeq et al., Two classes of magnetotail Dipolarization Fronts observed by Magnetospheric Multiscale Mission : A statistical overview, will be submitted to JGR, 2023.
3. Alqeeq et al., An overview of depolarization fronts (DFs) in the Earth's magnetotail, will be submitted to Space Science Reviews, 2023.

D.2 Communications

1. S. Alqeeq, et. al., Analysis of energy conversion processes at kinetic scales associated with a series of dipolarization fronts observed by MMS during a substorm, EGU General Assembly, Sharing Geoscience online, May 4-8, 2020. Oral presentation (https://www.egu2020.eu/sharing_geoscience_online/).
2. O. Le Contel, et. al., MMS/Cluster joint measurements at the vicinity of the plasma sheet boundary layer, EGU General Assembly, Sharing Geoscience online, May 4-8, 2020. Oral presentation (https://www.egu2020.eu/sharing_geoscience_online/).
3. Fall MMS SWT organized by GFSC, Online, Oct. 6 , 2020, oral presentation.
4. PLAS@PAR scientific day, Oct. 5 , 2020, Conference Center at Sorbonne Université, Poster.

5. S. Alqeeq, et. al., Energy conversion associated with a series of dipolarization fronts observed by MMS. Dec. 1-17, AGU, 2020. Poster with discussion, 2020 AGU General Assembly, Sharing Geoscience online, Virtual Poster Session SM041 (https://agu.confex.com/agu/fm20/meetingapp.cgi/Paper/722593).
6. Café Spatial, organized by LPP, May. 28th, 2021, on line, oral presentation. Alqeeq, S., O. Le Contel, P. Canu, et al., title : Homogeneity of energy conversion processes at DF.
7. S. Alqeeq et al., Investigation of the homogeneity of the energy conversion processes atdipolarization fronts observed by MMS, AGU abstract, Dec. 16, 2021, (https://agu.confex.com/agu/fm21/meetingapp.cgi/Paper/824112).
8. O. Le Contel et al., Multiscale analysis of a current sheet crossing associated with a fast earthward flow during a substorm event detected by MMS , AGU abstract, Dec. 16, 2021, (https://agu.confex.com/agu/fm21/meetingapp.cgi/Paper/822281).
9. Fall MMS SWT organized by GFSC, Online, Oct. 19-21, 2021, oral presentation.
10. PLAS@PAR scientific day, Oct. 8th, 2021, Conference Center at Sorbonne Université, Poster.
11. S. Alqeeq et al., Dissipation and acceleration at the vicinity of dipolarization fronts, CNES, JC2, Oct. 06-08 2021 (In person), Oral presentation.
12. S. Alqeeq et al., Dissipation and acceleration at the vicinity of dipolarization fronts, SF2A, June 07-11 2021 (virtual), Oral presentation.
13. S. Alqeeq et al., Investigation of the homogeneity of energy conversion processes at dipolarization fronts from MMS measurements. 5th Azarquiel School of Astronomy, Nov. 15 2021 (virtual), Oral presentation.
14. S. Alqeeq et al., A statistical study of dipolarization fronts observed by MMS, EGU abstract 18357, 2022, (https://meetingorganizer.copernicus.org/EGU22/EGU22-9532.html?pdf).
15. M. Baraka, et. al., Study of a dayside magnetopause reconnection event detected by MMS and related to a large-scale solar wind perturbation, EGU abstract 9556, 2022, (https://meetingorganizer.copernicus.org/EGU22/EGU22-9556.html?pdf).
16. O. Le Contel, et. al., Multiscale analysis of a current sheet crossing associated with a fast earthward flow during a substorm event detected by MMS, EGU abstract 9481, 2022, (https://meetingorganizer.copernicus.org/EGU22/EGU22-9481.html?pdf).
17. PhD Day, organized by LPP, Mar. 15th, 2022, in person, Oral presentation.

18. Elbereth conference, organized by PhD students, Mar. 22th, 2022, in person, Oral presentation.
19. S. Alqeeq et al., Investigation of the homogeneity of energy conversion processes at dipolarization fronts from MMS measurements. 3rd Smilei user training workshop, Mar 09-11, 2022 (In person), Oral presentation.
20. S. Alqeeq et al., A statistical study of dipolarization fronts observed by MMS. Conseil Scientifique du LPP, Mar 11 2022, (In person), Poster with discussion.
21. S. Alqeeq et al., A statistical study of dipolarization fronts observed by MMS. PNST 2022, (In person), Oral presentation (https://pnst-2022.sciencesconf.org/392260).
22. O. Le Contel, et. al., Analyse multi-échelle d'une couche de courant associée à un écoulement rapide pendant un sous-orage détecté par MMS, PNST 2022, (In person), Poster (https://pnst-2022.sciencesconf.org/399950).
23. M. Baraka, et. al., Study of a dayside magnetopause reconnection event detected by MMS and related to a large-scale solar wind perturbation, PNST 2022, (In person), Oral presentation (https://pnst-2022.sciencesconf.org/391901).
24. O. Le Contel, et. al., Multiscale analysis of a current sheet crossing embedded in a fast earthward flow during a substorm, the 8th MMS Workshop 2022, (virtual), Oral presentation. (https://commons.erau.edu/mms-conference/2022/wednesday/12/).
25. M. Baraka, et. al., Study of a dayside magnetopause reconnection event detected by MMS and related to a large-scale solar wind perturbation, the 8th MMS Workshop 2022, (virtual), Oral presentation (https://commons.erau.edu/mms-conference/2022/thursday/17/).
26. S. Alqeeq, et. al., A statistical study of dipolarization fronts observed by MMS, the 8th MMS Workshop 2022, (virtual), Oral presentation (https://commons.erau.edu/mms-conference/2022/thursday/19/).

D.3 Collaboration

1. Cosuperviser for a Master 2 student in Gaza with O. Le Contel, since September 2020.
2. Participate with other PhD students investigations with O. Le Contel 2021,2022.
3. Participate with O. Le Contel in pyspedas training session at the 5th edition of the School of Space Weather ISWI – MAGHREB – WEST AFRICA, (IMAO 2022).

Bibliography

A. F. Nagy, M. Blanc, C. R. Chappell, and N. Krupp. *Plasma Sources of Solar System Magnetospheres*, volume 52. 2016.

S. S. Board et al. *Understanding the Sun and Solar System Plasmas : Future Directions in Solar and Space Physics*. National Academies Press, 2004.

H. S. Fu, Y. V. Khotyaintsev, A. Vaivads, M. André, and S. Y. Huang. Electric structure of dipolarization front at sub-proton scale, *Geophys. Res. Lett.*, 39: L06105, March 2012a.

S. Y. Huang, H. S. Fu, Z. G. Yuan, M. Zhou, S. Fu, X. H. Deng, W. J. Sun, Y. Pang, D. D. Wang, H. M. Li, H. M. Li, and X. D. Yu. Electromagnetic energy conversion at dipolarization fronts : Multispacecraft results, *Journal of Geophysical Research (Space Physics)*, 120(6):4496–4502, June 2015.

H. Fu, E. E. Grigorenko, C. Gabrielse, C. Liu, S. Lu, K. J. Hwang, X. Zhou, Z. Wang, and F. Chen. Magnetotail dipolarization fronts and particle acceleration : A review, *Science China Earth Sciences*, 63(2):235–256, February 2020.

Y. Xu, H. S. Fu, C. M. Liu, and T. Y. Wang. Electron Acceleration by Dipolarization Fronts and Magnetic Reconnection : A Quantitative Comparison, , 853 (1):11, January 2018.

S.-I. Ohtani and T. Tamao. Does the ballooning instability trigger substorms in the near-Earth magnetotail ?, , 98(A11):19,369–19,379, November 1993.

M. Hamrin, O. Marghitu, P. Norqvist, S. Buchert, M. André, B. Klecker, L. M. Kistler, and I. Dandouras. Energy conversion regions as observed by Cluster in the plasma sheet, *Journal of Geophysical Research (Space Physics)*, 116:A00K08, July 2011.

W. J. Sun, S. Y. Fu, G. K. Parks, J. Liu, Z. H. Yao, Q. Q. Shi, Q. G. Zong, S. Y. Huang, Z. Y. Pu, and T. Xiao. Field-aligned currents associated with dipolarization fronts, , 40(17):4503–4508, September 2013.

C. R. Tooley, R. K. Black, B. P. Robertson, J. M. Stone, S. E. Pope, and G. T. Davis. The Magnetospheric Multiscale Constellation, , 199(1-4):23–76, March 2016.

J. L. Burch, T. E. Moore, R. B. Torbert, and B. L. Giles. Magnetospheric Multiscale Overview and Science Objectives, *Space Sci. Rev.*, May 2015.

C. T. Russell, B. J. Anderson, W. Baumjohann, K. R. Bromund, D. Dearborn, D. Fischer, G. Le, H. K. Leinweber, D. Leneman, W. Magnes, J. D. Means, M. B. Moldwin, R. Nakamura, D. Pierce, F. Plaschke, K. M. Rowe, J. A. Slavin, R. J. Strangeway, R. Torbert, C. Hagen, I. Jernej, A. Valavanoglou, and I. Richter. The Magnetospheric Multiscale Magnetometers, *Space Sci. Rev.*, 199:189–256, March 2016.

C. Pollock, T. Moore, A. Jacques, J. Burch, U. Gliese, Y. Saito, T. Omoto, L. Avanov, A. Barrie, V. Coffey, J. Dorelli, D. Gershman, B. Giles, T. Rosnack, C. Salo, S. Yokota, M. Adrian, C. Aoustin, C. Auletti, S. Aung, V. Bigio, N. Cao, M. Chandler, D. Chornay, K. Christian, G. Clark, G. Collinson, T. Corris, A. De Los Santos, R. Devlin, T. Diaz, T. Dickerson, C. Dickson, A. Diekmann, F. Diggs, C. Duncan, A. Figueroa-Vinas, C. Firman, M. Freeman, N. Galassi, K. Garcia, G. Goodhart, D. Guererro, J. Hageman, J. Hanley, E. Hemminger, M. Holland, M. Hutchins, T. James, W. Jones, S. Kreisler, J. Kujawski, V. Lavu, J. Lobell, E. LeCompte, A. Lukemire, E. MacDonald, A. Mariano, T. Mukai, K. Narayanan, Q. Nguyan, M. Onizuka, W. Paterson, S. Persyn, B. Piepgrass, F. Cheney, A. Rager, T. Raghuram, A. Ramil, L. Reichenthal, H. Rodriguez, J. Rouzaud, A. Rucker, Y. Saito, M. Samara, J. A. Sauvaud, D. Schuster, M. Shappirio, K. Shelton, D. Sher, D. Smith, K. Smith, S. Smith, D. Steinfeld, R. Szymkiewicz, K. Tanimoto, J. Taylor, C. Tucker, K. Tull, A. Uhl, J. Vloet, P. Walpole, S. Weidner, D. White, G. Winkert, P. S. Yeh, and M. Zeuch. Fast Plasma Investigation for Magnetospheric Multiscale, , 199(1-4):331–406, March 2016.

D. T. Young, J. L. Burch, R. G. Gomez, A. De Los Santos, G. P. Miller, P. Wilson, N. Paschalidis, S. A. Fuselier, K. Pickens, E. Hertzberg, C. J. Pollock, J. Scherrer, P. B. Wood, E. T. Donald, D. Aaron, J. Furman, D. George, R. S. Gurnee, R. S. Hourani, A. Jacques, T. Johnson, T. Orr, K. S. Pan, S. Persyn, S. Pope, J. Roberts, M. R. Stokes, K. J. Trattner, and J. M. Webster. Hot Plasma Composition Analyzer for the Magnetospheric Multiscale Mission, *Space Science Rev.*, 199:407–470, March 2016.

J. L. Burch, R. B. Torbert, T. D. Phan, L.-J. Chen, T. E. Moore, R. D. Ergun, J. P. Eastwood, D. J. Gershman, P. A. Cassak, M. R. Argall, S. Wang, M. Hesse, C. J. Pollock, B. L. Giles, R. Nakamura, B. H. Mauk, S. A. Fuselier, C. T. Russell, R. J. Strangeway, J. F. Drake, M. A. Shay, Y. V. Khotyaintsev, G. Lindqvist, P.-A.and Marklund, F. D. Wilder, D. T. Young, K. Torkar, J. Goldstein, J. C. Dorelli, L. A. Avanov, M. Oka, D. N. Baker, A. N. Jaynes, K. A. Goodrich, I. J.

Cohen, D. L. Turner, J. F. Fennell, J. B. Blake, J. Clemmons, M. Goldman, D. Newman, S. M. Petrinec, K. J. Trattner, B. Lavraud, P. H. Reiff, W. Baumjohann, W. Magnes, M. Steller, W. Lewis, Y. Saito, V. Coffey, and M. Chandler. Electron-Scale Measurements of Magnetic Reconnection in Space, *Science*, 2016.

W. Baumjohann, M. Hesse, S. Kokubun, T. Mukai, T. Nagai, and A. A. Petrukovich. Substorm dipolarization and recovery, , 104(A11):24995–25000, November 1999.

M. S. P. Williamson, M. F. Bonadonna, and M. R. Babcock. The national space weather program*Document No. FCM-P30-2010, Washington, DC*, 2010.

W. Baumjohann, G. Paschmann, and H. Luehr. Characteristics of high-speed ion flows in the plasma sheet, , 95(A4):3801–3809, April 1990.

V. Angelopoulos, W. Baumjohann, C. F. Kennel, F. V. Coronti, M. G. Kivelson, R. Pellat, R. J. Walker, H. Luehr, and G. Paschmann. Bursty Bulk Flows in the Inner Central Plasma Sheet, , 97(A4):4027–4039, April 1992.

A. T. Y. Lui. Current controversies in magnetospheric physics, *Reviews of Geophysics*, 39(4):535–563, November 2001.

V. Angelopoulos, J. P. McFadden, D. Larson, C. W. Carlson, S. B. Mende, H. Frey, T. Phan, D. G. Sibeck, K.-H. Glassmeier, U. Auster, E. Donovan, I. R. Mann, I. J. Rae, C. T. Russell, A. Runov, X.-Z. Zhou, and L. Kepko. Tail Reconnection Triggering Substorm Onset, *Science*, 321(5891):931, August 2008.

W. W. Liu, J. Liang, E. F. Donovan, and E. Spanswick. If substorm onset triggers tail reconnection, what triggers substorm onset ?, *Journal of Geophysical Research (Space Physics)*, 117(A11):A11220, November 2012.

M. Sitnov, J. Birn, B. Ferdousi, E. Gordeev, Y. Khotyaintsev, V. Merkin, T. Motoba, A. Otto, E. Panov, P. Pritchett, F. Pucci, J. Raeder, A. Runov, V. Sergeev, M. Velli, and X. Zhou. Explosive Magnetotail Activity, , 215(4):31, June 2019.

R. M. Dewey, J. A. Slavin, and J. M. Raines. MESSENGER observations of dipolarizations in Mercury's magnetotail. In *AGU Fall Meeting Abstracts*, volume 2018, pages SM42A–05, December 2018.

A. Runov, V. Angelopoulos, M. I. Sitnov, V. A. Sergeev, J. Bonnell, J. P. McFadden, D. Larson, K.-H. Glassmeier, and U. Auster. THEMIS observations of an earthward-propagating dipolarization front, *Geophys. Res. Lett.*, 36:L14106, July 2009.

V. Sergeev, V. Angelopoulos, S. Apatenkov, J. Bonnell, R. Ergun, R. Nakamura, J. McFadden, D. Larson, and A. Runov. Kinetic structure of the sharp injection/dipolarization front in the flow-braking region, , 36(21):L21105, November 2009.

S. B. Xu, S. Y. Huang, Z. G. Yuan, X. H. Deng, K. Jiang, Y. Y. Wei, J. Zhang, Z. H. Zhang, Q. Y. Xiong, L. Yu, R. T. Lin, and J. H. Waite. Global Spatial Distribution of Dipolarization Fronts in the Saturn's Magnetosphere : Cassini Observations, , 48(17):e92701, September 2021.

A. W. Smith, C. M. Jackman, M. F. Thomsen, N. Sergis, D. G. Mitchell, and E. Roussos. Dipolarization Fronts With Associated Energized Electrons in Saturn's Magnetotail, *Journal of Geophysical Research (Space Physics)*, 123(4): 2714–2735, April 2018.

A. V. Artemyev, S. Kasahara, A. Y. Ukhorskiy, and M. Fujimoto. Acceleration of ions in the Jupiter magnetotail : Particle resonant interaction with dipolarization fronts, , 82:134–148, July 2013.

A. V. Artemyev, G. Clark, B. Mauk, M. F. Vogt, and X. J. Zhang. Juno Observations of Heavy Ion Energization During Transient Dipolarizations in Jupiter Magnetotail, *Journal of Geophysical Research (Space Physics)*, 125(5):e27933, May 2020.

V. Angelopoulos, A. Runov, X. Z. Zhou, D. L. Turner, S. A. Kiehas, S. S. Li, and I. Shinohara. Electromagnetic Energy Conversion at Reconnection Fronts, *Science*, 341(6153):1478–1482, September 2013.

C. Escoubet and M. Goldstein. The Cluster Mission. In *AGU Fall Meeting Abstracts*, volume 2001, pages SM11D–01, December 2001.

R. Nakamura, A. Retinò, W. Baumjohann, M. Volwerk, N. Erkaev, B. Klecker, E. A. Lucek, I. Dandouras, M. André, and Y. Khotyaintsev. Evolution of dipolarization in the near-Earth current sheet induced by Earthward rapid flux transport, *Annales Geophysicae*, 27(4):1743–1754, April 2009.

M. I. Sitnov and M. Swisdak. Onset of collisionless magnetic reconnection in two-dimensional current sheets and formation of dipolarization fronts, *Journal of Geophysical Research (Space Physics)*, 116(A12):A12216, December 2011.

J. Liu, V. Angelopoulos, A. Runov, and X.-Z. Zhou. On the current sheets surrounding dipolarizing flux bundles in the magnetotail : The case for wedgelets, *Journal of Geophysical Research (Space Physics)*, 118:2000–2020, May 2013.

K. J. Hwang, M. L. Goldstein, T. E. Moore, B. M. Walsh, D. G. Baishev, A. V. Moiseyev, B. M. Shevtsov, and K. Yumoto. A tailward moving current sheet normal magnetic field front followed by an earthward moving dipolarization front, *Journal of Geophysical Research (Space Physics)*, 119(7):5316–5327, July 2014.

D. Schmid, R. Nakamura, F. Plaschke, M. Volwerk, and W. Baumjohann. Two states of magnetotail dipolarization fronts : A statistical study, *Journal of Geophysical Research (Space Physics)*, 120(2):1096–1108, February 2015.

M. Hosner, R. Nakamura, T. K. M. Nakamura, D. Schmid, E. V. Panov, and F. Plaschke. Statistical investigation of electric field fluctuations around the lower-hybrid frequency range at dipolarization fronts in the near-earth magnetotail, *Physics of Plasmas*, 29(1):012111, January 2022.

H. Breuillard, O. Le Contel, A. Retino, A. Chasapis, T. Chust, L. Mirioni, D. B. Graham, F. D. Wilder, I. Cohen, A. Vaivads, Y. V. Khotyaintsev, P.-A. Lindqvist, G. T. Marklund, J. L. Burch, R. B. Torbert, R. E. Ergun, K. A. Goodrich, J. Macri, J. Needell, M. Chutter, D. Rau, I. Dors, C. T. Russell, W. Magnes, R. J. Strangeway, K. R. Bromund, F. Plaschke, D. Fischer, H. K. Leinweber, B. J. Anderson, G. Le, J. A. Slavin, E. L. Kepko, W. Baumjohann, B. Mauk, S. A. Fuselier, and R. Nakamura. Multispacecraft analysis of dipolarization fronts and associated whistler wave emissions using MMS data, *Geophys. Res. Lett.*, 43:7279–7286, July 2016.

O. Le Contel, R. Nakamura, H. Breuillard, M. R. Argall, D. B. Graham, D. Fischer, A. Retinò, M. Berthomier, R. Pottelette, L. Mirioni, T. Chust, F. D. Wilder, D. J. Gershman, A. Varsani, P. A. Lindqvist, Y. V. Khotyaintsev, C. Norgren, R. E. Ergun, K. A. Goodrich, J. L. Burch, R. B. Torbert, J. Needell, M. Chutter, D. Rau, I. Dors, C. T. Russell, W. Magnes, R. J. Strangeway, K. R. Bromund, H. Y. Wei, F. Plaschke, B. J. Anderson, G. Le, T. E. Moore, B. L. Giles, W. R. Paterson, C. J. Pollock, J. C. Dorelli, L. A. Avanov, Y. Saito, B. Lavraud, S. A. Fuselier, B. H. Mauk, I. J. Cohen, D. L. Turner, J. F. Fennell, T. Leonard, and A. N. Jaynes. Lower Hybrid Drift Waves and Electromagnetic Electron Space-Phase Holes Associated With Dipolarization Fronts and Field-Aligned Currents Observed by the Magnetospheric Multiscale Mission During a Substorm, *Journal of Geophysical Research (Space Physics)*, 122(12):12,236–12,257, December 2017.

M. G. Kivelson, C. T. Russell, and S. W. H. Cowley. Book-Review - Introduction to Space Physics*The Observatory*, 115 :353, December 1995.

L. Biermann. Kometenschweife und solare Korpuskularstrahlung, 29 :274, January 1951.

E. N. Parker. Dynamics of the Interplanetary Gas and Magnetic Fields., , 128:664, November 1958.

A. H. Gabriel, F. Bely-Dubau, and P. Lemaire. The Contribution of Polar Plumes to the Fast Solar Wind, , 589(1):623–634, May 2003.

T. Ohmi, M. Kojima, M. Tokumaru, K. Fujiki, and K. Hakamada. Origin of the slow solar wind, *Advances in Space Research*, 33(5):689–695, January 2004.

J. A. Slavin, R. C. Elphic, C. T. Russell, J. H. Wolfe, and D. S. Intriligator. Position and shape of the Venus bow shock : Pioneer Venus Orbiter observations, , 6(11): 901–904, November 1979.

K. Shiokawa, W. Baumjohann, and G. Haerendel. Braking of high-speed flows in the near-Earth tail, , 24(10):1179–1182, January 1997.

K. Shiokawa, W. Baumjohann, G. Haerendel, G. Paschmann, J. F. Fennell, E. Friis-Christensen, H. Lühr, G. D. Reeves, C. T. Russell, P. R. Sutcliffe, and K. Takahashi. High-speed ion flow, substorm current wedge, and multiple Pi 2 pulsations, , 103(A3):4491–4508, March 1998.

M. I. Sitnov, M. Swisdak, and A. V. Divin. Dipolarization fronts as a signature of transient reconnection in the magnetotail, *Journal of Geophysical Research (Space Physics)*, 114(A4):A04202, April 2009.

J. F. Drake, M. Swisdak, P. A. Cassak, and T. D. Phan. On the 3-D structure and dissipation of reconnection-driven flow bursts, , 41(11):3710–3716, June 2014.

H. S. Fu, J. B. Cao, Y. V. Khotyaintsev, M. I. Sitnov, A. Runov, S. Y. Fu, M. Hamrin, M. André, A. Retinò, Y. D. Ma, H. Y. Lu, X. H. Wei, and S. Y. Huang. Dipolarization fronts as a consequence of transient reconnection : In situ evidence, , 40(23):6023–6027, December 2013.

P. L. Pritchett and F. V. Coroniti. A kinetic ballooning/interchange instability in the magnetotail, *Journal of Geophysical Research (Space Physics)*, 115(A6): A06301, June 2010.

J. Pontius, D. H. and R. A. Wolf. Transient flux tubes in the terrestrial magnetosphere, , 17(1):49–52, January 1990.

S.-I. Ohtani, M. A. Shay, and T. Mukai. Temporal structure of the fast convective flow in the plasma sheet : Comparison between observations and two-fluid simulations, *Journal of Geophysical Research (Space Physics)*, 109:A03210, March 2004.

Y. V. Khotyaintsev, C. M. Cully, A. Vaivads, M. André, and C. J. Owen. Plasma Jet Braking : Energy Dissipation and Nonadiabatic Electrons, *Physical Review Letters*, 106(16):165001, April 2011.

S. W. Alqeeq, O. Le Contel, P. Canu, A. Retinò, T. Chust, L. Mirioni, L. Richard, Y. Aït-Si-Ahmed, A. Alexandrova, A. Chuvatin, N. Ahmadi, S. M. Baraka, R. Nakamura, F. D. Wilder, D. J. Gershman, P. A. Lindqvist, Y. V. Khotyaintsev, R. E. Ergun, J. L. Burch, R. B. Torbert, C. T. Russell, W. Magnes, R. J. Strangeway, K. R. Bromund, H. Wei, F. Plaschke, B. J. Anderson, B. L. Giles, S. A. Fuselier, Y. Saito, and B. Lavraud. Investigation of the homogeneity of

energy conversion processes at dipolarization fronts from MMS measurements, *Physics of Plasmas*, 29(1):012906, January 2022.

R. Nakamura, W. Baumjohann, C. Mouikis, L. M. Kistler, A. Runov, M. Volwerk, Y. Asano, Z. Vörös, T. L. Zhang, B. Klecker, H. Rème, and A. Balogh. Spatial scale of high-speed flows in the plasma sheet observed by Cluster, , 31(9):L09804, May 2004.

Z. Y. Pu, K. B. Kang, A. Korth, S. Y. Fu, Q. G. Zong, Z. X. Chen, M. H. Hong, Z. X. Liu, C. G. Mouikis, R. W. H. Friedel, and T. Pulkkinen. Ballooning instability in the presence of a plasma flow : A synthesis of tail reconnection and current disruption models for the initiation of substorms, , 104(A5):10235–10248, May 1999.

A. T. Y. Lui. Reduction of the cross-tail current during near-Earth dipolarization with multisatellite observations, *Journal of Geophysical Research (Space Physics)*, 116(A12):A12239, December 2011.

C. L. Tang, L. Lu, M. Zhou, and Z. H. Yao. THEMIS observations of electron acceleration associated with the evolution of substorm dipolarization in the near-Earth tail, *Journal of Geophysical Research (Space Physics)*, 118(7):4237–4247, July 2013.

A. T. Y. Lui. Electron source at the outer boundary of the radiation belts : Storm time case, *Journal of Geophysical Research (Space Physics)*, 118(4):1545–1551, April 2013.

E. V. Panov, S. Lu, and P. L. Pritchett. Magnetotail Ion Structuring by Kinetic Ballooning-Interchange Instability, , 49(3):e96796, February 2022.

P. A. Cassak and M. A. Shay. Scaling of asymmetric magnetic reconnection : General theory and collisional simulations, *Physics of Plasmas*, 14(10):102114, October 2007.

B. Coppi, G. Laval, and R. Pellat. Dynamics of the Geomagnetic Tail, $\|, 16(26) : 1207 - -1210, June 1966$.

B. Lembege and R. Pellat. Stability of a thick two-dimensional quasineutral sheet, *Physics of Fluids*, 25(11):1995–2004, November 1982.

R. Pellat, F. V. Coroniti, and P. L. Pritchett. does ion tearing exist ?, , 18(2): 143–146, February 1991.

M. I. Sitnov, V. G. Merkin, M. Swisdak, T. Motoba, N. Buzulukova, T. E. Moore, B. H. Mauk, and S. Ohtani. Magnetic reconnection, buoyancy, and flapping motions in magnetotail explosions, *Journal of Geophysical Research (Space Physics)*, 119(9):7151–7168, September 2014.

A. Miura. Validity of the fluid description of critical β and Alfvén time scale of ballooning instability onset in the near-Earth collisionless high-β plasma, *Journal of Geophysical Research (Space Physics)*, 109(A2):A02211, February 2004.

O. A. Hurricane, R. Pellat, and F. V. Coroniti. A new approach to low-frequency "MHD-like" waves in magnetospheric plasmas, , 100(A10):19421–19428, October 1995.

P. L. Pritchett and F. V. Coroniti. Structure and consequences of the kinetic ballooning/interchange instability in the magnetotail, *Journal of Geophysical Research (Space Physics)*, 118(1):146–159, January 2013.

J. Birn, J. Raeder, Y. Wang, R. Wolf, and M. Hesse. On the propagation of bubbles in the geomagnetic tail, *Annales Geophysicae*, 22(5):1773–1786, May 2004.

K. Schindler and J. Birn. MHD stability of magnetotail equilibria including a background pressure, *Journal of Geophysical Research (Space Physics)*, 109(A10): A10208, October 2004.

J. Birn, R. Nakamura, E. V. Panov, and M. Hesse. Bursty bulk flows and dipolarization in MHD simulations of magnetotail reconnection, *Journal of Geophysical Research (Space Physics)*, 116(A1):A01210, January 2011.

P. N. Guzdar, A. B. Hassam, M. Swisdak, and M. I. Sitnov. A simple MHD model for the formation of multiple dipolarization fronts, , 37(20):L20102, October 2010.

H. Y. Lu, J. B. Cao, M. Zhou, H. S. Fu, R. Nakamura, T. L. Zhang, Y. V. Khotyaintsev, Y. D. Ma, and D. Tao. Electric structure of dipolarization fronts associated with interchange instability in the magnetotail, *Journal of Geophysical Research (Space Physics)*, 118(10):6019–6025, October 2013a.

H. Y. Lu, J. B. Cao, M. Zhou, H. S. Fu, R. Nakamura, T. L. Zhang, Y. V. Khotyaintsev, Y. D. Ma, and D. Tao. Electric structure of dipolarization fronts associated with interchange instability in the magnetotail, *Journal of Geophysical Research (Space Physics)*, 118(10):6019–6025, October 2013b.

M. Ashour-Abdalla, M. El-Alaoui, M. L. Goldstein, M. Zhou, D. Schriver, R. Richard, R. Walker, M. G. Kivelson, and K.-J. Hwang. Observations and simulations of non-local acceleration of electrons in magnetotail magnetic reconnection events, *Nature Physics*, 7(4):360–365, April 2011.

Q. Pan, M. Ashour-Abdalla, R. J. Walker, and M. El-Alaoui. Ion energization and transport associated with magnetic dipolarizations, , 41(16):5717–5726, August 2014.

H. S. Fu, J. B. Cao, Z. Zhima, Y. V. Khotyaintsev, V. Angelopoulos, O. Santolík, Y. Omura, U. Taubenschuss, L. Chen, and S. Y. Huang. First observation of rising-tone magnetosonic waves, , 41(21):7419–7426, November 2014.

G. Lapenta and L. Bettarini. Self-consistent seeding of the interchange instability in dipolarization fronts, , 38(11):L11102, June 2011.

D. Schmid, M. Volwerk, R. Nakamura, W. Baumjohann, and M. Heyn. A statistical and event study of magnetotail dipolarization fronts, *Annales Geophysicae*, 29 (9):1537–1547, September 2011.

S. Xiao, T. Zhang, G. Wang, M. Volwerk, Y. Ge, D. Schmid, R. Nakamura, W. Baumjohann, and F. Plaschke. Occurrence rate of dipolarization fronts in the plasma sheet : Cluster observations, *Annales Geophysicae*, 35(4):1015–1022, August 2017.

O. Le Contel, P. Leroy, A. Roux, C. Coillot, D. Alison, A. Bouabdellah, L. Mirioni, L. Meslier, A. Galic, M. C. Vassal, R. B. Torbert, J. Needell, D. Rau, I. Dors, R. E. Ergun, J. Westfall, D. Summers, J. Wallace, W. Magnes, A. Valavanoglou, G. Olsson, M. Chutter, J. Macri, S. Myers, S. Turco, J. Nolin, D. Bodet, K. Rowe, M. Tanguy, and B. de la Porte. The Search-Coil Magnetometer for MMS, , 199 (1-4):257–282, March 2016.

S. Y. Huang, M. Zhou, X. H. Deng, Z. G. Yuan, Y. Pang, Q. Wei, W. Su, H. M. Li, and Q. Q. Wang. Kinetic structure and wave properties associated with sharp dipolarization front observed by Cluster, *Annales Geophysicae*, 30(1):97–107, January 2012.

H. Viberg, Y. V. Khotyaintsev, A. Vaivads, M. André, H. S. Fu, and N. Cornilleau-Wehrlin. Whistler mode waves at magnetotail dipolarization fronts, *Journal of Geophysical Research (Space Physics)*, 119:2605–2611, April 2014.

H. Li, M. Zhou, X. Deng, Z. Yuan, L. Guo, X. Yu, Y. Pang, and S. Huang. A statistical study on the whistler waves behind dipolarization fronts, *Journal of Geophysical Research (Space Physics)*, 120(2):1086–1095, February 2015a.

E. E. Grigorenko, A. Y. Malykhin, D. R. Shklyar, S. Fadanelli, B. Lavraud, E. V. Panov, L. Avanov, B. Giles, and O. Le Contel. Investigation of Electron Distribution Functions Associated With Whistler Waves at Dipolarization Fronts in the Earth's Magnetotail : MMS Observations, *Journal of Geophysical Research (Space Physics)*, 125(9):e28268, September 2020.

A. Greco, A. Artemyev, G. Zimbardo, V. Angelopoulos, and A. Runov. Role of lower hybrid waves in ion heating at dipolarization fronts, *Journal of Geophysical Research (Space Physics)*, 122(5):5092–5104, May 2017.

A. Divin, Y. V. Khotyaintsev, A. Vaivads, and M. André. Lower hybrid drift instability at a dipolarization front, *Journal of Geophysical Research (Space Physics)*, 120(2):1124–1132, February 2015a.

Y. V. Khotyaintsev, A. Divin, A. Vaivads, M. André, and S. Markidis. Energy conversion at dipolarization fronts, , 44(3):1234–1242, February 2017.

D.-X. Pan, Y. V. Khotyaintsev, D. B. Graham, A. Vaivads, X.-Z. Zhou, M. André, P.-A. Lindqvist, R. E. Ergun, O. Le Contel, C. T. Russell, R. B. Torbert, B. Giles, and J. L. Burch. Rippled Electron-Scale Structure of a Dipolarization Front, , 45(22):12,116–12,124, November 2018.

T. K. M. Nakamura, T. Umeda, R. Nakamura, H. S. Fu, and M. Oka. Disturbance of the Front Region of Magnetic Reconnection Outflow Jets due to the Lower-Hybrid Drift Instability, $\|, 123(23) : 235101, December 2019a$.

H. Li, C. Zhu, L. Guo, Q. Cheng, and O. Le Contel. Magnetospheric Multiscale Observations of the Off-equatorial Dipolarization Front Dynamics in the Terrestrial Magnetotail, , 899(2):125, August 2020.

C. M. Liu, A. Vaivads, D. B. Graham, Y. V. Khotyaintsev, H. S. Fu, A. Johlander, M. André, and B. L. Giles. Ion-Beam-Driven Intense Electrostatic Solitary Waves in Reconnection Jet, , 46(22):12,702–12,710, November 2019.

L. Andersson, R. E. Ergun, J. Tao, A. Roux, O. Lecontel, V. Angelopoulos, J. Bonnell, J. P. McFadden, D. E. Larson, S. Eriksson, T. Johansson, C. M. Cully, D. N. Newman, M. V. Goldman, K.-H. Glassmeier, and W. Baumjohann. New Features of Electron Phase Space Holes Observed by the THEMIS Mission, *Physical Review Letters*, 102(22):225004, June 2009.

J. B. Tao, R. E. Ergun, L. Andersson, J. W. Bonnell, A. Roux, O. LeContel, V. Angelopoulos, J. P. McFadden, D. E. Larson, C. M. Cully, H.-U. Auster, K.-H. Glassmeier, W. Baumjohann, D. L. Newman, and M. V. Goldman. A model of electromagnetic electron phase-space holes and its application, *Journal of Geophysical Research (Space Physics)*, 116:A11213, November 2011.

M. Zhou, M. Ashour-Abdalla, X. Deng, D. Schriver, M. El-Alaoui, and Y. Pang. THEMIS observation of multiple dipolarization fronts and associated wave characteristics in the near-Earth magnetotail, *Geophys. Res. Lett.*, 36:L20107, October 2009.

J. D. Huba, N. T. Gladd, and K. Papadopoulos. The lower-hybrid-drift instability as a source of anomalous resistivity for magnetic field line reconnection, , 4(3): 125–128, March 1977.

I. H. Cairns and B. F. McMillan. Electron acceleration by lower hybrid waves in magnetic reconnection regions, *Physics of Plasmas*, 12(10):102110, October 2005.

C. C. Chaston, J. W. Bonnell, L. Clausen, and V. Angelopoulos. Energy transport by kinetic-scale electromagnetic waves in fast plasma sheet flows, *Journal of Geophysical Research (Space Physics)*, 117:A09202, September 2012.

M. Hamrin, T. Pitkänen, P. Norqvist, T. Karlsson, H. Nilsson, M. André, S. Buchert, A. Vaivads, O. Marghitu, B. Klecker, L. M. Kistler, and I. Dandouras. Evidence for the braking of flow bursts as they propagate toward the Earth, *Journal of Geophysical Research (Space Physics)*, 119(11):9004–9018, November 2014.

H. S. Fu, Y. V. Khotyaintsev, A. Vaivads, M. André, V. A. Sergeev, S. Y. Huang, E. A. Kronberg, and P. W. Daly. Pitch angle distribution of suprathermal electrons behind dipolarization fronts : A statistical overview, *Journal of Geophysical Research (Space Physics)*, 117(A12):A12221, December 2012b.

Z. H. Yao, I. J. Rae, R. L. Guo, A. N. Fazakerley, C. J. Owen, R. Nakamura, W. Baumjohann, C. E. J. Watt, K. J. Hwang, B. L. Giles, C. T. Russell, R. B. Torbert, A. Varsani, H. S. Fu, Q. Q. Shi, and X. J. Zhang. A direct examination of the dynamics of dipolarization fronts using MMS, *Journal of Geophysical Research (Space Physics)*, 122(4):4335–4347, April 2017.

C. M. Liu, H. S. Fu, Y. Xu, Y. V. Khotyaintsev, J. L. Burch, R. E. Ergun, D. G. Gershman, and R. B. Torbert. Electron-Scale Measurements of Dipolarization Front, , 45(10):4628–4638, May 2018.

J. Yang, J. B. Cao, H. S. Fu, T. Y. Wang, W. L. Liu, and Z. H. Yao. Broadband high-frequency waves detected at dipolarization fronts, *Journal of Geophysical Research (Space Physics)*, 122(4):4299–4307, April 2017a.

Z. H. Zhong, X. H. Deng, M. Zhou, W. Q. Ma, R. X. Tang, Y. V. Khotyaintsev, B. L. Giles, C. T. Russell, and J. L. Burch. Energy Conversion and Dissipation at Dipolarization Fronts : A Statistical Overview, , 46(22):12,693–12,701, November 2019.

L. Q. Zhang, W. Baumjohann, Y. V. Khotyaintsev, J. L. Burch, J. Webster, J. Y. Wang, C. Wang, L. Dai, and C. Y. Zhang. BBF Deceleration Down-Tail of X < -15 R_E From MMS Observation, *Journal of Geophysical Research (Space Physics)*, 125(2):e26837, February 2020.

A. Divin, Y. V. Khotyaintsev, A. Vaivads, M. André, S. Markidis, and G. Lapenta. Evolution of the lower hybrid drift instability at reconnection jet front, *Journal of Geophysical Research (Space Physics)*, 120(4):2675–2690, April 2015b.

Y. Yang, W. H. Matthaeus, T. N. Parashar, C. C. Haggerty, V. Roytershteyn, W. Daughton, M. Wan, Y. Shi, and S. Chen. Energy transfer, pressure tensor, and heating of kinetic plasma, *Physics of Plasmas*, 24(7):072306, July 2017b.

M. I. Sitnov, V. G. Merkin, V. Roytershteyn, and M. Swisdak. Kinetic Dissipation Around a Dipolarization Front, , 45(10):4639–4647, May 2018.

T. K. M. Nakamura, T. Umeda, R. Nakamura, H. S. Fu, and M. Oka. Disturbance of the Front Region of Magnetic Reconnection Outflow Jets due to the Lower-Hybrid Drift Instability, ‖, 123(23) : 235101, *December*2019*b*.

L. Palin, C. Jacquey, H. Opgenoorth, M. Connors, V. Sergeev, J.-A. Sauvaud, R. Nakamura, G. D. Reeves, H. J. Singer, V. Angelopoulos, and L. Turc. Three-dimensional current systems and ionospheric effects associated with small dipolarization fronts, *Journal of Geophysical Research (Space Physics)*, 120:3739–3757, May 2015.

Z. H. Yao, Z. Y. Pu, S. Y. Fu, V. Angelopoulos, M. Kubyshkina, X. Xing, L. Lyons, Y. Nishimura, L. Xie, X. G. Wang, C. J. Xiao, X. Cao, J. Liu, H. Zhang, M. Nowada, Q. G. Zong, R. L. Guo, J. Zhong, and J. X. Li. Mechanism of substorm current wedge formation : THEMIS observations, , 39(13):L13102, July 2012.

K. J. Hwang, M. L. Goldstein, E. Lee, and J. S. Pickett. Cluster observations of multiple dipolarization fronts, *Journal of Geophysical Research (Space Physics)*, 116:A00I32, April 2011.

M. S. Nakamura, H. Matsumoto, and M. Fujimoto. Interchange instability at the leading part of reconnection jets, *Geophys. Res. Lett.*, 29:1247, April 2002.

P. L. Pritchett, F. V. Coroniti, and Y. Nishimura. The kinetic ballooning/interchange instability as a source of dipolarization fronts and auroral streamers, *Journal of Geophysical Research (Space Physics)*, 119:4723–4739, June 2014.

Z. H. Yao, J. Liu, C. J. Owen, C. Forsyth, I. J. Rae, Z. Y. Pu, H. S. Fu, X. Z. Zhou, Q. Q. Shi, A. M. Du, R. L. Guo, and X. N. Chu. A physical explanation for the magnetic decrease ahead of dipolarization fronts, *Annales Geophysicae*, 33(10):1301–1309, October 2015.

S. Lu, A. V. Artemyev, V. Angelopoulos, Q. Lu, and J. Liu. On the current density reduction ahead of dipolarization fronts, *Journal of Geophysical Research (Space Physics)*, 121(5):4269–4278, May 2016.

R. E. Ergun, S. Tucker, J. Westfall, K. A. Goodrich, D. M. Malaspina, D. Summers, J. Wallace, M. Karlsson, J. Mack, N. Brennan, B. Pyke, P. Withnell, R. Torbert, J. Macri, D. Rau, I. Dors, J. Needell, P.-A. Lindqvist, G. Olsson, and C. M. Cully. The Axial Double Probe and Fields Signal Processing for the MMS Mission, *Space Sci. Rev.*, 199:167–188, March 2016.

S. A. Fuselier, W. S. Lewis, C. Schiff, R. Ergun, J. L. Burch, S. M. Petrinec, and K. J. Trattner. Magnetospheric Multiscale Science Mission Profile and Operations, , 199(1-4):77–103, March 2016.

D. N. Baker, L. Riesberg, C. K. Pankratz, R. S. Panneton, B. L. Giles, F. D. Wilder, and R. E. Ergun. Magnetospheric Multiscale Instrument Suite Operations and Data System, , 199(1-4):545–575, March 2016.

P.-A. Lindqvist, G. Olsson, R. B. Torbert, B. King, M. Granoff, D. Rau, G. Needell, S. Turco, I. Dors, P. Beckman, J. Macri, C. Frost, J. Salwen, A. Eriksson, L. Åhlén, Y. V. Khotyaintsev, J. Porter, K. Lappalainen, R. E. Ergun, W. Wermeer, and S. Tucker. The Spin-Plane Double Probe Electric Field Instrument for MMS, *Space Sci. Rev.*, 199:137–165, March 2016.

B. H. Mauk, J. B. Blake, D. N. Baker, J. H. Clemmons, G. D. Reeves, H. E. Spence, S. E. Jaskulek, C. E. Schlemm, L. E. Brown, S. A. Cooper, J. V. Craft, J. F. Fennell, R. S. Gurnee, C. M. Hammock, J. R. Hayes, P. A. Hill, G. C. Ho, J. C. Hutcheson, A. D. Jacques, S. Kerem, D. G. Mitchell, K. S. Nelson, N. P. Paschalidis, E. Rossano, M. R. Stokes, and J. H. Westlake. The Energetic Particle Detector (EPD) Investigation and the Energetic Ion Spectrometer (EIS) for the Magnetospheric Multiscale (MMS) Mission, , 199(1-4):471–514, March 2016.

R. B. Torbert, C. T. Russell, W. Magnes, R. E. Ergun, P.-A. Lindqvist, O. LeContel, H. Vaith, J. Macri, S. Myers, D. Rau, J. Needell, B. King, M. Granoff, M. Chutter, I. Dors, G. Olsson, Y. V. Khotyaintsev, A. Eriksson, C. A. Kletzing, S. Bounds, B. Anderson, W. Baumjohann, M. Steller, K. Bromund, G. Le, R. Nakamura, R. J. Strangeway, H. K. Leinweber, S. Tucker, J. Westfall, D. Fischer, F. Plaschke, J. Porter, and K. Lappalainen. The FIELDS Instrument Suite on MMS : Scientific Objectives, Measurements, and Data Products, *Space Sci. Rev.*, 199:105–135, March 2016a.

D. J. Gershman, J. C. Dorelli, A. F.-Viñas, and C. J. Pollock. The calculation of moment uncertainties from velocity distribution functions with random errors, *Journal of Geophysical Research (Space Physics)*, 120:6633–6645, August 2015.

B. U. Ö. Sonnerup and M. Scheible. Minimum and Maximum Variance Analysis*ISSI Scientific Reports Series*, 1 :185–220, January 1998.

C. C. Harvey. Spatial Gradients and the Volumetric Tensor*ISSI Scientific Reports Series*, 1 :307–322, January 1998.

G. Chanteur and C. Harvey. Spatial interpolation fo four spacecraft : Application to magnetic gradients. In G. Paschman and P. Daly, editors, *Analysis Methods for Multi-Spacecraft Data*, ISSI Scientific Report SR-001, chapter 15, pages 371–393. European Space Agency, July 1998.

M. W. Dunlop, A. Balogh, K. H. Glassmeier, and P. Robert. Four-point Cluster application of magnetic field analysis tools : The Curlometer, *Journal of Geophysical Research (Space Physics)*, 107(A11):1384, November 2002.

P. Robert, M. W. Dunlop, A. Roux, and G. Chanteur. Accuracy of Current Density Determination*ISSI Scientific Reports Series*, 1 :395–418, January 1998.

C. Chree. Magnetic Declination at Kew Observatory, 1890-1900, *Proceedings of the Royal Society of London Series A*, 80(536):113, February 1908.

S. Morley, J. Koller, D. Welling, B. Larsen, and J. Niehof. SpacePy : Python-Based Tools for the Space Science Community, January 2014.

T. N. Davis and M. Sugiura. Auroral electrojet activity index AE and its universal time variations, , 71(3):785–801, February 1966.

Q. Q. Shi, C. Shen, Z. Y. Pu, M. W. Dunlop, Q. G. Zong, H. Zhang, C. J. Xiao, Z. X. Liu, and A. Balogh. Dimensional analysis of observed structures using multipoint magnetic field measurements : Application to Cluster, , 32(12):L12105, June 2005.

Q. Q. Shi, C. Shen, M. W. Dunlop, Z. Y. Pu, Q. G. Zong, Z. X. Liu, E. Lucek, and A. Balogh. Motion of observed structures calculated from multi-point magnetic field measurements : Application to Cluster, , 33(8):L08109, April 2006.

Z. Yao, W. J. Sun, S. Y. Fu, Z. Y. Pu, J. Liu, V. Angelopoulos, X. J. Zhang, X. N. Chu, Q. Q. Shi, R. L. Guo, and Q. G. Zong. Current structures associated with dipolarization fronts, *Journal of Geophysical Research (Space Physics)*, 118(11): 6980–6985, November 2013.

H. S. Fu, Y. V. Khotyaintsev, M. André, and A. Vaivads. Fermi and betatron acceleration of suprathermal electrons behind dipolarization fronts, , 38(16): L16104, August 2011.

A. T. Y. Lui, Y. Zheng, H. RèMe, M. W. Dunlop, G. Gustafsson, and C. J. Owen. Breakdown of the frozen-in condition in the Earth's magnetotail, *Journal of Geophysical Research (Space Physics)*, 112(A4):A04215, April 2007.

R. B. Torbert, J. L. Burch, B. L. Giles, D. Gershman, C. J. Pollock, J. Dorelli, L. Avanov, M. R. Argall, J. Shuster, R. J. Strangeway, C. T. Russell, R. E. Ergun, F. D. Wilder, K. Goodrich, H. A. Faith, C. J. Farrugia, P. A. Lindqvist, T. Phan, Y. Khotyaintsev, T. E. Moore, G. Marklund, W. Daughton, W. Magnes, C. A. Kletzing, and S. Bounds. Estimates of terms in Ohm's law during an encounter with an electron diffusion region, , 43(12):5918–5925, June 2016b.

J. Sittler, E. C. and J. D. Scudder. An empirical polytrope law for solar wind thermal electrons between 0.45 and 4.76 AU : Voyager 2 and Mariner 10, , 85 (A10):5131–5137, October 1980.

J. Birn and M. Hesse. Energy release and conversion by reconnection in the magnetotail, *Annales Geophysicae*, 23:3365–3373, November 2005.

J. E. Stawarz, J. P. Eastwood, K. J. Genestreti, R. Nakamura, R. E. Ergun, D. Burgess, J. L. Burch, S. A. Fuselier, D. J. Gershman, B. L. Giles, O. Le Contel, P. A. Lindqvist, C. T. Russell, and R. B. Torbert. Intense Electric Fields and Electron-Scale Substructure Within Magnetotail Flux Ropes as Revealed by the Magnetospheric Multiscale Mission, , 45(17):8783–8792, September 2018.

R. C. Davidson and N. T. Gladd. Anomalous transport properties associated with the lower-hybrid-drift instability, *Physics of Fluids*, 18:1327–1335, October 1975.

J. D. Huba, N. T. Gladd, and K. Papadopoulos. Lower-hybrid-drift wave turbulence in the distant magnetotail, , 83:5217–5226, November 1978.

L. J. Chen, S. Wang, O. Le Contel, A. Rager, M. Hesse, J. Drake, J. Dorelli, J. Ng, N. Bessho, D. Graham, L. B. Wilson, T. Moore, B. Giles, W. Paterson, B. Lavraud, K. Genestreti, R. Nakamura, Y. V. Khotyaintsev, R. E. Ergun, R. B. Torbert, J. Burch, C. Pollock, C. T. Russell, P. A. Lindqvist, and L. Avanov. Lower-Hybrid Drift Waves Driving Electron Nongyrotropic Heating and Vortical Flows in a Magnetic Reconnection Layer, $\|, 125(2) : 025103, July 2020$.

G. Lapenta and AIDA H2020 Team. Processing big data from space missions and massively parallel simulations within the Horizon 2020 Project AIDA. In *Solar Heliospheric and INterplanetary Environment (SHINE 2019)*, page 44, May 2019.

H. Li, M. Zhou, X. Deng, Z. Yuan, L. Guo, X. Yu, Y. Pang, and S. Huang. A statistical study on the whistler waves behind dipolarization fronts, *Journal of Geophysical Research (Space Physics)*, 120(2):1086–1095, February 2015b.

L. Song, M. Zhou, Y. Yi, X. Deng, Z. Zhong, and H. Man. Force and Energy Balance of the Dipolarization Front, *Journal of Geophysical Research (Space Physics)*, 125(9):e28278, September 2020.

L. Wang, C. Huang, X. Cao, A. Du, and Y. S. Ge. Magnetic Energy Conversion and Transport in the Terrestrial Magnetotail Due to Dipolarization Fronts, *Journal of Geophysical Research (Space Physics)*, 125(10):e28568, October 2020.

T. Nagai, M. Fujimoto, Y. Saito, S. Machida, T. Terasawa, R. Nakamura, T. Yamamoto, T. Mukai, A. Nishida, and S. Kokubun. Structure and dynamics of magnetic reconnection for substorm onsets with Geotail observations, , 103(A3): 4419–4440, March 1998.

M. Zhou, S.-Y. Huang, X.-H. Deng, and Y. Pang. Observation of a Sharp Negative Dipolarization Front in the Reconnection Outflow Region, *Chinese Physics Letters*, 28(10):109402, October 2011.

A. Runov, V. Angelopoulos, and X. Z. Zhou. Multipoint observations of dipolarization front formation by magnetotail reconnection, *Journal of Geophysical Research (Space Physics)*, 117(A5):A05230, May 2012.

A. Runov, V. Angelopoulos, X. Z. Zhou, X. J. Zhang, S. Li, F. Plaschke, and J. Bonnell. A THEMIS multicase study of dipolarization fronts in the magnetotail plasma sheet, *Journal of Geophysical Research (Space Physics)*, 116(A5): A05216, May 2011.

J. Dargent, N. Aunai, B. Lavraud, S. Toledo-Redondo, M. A. Shay, P. A. Cassak, and K. Malakit. Kinetic simulation of asymmetric magnetic reconnection with cold ions, *Journal of Geophysical Research (Space Physics)*, 122(5):5290–5306, May 2017.

V. Angelopoulos, P. Cruce, A. Drozdov, E. W. Grimes, N. Hatzigeorgiu, D. A. King, D. Larson, J. W. Lewis, J. M. McTiernan, D. A. Roberts, C. L. Russell, T. Hori, Y. Kasahara, A. Kumamoto, A. Matsuoka, Y. Miyashita, Y. Miyoshi, I. Shinohara, M. Teramoto, J. B. Faden, A. J. Halford, M. McCarthy, R. M. Millan, J. G. Sample, D. M. Smith, L. A. Woodger, A. Masson, A. A. Narock, K. Asamura, T. F. Chang, C. Y. Chiang, Y. Kazama, K. Keika, S. Matsuda, T. Segawa, K. Seki, M. Shoji, S. W. Y. Tam, N. Umemura, B. J. Wang, S. Y. Wang, R. Redmon, J. V. Rodriguez, H. J. Singer, J. Vandegriff, S. Abe, M. Nose, A. Shinbori, Y. M. Tanaka, S. UeNo, L. Andersson, P. Dunn, C. Fowler, J. S. Halekas, T. Hara, Y. Harada, C. O. Lee, R. Lillis, D. L. Mitchell, M. R. Argall, K. Bromund, J. L. Burch, I. J. Cohen, M. Galloy, B. Giles, A. N. Jaynes, O. Le Contel, M. Oka, T. D. Phan, B. M. Walsh, J. Westlake, F. D. Wilder, S. D. Bale, R. Livi, M. Pulupa, P. Whittlesey, A. DeWolfe, B. Harter, E. Lucas, U. Auster, J. W. Bonnell, C. M. Cully, E. Donovan, R. E. Ergun, H. U. Frey, B. Jackel, A. Keiling, H. Korth, J. P. McFadden, Y. Nishimura, F. Plaschke, P. Robert, D. L. Turner, J. M. Weygand, R. M. Candey, R. C. Johnson, T. Kovalick, M. H. Liu, R. E. McGuire, A. Breneman, K. Kersten, and P. Schroeder. The Space Physics Environment Data Analysis System (SPEDAS), , 215(1):9, January 2019.

G. Lapenta. The AIDA Project : tools for ML in Space Weather and Space Science. In *44th COSPAR Scientific Assembly. Held 16-24 July*, volume 44, page 869, July 2022.

Titre: Processus de conversion d'énergie liés aux fronts de dipolarisation dans la queue géomagnétique **Mots clés:** Conversion d'énergie ; Fronts de Dipolarisation ; Magnétosphère terrestre ; Queue géomagnétique ; transport de plasma

Résumé: Des écoulements rapides de plasma ont été détectés depuis longtemps dans le côté nuit de la magnétosphère terrestre, la queue géomagnétique. Différents processus de formation tels que la reconnexion magnétique ou l'instabilité cinétique de ballonnement-interchange sont toujours étudiés. Lors de leur propagation vers la Terre, ces écoulements produisent une brusque augmentation de la composante nord du champ magnétique appelée front de dipolarisation (DF). Ces structures cinétiques contribuent de manière significative à la dissipation d'énergie dans la magnétosphère. Cette étude a pour but de mieux comprendre les processus de conversion d'énergie décrits par le terme $\mathbf{J} \cdot \mathbf{E}$ ($\mathbf{J}$ étant la densité de courant et $\mathbf{E}$ le champ électrique) qui se produisent au voisinage de ces fronts et à déterminer leur rôle dans le cycle global de l'énergie dans la magnétosphère. En utilisant les mesures *in situ* de la mission Magnétosphérique Multiscale, constituée de quatre satellites identiques évoluant dans une configuration tétraédrique et séparés à l'échelle des électrons, j'ai d'abord étudié les structures de densité de courant, les différents termes de la loi d'Ohm, et les processus de conversion d'énergie de 6 fronts. J'ai montré que les ions étaient découplés du champ magnétique principalement par l'effet du champ électrique de Hall mais que la contribution du gradient de pression électronique était aussi significative. Cela implique aussi que les électrons sont aussi découplés par leur propre gradient de pression au niveau du front. En ce qui concerne les processus de conversion d'énergie dans le référentiel du satellite, l'énergie est transférée des champs électromagnétiques au plasma en amont du front (région de dissipation ou de charge) alors qu'elle est transférée du plasma aux champs (région de dynamo ou de générateur) en aval. Cette inversion de la conversion d'énergie est causée par l'inversion du courant diamagnétique dominé par le gradient de pression des ions au niveau du front. Dans le référentiel fluide (électrons ou ions), l'énergie est transférée aux champs en raison du champ électrique associé au gradient de pression électronique ce qui pourrait contribuer au ralentissement de l'écoulement. De plus, il est montré que les processus de conversion d'énergie ne sont pas homogènes à l'échelle électronique principalement en raison des variations du champ électrique. Ces résultats d'études de cas ont été étendus grâce à une étude statistique réalisée sur l'ensemble de la saison 2017 durant laquelle MMS était localisée dans la queue géomagnétique. A partir de cette étude, il s'avère que deux classes de DF peuvent être distinguées. La classe I (74,4%) correspond aux propriétés standards des DF et à une dissipation d'énergie. La classe II (25,6%), qui est nouvelle, inclut les 6 DF précédemment discutés et correspond à une bosse du champ magnétique associée à un minimum des pressions ionique et électronique et à une inversion du processus de conversion d'énergie (dissipation puis dynamo). L'origine possible de cette deuxième classe est discutée. Pour les deux classes de DF, il est montré que le processus de conversion d'énergie dans le référentiel du satellite est gouverné par le courant diamagnétique dominé par le gradient de pression des ions. Dans le référentiel fluide, il est lié au gradient de pression des électrons.

Title: Title Energy Conversion Processes related to Dipolarisation Fronts in the Earth's magnetotail **Keywords:**Energy Conversion, Dipolarisation Fronts, Earth's magnetosphere ; Earth's magnetotail ; Plasma transport

Abstract: Fast plasma flows have been detected in the nightside of the Earth's magnetosphere, the magnetotail, for a long time. Different processes such as magnetic reconnection or kinetic ballooning-interchange instability are still investigated. While propagating Earthward, these flows generate a sharp increase of the northward component of the magnetic field named dipolarisation front (DF). These kinetic scale structures contribute significantly to the energy dissipation in the magnetosphere. This study aims at better understanding the energy conversion processes described by $\mathbf{J} \cdot \mathbf{E}$ ($\mathbf{J}$ being the current density and $\mathbf{E}$ the electric field) which occur in the vicinity of these fronts and at determining their role in the energy global cycle of the magnetosphere. Using in situ measurements from the Magnetospheric Multiscale mission, which consists of four identical satellites evolving in a tetrahedral configuration and separated at electron scales, I have first investigated the current density structures, the different terms of the Ohm's law, and the energy conversion processes for 6 DFs. I found that for all DFs, ions are mainly decoupled from the magnetic field by the Hall electric field but the electron pressure gradient could also contribute. It implies that electrons could be decoupled by the effect of their own pressure gradient term in the Ohm's law at DF. Regarding the energy conversion processes in the spacecraft frame, the energy is transferred from the electromagnetic fields to the plasma ahead of the DF (dissipation or loading region) whereas it is transferred from the plasma to the fields (dynamo or generator region) behind the front. This energy conversion reversal is caused by the reversal of the ion diamagnetic current at DF. In the fluid frame, the energy is always transferred to the fields, due to the electric field generated by the electron pressure gradient, which could contribute to the slowdown of the flow. Furthermore, it is shown that the energy conversion processes are not homogeneous at the electron scale mostly due to the variations of the electric fields. These case study results have been extended thanks to a statistical study carried out over the full 2017 magnetotail season. From this study, it turns out that two DF classes can be distinguished : class I (74.4%) corresponds to the standard DF properties and energy dissipation whereas a new class II (25.6%), which includes the 6 DF previously discussed, corresponds to a bump of the magnetic field associated with a minimum of the ion and electron pressures and a reversal of the energy conversion process. The possible origin of this second class is discussed. For both DF classes, it is shown that the energy conversion process in the spacecraft frame is driven by the diamagnetic current dominated by the ion pressure gradient. In the fluid frame, it is driven by the electron pressure gradient.

Sorbonne Université
Ecole Doctorale Astronomie et Astrophysique d'Ile de France
Campus Pierre et Marie Curie BC 90 4, place Jussieu, Paris, France

Titre: Processus de conversion d'énergie liés aux fronts de dipolarisation dans la queue géomagnétique **Mots clés:** Conversion d'énergie, Fronts de Dipolarisation, Magnétosphère terrestre ; Queue géoamgnétique ; Transport de plasma

Résumé pour le domaine public: Des écoulements rapides de plasma sont détectés depuis longtemps dans le côté nuit de la magnétosphère terrestre, la queue géomagnétique. En se propageant vers la Terre, ces écoulements produisent une forte augmentation de la composante nord du champ magnétique appelée front de dipolarisation (DF) et contribuent de manière significative à la dissipation d'énergie dans la magnétosphère. En utilisant les mesures *in situ* recueillies en 2017 par la mission Magnétosphérique Multiscale, constituée de quatre satellites identiques évoluant dans une configuration tétraédrique et séparés à l'échelle des électrons, deux classes de DF peuvent être distinguées. La classe I (74,4%) présente des propriétés DF standards et à une dissipation d'énergie alors qu'une nouvelle classe II (25,6%) correspond à une bosse du champ magnétique et une inversion du transfert d'énergie (dissipation puis dynamo) Pour les deux classes, le transfert d'énergie est gouverné par le gradient de pression des ions au niveau du DF.

Title: Energy Conversion Processes related to Dipolarisation Fronts in the Earth's magnetotail **Keywords:** Energy Conversion, Dipolarisation Fronts, Earth's magnetosphere ; Earth's magnetotail ; Plasma transport

Abstract for public domain: Fast plasma flows have been detected in the nightside of the Earth's magnetosphere, the magnetotail, for a long time. While propagating toward the Earth, these flows generate a sharp increase of the northward component of the magnetic field named dipolarisation front (DF) which contribute significantly to the energy dissipation in the magnetosphere. Using in situ measurements gathered in 2017 by the Magnetospheric Multiscale mission, which consists of four identical satellites evolving in a tetrahedral configuration and separated at electron scales, two DF classes can be distinguished. Class I (74.4%) presents standard DF properties and energy transfer from the electromagnetic fields to the plasma whereas a new class II (25.6%) corresponds to a bump of the magnetic field and a reversal of the energy transfer (dissipation then dynamo). For both classes, this energy transfer is driven by the ion pressure gradient at DF.

Sorbonne Université
Ecole Doctorale Astronomie et Astrophysique d'Ile de France
Campus Pierre et Marie Curie BC 90 4, place Jussieu, Paris, France